



저작자표시-비영리-변경금지 2.0 대한민국

이용자는 아래의 조건을 따르는 경우에 한하여 자유롭게

- 이 저작물을 복제, 배포, 전송, 전시, 공연 및 방송할 수 있습니다.

다음과 같은 조건을 따라야 합니다:



저작자표시. 귀하는 원저작자를 표시하여야 합니다.



비영리. 귀하는 이 저작물을 영리 목적으로 이용할 수 없습니다.



변경금지. 귀하는 이 저작물을 개작, 변형 또는 가공할 수 없습니다.

- 귀하는, 이 저작물의 재이용이나 배포의 경우, 이 저작물에 적용된 이용허락조건을 명확하게 나타내어야 합니다.
- 저작권자로부터 별도의 허가를 받으면 이러한 조건들은 적용되지 않습니다.

저작권법에 따른 이용자의 권리는 위의 내용에 의하여 영향을 받지 않습니다.

이것은 [이용허락규약\(Legal Code\)](#)을 이해하기 쉽게 요약한 것입니다.

[Disclaimer](#)

Doctoral Thesis

Design of Micro/Nanostructured Materials for  
Flexible Electronics and Sensing Applications

Seongdong Lim

Department of Chemical Engineering

Graduate School of UNIST

2019

# Design of Micro/Nanostructured Materials for Flexible Electronics and Sensing Applications

Seongdong Lim

Department of Chemical Engineering

Graduate School of UNIST

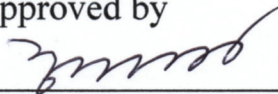
# Design of Micro/Nanostructured Materials for Flexible Electronics and Sensing Applications

A thesis/dissertation  
submitted to the Graduate School of UNIST  
in partial fulfillment of the  
requirements for the degree of  
Doctor of Philosophy

Seongdong Lim

May 20, 2019

Approved by



---

Advisor

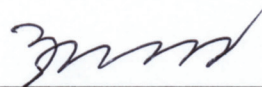
Hyunhyub Ko

# Design of Micro/Nanostructured Materials for Flexible Electronics and Sensing Applications

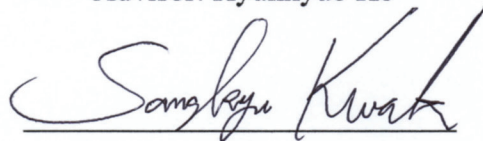
Seongdong Lim

This certifies that the thesis/dissertation of Seongdong Lim is approved.

May 20, 2019




Advisor: Hyunhyub Ko



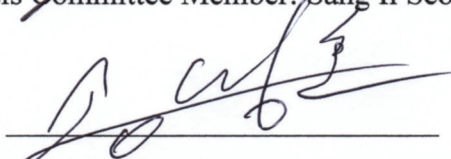
Thesis Committee Member: Sang Kyu Kwak



Thesis Committee Member: Chang Young Lee



Thesis Committee Member: Sang Il Seok



Thesis Committee Member: Myoung Hoon Song

## Abstract

Nowadays, the rapid development of modern society with the Fourth Industrial Revolution has initiated technological advances in electronic devices for improving the quality of human life. In addition, electronic devices have been evolved into human-interactive wearable electronics for smart healthcare systems, internet of things, augmented reality, and humanoid robots. Therefore, innovative and multirole-featured flexible sensing devices with advanced communication capability becomes considerably important for future electronics beyond the classical processing devices complying with Moore's law. In particular, photodetectors are essential for detecting light by transducing an electrical signal, enabling recognition and imaging of some objects with contactless detection. In addition, mechanosensors offer useful physical information such as touch and gesture through direct contact with objects. The introduction of micro/nanostructures into electronic sensors can be helpful to maximize the performance of both photodetectors and mechanosensors with improved light absorption and effective transmission of external forces, respectively. Furthermore, the novel design of device architectures with appropriate use of unique properties of the base materials allows diverse functionalities to flexible sensors, which is advantageous in next-generation electronic devices.

In this thesis, we demonstrate highly sensitive and multifunctional flexible sensing devices for future electronics *via* a novel design of micro/nanostructured materials. In Chapter 1, we briefly introduce the basic concepts and current technologies of flexible photodetectors and mechanosensors, respectively. In Chapter 2, we develop unique design of flexible photodetectors with both omnidirectional and broadband light-detection capabilities based on hierarchical ZnO nanowire arrays on flexible honeycomb-structured Si membranes. As another future proximity sensors, in Chapter 3, we suggest new fabrication method for hierarchical organic-inorganic hybrid perovskite nanoribbon arrays with controlled internal nanorod structures. The hierarchical perovskite nanoribbon based flexible photodetectors exhibit high photoresponsivity as well as self-powered operation and polarization-sensitive detection capabilities. Chapter 4 describes spacer-free, ultrathin, and highly sensitive triboelectric mechanosensors based on human skin-inspired hierarchical nanoporous and interlocked microridge structured polymers with gradient stiffness. Finally, we summarize this thesis with future prospects and challenges of this field in Chapter 5.



## Contents

Abstract .....	1
Contents .....	2
List of Figures .....	4
List of Tables and Videos .....	15
Nomenclature .....	16
Chapter 1. Introduction .....	17
1.1 Research Background .....	17
1.2 Flexible Photodetectors .....	18
1.2.1 Introduction to Flexible Photodetectors .....	18
1.2.2 Sensing Mechanism of Photodetectors .....	19
1.2.3 Figures of Merit for Flexible Photodetectors .....	20
1.2.4 Light Management Techniques for High-Performance Photodetectors .....	21
1.3 Flexible Mechanosensors .....	22
1.3.1 Introduction to Flexible Mechanosensors .....	22
1.3.2 Sensing Approaches .....	23
1.3.3 Figures of Merit for Flexible Mechanosensors .....	24
1.3.4 Design for Highly Sensitive Mechanosensors .....	25
1.4 References .....	26
Chapter 2. Broadband Omnidirectional Light Detection in Flexible and Hierarchical ZnO/Si Heterojunction Photodiodes .....	37
2.1 Introduction .....	37
2.2 Experimental Details .....	38
2.3 Results and Discussion .....	40
2.4 Conclusions .....	46
2.5 References .....	46



Chapter 3. Large-Area, Solution-Processed, Hierarchical MAPbI <sub>3</sub> Nanoribbon Arrays for Self-Powered Flexible Photodetectors -----	64
3.1 Introduction -----	64
3.2 Experimental Details -----	65
3.3 Results and Discussion -----	67
3.4 Conclusions -----	72
3.5 References -----	72
Chapter 4. Skin-Inspired Hierarchical Polymer Architectures with Gradient Stiffness for Space-Free, Ultrathin, and Highly Sensitive Triboelectric Sensors -----	86
4.1 Introduction -----	86
4.2 Experimental Details -----	88
4.3 Results and Discussion -----	90
4.4 Conclusions -----	96
4.5 References -----	97
Chapter 5. Summary and Future Perspectives -----	119
Appendix A: General Expressions of the Open-Circuit Voltage and Short-Circuit Current --	121
Appendix B: List of Achievements -----	122
Acknowledgements -----	126
감사의 글 -----	127

## List of Figures

### Chapter 1

**Figure 1.1** Evolution of electronic devices with the Fourth Industrial Revolution into human-interactive electronic devices. Reproduced from Ref. [2, 69–74].

**Figure 1.2** Required technologies for future electronics on the aspects of functionality and sensor. Reproduced from Ref. [75–81].

**Figure 1.3** The representative research strategies to achieve the required technologies for future electronics in terms of high flexibility, device sustainability, high-performance photodetectors, and highly-sensitive mechanosensors. Reproduced from Ref. [21] with permission. Copyright © 2015, Royal Society of Chemistry; Reproduced from Ref. [53] with permission. Copyright © 2015, WILEY-VCH Verlag GmbH & Co. KGaA, Weinheim; Reproduced from Ref. [63] with permission. Copyright © 2014, Nature Publishing Group; Reproduced from Ref. [66] with permission. Copyright © 2013 Nature Publishing Group; Reproduced from Ref. [67] with permission. Copyright © 2015 Elsevier Ltd.; Reproduced from Ref. [82–84].

**Figure 1.4** Summary of this thesis. Reproduced from Ref. [8] with permission. Copyright © 2017, Tsinghua University Press and Springer-Verlag Berlin Heidelberg; Reproduced from Ref. [68] with permission. Copyright © 2018, WILEY-VCH Verlag GmbH & Co. KGaA, Weinheim; Reproduced from Ref. [38] with permission. Copyright © 2018, American Chemical Society

**Figure 1.5** Five light management strategies through novel design of micro/nanostructures to enhance light absorption and thus accomplish high-performance optoelectronic devices. Reproduced from Ref. [10] with permission. Copyright © 2019, WILEY-VCH Verlag GmbH & Co. KGaA, Weinheim

**Figure 1.6** Schematic illustration of the increased light path length through light scattering in the complex hierarchical micro/nanostructures. Reproduced from Ref. [10] with permission. Copyright © 2019, WILEY-VCH Verlag GmbH & Co. KGaA, Weinheim

**Figure 1.7** Mechanism of antireflection effect in nanostructures with gradient refractive index. (a) Propagation of light into a thin film on a substrate ( $n_s > n$ ). (b) Promotion of multiple reflections of light in microstructures. (c) Interaction of light with the subwavelength nanostructure arrays. (d) Schematic of gradient refractive index changes in nanostructure arrays. Reproduced from Ref. [21]

with permission. Copyright © 2015, Royal Society of Chemistry

**Figure 1.8** Representative signal transduction approaches in mechanosensors. Reproduced from Ref. [30] with permission. Copyright © 2018, Royal Society of Chemistry

## Chapter 2

**Figure 2.1** (a) Top-view SEM image of sputtered ZnO film (thickness  $\approx 200$  nm). (b) Cross-sectional SEM images of vertically grown ZnO NW arrays on ZnO layer as a function of growth time. (c) Statistics for length and diameter as a function of the growth of ZnO NWs. (d) Aspect ratio of ZnO NWs as a function of the growth time. (e) X-ray diffraction (XRD) analysis for sputtered ZnO film and hydrothermally grown ZnO NWs.

**Figure 2.2** Hierarchical design of H-Si decorated with ZnO NWs. (a) Schematic illustration of the fabrication of ZnO NW/H-Si on SiO<sub>2</sub>/Si substrate. (b) Tilted SEM image of ZnO NWs on H-Si structure (diameter: 8.7  $\mu\text{m}$ ). (c) Tilted SEM image of ZnO NW/H-Si photodiode. (d)  $I$ - $V$  curve for ZnO NW/H-Si photodiode in dark state (without illumination). Inset shows a log current-linear voltage plot ( $\log I$ - $V$ ).

**Figure 2.3** HR-TEM images for interfaces between (a) ZnO film and hydrothermally grown ZnO NW and (b) sputtered ZnO film and Si.

**Figure 2.4**  $I$ - $V$  curves of Al-ZnO-Al and Cr/Au-Si-Cr/Au.

**Figure 2.5** A plot of natural log of current against voltage ( $\ln I$ - $V$ ) for ZnO NW/H-Si photodiode in dark state (without illumination of light).

**Figure 2.6** Photoresponsive properties of ZnO NW/H-Si photodiodes. (a)  $I$ - $V$  curves for reverse-biased region under dark conditions and with illumination at three different wavelengths (the optical power of the incident light was 800  $\mu\text{W}\cdot\text{cm}^{-2}$ ). (b) Spectral photoresponsivity of ZnO NW/H-Si photodiode spanning UV to NIR wavelength range at an applied voltage of  $-2$  V. (c) Photoresponse time of ZnO NW/H-Si photodiode under illumination at 365 and 620 nm. (d) Dependence of photoresponse on different illumination intensities under illumination at 365 nm at an applied voltage of  $-2$  V.

**Figure 2.7** Transfer curves of field-effect transistors based on (a) ZnO NWs and (b) H-Si.

**Figure 2.8** Energy band diagrams of p-Si/n-ZnO heterojunction photodiode under (a) zero bias and (b) reverse bias.

**Figure 2.9** Spectral photoresponsivity of metal-semiconductor-metal photodetector based on H-Si.

**Figure 2.10** Fast response of ZnO NWs/H-Si and ZnO NWs/F-Si photodiodes. (a) Rise and (b) decay time of ZnO NWs/H-Si photodiodes. (c) Rise and (d) decay time of ZnO NW/F-Si photodiodes. (e) Repeated photoresponse results under illumination of 365 and 620 nm light for ZnO NW/H-Si photodiodes.

**Figure 2.11**  $I-V$  hysteresis curve of ZnO NWs/H-Si photodiodes.

**Figure 2.12** (a) Plot for photoresponsive On/Off ratio under white light illumination of ZnO NW/Si photodiodes with ZnO film sputtered in different gas environments. (b)  $I-V$  curves for reverse-biased region of dark current and ON current under white light illumination as a function of the growth time. (c) XRD analysis for sputtered ZnO film and time-dependent ZnO NWs. (d) Photocurrent of ZnO NW/Si photodiodes under illumination of 380 and 620 nm light as a function of the growth time of ZnO NWs. (e) Variation of dark current and ON current (White light illumination) as a function of the growth time of ZnO NWs.

**Figure 2.13** Omnidirectional light-absorption properties of hierarchical hetero-structures of ZnO NWs on H-Si. (a) Photocurrent measurement system as a function of angle of incident light. (b) Variation of photocurrent for four different hetero-structured ZnO/Si photodiodes as a function of angle of incident light at 620 nm. 2D plots of UV–vis–NIR reflectance data for (c) F-Si, (d) H-Si, (e) ZnO NWs on F-Si, and (f) ZnO NWs on 8.7  $\mu\text{m}$  H-Si using variable angle specular reflectance accessory.

**Figure 2.14**  $I-V$  curves for three different kinds of hetero-structured ZnO/Si photodiodes. (Dotted lines and solid lines represent dark current and ON current with illumination of 570 nm light, respectively.)

**Figure 2.15** Characterization of H-Si and ZnO NW/H-Si. The cross-sectional SEM images for (a) H-Si and (b) ZnO NWs/H-Si as a function of the hexagonal hole size. (c) The tilted SEM images for ZnO NW/H-Si. (d) Magnified view of (c).

**Figure 2.16** Variation in photocurrent of ZnO NW/Si photodiode as a function of angle of incident light and hole sizes of H-Si.

**Figure 2.17** Schematics for light path with incident angles of 30°, 45°, and 60° into different hexagonal hole sizes.

**Figure 2.18** Simulated cross-sectional  $|E|^2$  distribution of the electromagnetic (EM) wave at 620 nm excitation with different morphologies: (a) F-Si, (b) H-Si, (c) ZnO NW/F-Si, and (d) ZnO NW/H-Si at angular incidence of 30°. Magnified view of EM wave distribution with different morphologies: (e) F-Si, (f) H-Si, (g) ZnO NW/F-Si, and (h) ZnO NW/H-Si (left: normal incidence, right: 30° incidence).

**Figure 2.19** Evaluation of flexibility and durability of flexible ZnO NW/H-Si photodiode on PI substrate. (a) Digital images and OM image of rolled H-Si membrane on tip of pipette. (b) Photograph and schematic showing the highly flexible ZnO NW/H-Si-based photodiode on polyimide. (c)  $I-V$  curves of flexible photodiode in dark state (dotted line) and under illumination with 365 nm light (solid line) as a function of the bending curvature. (d) Variation of photocurrent with increasing bending curvature. Background photograph shows photodiode bent with bending machine ( $r_B = 0.415$  cm). (e) Mechanical durability of ZnO NW/H-Si photodiode on PI substrate with increasing number of bending cycles with a bending radius of  $r_B = 1.025$  cm.

**Figure 2.20**  $I-V$  curves of ZnO NWs/H-Si photodiode on PI substrate under dark state and 365 nm light illumination.

**Figure 2.21** Digital images of bent photodiode arrays on PI substrate as a function of the bending radius.

**Figure 2.22** SEM images of ZnO NWs/H-Si photodiode on PI substrate after 10,000 cycles of mechanical bending test at bending.

### **Chapter 3**

**Figure 3.1** Fabrication of large-area and highly aligned hierarchical MAPbI<sub>3</sub> nanoribbon (NR) arrays. (a) Schematic illustration of the fabrication of MAPbI<sub>3</sub> NR arrays on the arbitrary substrates. (b) Photograph of large-area MAPbI<sub>3</sub> NR arrays on (i) SiO<sub>2</sub>/Si (2 cm × 1.5 cm), (ii) glass (2.5 cm × 2.5 cm, inset image shows nonreflected sample). (iii) MAPbI<sub>3</sub> NRs based flexible photodetectors on polyimide (PI) substrate attached to wrist. (c) Optical microscopy (OM) image of large-area MAPbI<sub>3</sub> NR arrays on SiO<sub>2</sub>/Si substrate.

**Figure 3.2** Detailed information about PMMA nanotemplates. (a) Photograph of PMMA

nanotemplates on SiO<sub>2</sub>/Si substrate. (b) Optical microscopy (OM) image of PMMA nanotemplates on SiO<sub>2</sub>/Si substrate. (c) Atomic force microscopy (AFM) image of PMMA nanotemplates on SiO<sub>2</sub>/Si substrate. The height of PMMA nanotemplate is 100 nm.

**Figure 3.3** SEM images of large-area and highly aligned MAPbI<sub>3</sub> NR arrays after removal of PMMA nanotemplates.

**Figure 3.4** Detailed fabrication process for hierarchical MAPbI<sub>3</sub> NR arrays. (a) Scanning electron microscopy (SEM) image and (b) atomic force microscopy (AFM) image of transferred PMMA nanotemplates on SiO<sub>2</sub>/Si substrate. (c) SEM image and (d) AFM image of MAPbI<sub>3</sub> NRs with PMMA nanotemplates. (e) SEM image and (f) AFM image of MAPbI<sub>3</sub> NRs after removal of PMMA nanotemplates by 1 h dipping in toluene.

**Figure 3.5** The size of internal nanorods in hierarchical MAPbI<sub>3</sub> NR arrays. Statistics for (a) length and (b) thickness of internal nanorods.

**Figure 3.6** Different morphologies of MAPbI<sub>3</sub> NRs according to the toluene drip treatment. SEM images of (a) MAPbI<sub>3</sub> NRs without toluene drip treatment and (b) MAPbI<sub>3</sub> NRs with toluene drip treatment.

**Figure 3.7** Surface morphology of MAPbI<sub>3</sub> film on a planar substrate. (a) SEM and (b) AFM images of MAPbI<sub>3</sub> film.

**Figure 3.8** The comparison of MAPbI<sub>3</sub> film and NR arrays in terms of optical property and crystallinity. (a) UV–vis absorption spectra of MAPbI<sub>3</sub> film, MAPbI<sub>3</sub> NRs with PMMA nanotemplates, and MAPbI<sub>3</sub> NRs after removal of PMMA nanotemplates. (b) Tauc plot of MAPbI<sub>3</sub> NRs to calculate optical band gap from the result of transmittance. (c) X-ray diffraction spectra of MAPbI<sub>3</sub> film, MAPbI<sub>3</sub> NRs with PMMA nanotemplates, and MAPbI<sub>3</sub> NRs after removal of PMMA nanotemplates.

**Figure 3.9** UV–vis transmittance spectra of MAPbI<sub>3</sub> film, MAPbI<sub>3</sub> NRs with PMMA nanotemplates, and MAPbI<sub>3</sub> NRs after removal of PMMA nanotemplates.

**Figure 3.10** Optoelectronic properties of hierarchical MAPbI<sub>3</sub> NRs based photodetectors. (a) OM images and schematic illustration of hierarchical MAPbI<sub>3</sub> NRs based photodetectors on SiO<sub>2</sub>/Si substrate. (b)  $I$ – $V$  curves of a MAPbI<sub>3</sub> NRs based photodetector in the voltage range from  $-7$  to  $7$  V

under dark condition and with illumination at 5 different wavelengths. (c) Photoresponsive rise and decay times of a MAPbI<sub>3</sub> NRs based photodetector under light illumination ( $\lambda = 500$  nm;  $P = 383.9$   $\mu\text{W}\cdot\text{cm}^{-2}$ ) at an applied voltage of 2 V. (d) Spectral specific detectivity of MAPbI<sub>3</sub> film and NRs based photodetectors from 300 to 800 nm wavelength range at an applied voltage of 2 V. (e) Dependence of photoresponse on different illumination intensities under illumination of 500 nm light at an applied voltage of 2 V.

**Figure 3.11** Stable photoswitching behavior of a MAPbI<sub>3</sub> NRs based photodetector under repeated on/off light illumination ( $\lambda = 500$  nm;  $P = 383.9$   $\mu\text{W}\cdot\text{cm}^{-2}$ ) at an applied voltage of 2 V.

**Figure 3.12** Spectral specific detectivity of MAPbI<sub>3</sub> film based photodetectors at an applied voltage of 2 V.

**Figure 3.13** Spectral photoresponsivity of MAPbI<sub>3</sub> film and NRs based photodetectors from 300 to 800 nm wavelength range at an applied voltage of 2 V.

**Figure 3.14** (a) Spectral specific detectivity and (b) photoresponsivity of MAPbI<sub>3</sub> NR photodetectors before and after the toluene drip treatment at an applied voltage of 2 V.

**Figure 3.15** Mechanical flexibility of MAPbI<sub>3</sub> NRs based photodetectors on PI substrate. (a) Schematic illustration of hierarchical MAPbI<sub>3</sub> NRs based flexible photodetectors on PI substrate. (b) Time-dependent  $I$ - $V$  curve of flexible MAPbI<sub>3</sub> NRs based photodetectors with 0.1 Hz switching of 500 nm light in the voltage range from -2 to 2 V. (c) Digital image of rolled flexible MAPbI<sub>3</sub> NRs based photodetectors on pen with  $r_B = 3.7$  mm. (d) Current variation of MAPbI<sub>3</sub> NRs photodetectors under dark and illumination states according to the bending curvature (scale bar: 1 cm).

**Figure 3.16** Self-powered and polarization sensitive light-detection capability of MAPbI<sub>3</sub> NRs based photodetectors. (a) Spectral specific detectivity of MAPbI<sub>3</sub> NRs based photodetectors from 300 to 800 nm wavelength range without an applied voltage. (b) Local piezoresponse force microscopy (PFM) hysteresis loops of MAPbI<sub>3</sub> film (blue: phase signal, red: amplitude signal). (c) Schematic illustration of polarization-sensitive photodetectors based on MAPbI<sub>3</sub> NRs. (d) Dependence of photoresponse on different polarization angle (parallel to NRs: 0°, vertical to NRs: 90°) under illumination of white light ( $P = 74.79$   $\text{mW}\cdot\text{cm}^{-2}$ ) at an applied voltage of 2 V.

**Figure 3.17** Spectral photoresponsivity of MAPbI<sub>3</sub> NRs based photodetectors from 300 to 800 nm wavelength range without an applied voltage.

## **Chapter 4**

**Figure 4.1** Skin-inspired and hierarchical polymer architectures for spacer-free, ultrathin, and highly sensitive triboelectric sensors (TESs). (a) Structural and functional characteristics of human skin. The different elastic modulus ( $E$ ) of epidermis–dermis layers with interlocked microridges effectively transfer the external stress to underlying mechanoreceptors. (b) Hierarchical and interlocked microridge structured P(VDF-TrFE) and PDMS-based TESs. Scanning electron microscopy (SEM) images of (c) nanoporous and microridge structured PDMS and (d) interlocked with hierarchically structured P(VDF-TrFE). (e) Photograph of ultrathin and flexible TESs. Inset shows the interlocked P(VDF-TrFE) and PDMS layers. (f) Scanning Kelvin probe microscopy (SKPM) image of surface potential distribution between P(VDF-TrFE) and PDMS.

**Figure 4.2** Fabrication of hierarchical polymeric architectures. Schematic illustration of detailed fabrication process for hierarchical nanoporous and microridge-structured polymers by using the solvent-assisted micro-molding technique.

**Figure 4.3** Control the porosity in PDMS depending on the ratio of mixed solvents (deionized water/ethanol). SEM images of porous PDMS based on (a) 40% of deionized water, (b) 20% of deionized water and 20% of ethanol, and (c) 10% of deionized water and 30% of ethanol mixed in PDMS solution (scale bar: 25  $\mu\text{m}$ ).

**Figure 4.4** SEM images of (a) tilted and (b) cross-sectional view with different width ( $w$ ) and pitch ( $p$ ) size ( $w/p = 100/120, 50/60, 25/30 \mu\text{m}$ ) of hierarchical microridge-structured and planar PDMS (scale bar: 100  $\mu\text{m}$ ).

**Figure 4.5** Statistical estimation of pore size distribution in nanoporous PDMS. MATLAB image processing of (a) mapping pores in SEM images (scale bar: 50  $\mu\text{m}$ ) and (b) statistically calculated size distribution of pores in nanoporous PDMS with planar and different width/pitch sized microridge structures.

**Figure 4.6** SEM images of (a) tilted and (b) cross-sectional view with different width ( $w$ ) and pitch ( $p$ ) sizes ( $w/p = 100/120, 50/60, 25/30 \mu\text{m}$ ) of hierarchical microridge-structured and planar P(VDF-TrFE) (scale bar: 100  $\mu\text{m}$ ).

**Figure 4.7** Surface topologies and electrostatic potential distribution between P(VDF-TrFE) and PDMS. (a) AFM image of nanofiber-like morphology of P(VDF-TrFE) with height information ( $\sim 1.01 \mu\text{m}$ ) and (b) SKPM image of surface potential distribution with potential differences ( $\sim 0.43 \text{ V}$ )



between the P(VDF-TrFE) and PDMS.

**Figure 4.8** Theoretical analysis of the gap distance change in the interlocked films. The finite element simulations by using ABAQUS software for the gap distance change ( $\Delta d$ ) from the initial gap in the interlocked microridge-structured and planar films with respect to the applied vertical pressure. Note that while the elastic modulus of P(VDF-TrFE) is constant as 1 GPa for all sizes of microridge arrays, that of PDMS decreases with the larger width/pitch size of microridge arrays (see the experimentally measured values of Figure 4.11).

**Figure 4.9** Working principle of self-powered TESs and triboelectric output performances. (a) Schematic illustration of triboelectric charge generation and current flow mechanism between hierarchical and interlocked microridge structured P(VDF-TrFE) and PDMS. Triboelectric output (b) voltage and (c) current density under vertical pressure of 19.6 kPa with 4 Hz. (d) Triboelectric output variations of voltage, current density, and power density with an external load resistance from  $10^3$  to  $10^9 \Omega$ . (e) Rectified triboelectric voltage connected with four bridge rectifier and the inset of capability for lighting LED driven by self-powered TES.

**Figure 4.10** Structural effect for triboelectric output performances and vertical pressure-sensitivity. Triboelectric (a) voltage and (b) current with the different structures including nanoporous, nonporous, and surface microridge-structured interlocked films following the applied vertical pressure.

**Figure 4.11** Compressive stress-strain curves with different structured PDMS. The loading and unloading of stress-strain curves and compressive elastic modulus with nonporous, porous and different width/pitch size of microridge-structured and planar PDMS.

**Figure 4.12** Triboelectric output performances with gradient elastic modulus of interlocked P(VDF-TrFE) and PDMS. Triboelectric output (a) voltage and (b) current density to verify the effect of gradient elastic modulus with (i, iii) upper PDMS/lower P(VDF-TrFE) layers and (ii, iv) upper P(VDF-TrFE)/lower PDMS layers for effective stress transmission as well as increase of triboelectric output performances following the applied vertical pressure.

**Figure 4.13** Theoretical analysis of the stress distribution in the interlocked films under the vertical pressure. The finite element simulations of the stress distribution depending on the elastic modulus of interlocked and microridge-structured polymers by using ABAQUS software. The elastic modulus of P(VDF-TrFE) and PDMS is 1 GPa and 3 MPa, respectively. (a) and (b) show the result for the contact interaction for the interlocked PDMS-PDMS and the P(VDF-TrFE)-PDMS layers, respectively.

**Figure 4.14** Porosity of nanoporous PDMS. Comparison of porosity in nanoporous PDMS with different width/pitch sized microridge structures.

**Figure 4.15** Theoretical analysis of the stress distribution and numerical calculation of the contact area between the interlocked microridges under the vertical pressure. The finite element simulations for the comparison of (a) vertical stress concentration with the different width/pitch size of interlocked and microridge-structured polymers by using ABAQUS software and coincident numerical calculation of (b) contact area and (c) relative contact areal change with respect to the applied vertical pressure. The elastic modulus of P(VDF-TrFE) is 1 GPa, and that of PDMS is varied depending on the width/pitch size of microridge arrays (see the experimental values of Figure 4.11).

**Figure 4.16** Triboelectric charge density with the different width/pitch size of microridge arrays and planar structure based interlocked films following the amount of applied (a) vertical pressure and (b) bending stress.

**Figure 4.17** Detection capabilities of vertical pressure and bending strain of ultraflexible TESs. (a) Schematic illustration of gap distance change of TESs under vertical pressure and theoretically calculated electric field distribution by COMSOL simulations depending on the width ( $w$ ) and pitch ( $p$ ) size of interlocked microridge arrays ( $w/p = 25/30, 50/60, \text{ and } 100/120 \mu\text{m}$ ) and planar structures. (b) Triboelectric voltage variations and pressure sensitivity following the size of interlocked microridge structured and planar films with the applied pressure. (c) Detection capability of radial artery pulse waves by ultraflexible TESs attached on the wrist. (d) Density of point contact between interlocked microridges under bending strain and coincident theoretically calculated electric field distribution by COMSOL simulations. The bending stress-induced (e) triboelectric voltage variations and bending sensitivity following the size of interlocked microridge structured and planar films with different bending angle. (f) Capability to monitor the different angle of finger bending motion by bending sensitive TESs.

**Figure 4.18** Triboelectric current density with the different width/pitch size of microridge arrays and planar structure based interlocked films following the amount of applied (a) vertical pressure and (b) bending stress.

**Figure 4.19** Theoretical analysis of the stress distribution and numerical calculation of the contact area between the interlocked microridges under the bending strain. The finite element simulations for the comparison of (a) bending stress concentration between the different width/pitch ( $w/p = 25/30, 50/60, 100/120 \mu\text{m}$ ) size of interlocked and microridge-structured polymers by using ABAQUS

software. (b) Comparison of the degree of inhomogeneity for the contact stress distribution between the different width/pitch size of interlocked microridge arrays. (c) Numerical calculation of contact area change between the interlocked and microridge-structured polymers with different width and pitch sizes as a function of bending strain. The elastic modulus of P(VDF-TrFE) is 1 GPa, and that of PDMS is varied depending on the width/pitch size of microridge arrays (see the experimental values of Figure 4.11).

**Figure 4.20** Fast responsive TESs for high-frequency dynamic force sensing and acoustic wave detection. Sensing capabilities of (a) contact vibrations from vibrating coin and frequency-dependent triboelectric (b) voltage and (c) current following the increase of vibrational frequency from 73 to 140 Hz. (d) Sound detection test of TESs at the sound pressure level (SPL) of  $\sim 92$  dB with a fixed distance ( $\sim 2$  cm) from a commercial speaker. The speaker played the sound with the words of “triboelectric sensor” in low and high speed toward the TES. (e) Variations of input voltage signals to the speaker and corresponding short-time Fourier transform (STFT) signals analyzed for the harmonic frequency of acoustic vibrations. (f) The readout triboelectric voltage signals oscillated by the sound of “triboelectric sensor” played by speaker and the STFT spectrogram matched with frequency domain of input source. (g) Capability of human voice recognition of TES with voice of  $\sim 78$  dB and leaving a space of  $\sim 15$  cm between TES and subjects. (h) The oscillated triboelectric voltage signals by talking with the sentences of “I am a girl” and “I am a boy” from the female and male and corresponding STFT spectrogram to distinguish the different frequency domain of female and male voice. (i) Repeatable test to recognize and differentiate the words of “UNIST” from the female and male voice and coincident STFT spectrogram.

**Figure 4.21** Bendable smart glove for sensing the hand motion of grip of objects. Photographs and contour mapping patterns for grip of (a) small radius ( $\sim 1.4$  cm) of object and (b) large radius ( $\sim 3.3$  cm) of object. The contour mapping arrays of (a)-i, (b)-ii and (a)-iii, (b)-iv demonstrate the responding current signals from the grip of objects in first time and after 100 cyclic folding and unfolding of one’s fist, respectively.

**Figure 4.22** Ultraflexible TESs for bendable smart glove and detection capabilities of sign language. (a) Photographs of bendable smart glove consisting of ultraflexible triboelectric sensing arrays at the joints on the human hand, performing the diverse motion matched with the different sign language of “I am”, “happy”, “to meet”, and “you”. (b) Contour mapping arrays from (i) to (iv) to analyze the triboelectric current signals from each TESs responding to the sign language. (c) Schematic illustration of location at each joints on the hand and corresponding abbreviation of thumb (T), index

finger (I), middle finger (M), ring finger (R), and pinky (P) in (i). The hand bones divided with three part of carpus (ii), phalange (iii), and metacarpus (iv) during the real-time monitoring of the triboelectric current signals responding to the sign language.

**Figure 4.23** Mechanical durability of TESs. Triboelectric output (a) voltage and (b) current density of interlocked and hierarchical microridge-structured P(VDF-TrFE) and PDMS with repeated loading and unloading ( $\sim 98$  kPa) cycles over 10,000 times. SEM images of nanoporous and microridge-structured (c) PDMS and (d) P(VDF-TrFE) with different width and pitch size after 10,000 cycle of pushing test.

**Figure 4.24** Ultraflexible and fully packaged designs for humid-insensitive TESs. (a) Schematic illustration of humid-insensitive TESs packaged with laminating tape to prevent the permeation of atmospheric moisture. Variations of triboelectric (b) voltage and (c) current signals from the change of ambient relative humidity (20–90% RH). (d) Detection of ultrasonic waves with analysis of the impact frequency level ( $\sim 21$  kHz) from the FFT signals. Inset demonstrates the lighting LED operated by the fully packaged TES in the ultrasonic water bath. (e) Real-time variations of ultrasonic waveforms analyzed by the STFT spectrogram.

## List of Tables and Videos

### Chapter 2

**Table 2.1** Comparison of results achieved this work and previously reported omnidirectional, flexible, and broadband optoelectronics.

### Chapter 3

**Table 3.1** Comparison of results achieved this work and previously reported MAPbI<sub>3</sub> based photodetectors excluding hybrid structures.

### Chapter 4

**Table 4.1** Comparison of triboelectric output performances and vertical pressure/bending sensitivity of the results achieved this work with previously reported TESs.

**Video 4.1** Performing the sign language of the sentence of “I am happy to meet you”.

**Video 4.2** Demonstration of fully-packaged TESs with responding to the ultrasonic waves and lighting a red LED operated by TESs in the ultrasonic water bath.

\*\*Videos are available on the ACS Publications website at DOI: 10.1021/acsnano.8b01557.

## Nomenclature

---

<b>2D</b>	Two-Dimensional
<b>AFM</b>	Atomic Force Microscopy
<b>DI</b>	Distilled
<b>DMF</b>	<i>N,N</i> -Dimethylformamide
<b>DRIE</b>	Deep Reactive-Ion Etching
<b>FDTD</b>	Finite-Difference Time-Domain
<b>FE-SEM</b>	Field Emission Scanning Electron Microscopy
<b>FFT</b>	Fast Fourier Transform
<b>FIB</b>	Focused Ion Beam
<b>HR-TEM</b>	High Resolution Transmission Electron Microscopy
<b>H-Si</b>	Honeycomb-Structured Si
<b>IoT</b>	Internet of Thing
<b><i>I-V</i></b>	Current–Voltage
<b>MAPbI<sub>3</sub></b>	Methylammonium Lead Iodide
<b>NIR</b>	Near-Infrared
<b>NR</b>	Nanoribbon
<b>NW</b>	Nanowire
<b>OM</b>	Optical Microscopy
<b>PDMS</b>	Poly(dimethylsiloxane)
<b>PET</b>	Polyethylene terephthalate
<b>PI</b>	Polyimide
<b>PMMA</b>	Polymethyl methacrylate
<b>PU</b>	Polyurethane
<b>PVDF-TrFE</b>	Poly(vinylidene fluoride-trifluoroethylene)
<b>RF</b>	Radio Frequency
<b>RTA</b>	Rapid Thermal Annealing
<b>SAM</b>	Self-Assembled Monolayer
<b>SKPM</b>	Scanning Kelvin Probe Microscopy
<b>SOI</b>	Silicon on insulator
<b>SPL</b>	Sound Pressure Level
<b>SS-PFM</b>	Switching Spectroscopy Piezoresponse Force Microscopy
<b>STFT</b>	Short-Time Fourier Transform
<b>TES</b>	Triboelectric Sensor
<b>UV</b>	Ultraviolet
<b>VASRA</b>	Variable Angle Specular Reflectance Accessory
<b>XRD</b>	X-Ray Diffractometer

---

## Chapter 1. Introduction

### 1.1 Research Background

Over the past few decades, conventional electronic devices have been grown in a direction to enhance their processing capability with scaling according to Moore's law.<sup>[1]</sup> However, the rapid development of modern society with the Fourth Industrial Revolution continuously leads to create new and innovative technologies, which require not only high performance, but also more functionality to next-generation electronic devices for improving the quality of life, human compatibility, and convenience (**Figure 1.1**).<sup>[2]</sup> Future electronic devices will evolve into much more human-interactive devices such as wearable and skin-attachable devices, augmented reality, and robotics beyond current wearable electronics including smart phones, smart watches, and virtual reality glasses. Moreover, the importance of developing multifunctional sensors with advanced communication capability has come to the fore worldwide with rapid growth of Internet of Thing (IoT) technologies that allows systematic connections of humans and everything.<sup>[3]</sup>

Looking at the technologies for future electronics (**Figure 1.2**), the most essential functionality is mechanical flexibility for potential applications on various curved surfaces including human skin and body. However, it is still challenging issue to assign high mechanical flexibility to electronic devices. Especially, main components in high-performance electronic devices involve metallic electrodes, insulating dielectric oxide layers, and inorganic semiconductors such as silicon (Si), germanium, and III-V compound semiconductors, which are brittle and easily broken from external stress.<sup>[4]</sup> In addition, for long-term use of electronic devices, it is significantly important to develop sustainable devices through self-charging with utilizing ambient energy.

On the aspect of sensors, photodetectors are irreplaceable electronic devices as a light sensing element, which converts electromagnetic radiation into electrical currents. Photodetectors allow to recognize some objects and make imaging through the contactless detection. In addition, photodetectors are key components for technological advancement in IoTs thanks to their ultrafast and wireless communication capability. On the other hand, mechanosensors provide physical information such as touch and gesture *via* direct contact with the objects. Thus, physical sensors are essential for personal health-monitoring applications such as blood pressure, pulse beats, and respiration.

Therefore, many researchers have been trying to realize and advance these technologies (**Figure 1.3**). The main strategy for high flexibility is to actively utilize soft materials and low-dimensional flexible nanomaterials with extremely low thickness or structural modification. For sustainable electronics, a variety of energy harvesting techniques based on piezoelectric, triboelectric, and photovoltaic effects have been developed. For high-performance photodetector, antireflective surfaces with unique designs of micro/nanostructures and biomimetic vision systems have been reported to maximize light collection efficiency and enhance light-detection capability. In addition, highly

sensitive mechanosensors have been demonstrated by designing novel structures for effective detection of external force.

The goal of this work is the development of highly sensitive and multifunctional flexible sensing devices for future electronics *via* a novel design of micro/nanostructured materials (**Figure 1.4**). This thesis is organized in the following format. A brief literature background of flexible photodetectors and mechanosensors is introduced in Chapter 1. In Chapter 2, we suggest hierarchical ZnO nanowires on honeycomb-structured Si platform for flexible photodetectors with omnidirectional light-detection capability. As another approach for future proximity sensors, in Chapter 3, we demonstrate organic-inorganic hybrid perovskite nanoribbon arrays based flexible photodetectors capable of self-powered operation and polarization-sensitive detection. Chapter 4 describes the hierarchical nanoporous and interlocked microridge structured polymers with gradient stiffness for spacer-free, ultrathin, and highly sensitive triboelectric mechanosensors. Finally, we summarize this thesis with future prospects and challenges of this field in Chapter 5.

## 1.2 Flexible Photodetectors

### 1.2.1 Introduction to Flexible Photodetectors

Photodetector is one of optoelectronic devices that can convert a light signal into a form of electrical signals, typically photocurrent or photovoltage.<sup>[5, 6]</sup> It is significantly important to develop high-performance photodetectors due to their broad application areas such as digital camera, optical communications, flame detection, biomedical imaging, environmental monitoring, astronomy, military night vision, and security.<sup>[6, 7]</sup> With the growth of interest in flexible electronics, flexible photodetectors have attracted tremendous attention as proximity sensors, which have wide future applications such as wearable electronics, augmented reality, autonomous car, robotics, advanced defense, and smart health-monitoring.

Traditionally, inorganic semiconductors such as bulk Si, Ge, and InGaAs are mainly used as raw materials for photodetectors by virtue of broad detection range from visible to near-infrared (NIR) spectrum as well as easy fabrication process based on conventional photolithographic techniques. However, inorganic semiconductors have severe drawbacks of fragility and tough deformation, which restricts their wide usage in flexible photodetectors. Therefore, various functional materials with excellent electrical and optical properties as well as high mechanical flexibility, have been investigated as a building block for flexible photodetectors, which include multi-dimensional nanostructured materials, organic semiconductors, organic-inorganic hybrid perovskite materials and so on.<sup>[7]</sup>

To achieve both high photoresponsivity and mechanical flexibility in flexible photodetectors, it is important to select appropriate materials and design such materials based effective device structures with optimization of fabrication process. For instance, the processing temperature should be



inevitably constrained below 400 °C because most plastic substrates such as polyethylene terephthalate (PET), polyethylene naphthalate, polyimide (PI) cannot maintain their physical properties under high temperature. However, active materials require additional annealing process to enhance their crystallinity with improving physical, electrical, and optical properties. Therefore, many researches have investigated to develop heat-resisting flexible substrates and achieve low-temperature synthesis of active materials. Furthermore, new device architectures capable of improving light absorption as well as mechanical robustness have been widely studied to enhance the performance of flexible photodetectors.<sup>[7, 8]</sup>

### 1.2.2 Sensing Mechanism of Photodetectors

Photodetection process can be divided into three main steps including absorption of photons, the generation of electron-hole pairs, and change of electrical signals according to the collection of photogenerated charge carriers to electrodes. There are several sensing mechanisms for sensing incident light depending on the device architecture and active materials.<sup>[7, 9]</sup> Here, we introduce two representative mechanisms that are associated with the types of flexible photodetectors discussed in this thesis including photoconductive and photovoltaic effect.

**Photoconductive effect:** In general, photoconductive devices consist of photoactive semiconductor channels with two Ohmic contact metals at opposite ends for applying bias and collect charge carriers. The photoconductive effect is mainly attributed to the reduction of electrical resistance in the active semiconductors according to the generation of additional free charges by optical input. The amount of current level between the electrodes with an applied bias is established by the innate electrical properties of semiconductors, which is typically low in the dark state (dark current,  $I_d$ ). Under the illumination of light, high energy photons over the band gap of the semiconductors can be absorbed and induce the generation of electron-hole pairs. The subsidiary charges experience separation and drift toward the anode and cathode by the applied bias, which results in a net increase of current (photocurrent,  $I_{ph}$ ). Because the recombination of photoinduced electron-holes pairs at crystal defects, impurities, and surface dangling bonds vitally affect to the level of photocurrent, it is important to suppress recombination sites as well as modulate carrier mobility of the channel for the development of highly photoresponsive devices. Furthermore, applying moderate bias is another factor to determine the level of both dark and photocurrent in photoconductive devices.

**Photovoltaic effect:** An interfacial junction between two materials having different work functions induces built-in potential, resulting in the separation of photocarriers, so-called photovoltaic effect. The photodetectors based on the photovoltaic phenomena are regarded as photodiodes including PN junction and metal-semiconductor Schottky junction diodes. Commonly, photodiodes exhibit nonlinear rectifying behavior in current–voltage ( $I$ – $V$ ) characteristics without illumination of light. When being exposed to irradiation, photoinduced electron-hole pairs can be separated by the built-in

electric field without an external bias, which allows the generation of photocurrent. Because the collection of photocarriers into electrodes do not require any power source, photovoltaic devices have been widely studied to develop solar cells for energy harvesting as well as self-powered photodetectors. In addition, their low dark current under zero bias is advantageous to maximize specific detectivity of photodetectors. It is noteworthy that photodiodes can be operated with photoconductive mode under reverse bias. The separation and drift of electron-hole pairs occurs more efficiently with adequate external electric field towards built-in potential as compared to photovoltaic mode, improving responsivity and response time as a consequence of reduced carrier transit time. The level of reverse bias should be properly adjusted likewise the general photoconductive devices because the breakdown of photodiodes arises from the strong electric field under large reverse bias.

### 1.2.3 Figures of Merit for Flexible Photodetectors

Flexible photodetectors can be assessed at several criteria including responsivity, response time, specific detectivity, spectral response range, on/off ratio, and mechanical flexibility. We briefly explain about the knowledge of basic parameter that is critical for setting up a target performance and requirement of flexible photodetectors.

**Photoresponsivity ( $R_{ph}$ ):** Photoresponsivity represents the efficiency of light conversion into output photocurrent ( $I_{ph} = I_T - I_d$ ) or photovoltage ( $V_{ph} = V_T - V_d$ ), where  $I_T$  and  $V_T$  is the total current and voltage under light illumination, which can be expressed as  $R_{ph} = \frac{I_{ph} \text{ or } V_{ph}}{PA}$ , where  $P$  is the optical power of incident light, and  $A$  is the active area.

**Response time:** Response time indicates the switching speed of the photodetectors according to the rapidly changed optical signals. Generally, the rise and decay time ( $t_r$  and  $t_d$ ), which can be estimated from the time required for the changes of photoresponse from 10/90% to 90/10% of its peak value, are evaluated, respectively.

**Specific detectivity ( $D^*$ ):** Specific detectivity is a crucial parameter to compare the performance of photodetectors with different materials and device structures, which can be defined as  $D^* = \frac{(A\Delta f)^{1/2}}{NEP}$ , where  $A$  is the active area,  $\Delta f$  is the bandwidth, and NEP is noise equivalent power. In case of shot noise dominant device, it is often estimated by  $D^* \approx \frac{A^{1/2}R_{ph}}{(2eI_d)^{1/2}}$ , where  $e$  is the elementary charge.

**On/off ratio:** On/off ratio indicates the sensitivity of the photodetectors, which can be obtained by dividing the photocurrent into dark current at certain optical power and bias voltage.

**Spectral response range:** Photodetectors have detectability only under illumination of light with a specific wavelength spectrum region, which is called the spectral response range. It is commonly decided by the band gap of active semiconductors. According to the purpose of photodetectors, broadband (panchromatic) and selective (monochromatic) photodetectors have been developed.

**Bending curvature and mechanical durability:** Flexible photodetectors must work normally without sacrificing the photoresponsive performance under repeated bending strain. Therefore, the number of repeated bending cycles, maximum bending curvatures, and change in the device performance under specific bending conditions should be noted to evaluate the mechanical flexibility and durability of the devices.

#### 1.2.4 Light Management Techniques for High-Performance Photodetectors

Light management techniques are essential for improving the performance of optoelectronic devices. In particular, the number of absorbed photons has an affinity with responsivity for photodetectors. One attractive strategy to enhance light absorption for high photon conversion efficiency is effective photon management through a novel design of micro/nanostructures (**Figure 1.5**).<sup>[10, 11]</sup> Therefore, diverse micro/nanostructure arrays have been extensively explored for manipulating reflection and propagation of incident light in optoelectronic devices in the form of domes,<sup>[12, 13]</sup> cones,<sup>[14, 15]</sup> hollow spheres<sup>[16, 17]</sup> as well as hierarchical architectures.<sup>[8, 18, 19]</sup> Here, we introduce three primary strategies that are used to design micro/nanostructures for high-performance photodetectors discussed in this thesis including scattering enhancement, antireflective effect, and plasmonics.

**Scattering enhancement:** In theory, the maximal enhancement factor of light absorption in a film can be defined as the Lambertian limit of  $4n^2$ , where  $n$  is the refractive index of the film. Up to the present, a plenty of periodic nanostructured arrays with pyramidal and rod shapes, have been suggested to reach or exceed the Lambertian limit.<sup>[20]</sup> Generally, scattering of light within the structures can increase the optical path length and thus enhanced light absorption if the unit size of the periodic arrays is larger than the wavelength of the light. It is worth noting that structure with a high aspect ratio offers forward scattering with reduced reflection losses, which is advantageous for effective light absorption. In addition, hierarchical structures of micro- and nanostructures with subwavelength sizes allow complex scattering for dramatic increase in light path length (**Figure 1.6**).<sup>[10]</sup> Scattering of incident light with multiple reflections and refractions *via* micro/nanostructures enables to further prolong the optical path length within optoelectronic devices. But more importantly, the design of flexible photodetectors with micro/nanostructures should consider not only the improved optical properties, but also electrical properties and mechanical flexibility.

**Antireflection effect:** The reduction of broadband reflection of light under various incident angle is important for enhancing the performance of photodetectors with increasing the amount of net light absorption. Thus, antireflective surfaces or coatings with micro/nanostructured arrays, which provide broadband and omnidirectional antireflection, have been widely studied.<sup>[21]</sup> Similar to scattering enhancement, the efficiency of antireflection is closely related to the unit size, depth, and space between the structures. According to the Fresnel equation, the difference in refractive index between

two media is crucial to determine the amount of reflection. Therefore, one desirable strategy that allows efficient antireflection with broadband, omnidirectional, and polarization insensitive performance is the design of nanostructures possessing gradual refractive index from air to bulk material (**Figure 1.7**).<sup>[14, 21]</sup> For this reason, many researchers have endeavored to make perfect antireflective surfaces or coatings based on various materials, such as Si,<sup>[22]</sup> III–V compound semiconductors,<sup>[23]</sup> metal oxides<sup>[18, 24]</sup> as well as polymers.<sup>[25]</sup> Furthermore, hierarchical micro/nanostructures are immensely beneficial to improve the performance of antireflection effect owing to their omnidirectional morphology and smoother change of the refractive index than monotonous nanostructures.<sup>[24]</sup>

**Plasmonics:** As another approach for light management, plasmonics, in particular plasmonic nanoarrays, has been spotlighted due to its significant light absorption enhancement by scattering and redistribution of the electromagnetic field.<sup>[26, 27]</sup> Periodic metal nanopatterns can be manufactured by conventional lithographic techniques with different shapes and sizes for tailoring optical properties. There are three representative mechanisms to boost the light absorption in plasmonic nanostructures. First of all, metallic nanoparticles, which effectively confine incident light into a thin absorption layer, play a key role to promote subwavelength scattering and thus coupling and trapping of incident light. Secondly, metallic nanoparticles can act as subwavelength antennas in optoelectronic devices, which allow the enhancement of cross-sectional absorption. Finally, in case of structural metallic film, the coupling of incident light from the surface plasmon polariton and guided modes can generate subsidiary photocarriers. To conclude, the utilization of plasmonic nanostructures in optoelectronic devices can foster the performance of optoelectronics through coordinating the light interaction with subwavelength ranges.

## 1.3 Flexible Mechanosensors

### 1.3.1 Introduction to Flexible Mechanosensors

Flexible mechanosensors that convert external mechanical stimuli input into electrical signals have attracted with the rapid growth of emerging wearable electronics and IoT technologies.<sup>[28-31]</sup> However, the development of flexible mechanosensors is more challenging than that of proximity sensors based on photodetectors with the following reasons. First of all, mechanosensors directly interact with objects as well as harsh physical stimuli such as pressure, strain, vibration, and torsion. Thus, it has been hardly no sinecure to achieve suitable mechanosensors with high durability, abrasion resistance, and compatibility based on commonly used brittle semiconductors. Secondly, since the physical stimuli involve multiple signals, the selective detection of physical stimuli should be reflected in the design of flexible mechanosensors.

Notwithstanding some major technical difficulties, flexible mechanosensors are essential electronic components for providing information about the target objects or activities through direct physical

contact in future electronics such as smart healthcare system, electronic skin, soft robotics, and human–machine interfaces.<sup>[30, 32, 33]</sup> Therefore, many researchers have been trying to realize superior flexible mechanosensors with advances in flexible electronics and nanotechnology. Typically, to attain high sensing performance without severe loss of mechanical deformability, a variety of functional nanomaterials<sup>[30, 34]</sup> and flexible polymeric substrates<sup>[35]</sup> have been extensively explored with various sensing approaches and device architectures. Recently, human skin has offered big inspiration to develop ideal flexible mechanosensors because of its effective structures and functions for excellent sensing capabilities.<sup>[36-38]</sup>

### 1.3.2 Sensing Approaches

Structural modification in flexible mechanosensors provides dramatic deformation to active sensing materials in response to external mechanical stress, which enables highly sensitive signal transduction from mechanical stimuli to electrical signals. Commonly, there are four kinds of signal transduction for mechanical stimuli perception using resistivity and capacitance changes in materials as well as the uptake of piezoelectric and triboelectric effects (**Figure 1.8**).<sup>[29, 30]</sup>

**Resistivity:** Piezoresistive sensors transduce external mechanical stimuli into resistance changes of conducting or semiconducting active materials. Active sensing materials generally require satisfactory current flow paths as well as moderate elasticity for bearing up against diverse mechanical deformations. One popular design for piezoresistive sensor is usage of composite including conductive fillers within the elastic matrix. Up to now, a variety of conductive fillers, including metallic nanomaterials such as Au and Ag nanowires,<sup>[39, 40]</sup> carbon based materials such as graphene,<sup>[41, 42]</sup> carbon nanotube,<sup>[43, 44]</sup> MXene,<sup>[45]</sup> and conductive polymers such as polyaniline,<sup>[46]</sup> have been demonstrated. In addition, elastomers (e.g. poly(dimethylsiloxane) (PDMS)<sup>[39, 40, 43, 47]</sup> and polyurethane (PU)<sup>[44]</sup>) and hydrogels (e.g. polyacrylamide<sup>[48]</sup>) have been widely used as substrates for high deformability and resilience.

**Capacitance:** Piezocapacitive sensors recognize the capacitance variations of devices composed of deformable dielectric materials (e.g. PDMS,<sup>[49]</sup> PU,<sup>[50]</sup> and Ecoflex<sup>[51, 52]</sup>) with two plate electrodes. Generally, the capacitance ( $C$ ) can be defined as  $C = \frac{\epsilon_0 \epsilon_r A}{d}$ , where  $\epsilon_0$  is the permittivity of vacuum,  $\epsilon_r$  is the relative permittivity of the dielectric material,  $A$  is the effective area of the capacitor, and  $d$  is the distance between the electrodes. Therefore, the stress-induced changes of effective area and distance between the two plates vary the capacitance to detect the pressure and strain. It is noteworthy that air-embedded structures are profitable to improve sensing performance of piezocapacitive sensors because of their low elastic modulus and the variation of effective dielectric constant in response to external stress.<sup>[49, 52]</sup>

**Piezoelectricity:** Piezoelectric sensors utilize piezoelectric effect appeared in specific groups of crystalline ceramics (e.g. ZnO,<sup>[53]</sup> BaTiO<sub>3</sub>,<sup>[54]</sup> lead zirconate titanate<sup>[55]</sup>) and polar polymers (e.g.

poly(vinylidene fluoride)<sup>[56]</sup> and poly(vinylidene fluoride-trifluoroethylene) (PVDF-TrFE)<sup>[57]</sup>.<sup>[30]</sup> This phenomenon is referred to as the spatial separation of positive and negative charges in materials with response to external mechanical stress such as normal pressure and lateral strain. Under the applied pressure, piezoelectric materials experienced the change in polarization and rearrangement of the dipole moment, resulting in the generation of reversible current and voltage signals in the devices. In contrast to the resistive and capacitive transduction modes, instant response of piezoelectric output signals enables dynamic sensing capability such as high-frequency vibration detection.

**Triboelectricity:** Triboelectricity is easily discoverable phenomenon in everyday life, which can be arisen from friction between two different contact materials.<sup>[58]</sup> Similar to piezoelectric sensors, triboelectric sensors can produce electricity without external power but use outside mechanical energy, which allows the self-powered operation. On the other hand, the friction-induced charge generation and polarization by triboelectric effect can occur in any materials contrary to piezoelectricity, which facilitates the widespread usage in mechanosensors. However, in order to achieve high output electrical signals, triboelectric sensors should secure a sufficient air gap between two contact materials, which requires the large volumetric design and thus restricts flexibility.<sup>[59]</sup> Therefore, many researchers have striven for inventing effective structures incorporating large air gap with superior deformability for desirable flexible mechanosensors.

### 1.3.3 Figures of Merit for Flexible Mechanosensors

There are several important figures of merit to fairly compare the performance of flexible mechanosensors prepared with different materials, device architectures, and working principles. In the following part, we briefly describe these performance figure-of-merits.

**Sensitivity (S):** Sensitivity evaluates the ability of sensors to convert mechanical signals into electrical signals. The sensitivity is defined as  $S = \frac{\Delta E}{E_0 P}$ , where  $\Delta E$  is the variation of electrical signals such as current, voltage, and capacitance,  $\Delta P$  is the amount of applied mechanical stress, typically pressure, and  $E_0$  denotes the default electrical signal without external stress. High sensitivity is considered as the primary property whenever we design the mechanosensors.

**Response time:** Response time is calculated by measuring the interval time for 90% changes of electrical signals before and after applying external stress. The viscoelastic property of soft matrix or time for changing innate electrical properties of active materials can be directly reflected to response time as well as hysteresis of electrical signals.

**Detection range:** Wide dynamic range is promising for broad applications by a single device, which requires precise detection of mechanical stimuli with varying intensity. In addition, sensing capability with linear signal response to an increasing amount of applied stress is highly demanded for convenient data processing.

**Mechanical durability and environmental stability:** In order to detect the physical stimuli, flexible mechanosensors inevitably suffer from harsh mechanical stress such as pressure, strain, shear, and torsion, which exerts a negative effect on durability. Furthermore, the flexible mechanosensors fatally have possibility to get damaged by other chemicals and humidity due to their easily accessible designs for external physical signals. Therefore, newly developed flexible mechanosensors is needed to examine their stability under repeated mechanical stress as well as environmental factors.

**Output power density (P):** In case of the piezoelectric and triboelectric mechanosensors, the current and voltage signals can be generated by external mechanical forces. The electrical signals enable self-powered detection of various stimuli as well as supply power to operate other connected devices, which is desirable for enhancing sustainability of wearable electronics. Therefore, the output power density, which can be obtained from the multiplication of current density and voltage, is often mentioned in the literatures.

### 1.3.4 Design of Highly Sensitive Mechanosensors

In general, the planar design of mechanosensors cannot provide sufficient sensing capabilities in terms of high sensitivity, detection range, and response time as well as functionalities.<sup>[60]</sup> Therefore, a plenty of the surface modifications with microstructures such as pillar, pyramid, and dome have been demonstrated by micromolding techniques.<sup>[38, 43, 60]</sup> Compared to planar structure, microstructures with lower modulus of elastomer lead to dramatic changes of surface contact area in response to external stress and thus increase the sensitivity of mechanosensors regardless of sensing mode. In addition, it is well-known that hybrid micro/nanostructures based hierarchical surface morphologies can further enhance the sensitivity with effective transmission of external mechanical stress and extremely large contact area.<sup>[38, 61, 62]</sup>

Recently, mimicking the structures and functions of nature, bio-inspired design of micro/nanostructured materials have been spotlighted as another approach to improve the sensing performance of mechanosensors. For example, the inspiration from nanoscale cracks in spider's slit that can detect minute vibration enabled to fabricate artificial nanocracks with reversibly controllable nanogaps, resulting in the development of vibration-sensitive mechanosensor.<sup>[63]</sup> In addition, interlocked architectures in dragonfly's head arrester and under human skin provide crucial inspiration to make highly sensitive mechanosensors with large surface areal differences and effective transmission of tiny stress.<sup>[38, 53, 64, 65]</sup> In conclusion, the high-performance and flexible mechanosensors can be prepared by exploring appropriate active sensing elements and soft matrix with novel structural designs.

#### 1.4 References

- [1] Moore, G. E. Moore's Law at 40. In *Understanding Moore's Law: Four Decades of Innovation*; Brock, D. C., Ed.; Chemical Heritage Foundation: Philadelphia, PA, 2006; pp 67–84.
- [2] Troadec, C. MEMS and Sensors Challenges and Opportunities for the Next Decade. Presented at the MIG Technical Congress, Munich, Germany, March 7–8, 2016.
- [3] Razzaque, M. A.; Milojevic-Jevric, M.; Palade, A.; Clarke, S. Middleware for Internet of Things: A Survey. *IEEE Internet Things J.* **2016**, *3*, 70–95.
- [4] Ma, Z.; Qin, G. Fast Flexible Electronics Made from Nanomembranes Derived from High-Quality Wafers. In *Semiconductor Nanomaterials for Flexible Technologies: From Photovoltaics and Electronics to Sensors and Energy Storage*; Sun, Y., Rogers, J. A., Eds.; Micro and Nano Technologies; William Andrew: Norwich, NY, 2010; pp 67–104.
- [5] Teng, F.; Hu, K.; Ouyang, W.; Fang, X. Photoelectric Detectors Based on Inorganic P-Type Semiconductor Materials. *Adv. Mater.* **2018**, *30*, 1706262.
- [6] Cai, S.; Xu, X.; Yang, W.; Chen, J.; Fang, X. Materials and Designs for Wearable Photodetectors. *Adv. Mater.* **2019**, *31*, 1808138.
- [7] Xie, C.; Yan, F. Flexible Photodetectors Based on Novel Functional Materials. *Small* **2017**, *13*, 1701822.
- [8] Lim, S.; Um, D.-S.; Ha, M.; Zhang, Q.; Lee, Y.; Lin, Y.; Fan, Z.; Ko, H. Broadband Omnidirectional Light Detection in Flexible and Hierarchical ZnO/Si Heterojunction Photodiodes. *Nano Res.* **2017**, *10*, 22–36.
- [9] Konstantatos, G.; Sargent, E. H. Nanostructured Materials for Photon Detection. *Nat. Nanotechnol.* **2010**, *5*, 391–400.
- [10] Wang, W.; Qi, L. Light Management with Patterned Micro- and Nanostructure Arrays for Photocatalysis, Photovoltaics, and Optoelectronic and Optical Devices. *Adv. Funct. Mater.* **2019**, *29*, 1807275.
- [11] Leung, S. F.; Zhang, Q.; Xiu, F.; Yu, D.; Ho, J. C.; Li, D.; Fan, Z. Light Management with Nanostructures for Optoelectronic Devices. *J. Phys. Chem. Lett.* **2014**, *5*, 1479–1495.
- [12] Ko, D.-H.; Tumbleston, J. R.; Henderson, K. J.; Euliss, L. E.; DeSimone, J. M.; Lopez, R.; Samulski, E. T. Biomimetic Microlens Array with Antireflective “Moth-Eye” Surface. *Soft Matter* **2011**, *7*, 6404–6407.
- [13] Ou, Y.; Zhu, X.; Jokubavicius, V.; Yakimova, R.; Mortensen, N. A.; Syvajarvi, M.; Xiao, S.; Ou, H. Broadband Antireflection and Light Extraction Enhancement in Fluorescent SiC with Nanodome Structures. *Sci. Rep.* **2014**, *4*, 4662.
- [14] Zhu, J.; Yu, Z.; Burkhard, G. F.; Hsu, C. M.; Connor, S. T.; Xu, Y.; Wang, Q.; McGehee, M.; Fan, S.; Cui, Y. Optical Absorption Enhancement in Amorphous Silicon Nanowire and Nanocone Arrays. *Nano Lett.* **2009**, *9*, 279–282.



- [15] Lin, Q.; Leung, S. F.; Lu, L.; Chen, X.; Chen, Z.; Tang, H.; Su, W.; Li, D.; Fan, Z. Inverted Nanocone-Based Thin Film Photovoltaics with Omnidirectionally Enhanced Performance. *ACS Nano* **2014**, *8*, 6484–6490.
- [16] Chen, X.; Yang, H.; Liu, G.; Gao, F.; Dai, M.; Hu, Y.; Chen, H.; Cao, W.; Hu, P.; Hu, W. Hollow Spherical Nanoshell Arrays of 2D Layered Semiconductor for High-Performance Photodetector Device. *Adv. Funct. Mater.* **2018**, *28*, 1705153.
- [17] Hu, L.; Chen, M.; Shan, W.; Zhan, T.; Liao, M.; Fang, X.; Hu, X.; Wu, L. Stacking-Order-Dependent Optoelectronic Properties of Bilayer Nanofilm Photodetectors Made from Hollow ZnS and ZnO Microspheres. *Adv. Mater.* **2012**, *24*, 5872–5877.
- [18] Wu, W. Q.; Feng, H. L.; Rao, H. S.; Xu, Y. F.; Kuang, D. B.; Su, C. Y. Maximizing Omnidirectional Light Harvesting in Metal Oxide Hyperbranched Array Architectures. *Nat. Commun.* **2014**, *5*, 3968.
- [19] Wei, W. R.; Tsai, M. L.; Ho, S. T.; Tai, S. H.; Ho, C. R.; Tsai, S. H.; Liu, C. W.; Chung, R. J.; He, J. H. Above-11%-Efficiency Organic-Inorganic Hybrid Solar Cells with Omnidirectional Harvesting Characteristics by Employing Hierarchical Photon-Trapping Structures. *Nano Lett.* **2013**, *13*, 3658–3663.
- [20] Han, S. E.; Chen, G. Toward the Lambertian Limit of Light Trapping in Thin Nanostructured Silicon Solar Cells. *Nano Lett.* **2010**, *10*, 4692–4696.
- [21] Cai, J.; Qi, L. Recent Advances in Antireflective Surfaces Based on Nanostructure Arrays. *Mater. Horiz.* **2015**, *2*, 37–53.
- [22] Zhao, J.; Green, M. A. Optimized Antireflection Coatings for High-Efficiency Silicon Solar-Cells. *IEEE Trans. Electron Devices* **1991**, *38*, 1925–1934.
- [23] Diedenhofen, S. L.; Grzela, G.; Haverkamp, E.; Bauhuis, G.; Schermer, J.; Rivas, J. G. Broadband and Omnidirectional Anti-Reflection Layer for III/V Multi-Junction Solar Cells. *Sol. Energy Mater. Sol. Cells* **2012**, *101*, 308–314.
- [24] Cho, I. S.; Chen, Z.; Forman, A. J.; Kim, D. R.; Rao, P. M.; Jaramillo, T. F.; Zheng, X. Branched TiO<sub>2</sub> Nanorods for Photoelectrochemical Hydrogen Production. *Nano Lett.* **2011**, *11*, 4978–4984.
- [25] Choi, K.; Park, S. H.; Song, Y. M.; Lee, Y. T.; Hwangbo, C. K.; Yang, H.; Lee, H. S. Nano-Tailoring the Surface Structure for the Monolithic High-Performance Antireflection Polymer Film. *Adv. Mater.* **2010**, *22*, 3713–3718.
- [26] Ozbay, E. Plasmonics: Merging Photonics and Electronics at Nanoscale Dimensions. *Science* **2006**, *311*, 189–193.
- [27] Gramotnev, D. K.; Bozhevolnyi, S. I. Plasmonics Beyond the Diffraction Limit. *Nat. Photonics* **2010**, *4*, 83–91.
- [28] Gao, W.; Ota, H.; Kiriya, D.; Takei, K.; Javey, A. Flexible Electronics toward Wearable Sensing. *Acc. Chem. Res.* **2019**, *52*, 523–533.

- [29] Huang, Y.; Fan, X.; Chen, S. C.; Zhao, N. Emerging Technologies of Flexible Pressure Sensors: Materials, Modeling, Devices, and Manufacturing. *Adv. Funct. Mater.* **2019**, *29*, 1808509.
- [30] Ha, M.; Lim, S.; Ko, H. Wearable and Flexible Sensors for User-Interactive Health-Monitoring Devices. *J. Mater. Chem. B* **2018**, *6*, 4043–4064.
- [31] Yang, T.; Xie, D.; Li, Z.; Zhu, H. Recent Advances in Wearable Tactile Sensors: Materials, Sensing Mechanisms, and Device Performance. *Mater. Sci. Eng. R Rep.* **2017**, *115*, 1–37.
- [32] Wang, X.; Dong, L.; Zhang, H.; Yu, R.; Pan, C.; Wang, Z. L. Recent Progress in Electronic Skin. *Adv. Sci.* **2015**, *2*, 1500169.
- [33] Hammock, M. L.; Chortos, A.; Tee, B. C.; Tok, J. B.; Bao, Z. 25th Anniversary Article: The Evolution of Electronic Skin (E-Skin): A Brief History, Design Considerations, and Recent Progress. *Adv. Mater.* **2013**, *25*, 5997–6038.
- [34] Kim, J.; Lee, J.; Son, D.; Choi, M. K.; Kim, D. H. Deformable Devices with Integrated Functional Nanomaterials for Wearable Electronics. *Nano Converg.* **2016**, *3*, 4.
- [35] Malik, A.; Kandasubramanian, B. Flexible Polymeric Substrates for Electronic Applications. *Polym. Rev.* **2018**, *58*, 630–667.
- [36] Skin to E-Skin. *Nat. Nanotechnol.* **2017**, *12*, 1017.
- [37] Son, D.; Bao, Z. Nanomaterials in Skin-Inspired Electronics: Toward Soft and Robust Skin-Like Electronic Nanosystems. *ACS Nano* **2018**, *12*, 11731–11739.
- [38] Ha, M.; Lim, S.; Cho, S.; Lee, Y.; Na, S.; Baig, C.; Ko, H. Skin-Inspired Hierarchical Polymer Architectures with Gradient Stiffness for Spacer-Free, Ultrathin, and Highly Sensitive Triboelectric Sensors. *ACS Nano* **2018**, *12*, 3964–3974.
- [39] Gong, S.; Schwalb, W.; Wang, Y.; Chen, Y.; Tang, Y.; Si, J.; Shirinzadeh, B.; Cheng, W. A Wearable and Highly Sensitive Pressure Sensor with Ultrathin Gold Nanowires. *Nat. Commun.* **2014**, *5*, 3132.
- [40] Amjadi, M.; Pichitpajongkit, A.; Lee, S.; Ryu, S.; Park, I. Highly Stretchable and Sensitive Strain Sensor Based on Silver Nanowire-Elastomer Nanocomposite. *ACS Nano* **2014**, *8*, 5154–5163.
- [41] Tao, L. Q.; Zhang, K. N.; Tian, H.; Liu, Y.; Wang, D. Y.; Chen, Y. Q.; Yang, Y.; Ren, T. L. Graphene-Paper Pressure Sensor for Detecting Human Motions. *ACS Nano* **2017**, *11*, 8790–8795.
- [42] Chen, Z.; Ming, T.; Goulamaly, M. M.; Yao, H.; Nezhich, D.; Hempel, M.; Hofmann, M.; Kong, J. Enhancing the Sensitivity of Percolative Graphene Films for Flexible and Transparent Pressure Sensor Arrays. *Adv. Funct. Mater.* **2016**, *26*, 5061–5067.
- [43] Park, J.; Lee, Y.; Hong, J.; Ha, M.; Jung, Y. D.; Lim, H.; Kim, S. Y.; Ko, H. Giant Tunneling Piezoresistance of Composite Elastomers with Interlocked Microdome Arrays for Ultrasensitive and Multimodal Electronic Skins. *ACS Nano* **2014**, *8*, 4689–4697.
- [44] Chen, H.; Su, Z.; Song, Y.; Cheng, X.; Chen, X.; Meng, B.; Song, Z.; Chen, D.; Zhang, H. Omnidirectional Bending and Pressure Sensor Based on Stretchable CNT-PU Sponge. *Adv. Funct.*

*Mater.* **2017**, *27*, 1604434.

[45] Ma, Y.; Liu, N.; Li, L.; Hu, X.; Zou, Z.; Wang, J.; Luo, S.; Gao, Y. A Highly Flexible and Sensitive Piezoresistive Sensor Based on MXene with Greatly Changed Interlayer Distances. *Nat. Commun.* **2017**, *8*, 1207.

[46] Wu, W.; Wang, B.; Segev-Bar, M.; Dou, W.; Niu, F.; Horev, Y. D.; Deng, Y.; Plotkin, M.; Huynh, T.-P.; Jeries, R.; Zhu, H.; Garaa, A. I.; Badarneh, S.; Chen, L.; Du, M.; Hu, W.; Haick, H. Free-Standing and Eco-Friendly Polyaniline Thin Films for Multifunctional Sensing of Physical and Chemical Stimuli. *Adv. Funct. Mater.* **2017**, *27*, 1703147.

[47] Huang, Y.; Chen, Y.; Fan, X.; Luo, N.; Zhou, S.; Chen, S. C.; Zhao, N.; Wong, C. P. Wood Derived Composites for High Sensitivity and Wide Linear-Range Pressure Sensing. *Small* **2018**, *14*, 1801520.

[48] Duan, J.; Liang, X.; Guo, J.; Zhu, K.; Zhang, L. Ultra-Stretchable and Force-Sensitive Hydrogels Reinforced with Chitosan Microspheres Embedded in Polymer Networks. *Adv. Mater.* **2016**, *28*, 8037–8044.

[49] Mannsfeld, S. C.; Tee, B. C.; Stoltenberg, R. M.; Chen, C. V.; Barman, S.; Muir, B. V.; Sokolov, A. N.; Reese, C.; Bao, Z. Highly Sensitive Flexible Pressure Sensors with Microstructured Rubber Dielectric Layers. *Nat. Mater.* **2010**, *9*, 859–864.

[50] Wang, J.; Jiu, J.; Nogi, M.; Sugahara, T.; Nagao, S.; Koga, H.; He, P.; Suganuma, K. A Highly Sensitive and Flexible Pressure Sensor with Electrodes and Elastomeric Interlayer Containing Silver Nanowires. *Nanoscale* **2015**, *7*, 2926–2932.

[51] Yao, S.; Zhu, Y. Wearable Multifunctional Sensors Using Printed Stretchable Conductors Made of Silver Nanowires. *Nanoscale* **2014**, *6*, 2345–2352.

[52] Kwon, D.; Lee, T. I.; Shim, J.; Ryu, S.; Kim, M. S.; Kim, S.; Kim, T. S.; Park, I. Highly Sensitive, Flexible, and Wearable Pressure Sensor Based on a Giant Piezocapacitive Effect of Three-Dimensional Microporous Elastomeric Dielectric Layer. *ACS Appl. Mater. Interfaces* **2016**, *8*, 16922–16931.

[53] Ha, M.; Lim, S.; Park, J.; Um, D.-S.; Lee, Y.; Ko, H. Bioinspired Interlocked and Hierarchical Design of ZnO Nanowire Arrays for Static and Dynamic Pressure-Sensitive Electronic Skins. *Adv. Funct. Mater.* **2015**, *25*, 2841–2849.

[54] Koka, A.; Sodano, H. A. High-Sensitivity Accelerometer Composed of Ultra-Long Vertically Aligned Barium Titanate Nanowire Arrays. *Nat. Commun.* **2013**, *4*, 2682.

[55] Park, D. Y.; Joe, D. J.; Kim, D. H.; Park, H.; Han, J. H.; Jeong, C. K.; Park, H.; Park, J. G.; Joung, B.; Lee, K. J. Self-Powered Real-Time Arterial Pulse Monitoring Using Ultrathin Epidermal Piezoelectric Sensors. *Adv. Mater.* **2017**, *29*, 1702308.

[56] Shirinov, A. V.; Schomburg, W. K. Pressure Sensor from a PVDF Film. *Sens. Actuators, A* **2008**, *142*, 48–55.

- [57] Sharma, T.; Je, S.-S.; Gill, B.; Zhang, J. X. J. Patterning Piezoelectric Thin Film PVDF-TrFE Based Pressure Sensor for Catheter Application. *Sens. Actuators, A* **2012**, *177*, 87–92.
- [58] Ha, M.; Park, J.; Lee, Y.; Ko, H. Triboelectric Generators and Sensors for Self-Powered Wearable Electronics. *ACS Nano* **2015**, *9*, 3421–3427.
- [59] Wang, Z. L.; Chen, J.; Lin, L. Progress in Triboelectric Nanogenerators as a New Energy Technology and Self-Powered Sensors. *Energy Environ. Sci.* **2015**, *8*, 2250–2282.
- [60] Park, J.; Kim, J.; Hong, J.; Lee, H.; Lee, Y.; Cho, S.; Kim, S.-W.; Kim, J. J.; Kim, S. Y.; Ko, H. Tailoring Force Sensitivity and Selectivity by Microstructure Engineering of Multidirectional Electronic Skins. *NPG Asia Mater.* **2018**, *10*, 163–176.
- [61] Bae, G. Y.; Pak, S. W.; Kim, D.; Lee, G.; Kim do, H.; Chung, Y.; Cho, K. Linearly and Highly Pressure-Sensitive Electronic Skin Based on a Bioinspired Hierarchical Structural Array. *Adv. Mater.* **2016**, *28*, 5300–5306.
- [62] Han, Z.; Cheng, Z.; Chen, Y.; Li, B.; Liang, Z.; Li, H.; Ma, Y.; Feng, X. Fabrication of Highly Pressure-Sensitive, Hydrophobic, and Flexible 3D Carbon Nanofiber Networks by Electrospinning for Human Physiological Signal Monitoring. *Nanoscale* **2019**, *11*, 5942–5950.
- [63] Kang, D.; Pikhitsa, P. V.; Choi, Y. W.; Lee, C.; Shin, S. S.; Piao, L.; Park, B.; Suh, K. Y.; Kim, T. I.; Choi, M. Ultrasensitive Mechanical Crack-Based Sensor Inspired by the Spider Sensory System. *Nature* **2014**, *516*, 222–226.
- [64] Gorb, S. N.; Beutel, R. G.; Gorb, E. V.; Jiao, Y.; Kastner, V.; Niederegger, S.; Popov, V. L.; Scherge, M.; Schwarz, U.; Votsch, W. Structural Design and Biomechanics of Friction-Based Releasable Attachment Devices in Insects. *Integr. Comp. Biol.* **2002**, *42*, 1127–1139.
- [65] Park, J.; Kim, M.; Lee, Y.; Lee, H. S.; Ko, H. Fingertip Skin-Inspired Microstructured Ferroelectric Skins Discriminate Static/Dynamic Pressure and Temperature Stimuli. *Sci. Adv.* **2015**, *1*, e1500661.
- [66] Song, Y. M.; Xie, Y.; Malyarchuk, V.; Xiao, J.; Jung, I.; Choi, K.-J.; Liu, Z.; Park, H.; Lu, C.; Kim, R.-H.; Li, R.; Crozier, K. B.; Huang, Y.; Rogers J. A. Digital Cameras with Designs Inspired by the Arthropod Eye. *Nature* **2013**, *497*, 95–99.
- [67] Siddiqui, S.; Kim, D.-I.; Duy, L. T.; Nguyen, M. T.; Muhammad, S.; Yoon, W.-S.; Lee, N.-E. High-Performance Flexible Lead-Free Nanocomposite Piezoelectric Nanogenerator for Biomechanical Energy Harvesting and Storage. *Nano Energy* **2015**, *15*, 177–185.
- [68] Lim, S.; Ha, M.; Lee, Y.; Ko, H. Large-Area, Solution-Processed, Hierarchical MAPbI<sub>3</sub> Nanoribbon Arrays for Self-Powered Flexible Photodetectors. *Adv. Optical Mater.* **2018**, *6*, 1800615.
- [69] Hallels Home page, <http://www.hallels.com/articles/2533/20140717/google-smart-lens-an-eye-lens-that-can-measure-your-blood-sugar-level-and-correct-vision-using-auto-focus-technology.htm> (accessed May 2, 2019)
- [70] SciNews.com Home page, <https://scinews.com/tr/teknoloji/1330-ak-ll-kuma-yapacak-herhangi->

bir-giysi-fitness-izci.html (accessed May 2, 2019)

[71] Smart Gadget Genius Home page, <https://smartgadgetgenius.com/wearable-technology/> (accessed May 2, 2019)

[72] Internetdevels Home Page, <https://internetdevels.com/blog/artificial-intelligence-drupal-8> (accessed May 2, 2019)

[73] Metro Home page, <https://metro.co.uk/2018/11/05/robots-deserve-human-rights-why-activists-want-to-protect-machines-from-their-creators-8097696/> (accessed May 2, 2019)

[74] Motor Authority Home page, [https://www.motorauthority.com/news/1081957\\_bosch-gives-up-date-on-its-autonomous-car-development-video](https://www.motorauthority.com/news/1081957_bosch-gives-up-date-on-its-autonomous-car-development-video) (accessed May 2, 2019)

[75] Cult of Mac Home Page, <https://www.cultofmac.com/177614/this-futuristic-iphone-concept-is-a-bizarre-new-take-on-wearable-technology-gallery/> (accessed May 2, 2019)

[76] AsianScientist Home page, <https://www.asianscientist.com/2017/07/tech/breathable-biocompatible-wearable/> (accessed May 2, 2019)

[77] The Washington Post Home page, [https://www.washingtonpost.com/national/health-science/how-the-body-could-power-pacemakers-and-other-implantable-devices/2018/06/08/16d287b0-5559-11e8-a551-5b648abe29ef\\_story.html?noredirect=on&utm\\_term=.a9a62c49567e](https://www.washingtonpost.com/national/health-science/how-the-body-could-power-pacemakers-and-other-implantable-devices/2018/06/08/16d287b0-5559-11e8-a551-5b648abe29ef_story.html?noredirect=on&utm_term=.a9a62c49567e) (accessed May 2, 2019)

[78] Everything Tech Gear Home page, <https://everythingtechgear.com/products/new-waterproof-solar-power-bank-10000mah-dual-usb-li-polymer-solar-battery-charger-travel-powerbank-with-a-compass-2> (accessed May 2, 2019)

[79] Electronic Design Home Page, <https://www.electronicdesign.com/industrial-automation/entering-new-robotics-age-machine-learning> (accessed May 2, 2019)

[80] Instructables Home page, <https://www.instructables.com/id/Augmented-Reality-Eyeglass-With-Thermal-Vision-Bui/> (accessed May 2, 2019)

[81] Futurity Home page, <https://www.futurity.org/neuroprosthetics-touch-1282822-2/> (accessed May 2, 2019)

[82] Lu Research Group Home Page, <http://www.ae.utexas.edu/facultysites/lu/index.php/9-uncategorised/94-strain-isolation> (accessed May 2, 2019)

[83] Chemical & Engineering News Home page, <https://cen.acs.org/articles/94/i46/healable-polymer-stretchable-electronics.html> (accessed May 2, 2019)

[84] Alternative Energy Systems Home page, <http://www.aes-tunisie.com/en/products/photovoltaics/modules/> (accessed May 2, 2019)

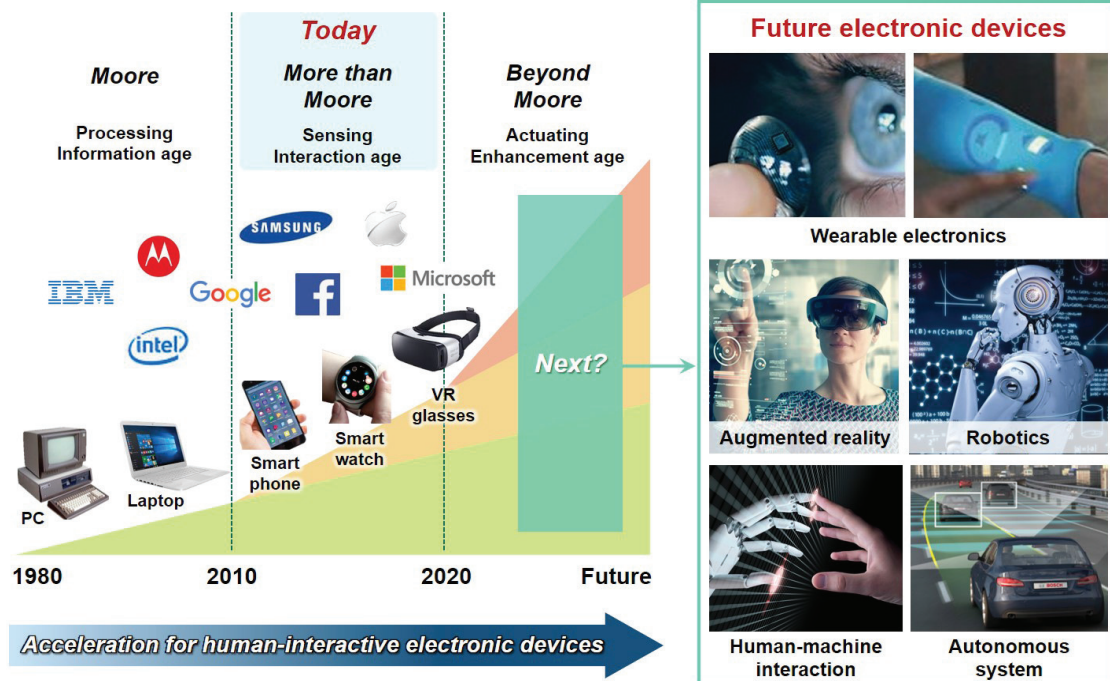


**Figure 1.1** Evolution of electronic devices with the Fourth Industrial Revolution into human-interactive electronic devices. Reproduced from Ref. [2, 69–74].

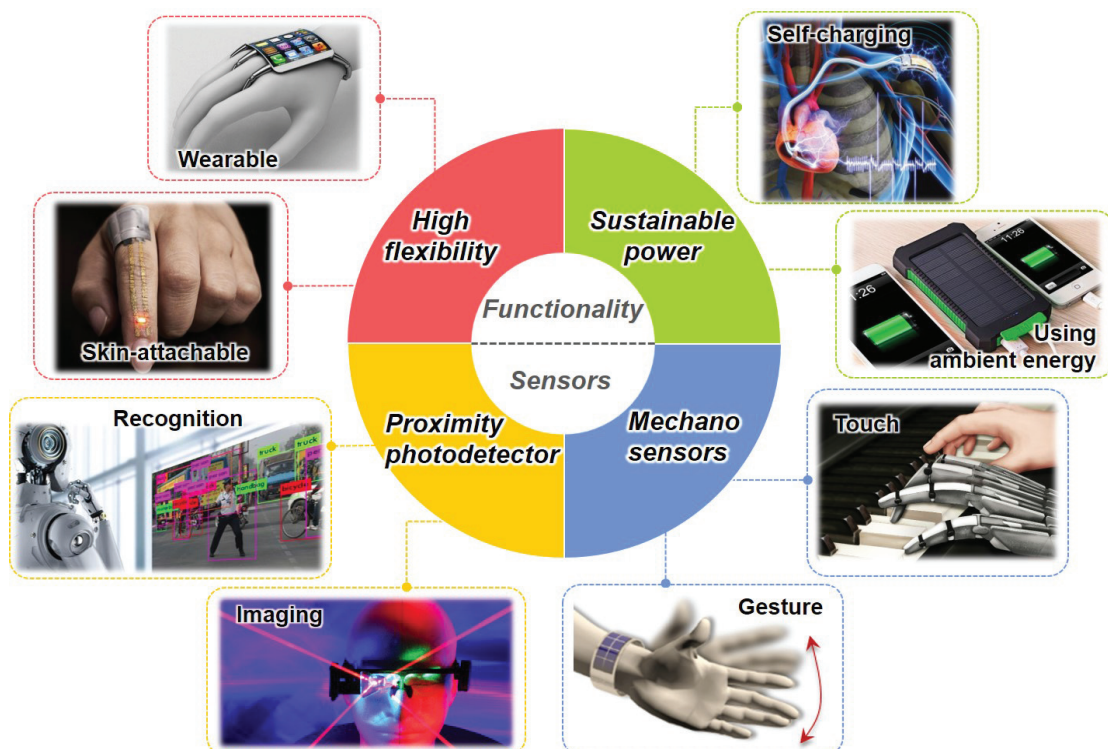


**Figure 1.2** Required technologies for future electronics on the aspects of functionality and sensor. Reproduced from Ref. [75–81].

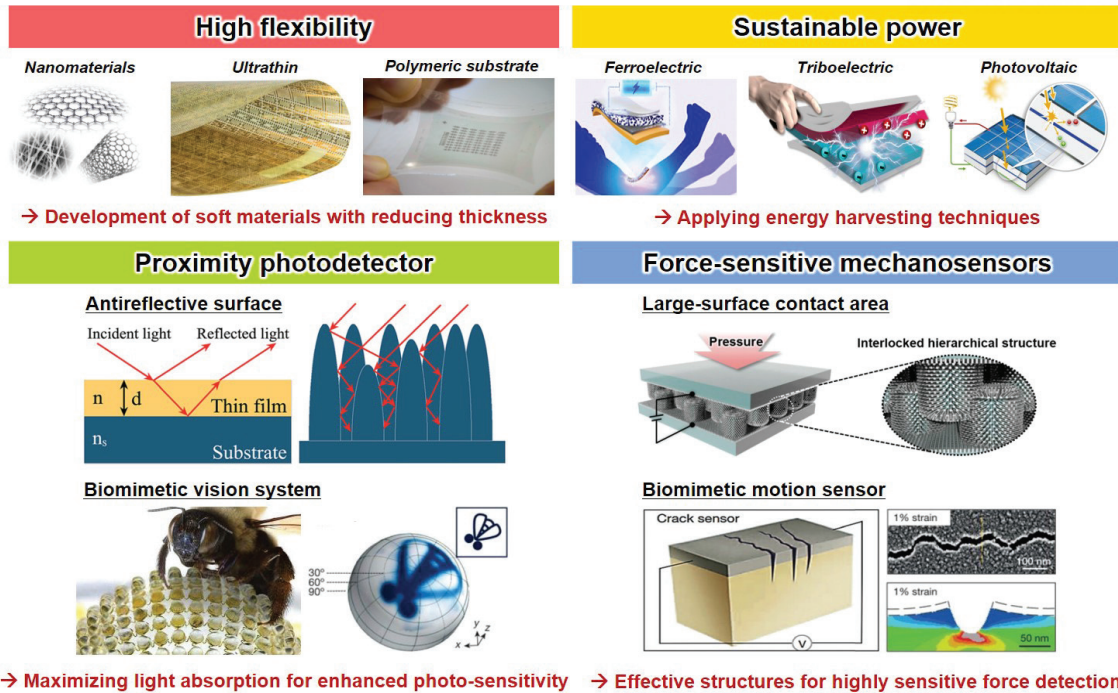


**Figure 1.3** The representative research strategies to achieve the required technologies for future electronics in terms of high flexibility, device sustainability, high-performance photodetectors, and highly-sensitive mechanosensors. Reproduced from Ref. [21] with permission. Copyright © 2015, Royal Society of Chemistry; Reproduced from Ref. [53] with permission. Copyright © 2015, WILEY-VCH Verlag GmbH & Co. KGaA, Weinheim; Reproduced from Ref. [63] with permission. Copyright © 2014, Nature Publishing Group; Reproduced from Ref. [66] with permission. Copyright © 2013 Nature Publishing Group; Reproduced from Ref. [67] with permission. Copyright © 2015 Elsevier Ltd.; Reproduced from Ref. [82–84].

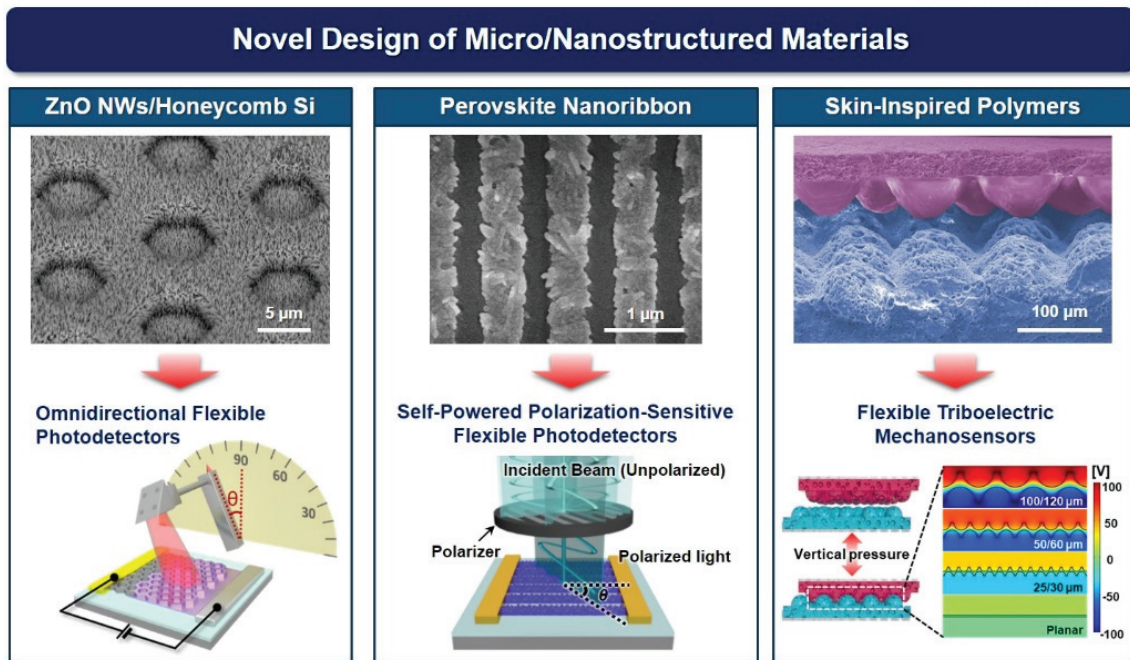


**Figure 1.4** Summary of this thesis. Reproduced from Ref. [8] with permission. Copyright © 2017, Tsinghua University Press and Springer-Verlag Berlin Heidelberg; Reproduced from Ref. [68] with permission. Copyright © 2018, WILEY-VCH Verlag GmbH & Co. KGaA, Weinheim; Reproduced from Ref. [38] with permission. Copyright © 2018, American Chemical Society

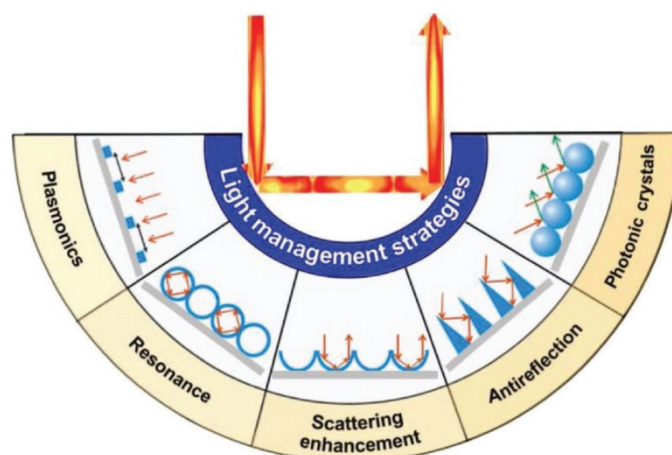


**Figure 1.5** Five light management strategies through novel design of micro/nanostructures to enhance light absorption and thus accomplish high-performance optoelectronic devices. Reproduced from Ref. [10] with permission. Copyright © 2019, WILEY-VCH Verlag GmbH & Co. KGaA, Weinheim



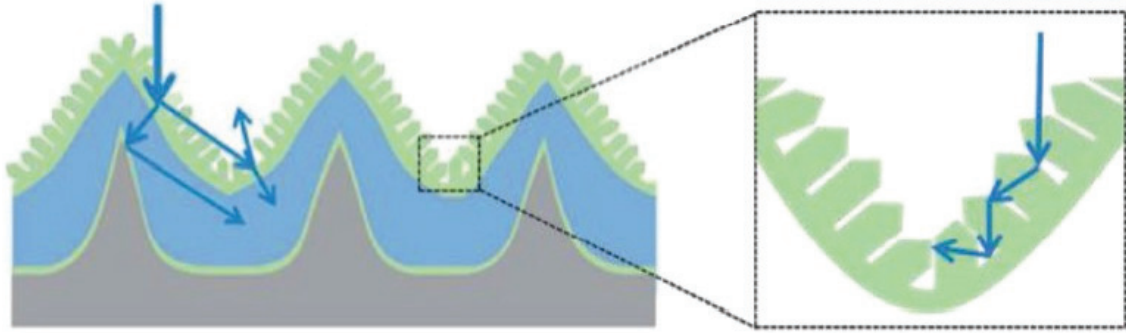


**Figure 1.6** Schematic illustration of the increased light path length through light scattering in the complex hierarchical micro/nanostructures. Reproduced from Ref. [10] with permission. Copyright © 2019, WILEY-VCH Verlag GmbH & Co. KGaA, Weinheim

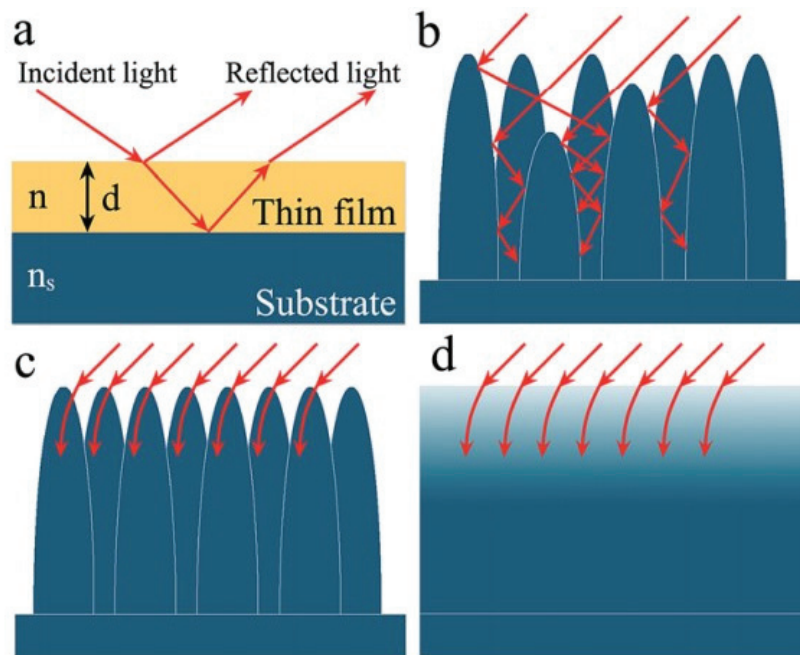


**Figure 1.7** Mechanism of antireflection effect in nanostructures with gradient refractive index. (a) Propagation of light into a thin film on a substrate ( $n_s > n$ ). (b) Promotion of multiple reflections of light in microstructures. (c) Interaction of light with the subwavelength nanostructure arrays. (d) Schematic of gradient refractive index changes in nanostructure arrays. Reproduced from Ref. [21] with permission. Copyright © 2015, Royal Society of Chemistry

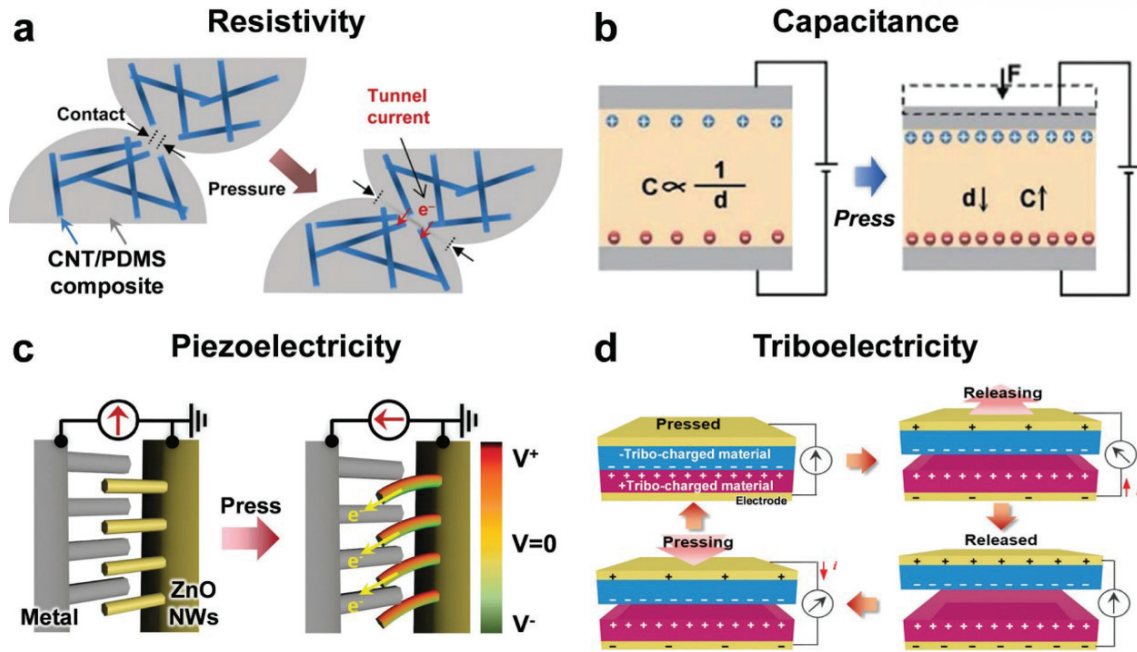


**Figure 1.8** Representative signal transduction approaches in mechanosensors. Reproduced from Ref. [30] with permission. Copyright © 2018, Royal Society of Chemistry

## Chapter 2. Broadband Omnidirectional Light Detection in Flexible and Hierarchical ZnO/Si Heterojunction Photodiodes

### 2.1 Introduction

Flexible photodetectors are important for future bendable/foldable electronics for diverse applications such as flexible image sensors,<sup>[1–3]</sup> artificial retina,<sup>[4–6]</sup> biomedical imaging,<sup>[7, 8]</sup> and smart wearable systems.<sup>[9–11]</sup> Significant progress has been made in the development of flexible photodetectors based on organic and nanostructured materials such as conducting polymers,<sup>[3, 12–14]</sup> quantum dots,<sup>[15, 16]</sup> nanowires (NWs),<sup>[17–19]</sup> two-dimensional (2D) materials,<sup>[14, 20–23]</sup> and inorganic nanomembranes.<sup>[24, 25]</sup> These devices exhibit high bendability while providing great photoresponsivity and fast sensing performance. Broadband flexible photodetectors have also been demonstrated,<sup>[23, 26–31]</sup> the properties of which are advantageous in applications such as charge-coupled devices, optical communications, remote sensing, astronomy, and defense. However, when flexible photodetectors are employed in curved geometry, most of the incident light is at an oblique angle to the photodetector surfaces, which results in increased light reflectance, thus greatly diminishing the performance of the photodetectors.<sup>[32–34]</sup> One critical limitation of previous flexible photodetectors has been the lack of omnidirectional light-detection capability, which would provide a wide field-of-view and thus enable precise monitoring of a moving object using light.

The natural light-sensitive organs found in arthropods have evolved into unique imaging systems for sensitive and wide field-of-view light detection. For example, the compound eyes of moths consist of hexagonally-packed, multiple ommatidia on the hemisphere, which enables individual imaging with a large field-of-view.<sup>[35]</sup> Mimicking the great vision systems in nature, the fabrication of biomimetic image sensors based on microlens arrays omnidirectionally arranged on a hemispherical dome has undergone great progress, resulting in a similar wide field-of-view.<sup>[4, 5, 36, 37]</sup> However, these photodetectors require special and complicated integration strategies for fabrication of nonplanar sensor arrays. Apart from the use of biomimetic microlens arrays for photodetectors, various structural designs have been suggested for effective omnidirectional light harvesting and achieving enhanced photovoltaic efficiency: for example, antireflective multilayer coatings with graded refractive index,<sup>[38, 39]</sup> antireflective nanostructure designs such as nanodomes,<sup>[40]</sup> inverted nanocones,<sup>[41]</sup> nanopencils,<sup>[42]</sup> and hierarchical micro/nanostructures.<sup>[43, 44]</sup> Although these structures have been explored for their omnidirectional light-absorption properties in photovoltaic applications, there has been no attempt to demonstrate flexible photodetectors with omnidirectional light-detection capabilities.

Here, we report the first demonstration of a flexible photodetector with both omnidirectional and broadband light-absorption capabilities (the figure-of-merit characteristics of recently reported photodetectors are summarized and compared in **Table 2.1**). The device structure is based on the bio-

inspired design of hierarchical zinc oxide (ZnO) nanowire (NW) arrays on honeycomb-structured Si (H-Si) membranes, which leads to ZnO NW/H-Si n-p heterojunction structures. In this device design, the hierarchical ZnO NWs on honeycomb structures provide enhanced light-absorption efficiency as well as mechanical flexibility due to the mechanically stable honeycomb structure, which cannot be achieved with traditional crystalline Si membranes. Furthermore, this structure provides omnidirectional light-absorption properties without the use of a hemispherical microlens assembly with multiple photodetectors. The omnidirectional property of flexible photodetectors based on ZnO NWs/H-Si membranes provides stable light detection to furnish a large incident angle range, which enables clear imaging and wide-range detection of objects even though the photodetectors are located on the curved surface. In addition, the ZnO NWs/H-Si photodetectors on flexible polyimide (PI) substrates show stable photodetector performance at a bending radius of 3 mm and over 10,000 bending cycles.

## 2.2 Experimental Details

***Fabrication of honeycomb-structured Si membranes:*** Honeycomb patterns with various sizes were formed on a silicon-on-insulator (SOI) wafer *via* conventional photolithography (MA-6, SUSS MicroTec, Germany) with an AZ nLOF 2035 photoresist. The top Si layer was etched by deep reactive-ion etching (DRIE, Tegal 200, TEGAL, France) with a SiO<sub>2</sub> etch-stop layer for 50 s. The H-Si membrane was spontaneously separated from the mother substrate by selective wet etching with a buffered oxide etch solution, which comprised a 6:1 mixture of 40% ammonium fluoride (NH<sub>4</sub>F) and hydrofluoric acid (HF). The separated freestanding Si membrane was rinsed with distilled (DI) water repeatedly.

***Hydrothermal synthesis of ZnO NWs:*** A 200-nm-thick uniform ZnO layer was deposited by radio frequency (RF) sputtering under conditions of 500 W and 10 mTorr with O<sub>2</sub> gas at a flow rate of 20 sccm (SRN-120D, SORONA, Korea), as a seed layer to grow ZnO NWs on the fabricated H-Si substrate. The thickness of the deposited ZnO layer was accurately measured by using an ellipsometer (Elli-SE-UaM8, Elipso Technology, Korea). For hydrothermal growth of the ZnO NWs, the growth solution was prepared by mixing equimolar amounts ( $25 \times 10^{-3}$  M) of Zn(NO<sub>3</sub>)<sub>2</sub>·xH<sub>2</sub>O (99.9%, Sigma-Aldrich) and hexamethylenetetramine (HMTA) (≥99.0%, Sigma-Aldrich) in DI water with dispersion by sonication. After preheating the growth solution for 5–10 min at 90 °C in a convection oven, the ZnO-deposited H-Si substrates were floated on the surface of the growth solution. The length and diameter of the ZnO NWs were varied by controlling the growth time (**Figure 2.1**). After the growth step, the surface of the ZnO NWs was rinsed with DI water.

***Fabrication of heterojunction photodetector array:*** Reactive-ion etching (Lab Star, TTL, Korea) followed by photolithography was used to fabricate the arrays of the H-Si membrane (20 sccm of SF<sub>6</sub>, 60 sccm of Ar, 10 mTorr, 300 W of RF power). After depositing the ZnO layer and growing the ZnO

NWs for 1 h on the selectively patterned H-Si membrane, the ZnO NW/Si hetero-structures were annealed at 600 °C by rapid thermal annealing (MILA-5000, ULVAC, USA) to improve the quality of the junction properties. Al (100 nm) and Cr/Au (3 nm/97 nm) were selectively deposited on the ZnO and Si regions to form an Ohmic contact by e-beam evaporation (FC-2000, Temescal, USA).

***Fabrication of flexible photodetector array:*** A polyimide (PI) solution was spin coated onto a commercial PI film attached to a glass substrate. Liquid PI was cured at 200 °C on a hot plate for 3 h. A liquid-bridge-mediated transfer printing process was utilized to attach freestanding H-Si membranes to the PI substrate. The prepared freestanding H-Si membranes were fixed on the PI substrate with few drops of ethanol by placing them on a hot plate at 70 °C; thus, the H-Si membranes became tightly attached to the PI surface upon evaporation of the ethanol. Here, the attractive capillary force between the H-Si membrane and PI substrate generated by the evaporation of ethanol induced conformal contact and tight binding between the two substrates. The same process was used to fabricate flexible photodetector arrays with the H-Si/PI substrate, except for the high-temperature rapid thermal annealing (RTA). After depositing the contact metal by e-beam evaporation, RTA was performed at 150 °C to form better junctions between the metal and semiconductor.

***Characterizations:*** The morphologies of the ZnO NWs, H-Si, and hierarchical ZnO NW/H-Si hetero-structures were characterized by field emission scanning electron microscopy (FE-SEM) (S-4800, Hitachi, Japan). The crystal structures of the ZnO layer and ZnO NWs were characterized using a normal X-ray diffractometer (XRD) (D8 Advance, Bruker, USA). The omnidirectional reflection properties of flat Si, H-Si, and ZnO NW/H-Si were verified by UV–vis–NIR spectroscopy with a variable angle specular reflectance accessory (Cary 5000, Agilent, USA). Formation of the interface between the ZnO layer and Si was confirmed by high-resolution transmission electron microscopy (HR-TEM) (JEM-2100F, JEOL, Japan). The TEM samples were prepared using a dual-beam focused ion beam (FIB) (Helios NanoLab 450, FEI, USA). The optical images of the H-Si membrane and fabricated photodetectors were characterized by optical microscopy (OM) (BX-53, Olympus, Japan).

***Electrical and optical measurements:*** The general electrical characteristics of the heterojunction photodiodes were measured by using the two-probe method at room temperature (4200-SCS, Keithley, USA). A monochromator (Cornerstone™ 130 1/8 m Monochromators, Newport, USA) with a variable slit and a Xe arc lamp (300 W) was employed to measure the photo-induced current generated upon illumination with various wavelengths of light. To define the relationship between the photocurrent and the optical power of the incident light, the optical power of a commercial 365 nm light-emitting diode (LED) was varied by changing the input voltage into the LED by using a function generator (AFG3011C, Tektronix, USA). The optical intensity of the light source as a function of the wavelength was measured with a calibrated optical power meter (1916-R, Newport, USA) incorporating a Si photodetector (818-UV, Newport, USA) and a Ge photodetector (818-IR, Newport, USA). The fast photoresponse time for the photocurrent was characterized with a sourcemeter (2450-

SCPI, Keithley, USA). The mechanical flexibility and durability of the flexible photodetector were verified by using a bending tester (JIBT-200, JUNIL TECH, Korea).

**Optical simulation:** The finite-difference time-domain (FDTD) method was utilized to simulate the optical properties of the different structures, including flat Si (F-Si), H-Si, ZnO NW/F-Si, and ZnO NW/H-Si. All ZnO NWs had a diameter of 80 nm, a pitch of 200 nm, and a length of 1  $\mu\text{m}$ . In the case of H-Si, the diameter was 8.7  $\mu\text{m}$ . The light source was located at  $z = 2.5 \mu\text{m}$  and was propagated downwards. Normal incidence ( $0^\circ$ ) and oblique incidence ( $30^\circ$ ) situations were simulated with periodic boundary conditions and Bloch boundary conditions, respectively. Furthermore, the  $|E|^2$  values obtained under 365 and 620 nm excitation were plotted to indicate the light intensity.

### 2.3 Results and Discussion

**Fabrication of omnidirectional ZnO NWs/H-Si:** Hierarchical H-Si membrane structures decorated with ZnO NWs were fabricated for use in omnidirectional photodetectors. **Figure 2.2a** illustrates the fabrication process for the ZnO NWs/H-Si photodetectors on  $\text{SiO}_2/\text{Si}$  substrates. H-Si membranes were fabricated by patterning and etching of commercially available SOI substrates with a 2- $\mu\text{m}$ -thick p-Si top layer (resistivity range: 1–5  $\text{Ohm}\cdot\text{cm}$ ). For growth of the hierarchical ZnO NW arrays on H-Si membranes, a ZnO seed film (200 nm thick) was deposited by using a RF magnetron sputtering system with  $\text{O}_2$ , and ZnO NWs were subsequently grown by using a hydrothermal method.<sup>[58–60]</sup> The SEM images of the sputtered ZnO layer and the hydrothermally grown ZnO NWs with different growth times are presented in **Figure 2.1a** and **2.1b**, which show the densely packed and regular grain sizes of the ZnO crystals in the seed layer and the vertically aligned ZnO NWs grown on the seed layer. The length and diameter of the ZnO NWs could be precisely controlled by controlling the growth time (**Figure 2.1c** and **2.1d**). The ZnO NWs were uniformly grown on H-Si membranes, resulting in hierarchical ZnO NWs/H-Si structures (**Figure 2.2b**). XRD analysis of both the ZnO seed layer and the ZnO NWs in **Figure 2.1e** shows the highest (002) plane peak and three minor peaks of the (100), (101), and (102) planes, resulting from the c-axis crystal growth and the hexagonal symmetry of the wurtzite structure. The cross-sectional HR-TEM images in **Figure 2.3a** confirm epitaxial growth of the ZnO NWs on the ZnO seed films with a well-matched (002) growth plane with a lattice spacing of 0.26 nm. After growing the ZnO NWs on H-Si, Al ( $\sim 100$  nm thickness) and Cr/Au (3 nm/97 nm) electrodes were deposited on the ZnO NWs and H-Si n–p junction photodiode area, respectively, to form an Ohmic contact (**Figure 2.4** shows the linear  $I$ – $V$  curves of Al-ZnO-Al and Cr/Au-Si-Cr/Au). Here, Al deposition increased the number of oxygen defects of the ZnO layer due to the formation of  $\text{Al}_2\text{O}_3$  at the interface between Al and ZnO,<sup>[61]</sup> which improved the forward current of the diode device due to the surface doping effects.

**Figure 2.2c** shows the tilted-view SEM image of the ZnO NW/H-Si photodetector on the  $\text{SiO}_2/\text{Si}$  substrate. The Si–ZnO interface in the n–p ZnO NW/H-Si hetero-structure was investigated by cross-

sectional HR-TEM image analysis. The results show a sharp Si–ZnO interface and a thin native SiO<sub>2</sub> layer (Figure 2.3b).<sup>[62]</sup> Formation of the high-quality ZnO/Si junction in the n–p ZnO NW/H-Si heterostructure was also confirmed by analyzing the current versus voltage ( $I$ – $V$ ) plot in Figure 2.2d, which shows a high rectification ratio of ~160 at an applied voltage of 2 V. The current in the forward biased region (0.2–2 V) increased exponentially in accord with the relation  $I \approx \exp(\alpha V)$ . This behavior indicates charge transport by a recombination tunneling mechanism that is commonly observed for wide-band-gap p–n diodes.<sup>[63]</sup> The ideality factor of 3.1 was calculated from the slope of the low forward bias condition (red line in **Figure 2.5**) using the following equation:

$$n = \frac{q}{kT} \left( \frac{\partial V}{\partial \ln I} \right)$$

where  $k$  is Boltzmann’s constant,  $T$  is the temperature in Kelvin, and  $q$  is the electron charge. The large value for the ideality factor results from the heterojunction comprising different band gap materials and the formation of an interfacial oxide layer. The obtained value is still adequate in comparison with the ideality factors of previously studied ZnO/Si heterojunctions (2.4, 3.18, and 3.91).<sup>[64–66]</sup>

**Optoelectronic characteristics of ZnO NW/H-Si n–p junction photodiode:** **Figure 2.6** shows the typical photoresponsive properties of the n–p ZnO NW/H-Si photodetectors on SiO<sub>2</sub>/Si substrates (the transfer curves of the field-effect transistors based on n-type ZnO NWs and p-type H-Si channel materials are presented in **Figure 2.7**). The  $I$ – $V$  curves in Figure 2.6a indicate that the photocurrent generated under reverse bias increased significantly and was dependent on the illuminating light. **Figure 2.8** shows the energy band diagram of the n-ZnO/p-Si heterojunction.<sup>[67, 68]</sup> Visible and NIR light mainly pass through the ZnO layer and are absorbed in the depleted p-Si region, which generates photo-induced electrons. On the other hand, UV light is absorbed in the ZnO region and generates photo-induced holes. Under reverse bias conditions, the generated photo-induced minority carriers can flow and are collected at the electrode in response to an external electric field, resulting in an increase of the current (generation of photocurrent). The photocurrent generated under 570 nm illumination is much larger than that generated under 365 and 620 nm illumination with same light intensity of 800  $\mu\text{W}\cdot\text{cm}^{-2}$ . This result coincides with the spectral photoresponsivity data presented in Figure 2.6b. The photodiodes exhibit a broad spectral range from the UV to NIR region, and the spectral photoresponsivity has a maximum at 540 nm. The wavelength of highest photoresponsivity was blue-shifted in comparison to that of the H-Si based photodetectors (the spectral photoresponsivity data for the metal-semiconductor-metal photodetector based on the H-Si membrane are presented in **Figure 2.9**), which can be attributed to the enhanced UV photoresponsivity conferred by the ZnO NWs.<sup>[69]</sup> The relatively low photoresponsivity at wavelengths over 700 nm is a consequence of the reduced thickness of the Si membrane because the penetration depth of the incident light is dependent on the wavelength, and wavelengths over 700 nm cannot be sufficiently absorbed by the thin Si membrane (2

$\mu\text{m}$  thickness). Si membranes show reduced absorption of red and NIR light when the thickness decreases.<sup>[70]</sup> Optimization of the thickness of the Si membrane enables achievement of a better photoresponse in the NIR region in comparison with this result.

Figure 2.6c and **Figure 2.10** indicate the fast response time ( $\sim 11$  ms rise time and  $\sim 12$  ms decay time) of the ZnO NW/H-Si photodiodes under illumination with both UV and visible light due to the p–n junction photodetection mechanism. It was also confirmed that the response time is similar for both ZnO NW/H-Si and ZnO NW/F-Si regardless of the structural difference between the Si photodiodes (Figure 2.10a–d). This result can be favorably compared to that obtained with conventional ZnO photodetectors, which show a slow response time ( $>100$  s) and a narrow UV response range mainly because of the surface oxygen adsorption/desorption mechanism in the photodetection processes.<sup>[71, 72]</sup> The repeatability of the photoresponse under illumination with 365 and 620 nm light indicates the stability of the photodiodes (Figure 2.10e). To investigate the generation and recombination behavior of the photo-induced current under incident light, the photocurrent was measured as a function of the optical power of the incident light (Figure 2.6d). The exponent  $\theta$  in the power law relation ( $I_{\text{ph}} \approx P^\theta$ ) provides information on the generation and recombination behavior of a photo-induced current.<sup>[73]</sup> A  $\theta$  value of unity indicates the ideal state, where the photo-induced current increases linearly with increasing incident power. The value of  $\theta$  falls below unity depending on the number of trap states in the photodetector.<sup>[74]</sup> The developed photodiode exhibits a near-ideal power relation with  $\theta = 0.99$  (Figure 2.6d), which indicates excellent junction properties with a low density of trap states between ZnO and Si. In accordance with the near-ideal power relation, the  $I$ – $V$  curve of ZnO NW/H-Si (**Figure 2.11**) showed no hysteresis behavior, which indicates a small amount of charge trap states at the junction.

The photoresponsivity of the ZnO NW/Si heterostructured photodiodes depends on the chamber environment during sputtering of the ZnO layer and depends on the growth time of the ZnO NWs. In particular, the number of oxygen vacancies in the sputtered ZnO layer affects the photoresponsivity. A ZnO layer sputtered under an  $\text{O}_2$  environment has better crystallinity with a smaller number of oxygen vacancies than a ZnO layer without an  $\text{O}_2$  environment. As shown in **Figure 2.12a**, the ZnO NW/Si photodetectors based on the ZnO layer sputtered under an  $\text{O}_2$  environment showed a higher photoresponsive on/off ratio than those based on the ZnO layer sputtered under a  $\text{N}_2$  environment. This result can be attributed to the reduced dark current (reverse saturation current) in p–n junction diodes, resulting from the improved quality of the ZnO film.<sup>[75]</sup> The generation and recombination of carriers decreases with prolonged minority carrier lifetime because the high-crystallinity ZnO layer forms a good interface with Si, thus the reverse current decreases.<sup>[76–78]</sup> The growth time of the ZnO NWs also affects the photoresponsivity of the ZnO NW/Si photodetectors. Figure 2.12b shows the increase of both the dark current and ON current as a function of the growth time. The increase of the growth time results in a decrease of the photoresponsive on/off ratio (Figure 2.12a), which can be



attributed to the increase of the dark current with the increasing crystallinity of the ZnO NWs. The high crystallinity of the ZnO NWs results in less carrier scattering during the transport process, thus reducing the possibility of recombination of drift carriers through the NWs to the electrode.<sup>[79]</sup> The increase of the crystallinity of the ZnO NWs with increasing growth time can be confirmed from the XRD data presented in Figure 2.12c, where the intensity of the (002) peaks increases with increasing growth time. Notably, the enhanced intensity of the (002) peaks is mainly attributed to the increased crystallinity of the ZnO NWs with increasing growth time, not to the amount of ZnO NWs. It was also observed that the increased growth time induced a slight increase of the photocurrent (Figure 2.12d). The slight increase of the photocurrent can be attributed to effective light scattering and absorption by the ZnO NW arrays, which enhances light absorption in the ZnO/Si junction area. However, the predominant increase of the dark current compared to the ON current results in a decrease of the photoresponse on/off ratio with increasing growth time (Figure 2.12e).

**Characterization of omnidirectional property of ZnO NWs/H-Si photodetector:** To evaluate the omnidirectional light-detection capability of the hierarchical ZnO NW/H-Si heterojunction photodiodes (**Figure 2.13a**), four different types of hetero-structured photodiodes (ZnO film/F-Si, ZnO film/H-Si, ZnO NWs/F-Si, and ZnO NWs/H-Si) were fabricated. All four types of photodiodes showed clear rectification behavior and high photocurrent in the reverse-biased region (**Figure 2.14**). The variation of the photocurrent (PC) (the photocurrent ratio at an incident angle to normal incidence,  $I_A/I_0$ ) depending on the angle of incident light at 620 nm shown in Figure 13b, indicates the excellent omnidirectional light-detection ability of the hierarchical ZnO NW/H-Si structure as compared to those of the other structures ( $I_0$  of ZnO film/F-Si, ZnO film/H-Si, ZnO NWs/F-Si, and ZnO NWs/H-Si was 120, 102, 115, and 96.8 nA, respectively). The photocurrent of the ZnO film/F-Si photodiode decreased sharply ( $I_A/I_0 = 0.1$  over  $60^\circ$ ) with increasing incident angle of light. In the case of the ZnO NW/F-Si diode, the photocurrent decreased below  $I_A/I_0 = 0.4$  at an incident angle of  $70^\circ$ , despite the omnidirectional light absorption ability of the NW structures due to the graded refractive index profile from air to the bottom layer of the ZnO NWs.<sup>[57, 80]</sup> For the ZnO film/H-Si structures, the device showed better omnidirectional light-detection ability than the ZnO Film/F-Si structures, which can be attributed to the role of H-Si to effectively absorb and guide the direction of the incident light even at high incident angles *via* scattering processes.<sup>[81, 82]</sup> Thus, the photocurrent of the hierarchical ZnO NW/H-Si structures was maintained above  $I_A/I_0 = 0.7$  at an incident angle of  $70^\circ$  as compared to the photocurrent at normal incident angle ( $I_0$ ). These results indicate that the hierarchical structures of the NWs on the honeycomb Si micropatterns can enhance the light absorption, as well as the omnidirectional property. The higher omnidirectionality of the hierarchical ZnO NW/H-Si structures as compared to the ZnO NW/F-Si structures can be attributed to the effective light absorption and guidance of the honeycomb structures. In addition, antireflective ZnO NW arrays with hierarchical structures enable excellent light absorption. Therefore, hierarchical ZnO NW/H-Si photodetectors

show the best omnidirectional light-detection ability in comparison to the other structures.

To investigate the effects of the size of the hexagonal holes on the omnidirectional light-detection ability of the honeycomb structures, hierarchical structures with four different hole sizes were prepared (**Figure 2.15**). The omnidirectional light-detection ability was enhanced with increasing size of the hexagonal holes (**Figure 2.16**). At low incident angles (below  $40^\circ$ ), the variation of the photocurrent as a function of the incident angle was similar for all hole sizes. However, at high incident angles (over  $40^\circ$ ), the larger hexagonal holes showed better omnidirectionality because greater light absorption and scattering was possible with the larger holes. As seen in **Figure 2.17**, at a low angle of incidence ( $30^\circ$ ), light absorption occurred throughout the honeycomb structure, regardless of the size of the hexagonal holes. However, at an intermediate angle of incidence ( $45^\circ$ ), light absorption did not occur at the bottom parts of the honeycomb structures for the smaller hexagonal holes ( $2.2 \mu\text{m}$ ). Furthermore, at a high incident angle ( $60^\circ$ ), light absorption occurred only at the wall of the honeycomb structure for the smaller hexagonal holes ( $2.2 \mu\text{m}$ ). For the larger hexagonal holes ( $8.7 \mu\text{m}$ ), light absorption occurred at both the wall and the bottom of the honeycomb structure, even at a high incident angle ( $60^\circ$ ), resulting in minimal photocurrent variation as compared to that at low incident angles. Therefore, hexagonal hole arrays with larger holes provide better omnidirectionality than structures with smaller hexagonal holes.

To further investigate the omnidirectional light-absorption ability of the hierarchical ZnO NW/H-Si structures, the angle-dependent light-absorption properties of four different structures were compared, i.e., F-Si, H-Si, ZnO NW/F-Si, and ZnO NW/H-Si, by using UV-vis-NIR spectroscopy with a variable angle specular reflectance accessory (VASRA) (**Figure 2.13c-f**). Here, the spectroscopic data show the reflectance of light with incident angles from  $20^\circ$  to  $70^\circ$ . For the F-Si substrates, although the reflectance of UV light was above  $\sim 50\%$ , the reflectance in the visible/NIR range was lower than that of the UV region due to the absorption of visible/NIR light by Si (**Figure 2.13c**). H-Si showed much lower reflectance in the UV to visible/ NIR region than F-Si (**Figure 2.13d**), which is attributed to the increased light scattering and absorption of the hexagonal hole arrays. For the ZnO NWs grown on F-Si, the reflectance of UV light declined remarkably below 5% due to absorption of UV light by the ZnO, as well as the large decrease in the reflectance in the visible/NIR region due to antireflection effect by the nanowire structures (**Figure 2.13e**). For the ZnO NWs grown on H-Si, the hierarchical ZnO NW/H-Si structures exhibited excellent omnidirectional light-absorption ability with greatly diminished reflectance over the entire spectral range from UV to NIR (**Figure 2.13f**), which can be attributed to the combined effects of the ZnO NWs and the honeycomb Si structure. The reflectance data obtained with VASRA are in good agreement with the angle-dependent photocurrent variation.

To further elucidate the morphology-dependent omnidirectional light absorption behavior, the  $|E|^2$  distribution for various morphologies was calculated by the FDTD method. **Figure 2.18** shows the

cross-sectional  $|E|^2$  distribution at 620 nm with an angle of incidence of  $30^\circ$  for different morphologies. As compared to F-Si, the H-Si structure provided scattering-induced multiple light absorption, resulting in enhancement of the E-fields on the surface of Si (Figure 2.18a and 2.18b). As shown in Figure 2.18c, strong E-field resonances occurred between the ZnO NWs on F-Si, which improved the light absorption. In accordance with the results, the additional ZnO NWs on H-Si dramatically enhanced the E-fields on the surface of ZnO NW/H-Si (Figure 2.18d). Figure 2.18e–h show a comparison of the E-field intensity distributions at 620 nm excitation with normal incidence and  $30^\circ$  incidence. For the ZnO NW/F-Si structure, the resonance of the E-field between the ZnO NWs was stronger with normal incidence than with  $30^\circ$  incidence. However, the E-field inside the honeycomb structures with normal incidence was smaller than that with  $30^\circ$  incidence due to the weaker light scattering effect. This result indicates that the light scattering effect in the honeycomb structures is beneficial for E-field enhancement.

***Mechanical flexibility and durability of ZnO NW/H-Si photodetector on PI substrate:*** Figure 2.19a shows photographic and OM images of a free-standing H-Si membrane rolled on the tip of a pipette, which confirms the excellent flexibility of the H-Si membrane. To fabricate flexible photodetectors, we utilized liquid-bridge-mediated transfer printing to attach the separated H-Si membrane onto the flexible PI substrate.<sup>[83]</sup> In the transfer printing process, the attractive capillary force generated between the H-Si membrane and the PI substrate by solvent evaporation induces conformal contact and tight binding between the two substrates. Figure 2.19b shows a photograph and schematic illustration of the flexible ZnO NW/H-Si photodetector arrays on the PI substrate. The flexible photodetector showed high rectification behavior ( $\sim 74$  at an applied voltage of 3 V) and photocurrent in the reverse-biased region under illumination with 365 nm light (Figure 2.20). Notably, the honeycomb structures enabled uniform distribution of the external mechanical strain to the triangular region, thus providing excellent mechanical stability.<sup>[84]</sup> The flexibility of the developed hierarchical-structured, flexible photodiode was proven by mechanical bending tests as a function of the bending curvature, as shown in Figure 2.21. The ZnO NW/H-Si flexible photodiodes showed stable photoresponsive properties without a significant change of the  $I$ - $V$  curve at a high bending curvature ( $r_B = 0.415$  cm) (Figure 2.19c). With increasing bending curvature, the photocurrent was maintained at up to 90% of the initial photocurrent at a bending radius of 3 mm (Figure 2.19d). This behavior is attributed to the advantageous honeycomb structure that provides better mechanical flexibility.<sup>[84, 85]</sup> The ZnO NW/H-Si flexible photodiodes also showed extremely high mechanical durability. As seen in Figure 2.19e, the photodetector provided stable dark/ON currents and minimal photocurrent variations for 10,000 bending cycles. SEM analysis of the photodetector after 10,000 bending cycles did not show any mechanical failures such as cracks or delamination of the ZnO NWs from the ZnO NW/H-Si photodetectors (Figure 2.22).

## 2.4 Conclusions

In summary, a highly efficient flexible photodetector with omnidirectional and broadband light-detection capability was developed by using an ultraflexible and hierarchical ZnO nanowire/Si honeycomb photodiode membrane. The developed ZnO NW/H-Si-based photodiodes have a fast response time of ~11 ms and a broad photoresponse range spanning the UV to NIR. Notably, the developed hierarchical ZnO NWs on the H-Si membrane can detect omnidirectional light (maintain high photocurrents up to incident angles of 70°), which was previously achievable only with complicated nonplanar photodetectors with microlens arrays in previous reports. Furthermore, the device fabricated with the honeycomb-structured Si membrane resulted in flexible photodetectors with high mechanical flexibility and durability with minimal photocurrent variation. We anticipate that the developed omnidirectional and flexible photodetectors based on hierarchically structured honeycomb micromembranes will find numerous applications for high-performance flexible optoelectronic systems such as wearable electronics, artificial retina, bio-medical imaging, and future energy harvesting.

## 2.5 References

- [1] Nau, S.; Wolf, C.; Sax, S.; List-Kratochvil, E. J. W. Organic Non-Volatile Resistive Photo-Switches for Flexible Image Detector Arrays. *Adv. Mater.* **2015**, *27*, 1048–1052.
- [2] Zhang, L.; Wu, T.; Guo, Y.; Zhao, Y.; Sun, X.; Wen, Y.; Yu, G.; Liu, Y. Large-Area, Flexible Imaging Arrays Constructed by Light-Charge Organic Memories. *Sci. Rep.* **2013**, *3*, 1080.
- [3] Someya, T.; Kato, Y.; Iba, S.; Noguchi, Y.; Sekitani, T.; Kawaguchi, H.; Sakurai, T. Integration of Organic FETs with Organic Photodiodes for a Large Area, Flexible, and Lightweight Sheet Image Scanners. *IEEE Trans. Electron Devices* **2005**, *52*, 2502–2511.
- [4] Floreano, D.; Pericet-Camara, R.; Viollet, S.; Ruffier, F.; Bruckner, A.; Leitel, R.; Buss, W.; Menouni, M.; Expert, F.; Juston, R. *et al.* Miniature Curved Artificial Compound Eyes. *Proc. Natl. Acad. Sci. USA* **2013**, *110*, 9267–9272.
- [5] Ko, H. C.; Stoykovich, M. P.; Song, J. Z.; Malyarchuk, V.; Choi, W. M.; Yu, C. J.; Geddes, J. B.; Xiao, J. L.; Wang, S. D.; Huang, Y. G. *et al.* A Hemispherical Electronic Eye Camera Based on Compressible Silicon Optoelectronics. *Nature* **2008**, *454*, 748–753.
- [6] Lee, L. P.; Szema, R. Inspirations from Biological Optics for Advanced Photonic Systems. *Science* **2005**, *310*, 1148–1150.
- [7] Lochner, C. M.; Khan, Y.; Pierre, A.; Arias, A. C. All-Organic Optoelectronic Sensor for Pulse Oximetry. *Nat. Commun.* **2014**, *5*, 5745.
- [8] Lee, C. M.; Engelbrecht, C. J.; Soper, T. D.; Helmchen, F.; Seibel, E. J. Scanning Fiber Endoscopy With Highly Flexible, 1 mm Catheterscopes for Wide-Field, Full-Color Imaging. *J. Biophotonics* **2010**, *3*, 385–407.

- [9] Huang, S. Y.; Guo, C. F.; Zhang, X.; Pan, W.; Luo, X.; Zhao, C. S.; Gong, J. H.; Li, X. Y.; Ren, Z. F.; Wu, H. Buckled Tin Oxide Nanobelt Webs as Highly Stretchable and Transparent Photosensors. *Small* **2015**, *11*, 5712–5718.
- [10] Gao, Y.; Sim, K.; Sun, S. C.; Chen, Z.; Song, J. Z.; Yu, C. J. Crack-Insensitive Wearable Electronics Enabled through High-Strength Kevlar Fabrics. *IEEE Trans. Compon., Packag., Manuf. Technol.* **2015**, *5*, 1230–1236.
- [11] Wang, Z. R.; Wang, H.; Liu, B.; Qiu, W. Z.; Zhang, J.; Ran, S. H.; Huang, H. T.; Xu, J.; Han, H. W.; Chen, D. *et al.* Transferable and Flexible Nanorod-Assembled TiO<sub>2</sub> Cloths for Dye-Sensitized Solar Cells, Photodetectors, and Photocatalysts. *ACS Nano* **2011**, *5*, 8412–8419.
- [12] Rim, Y. S.; Yang, Y. M.; Bae, S. H.; Chen, H. J.; Li, C.; Goorsky, M. S.; Yang, Y. Ultrahigh and Broad Spectral Photodetectivity of an Organic–Inorganic Hybrid Phototransistor for Flexible Electronics. *Adv. Mater.* **2015**, *27*, 6885–6891.
- [13] Pace, G.; Grimoldi, A.; Natali, D.; Sampietro, M.; Coughlin, J. E.; Bazan, G. C.; Caironi, M. All-Organic and Fully-Printed Semitransparent Photodetectors Based on Narrow Bandgap Conjugated Molecules. *Adv. Mater.* **2014**, *26*, 6773–6777.
- [14] Jang, S.; Hwang, E.; Lee, Y.; Lee, S.; Cho, J. H. Multifunctional Graphene Optoelectronic Devices Capable of Detecting and Storing Photonic Signals. *Nano Lett.* **2015**, *15*, 2542–2547.
- [15] Sun, Z. H.; Liu, Z. K.; Li, J. H.; Tai, G. A.; Lau, S. P.; Yan, F. Infrared Photodetectors Based on CVD-Grown Graphene and PbS Quantum Dots with Ultrahigh Responsivity. *Adv. Mater.* **2012**, *24*, 5878–5883.
- [16] Lee, J. S.; Kovalenko, M. V.; Huang, J.; Chung, D. S.; Talapin, D. V. Band-Like Transport, High Electron Mobility and High Photoconductivity in All-Inorganic Nanocrystal Arrays. *Nat. Nanotechnol.* **2011**, *6*, 348–352.
- [17] Xie, X. M.; Shen, G. Z. Single-Crystalline In<sub>2</sub>S<sub>3</sub> Nanowire-Based Flexible Visible-Light Photodetectors with an Ultra-High Photoresponse. *Nanoscale* **2015**, *7*, 5046–5052.
- [18] Tian, W.; Zhang, C.; Zhai, T. Y.; Li, S. L.; Wang, X.; Liu, J. W.; Jie, X.; Liu, D. Q.; Liao, M. Y.; Koide, Y. *et al.* Flexible Ultraviolet Photodetectors with Broad Photoresponse Based on Branched ZnS-ZnO Heterostructure Nanofilms. *Adv. Mater.* **2014**, *26*, 3088–3093.
- [19] Liu, X.; Gu, L. L.; Zhang, Q. P.; Wu, J. Y.; Long, Y. Z.; Fan, Z. Y. All-Printable Band-Edge Modulated ZnO Nanowire Photodetectors With Ultra-High Detectivity. *Nat. Commun.* **2014**, *5*, 4007.
- [20] Zheng, W. S.; Xie, T.; Zhou, Y.; Chen, Y. L.; Jiang, W.; Zhao, S. L.; Wu, J. X.; Jing, Y. M.; Wu, Y.; Chen, G. C. *et al.* Patterning Two-Dimensional Chalcogenide Crystals of Bi<sub>2</sub>Se<sub>3</sub> and In<sub>2</sub>Se<sub>3</sub> and Efficient Photodetectors. *Nat. Commun.* **2015**, *6*, 6972.
- [21] Yuan, X.; Tang, L.; Liu, S. S.; Wang, P.; Chen, Z. G.; Zhang, C.; Liu, Y. W.; Wang, W. Y.; Zou, Y. C.; Liu, C. *et al.* Arrayed van der Waals Vertical Heterostructures Based on 2D GaSe Grown by Molecular Beam Epitaxy. *Nano Lett.* **2015**, *15*, 3571–3577.

- [22] Liu, N.; Tian, H.; Schwartz, G.; Tok, J. B. H.; Ren, T. L.; Bao, Z. Large-Area, Transparent, and Flexible Infrared Photodetector Fabricated Using P–N Junctions Formed by N-Doping Chemical Vapor Deposition Grown Graphene. *Nano Lett.* **2014**, *14*, 3702–3708.
- [23] Tamalampudi, S. R.; Lu, Y. Y.; Kumar, U. R.; Sankar, R.; Liao, C. D.; Moorthy, B. K.; Cheng, C. H.; Chou, F. C.; Chen, Y. T. High Performance and Bendable Few-Layered InSe Photodetectors with Broad Spectral Response. *Nano Lett.* **2014**, *14*, 2800–2806.
- [24] Seo, J.-H.; Oh, T.-Y.; Park, J.; Zhou, W. D.; Ju, B.-K.; Ma, Z. Q. A Multifunction Heterojunction Formed between Pentacene and a Single-Crystal Silicon Nanomembrane. *Adv. Funct. Mater.* **2013**, *23*, 3398–3403.
- [25] Yuan, H.-C.; Shin, J.; Qin, G. X.; Sun, L.; Bhattacharya, P.; Lagally, M. G.; Celler, G. K.; Ma, Z. Q. Flexible Photodetectors on Plastic Substrates by Use of Printing Transferred Single-Crystal Germanium Membranes. *Appl. Phys. Lett.* **2009**, *94*, 013102.
- [26] Liu, Y. L.; Yu, C. C.; Lin, K. T.; Yang, T. C.; Wang, E. Y.; Chen, H. L.; Chen, L. C.; Chen, K. H. Transparent, Broadband, Flexible, and Bifacial-Operable Photodetectors Containing a Large-Area Graphene-Gold Oxide Heterojunction. *ACS Nano* **2015**, *9*, 5093–5103.
- [27] Hu, X.; Zhang, X. D.; Liang, L.; Bao, J.; Li, S.; Yang, W. L.; Xie, Y. High-Performance Flexible Broadband Photodetector Based on Organolead Halide Perovskite. *Adv. Funct. Mater.* **2014**, *24*, 7373–7380.
- [28] Wang, X. F.; Song, W. F.; Liu, B.; Chen, G.; Chen, D.; Zhou, C. W.; Shen, G. Z. High-Performance Organic–Inorganic Hybrid Photodetectors Based on P3HT:CdSe Nanowire Heterojunctions on Rigid and Flexible Substrates. *Adv. Funct. Mater.* **2013**, *23*, 1202–1209.
- [29] Manga, K. K.; Wang, J. Z.; Lin, M.; Zhang, J.; Nesladek, M.; Nalla, V.; Ji, W.; Loh, K. P. High-Performance Broadband Photodetector Using Solution-Processible PbSe-TiO<sub>2</sub>-Graphene Hybrids. *Adv. Mater.* **2012**, *24*, 1697–1702.
- [30] Hu, K.; Chen, H. Y.; Jiang, M. M.; Teng, F.; Zheng, L. X.; Fang, X. S. Broadband Photoresponse Enhancement of a High-Performance *t*-Se Microtube Photodetector by Plasmonic Metallic Nanoparticles. *Adv. Funct. Mater.* **2016**, *26*, 6641–6648.
- [31] Chen, H. Y.; Liu, H.; Zhang, Z. M.; Hu, K.; Fang, X. S. Nanostructured Photodetectors: From Ultraviolet to Terahertz. *Adv. Mater.* **2016**, *28*, 403–433.
- [32] Wang, A.; Gill, P.; Molnar, A. Light Field Image Sensors Based on the Talbot Effect. *Appl. Opt.* **2009**, *48*, 5897–5905.
- [33] Martin, N.; Ruiz, J. M. Calculation of the PV Modules Angular Losses under Field Conditions by Means of an Analytical Model. *Sol. Energy Mater. Sol. Cells* **2001**, *70*, 25–38.
- [34] Courtial, J.; Oxburgh, S.; Tyc, T. Direct Stigmatic Imaging with Curved Surfaces. *J. Opt. Soc. Am. A* **2015**, *32*, 478–481.
- [35] Ko, D.-H.; Tumbleston, J. R.; Henderson, K. J.; Euliss, L. E.; DeSimone, J. M.; Lopez, R.;

- Samulski, E. T. Biomimetic Microlens Array with Antireflective “Moth-Eye” Surface. *Soft Matter* **2011**, *7*, 6404–6407.
- [36] Jeong, K. H.; Kim, J.; Lee, L. P. Biologically Inspired Artificial Compound Eyes. *Science* **2006**, *312*, 557–561.
- [37] Song, Y. M.; Xie, Y. Z.; Malyarchuk, V.; Xiao, J. L.; Jung, I.; Choi, K. J.; Liu, Z. J.; Park, H.; Lu, C. F.; Kim, R. H. *et al.* Digital Cameras with Designs Inspired by the Arthropod Eye. *Nature* **2013**, *497*, 95–99.
- [38] Fang, C.-Y.; Liu, Y.-L.; Lee, Y.-C.; Chen, H.-L.; Wan, D.-H.; Yu, C.-C. Nanoparticle Stacks with Graded Refractive Indices Enhance the Omnidirectional Light Harvesting of Solar Cells and the Light Extraction of Light-Emitting Diodes. *Adv. Funct. Mater.* **2013**, *23*, 1412–1421.
- [39] Yan, X.; Poxson, D. J.; Cho, J.; Welser, R. E.; Sood, A. K.; Kim, J. K.; Schubert, E. F. Enhanced Omnidirectional Photovoltaic Performance of Solar Cells Using Multiple-Discrete-Layer Tailored- and Low-Refractive Index Anti-Reflection Coatings. *Adv. Funct. Mater.* **2013**, *23*, 583–590.
- [40] Ou, Y. Y.; Zhu, X. L.; Jokubavicius, V.; Yakimova, R.; Mortensen, N. A.; Syväjärvi, M.; Xiao, S. S.; Ou, H. Y. Broadband Antireflection and Light Extraction Enhancement in Fluorescent SiC with Nanodome Structures. *Sci. Rep.* **2014**, *4*, 4662.
- [41] Lin, Q. F.; Leung, S. F.; Lu, L. F.; Chen, X. Y.; Chen, Z.; Tang, H. N.; Su, W. J.; Li, D. D.; Fan, Z. Y. Inverted Nanocone-Based Thin Film Photovoltaics with Omnidirectionally Enhanced Performance. *ACS Nano* **2014**, *8*, 6484–6490.
- [42] Lin, H.; Xiu, F.; Fang, M.; Yip, S.; Cheung, H. Y.; Wang, F. Y.; Han, N.; Chan, K. S.; Wong, C. Y.; Ho, J. C. Rational Design of Inverted Nanopencil Arrays for Cost-Effective, Broadband, and Omnidirectional Light Harvesting. *ACS Nano* **2014**, *8*, 3752–3760.
- [43] Wu, W. Q.; Feng, H. L.; Rao, H. S.; Xu, Y. F.; Kuang, D. B.; Su, C. Y. Maximizing Omnidirectional Light Harvesting in Metal Oxide Hyperbranched Array Architectures. *Nat. Commun.* **2014**, *5*, 3968.
- [44] Wang, H. P.; Lin, T. Y.; Hsu, C. W.; Tsai, M. L.; Huang, C. H.; Wei, W. R.; Huang, M. Y.; Chien, Y. J.; Yang, P. C.; Liu, C. W. *et al.* Realizing High-Efficiency Omnidirectional N-Type Si Solar Cells via the Hierarchical Architecture Concept with Radial Junctions. *ACS Nano* **2013**, *7*, 9325–9335.
- [45] Wang, H. P.; Lin, T. Y.; Tsai, M. L.; Tu, W. C.; Huang, M. Y.; Liu, C. W.; Chueh, Y. L.; He, J. H. Toward Efficient and Omnidirectional N-Type Si Solar Cells: Concurrent Improvement in Optical and Electrical Characteristics by Employing Microscale Hierarchical Structures. *ACS Nano* **2014**, *8*, 2959–2969.
- [46] Wei, W. R.; Tsai, M. L.; Ho, S. T.; Tai, S. H.; Ho, C. R.; Tsai, S. H.; Liu, C. W.; Chung, R. J.; He, J. H. Above 11%-Efficiency Organic–Inorganic Hybrid Solar Cells with Omnidirectional Harvesting Characteristics by Employing Hierarchical Photon-Trapping Structures. *Nano Lett.* **2013**, *13*, 3658–3663.

- [47] Lin, C. A.; Lai, K. Y.; Lien, W. C.; He, J. H. An Efficient Broadband and Omnidirectional Light-Harvesting Scheme Employing a Hierarchical Structure Based on a ZnO Nanorod/Si<sub>3</sub>N<sub>4</sub>-Coated Si Microgroove on 5-Inch Single Crystalline Si Solar Cells. *Nanoscale* **2012**, *4*, 6520–6526.
- [48] Manekkathodi, A.; Lu, M. Y.; Wang, C. W.; Chen, L. J. Direct Growth of Aligned Zinc Oxide Nanorods on Paper Substrates for Low-Cost Flexible Electronics. *Adv. Mater.* **2010**, *22*, 4059–4063.
- [49] Hu, P. A.; Wang, L. F.; Yoon, M.; Zhang, J.; Feng, W.; Wang, X. N.; Wen, Z. Z.; Idrobo, J. C.; Miyamoto, Y.; Geohegan, D. B. *et al.* Highly Responsive Ultrathin GaS Nanosheet Photodetectors on Rigid and Flexible Substrates. *Nano Lett.* **2013**, *13*, 1649–1654.
- [50] An, X. H.; Liu, F. Z.; Jung, Y. J.; Kar, S. Tunable Graphene-Silicon Heterojunctions for Ultrasensitive Photodetection. *Nano Lett.* **2013**, *13*, 909–916.
- [51] Qiao, H.; Yuan, J.; Xu, Z. Q.; Chen, C. Y.; Lin, S. H.; Wang, Y. S.; Song, J. C.; Liu, Y.; Khan, Q.; Hoh, H. Y. *et al.* Broadband Photodetectors Based on Graphene-Bi<sub>2</sub>Te<sub>3</sub> Heterostructure. *ACS Nano* **2015**, *9*, 1886–1894.
- [52] Buscema, M.; Groenendijk, D. J.; Blanter, S. I.; Steele, G. A.; van der Zant, H. S.; Castellanos-Gomez, A. Fast and Broadband Photoresponse of Few-Layer Black Phosphorus Field-Effect Transistors. *Nano Lett.* **2014**, *14*, 3347–3352.
- [53] Zhang, Y. Z.; Liu, T.; Meng, B.; Li, X. H.; Liang, G. Z.; Hu, X. N.; Wang, Q. J. Broadband High Photoresponse from Pure Monolayer Graphene Photodetector. *Nat. Commun.* **2013**, *4*, 1811.
- [54] Tang, L. B.; Ji, R. B.; Li, X. M.; Bai, G. X.; Liu, C. P.; Hao, J. H.; Lin, J. Y.; Jiang, H. X.; Teng, K. S.; Yang, Z. B. *et al.* Deep Ultraviolet to Near-Infrared Emission and Photoresponse in Layered N-Doped Graphene Quantum Dots. *ACS Nano* **2014**, *8*, 6312–6320.
- [55] Saran, R.; Nordin, M. N.; Curry, R. J. Facile Fabrication of PbS Nanocrystal:C60 Fullerite Broadband Photodetectors with High Detectivity. *Adv. Funct. Mater.* **2013**, *23*, 4149–4155.
- [56] Tsai, D. S.; Liu, K. K.; Lien, D. H.; Tsai, M. L.; Kang, C. F.; Lin, C. A.; Li, L. J.; He, J. H. Few-Layer MoS<sub>2</sub> with High Broadband Photogain and Fast Optical Switching for Use in Harsh Environments. *ACS Nano* **2013**, *7*, 3905–3911.
- [57] Tsai, D. S.; Lin, C. A.; Lien, W. C.; Chang, H. C.; Wang, Y. L.; He, J. H. Ultra-High-Responsivity Broadband Detection of Si Metal-Semiconductor-Metal Schottky Photodetectors Improved by ZnO Nanorod Arrays. *ACS Nano* **2011**, *5*, 7748–7753.
- [58] Greene, L. E.; Law, M.; Goldberger, J.; Kim, F.; Johnson, J. C.; Zhang, Y. F.; Saykally, R. J.; Yang, P. D. Low-Temperature Wafer-Scale Production of ZnO Nanowire Arrays. *Angew. Chem. Int. Ed.* **2003**, *42*, 3031–3034.
- [59] Ko, H.; Zhang, Z. X.; Takei, K.; Javey, A. Hierarchical Polymer Micropillar Arrays Decorated With ZnO Nanowires. *Nanotechnology* **2010**, *21*, 295305.
- [60] Ha, M.; Lim, S.; Park, J.; Um, D.-S.; Lee, Y.; Ko, H. Bioinspired Interlocked and Hierarchical Design of ZnO Nanowire Arrays for Static and Dynamic Pressure-Sensitive Electronic Skins. *Adv.*



*Funct. Mater.* **2015**, *25*, 2841–2849.

- [61] Kim, H.-K.; Kim, K.-K.; Park, S.-J.; Seong, T.-Y.; Adesida, I. Formation of Low Resistance Nonalloyed Al/Pt Ohmic Contacts on N-Type ZnO Epitaxial Layer. *J. Appl. Phys.* **2003**, *94*, 4225–4227.
- [62] Huang, C.-Y.; Yang, Y.-J.; Chen, J.-Y.; Wang, C.-H.; Chen, Y.-F.; Hong, L.-S.; Liu, C.-S.; Wu, C.-Y. P-Si Nanowires/SiO<sub>2</sub>/N-ZnO Heterojunction Photodiodes. *Appl. Phys. Lett.* **2010**, *97*, 013503.
- [63] Ghosh, R.; Basak, D. Electrical and Ultraviolet Photoresponse Properties of Quasialigned ZnO Nanowires/P-Si Heterojunction. *Appl. Phys. Lett.* **2007**, *90*, 243106.
- [64] Hwang, J. D.; Chen, Y. H. Carrier Transport Mechanism on ZnO Nanorods/P-Si Heterojunction Diodes with Various Atmospheres Annealing Hydrothermal Seed-Layer. *Thin Solid Films* **2012**, *520*, 5409–5412.
- [65] Yakuphanoglu, F.; Caglar, Y.; Caglar, M.; Ilican, S. ZnO/P-Si Heterojunction Photodiode by Sol–Gel Deposition of Nanostructure N-ZnO Film on P-Si Substrate. *Mat. Sci. Semicon. Proc.* **2010**, *13*, 137–140.
- [66] Klason, P.; Rahman, M. M.; Hu, Q. H.; Nur, O.; Turan, R.; Willander, M. Fabrication and Characterization of P-Si/N-ZnO Heterostructured Junctions. *Microelect. J.* **2009**, *40*, 706–710.
- [67] Mridha, S.; Basak, D. Ultraviolet and Visible Photoresponse Properties of N-ZnO/P-Si Heterojunction. *J. Appl. Phys.* **2007**, *101*, 083102.
- [68] Bai, Z. M.; Yan, X. Q.; Chen, X.; Cui, Y.; Lin, P.; Shen, Y. W.; Zhang, Y. Ultraviolet and Visible Photoresponse Properties of a ZnO/Si Heterojunction at Zero Bias. *RSC Adv.* **2013**, *3*, 17682–17688.
- [69] Liao, Q. L.; Liang, M. Y.; Zhang, Z.; Zhang, G. J.; Zhang, Y. Strain-Modulation and Service Behavior of Au–MgO–ZnO Ultraviolet Photodetector by Piezo-Phototronic Effect. *Nano Res.* **2015**, *8*, 3772–3779.
- [70] Sharma, M.; Pudasaini, P. R.; Ruiz-Zepeda, F.; Elam, D.; Ayon, A. A. Ultrathin, Flexible Organic-Inorganic Hybrid Solar Cells Based on Silicon Nanowires and PEDOT:PSS. *ACS Appl. Mater. Interfaces* **2014**, *6*, 4356–4363.
- [71] Soci, C.; Zhang, A.; Xiang, B.; Dayeh, S. A.; Aplin, D. P. R.; Park, J.; Bao, X. Y.; Lo, Y. H.; Wang, D. ZnO Nanowire UV Photodetectors with High Internal Gain. *Nano Lett.* **2007**, *7*, 1003–1009.
- [72] Dhara, S.; Giri, P. K. ZnO Nanowire Heterostructures: Intriguing Photophysics and Emerging Applications. *Rev. Nanosci. Nanotechnol.* **2013**, *2*, 147–170.
- [73] Kind, H.; Yan, H. Q.; Messer, B.; Law, M.; Yang, P. D. Nanowire Ultraviolet Photodetectors and Optical Switches. *Adv. Mater.* **2002**, *14*, 158–160.
- [74] Zeng, L. H.; Wang, M. Z.; Hu, H.; Nie, B.; Yu, Y. Q.; Wu, C. Y.; Wang, L.; Hu, J. G.; Xie, C.; Liang, F. X. *et al.* Monolayer Graphene/Germanium Schottky Junction as High-Performance Self-Driven Infrared Light Photodetector. *ACS Appl. Mater. Interfaces* **2013**, *5*, 9362–9366.
- [75] Qi, H. X.; Li, Q. S.; Zhao, B.; Zheng, M. M.; Li, X. S.; Zhang, N. Influence of ZnO Homobuffer

Layer on N-ZnO/P-Si Photodiode. *Mater. Sci. Technol.* **2008**, *24*, 1002–1004.

[76] Schubert, E. F. *Light-Emitting Diodes*, 2nd ed.; Cambridge University Press: Cambridge, UK, 2006.

[77] Liu, Y.; Gorla, C. R.; Liang, S.; Emanetoglu, N.; Lu, Y.; Shen, H.; Wraback, M. Ultraviolet Detectors Based on Epitaxial ZnO Films Grown by MOCVD. *J. Electron. Mater.* **2000**, *29*, 69–74.

[78] Sieg, R. M.; Carlin, J. A.; Boeckl, J. J.; Ringel, S. A.; Currie, M. T.; Ting, S. M.; Langdo, T. A.; Taraschi, G.; Fitzgerald, E. A.; Keyes, B. M. High Minority-Carrier Lifetimes In GaAs Grown on Low-Defect-Density Ge/GeSi/Si Substrates. *Appl. Phys. Lett.* **1998**, *73*, 3111–3113.

[79] Ridhuan, N. S.; Razak, K. A.; Lockman, Z.; Abdul Aziz, A. Structural and Morphology of ZnO Nanorods Synthesized Using ZnO Seeded Growth Hydrothermal Method and Its Properties as UV Sensing. *PLoS One* **2012**, *7*, e50405.

[80] Chao, Y. C.; Chen, C. Y.; Lin, C. A.; Dai, Y. A.; He, J. H. Antireflection Effect of ZnO Nanorod Arrays. *J. Mater. Chem.* **2010**, *20*, 8134–8138.

[81] Zhao, J. H.; Wang, A. H.; Green, M. A.; Ferrazza, F. 19.8% Efficient “Honeycomb” Textured Multicrystalline and 24.4% Monocrystalline Silicon Solar Cells. *Appl. Phys. Lett.* **1998**, *73*, 1991–1993.

[82] Sai, H.; Saito, K.; Kondo, M. Investigation of Textured Back Reflectors with Periodic Honeycomb Patterns in Thin-Film Silicon Solar Cells for Improved Photovoltaic Performance. *IEEE J. Photovolt.* **2013**, *3*, 5–10.

[83] Hwang, J. K.; Cho, S.; Dang, J. M.; Kwak, E. B.; Song, K.; Moon, J.; Sung, M. M. Direct Nanoprinting by Liquid-Bridge-Mediated Nanotransfer Moulding. *Nat. Nanotechnol.* **2010**, *5*, 742–748.

[84] Davami, K.; Zhao, L.; Lu, E.; Cortes, J.; Lin, C.; Lilley, D. E.; Purohit, P. K.; Bargatin, I. Ultralight Shape-Recovering Plate Mechanical Metamaterials. *Nat. Commun.* **2015**, *6*, 10019.

[85] Takahashi, T.; Takei, K.; Gillies, A. G.; Fearing, R. S.; Javey, A. Carbon Nanotube Active-Matrix Backplanes for Conformal Electronics and Sensors. *Nano Lett.* **2011**, *11*, 5408–5413.

\*\*Reprinted in part with permission from S. Lim, H. Ko<sup>\*</sup> *et al.*, *Nano Res.* **2017**, *10*, 22–36. Copyright © 2017, Tsinghua University Press and Springer-Verlag Berlin Heidelberg

**Table 2.1** Comparison of results achieved this work and previously reported omnidirectional, flexible, and broadband optoelectronics.

Type of device	Active layer materials	Omnidirectional property	Flexibility	Detection range (nm)
Solar cell <sup>[45]</sup>	Si	60% decreased $P_{\max}^a$ at 60° of AOI <sup>b</sup>	–	300–1100
Solar cell <sup>[46]</sup>	PEDOT, Si	90% decreased $P_{\max}$ at 60° of AOI	–	400–1100
Solar cell <sup>[44]</sup>	Si	60% decreased $P_{\max}$ at 60° of AOI	–	300–1100
Solar cell <sup>[47]</sup>	ZnO nanorod, Si	5.3% decreased $J_{sc}^c$ at 60° of AOI	–	400–1000
PN junction photodiode <sup>[22]</sup>	Graphene	–	80% $R_{ph}^d$ at $D_B^e = 80^\circ$	>780
PN junction photodiode <sup>[48]</sup>	ZnO nanorod, PEDOT:PSS	–	Up to $D_B = 75^\circ$	Ultraviolet
Phototransistor <sup>[23]</sup>	Few-layer InSe	–	50% $R_{ph}$ at $r_B^f = 3$ cm	450–785
Phototransistor <sup>[49]</sup>	GaS nanosheet	–	Up to $D_B = 60^\circ$	250–600
MSM <sup>g</sup> photodetector <sup>[27]</sup>	CH <sub>3</sub> NH <sub>3</sub> PbI <sub>3</sub>	–	No data	310–780
MSM photodetector <sup>[28]</sup>	P3HT:CdSe nanowire	–	No data	350–850
MSM photodetector <sup>[30]</sup>	PbSe, TiO <sub>2</sub> , Graphene	–	Up to $r_B = 6$ mm	300–2000
Schottky diode <sup>[50]</sup>	Si, Graphene	–	–	200–1100
Phototransistor <sup>[51]</sup>	Graphene, Bi <sub>2</sub> Te <sub>3</sub>	–	–	400–1550
Phototransistor <sup>[52]</sup>	Few-layer black phosphorus	–	–	Visible to 940
Phototransistor <sup>[53]</sup>	Graphene	–	–	Visible to mid-IR
MSM photodetector <sup>[54]</sup>	Graphene quantum dots	–	–	Ultraviolet to near-IR
MSM photodetector <sup>[55]</sup>	PbS, C <sub>60</sub> fullerite	–	–	400–1350
MSM photodetector <sup>[56]</sup>	Few-layer MoS <sub>2</sub>	–	–	380–800
MSM photodetector <sup>[57]</sup>	ZnO nanowire, Si	–	–	350–800
<b>PN junction photodiode [This work]</b>	<b>ZnO nanowire, Si</b>	<b>30% decreased <math>I_{PC}^h</math> at 70° of AOI</b>	<b>90% <math>I_{PC}</math> at <math>r_B = 1</math> cm</b>	<b>365–1100</b>

<sup>a</sup>AOI: angle of incidence, <sup>b</sup>MSM: metal-semiconductor-metal, <sup>c</sup> $P_{\max}$ : maximum power, <sup>d</sup> $J_{sc}$ : short-circuit current density, <sup>e</sup> $I_{PC}$ : photocurrent, <sup>f</sup> $R_{ph}$ : photoresponsivity, <sup>g</sup> $D_B$ : degree of bending curvature, <sup>h</sup> $r_B$ : bending radius.

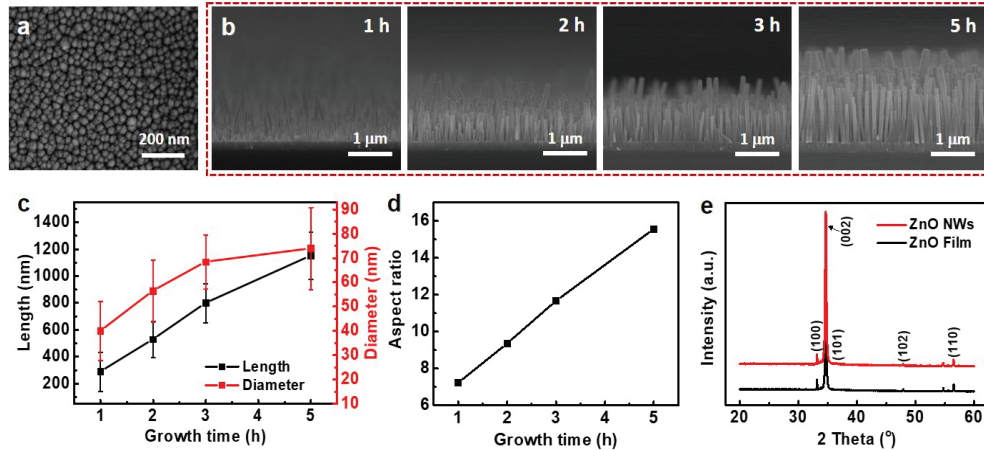


**Figure 2.1** (a) Top-view SEM image of sputtered ZnO film (thickness  $\approx 200$  nm). (b) Cross-sectional SEM images of vertically grown ZnO NW arrays on ZnO layer as a function of growth time. (c) Statistics for length and diameter as a function of the growth of ZnO NWs. (d) Aspect ratio of ZnO NWs as a function of the growth time. (e) X-ray diffraction (XRD) analysis for sputtered ZnO film and hydrothermally grown ZnO NWs.

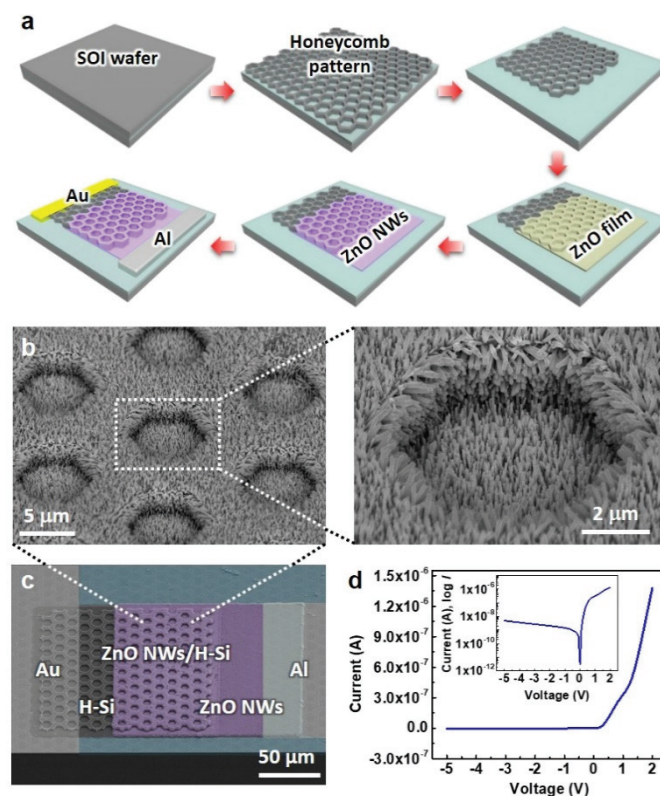


**Figure 2.2** Hierarchical design of H-Si decorated with ZnO NWs. (a) Schematic illustration of the fabrication of ZnO NW/H-Si on  $\text{SiO}_2/\text{Si}$  substrate. (b) Tilted SEM image of ZnO NWs on H-Si structure (diameter:  $8.7 \mu\text{m}$ ). (c) Tilted SEM image of ZnO NW/H-Si photodiode. (d)  $I$ - $V$  curve for ZnO NW/H-Si photodiode in dark state (without illumination). Inset shows a log current-linear voltage plot ( $\log I$ - $V$ ).

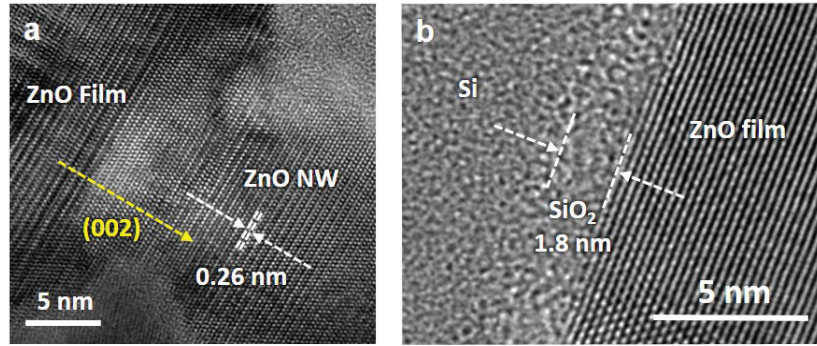


**Figure 2.3** HR-TEM images for interfaces between (a) ZnO film and hydrothermally grown ZnO NW and (b) sputtered ZnO film and Si.

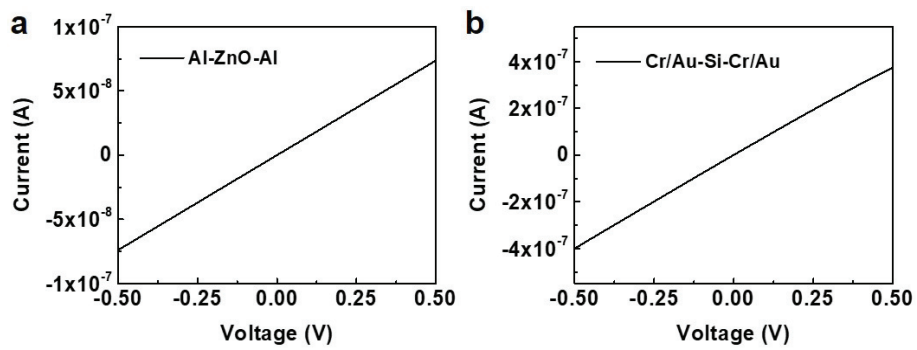


**Figure 2.4**  $I$ - $V$  curves of Al-ZnO-Al and Cr/Au-Si-Cr/Au.

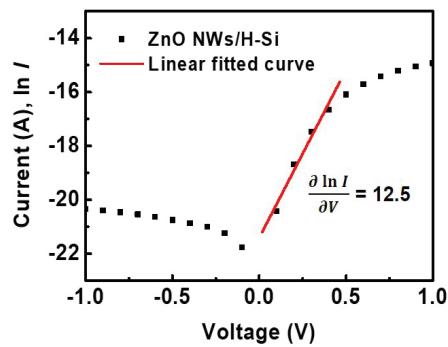


**Figure 2.5** A plot of natural log of current against voltage ( $\ln I$ - $V$ ) for ZnO NW/H-Si photodiode in dark state (without illumination of light).

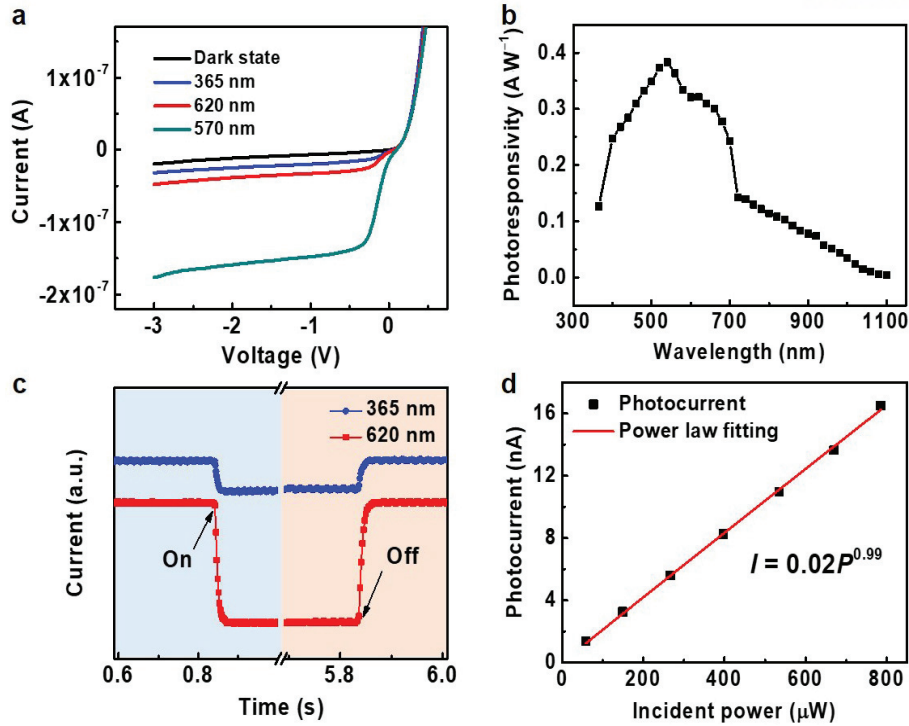


**Figure 2.6** Photoresponsive properties of ZnO NW/H-Si photodiodes. (a)  $I-V$  curves for reverse-biased region under dark conditions and with illumination at three different wavelengths (the optical power of the incident light was  $800 \mu\text{W}\cdot\text{cm}^{-2}$ ). (b) Spectral photoresponsivity of ZnO NW/H-Si photodiode spanning UV to NIR wavelength range at an applied voltage of  $-2$  V. (c) Photoresponse time of ZnO NW/H-Si photodiode under illumination at 365 and 620 nm. (d) Dependence of photoresponse on different illumination intensities under illumination at 365 nm at an applied voltage of  $-2$  V.

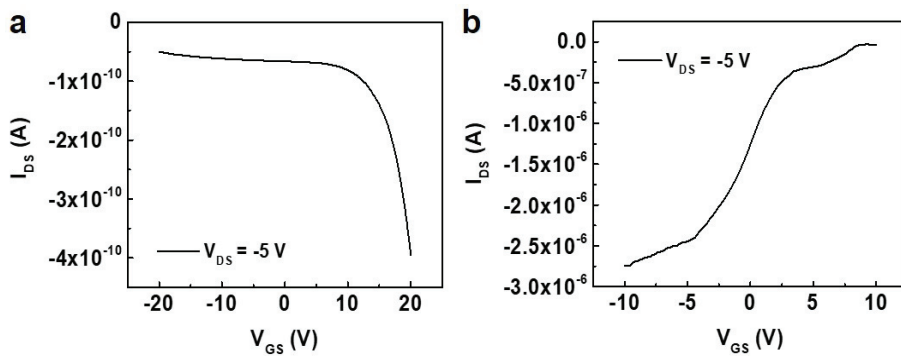


**Figure 2.7** Transfer curves of field-effect transistors based on (a) ZnO NWs and (b) H-Si.

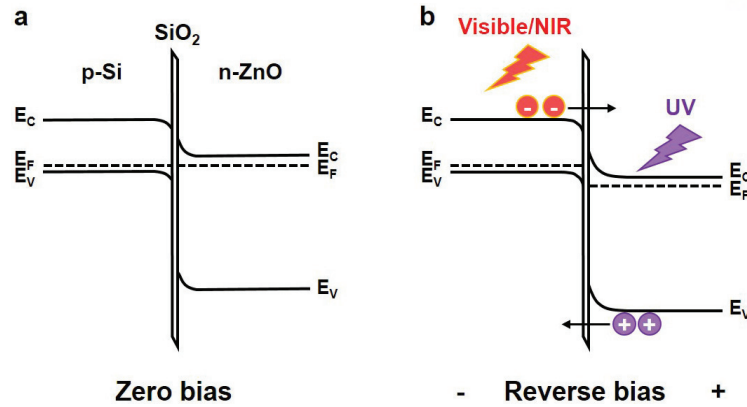


**Figure 2.8** Energy band diagrams of p-Si/n-ZnO heterojunction photodiode under (a) zero bias and (b) reverse bias.

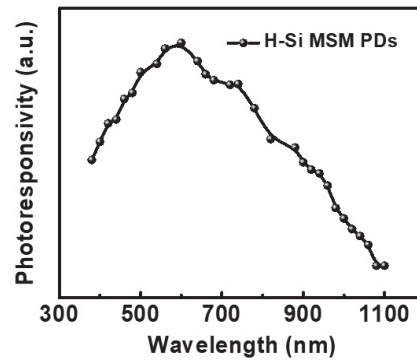


**Figure 2.9** Spectral photoresponsivity of metal-semiconductor-metal photodetector based on H-Si.

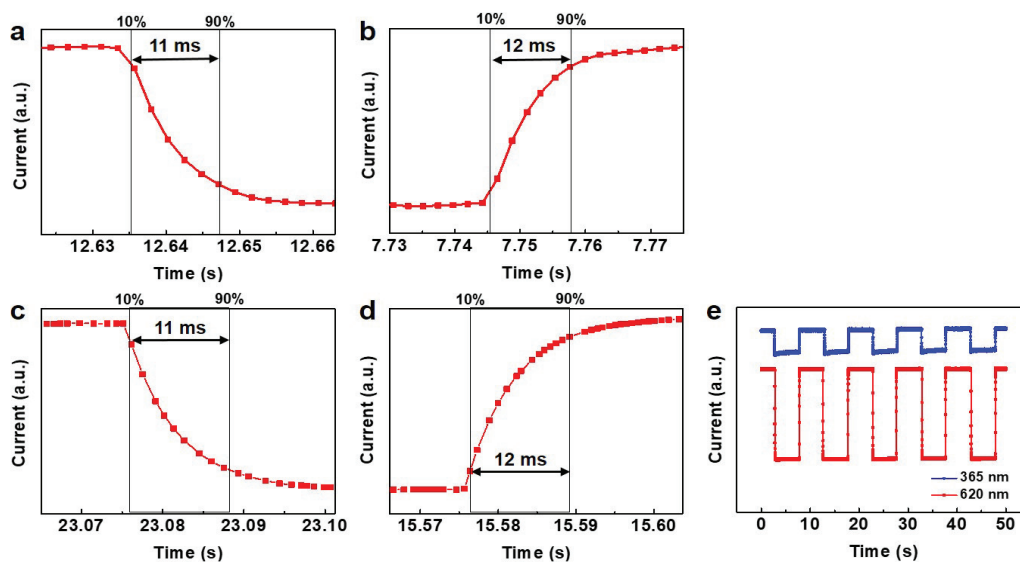


**Figure 2.10** Fast response of ZnO NWs/H-Si and ZnO NWs/F-Si photodiodes. (a) Rise and (b) decay time of ZnO NWs/H-Si photodiodes. (c) Rise and (d) decay time of ZnO NW/F-Si photodiodes. (e) Repeated photoresponse results under illumination of 365 and 620 nm light for ZnO NW/H-Si photodiodes.

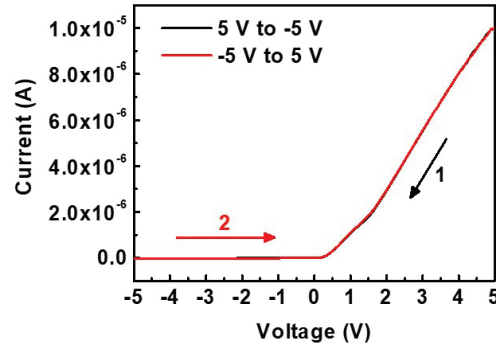


Figure 2.11  $I$ - $V$  hysteresis curve of ZnO NWs/H-Si photodiodes.

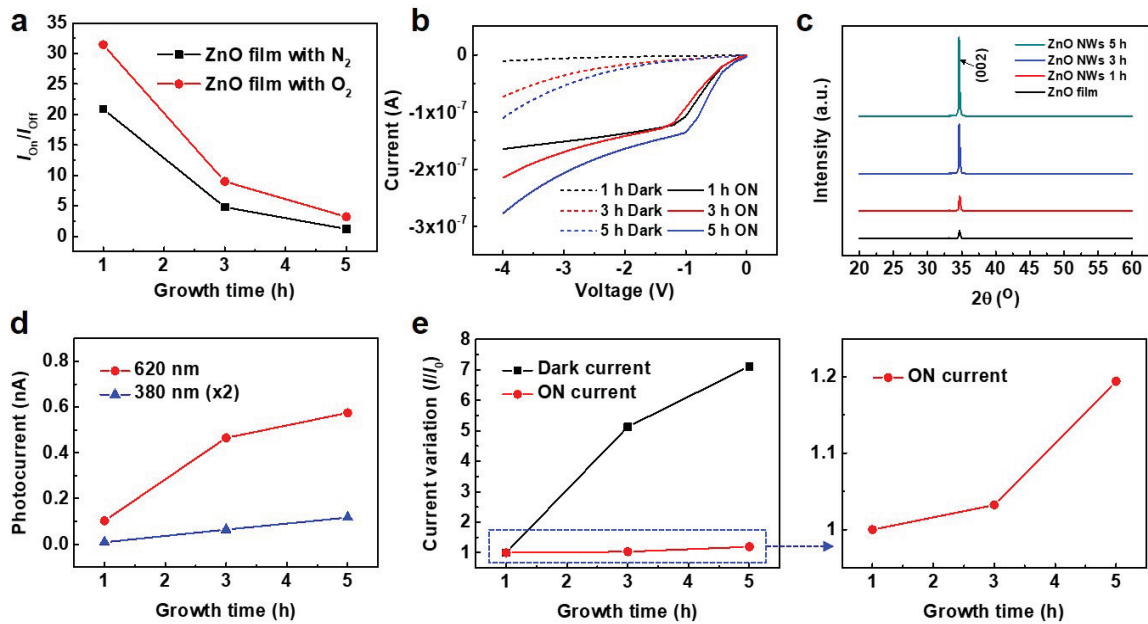
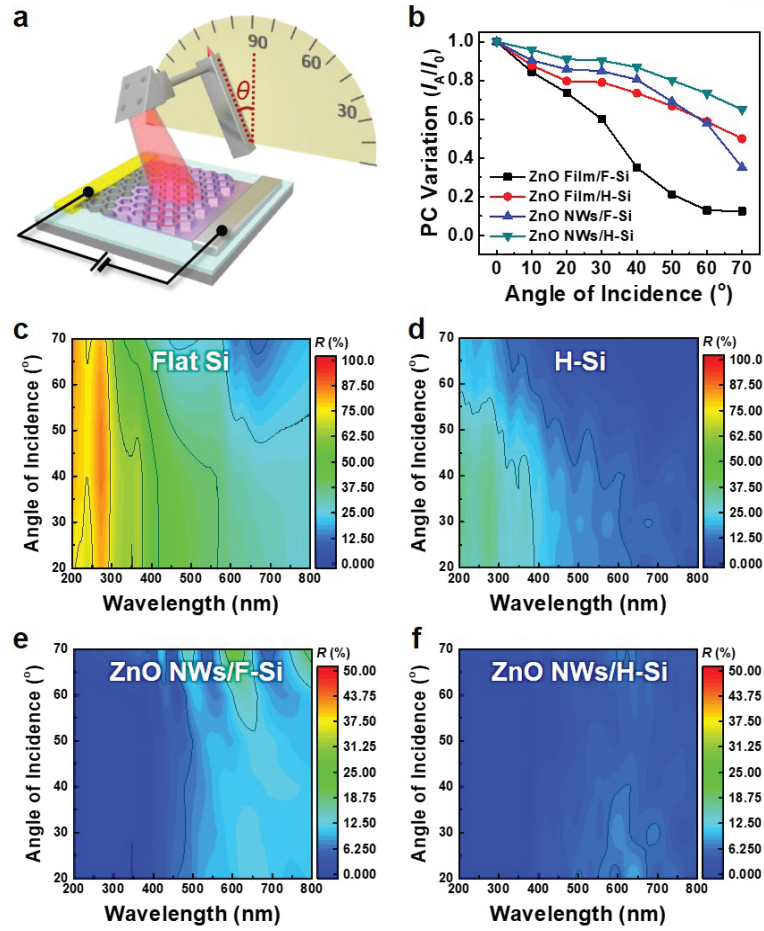
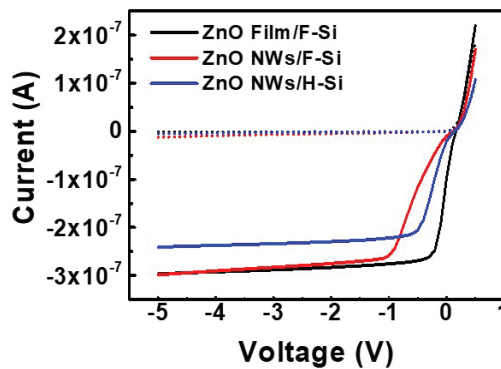


Figure 2.12 (a) Plot for photoresponsive On/Off ratio under white light illumination of ZnO NW/Si photodiodes with ZnO film sputtered in different gas environments. (b)  $I$ - $V$  curves for reverse-biased region of dark current and ON current under white light illumination as a function of the growth time. (c) XRD analysis for sputtered ZnO film and time-dependent ZnO NWs. (d) Photocurrent of ZnO NW/Si photodiodes under illumination of 380 and 620 nm light as a function of the growth time of ZnO NWs. (e) Variation of dark current and ON current (White light illumination) as a function of the growth time of ZnO NWs.





**Figure 2.13** Omnidirectional light-absorption properties of hierarchical hetero-structures of ZnO NWs on H-Si. (a) Photocurrent measurement system as a function of angle of incident light. (b) Variation of photocurrent for four different hetero-structured ZnO/Si photodiodes as a function of angle of incident light at 620 nm. 2D plots of UV–vis–NIR reflectance data for (c) F-Si, (d) H-Si, (e) ZnO NWs on F-Si, and (f) ZnO NWs on 8.7  $\mu\text{m}$  H-Si using variable angle specular reflectance accessory.



**Figure 2.14**  $I$ – $V$  curves for three different kinds of hetero-structured ZnO/Si photodiodes. (Dotted lines and solid lines represent dark current and ON current with illumination of 570 nm light, respectively.)

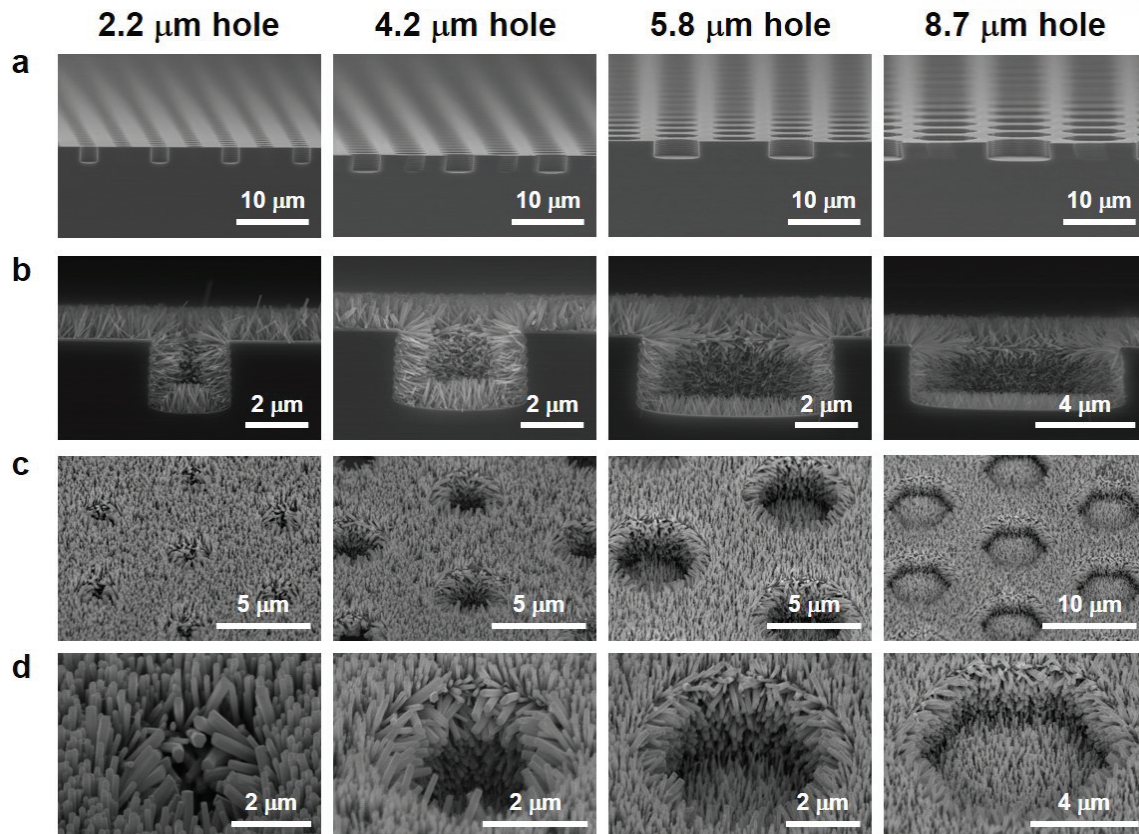


**Figure 2.15** Characterization of H-Si and ZnO NW/H-Si. The cross-sectional SEM images for (a) H-Si and (b) ZnO NWs/H-Si as a function of the hexagonal hole size. (c) The tilted SEM images for ZnO NW/H-Si. (d) Magnified view of (c).

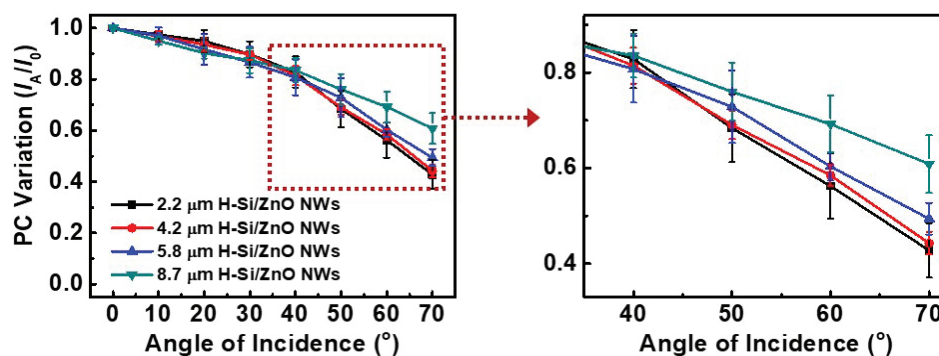


**Figure 2.16** Variation in photocurrent of ZnO NW/Si photodiode as a function of angle of incident light and hole sizes of H-Si.

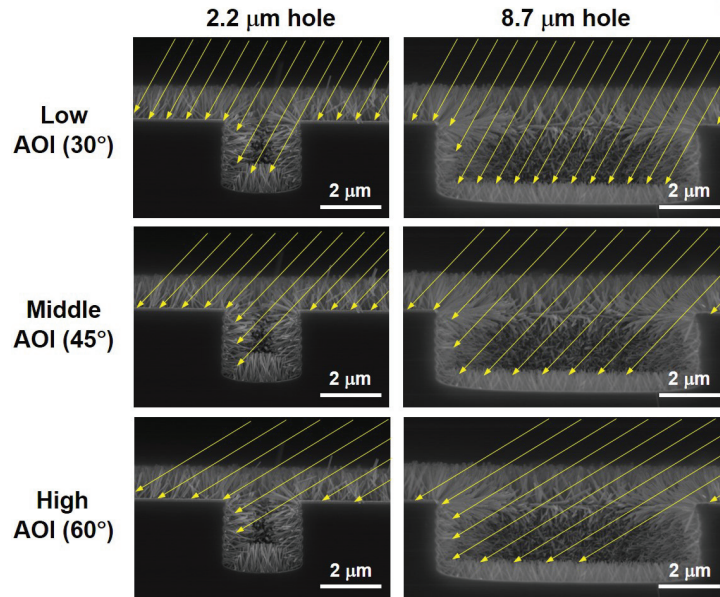


**Figure 2.17** Schematics for light path with incident angles of 30°, 45°, and 60° into different hexagonal hole sizes.

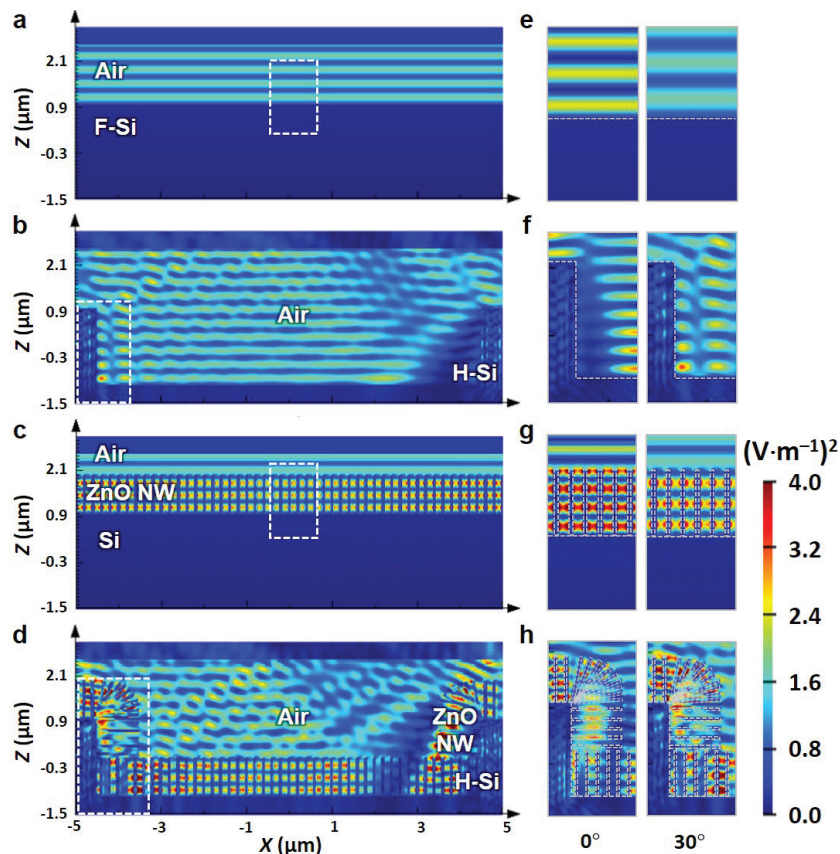


**Figure 2.18** Simulated cross-sectional  $|E|^2$  distribution of the electromagnetic (EM) wave at 620 nm excitation with different morphologies: (a) F-Si, (b) H-Si, (c) ZnO NW/F-Si, and (d) ZnO NW/H-Si at angular incidence of 30°. Magnified view of EM wave distribution with different morphologies: (e) F-Si, (f) H-Si, (g) ZnO NW/F-Si, and (h) ZnO NW/H-Si (left: normal incidence, right: 30° incidence).

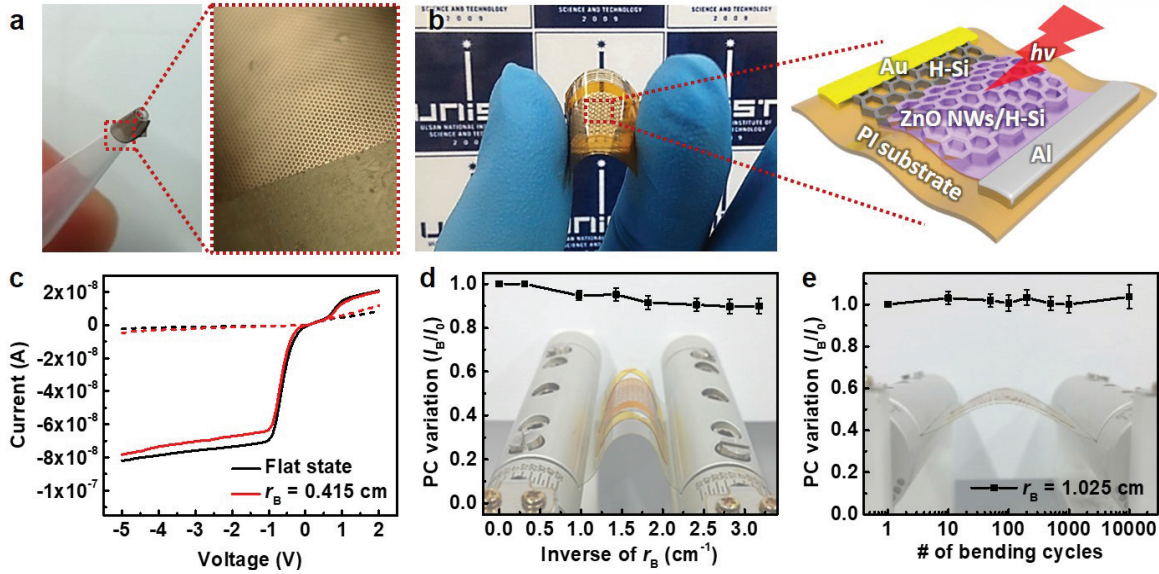


**Figure 2.19** Evaluation of flexibility and durability of flexible ZnO NW/H-Si photodiode on PI substrate. (a) Digital images and OM image of rolled H-Si membrane on tip of pipette. (b) Photograph and schematic showing the highly flexible ZnO NW/H-Si-based photodiode on polyimide. (c)  $I$ - $V$  curves of flexible photodiode in dark state (dotted line) and under illumination with 365 nm light (solid line) as a function of the bending curvature. (d) Variation of photocurrent with increasing bending curvature. Background photograph shows photodiode bent with bending machine ( $r_B = 0.415$  cm). (e) Mechanical durability of ZnO NW/H-Si photodiode on PI substrate with increasing number of bending cycles with a bending radius of  $r_B = 1.025$  cm.

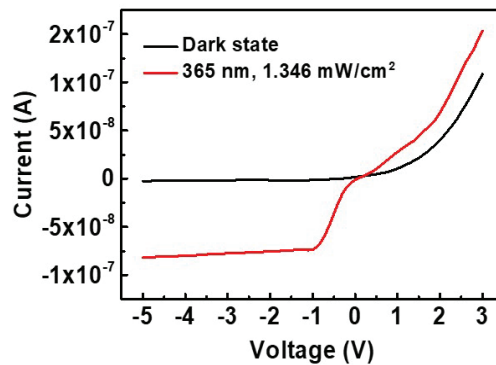


**Figure 2.20**  $I$ - $V$  curves of ZnO NWs/H-Si photodiode on PI substrate under dark state and 365 nm light illumination.

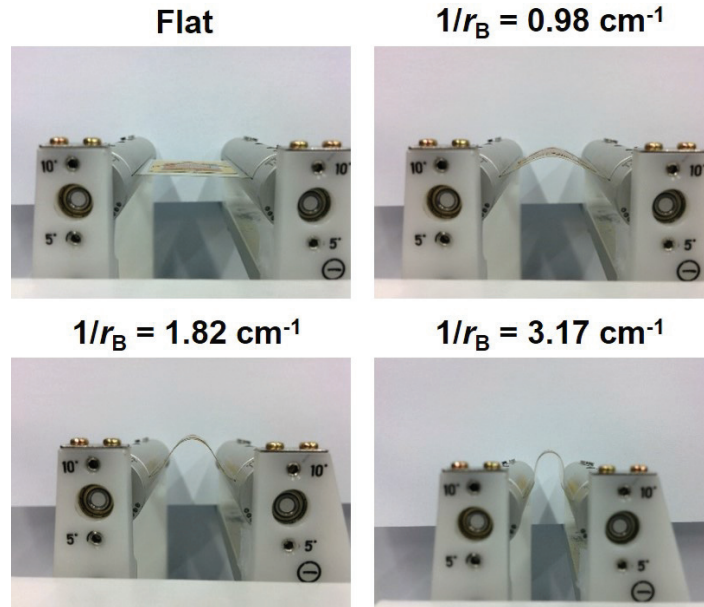


**Figure 2.21** Digital images of bent photodiode arrays on PI substrate as a function of the bending radius.

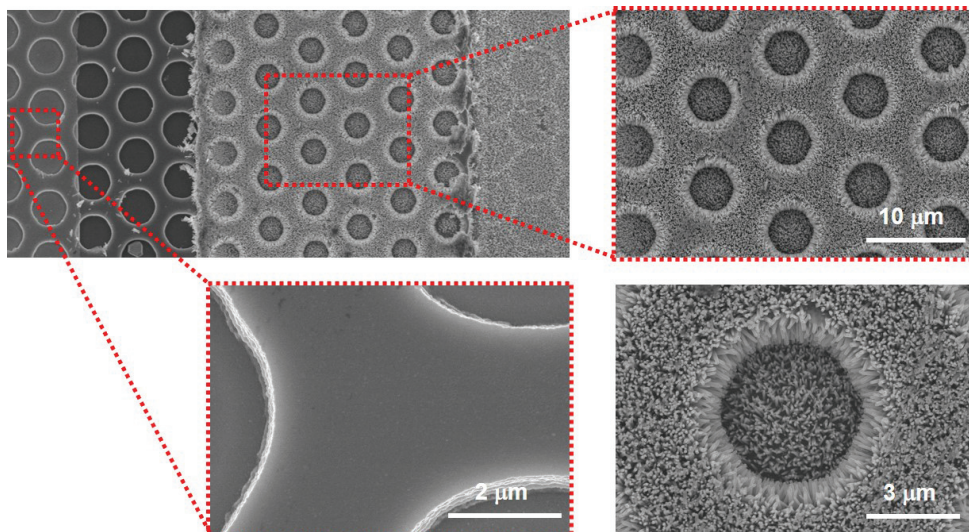


**Figure 2.22** SEM images of ZnO NWs/H-Si photodiode on PI substrate after 10,000 cycles of mechanical bending test at bending.

## Chapter 3. Large-Area, Solution-Processed, Hierarchical MAPbI<sub>3</sub> Nanoribbon Arrays for Self-Powered Flexible Photodetectors

### 3.1 Introduction

Recently, the growing interest in wearable electronics has inspired the development of high-performance electronic sensors with diverse functionalities for applications in the fields of smart healthcare systems, augmented reality, internet of things, and robotics. In particular, photodetectors have attracted much attention as light-sensing elements, with their current development focusing not only on enhancing responsivity,<sup>[1, 2]</sup> response time,<sup>[3]</sup> and broadband detection capability,<sup>[2, 3]</sup> but also on the introduction of extra functionalities such as mechanical flexibility,<sup>[4]</sup> self-powered detection,<sup>[2, 5]</sup> and polarization sensitivity.<sup>[6-8]</sup> To realize these properties, a number of micro-/nanostructures with unique optical, electrical, and mechanical properties have been suggested.<sup>[7, 9-11]</sup> For example, 1D nanostructures (e.g., nanowires, nanorods, and nanotubes) exhibiting large surface-to volume ratios, stress relaxation behavior, quantum confinement effects, and polarization dependency of light absorption hold great promise as constituents of wearable sensors.<sup>[7]</sup> In addition, hierarchical micro-/nanoarchitectures based on multiscale hybridization of nanomaterials are promising photon management structures for high-efficiency photodetectors<sup>[10, 11]</sup> and energy-harvesting devices.<sup>[12]</sup>

In recent years, organic-inorganic hybrid perovskites, in particular CH<sub>3</sub>NH<sub>3</sub>PbX<sub>3</sub> (X = Cl, Br, I), have attracted great attention as prospective materials for the fabrication of high-performance optoelectronic devices such as solar cells,<sup>[13]</sup> light-emitting diodes,<sup>[14]</sup> and photodetectors<sup>[15]</sup> due to their outstanding optical and electrical properties, e.g., high absorbance over a broad wavelength range, large carrier diffusion length, high carrier mobility, band gap tunability, and mechanical flexibility.<sup>[16]</sup> In addition, the above perovskites can be processed by low-cost and facile solution-based methods, which allows the development of practical and cost-effective devices. Nevertheless, the low stability of these perovskites in polar solvents (e.g., water, acetone, alcohol, and tetramethylammonium hydroxide) employed in conventional patterning<sup>[17]</sup> significantly complicates the fabrication of complex micro-/nanostructures and their application in high-performance optoelectronic devices. To circumvent this problem, numerous nonconventional patterning approaches have been adopted to realize micro-/nanostructured perovskite-based photodetectors with improved optoelectronic performances as a result of enlarged irradiation area and reduced number of recombination sites. For example, hybrid perovskite morphologies such as nanowires,<sup>[18, 19]</sup> planar microribbons,<sup>[8, 20]</sup> and nanonetworks/islands<sup>[21, 22]</sup> have been realized by controlling the crystallization process. In particular, anisotropic 1D nanostructures showed an additional polarization dependency along their axis,<sup>[8, 19]</sup> thus being well suited for applications such as quantum cryptography,<sup>[23]</sup> remote sensing,<sup>[24]</sup> and biomedical imaging.<sup>[25, 26]</sup> Moreover, micro-/nanoscale gratings can be introduced into

hybrid perovskite films *via* nanoimprinting,<sup>[27, 28]</sup> direct deposition on nanostructured templates,<sup>[29, 30]</sup> and crystallization of perovskite films confined by patterned poly(dimethylsiloxane) (PDMS) covers.<sup>[29, 31, 32]</sup> Notably, the micro-/nanoscale gratings facilitate the formation of highly crystalline perovskite films with large grain size and enhanced light absorption capability.<sup>[27, 29]</sup> Although hierarchical architectures have shown great potential as photon management structures in previously described (in)organic optoelectronic devices,<sup>[10–12]</sup> the utilization of hierarchically structured perovskites with controlled morphology to improve the functionality and performance of photodetectors has not been attempted due to the difficulty of fabricating complex micro-/nanostructures.

Herein, we describe the fabrication of hierarchically structured methylammonium lead iodide (MAPbI<sub>3</sub>) nanoribbon (NR) arrays with controlled internal nanorod structures by simple spin-coating on polymeric nanotemplates with alternating hydrophobic and hydrophilic patterned surfaces. Specifically, we show that the spin-coating of MAPbI<sub>3</sub> precursor solution on polymeric nanotemplates induces the selective deposition of MAPbI<sub>3</sub> between polymethyl methacrylate (PMMA) line patterns and results in the formation of MAPbI<sub>3</sub> NRs. For polymeric nanotemplates with selective perovskite coating behavior, liquid bridge-mediated transfer printing was used to uniformly transfer PMMA line patterns from PDMS nanostamps onto various substrates including SiO<sub>2</sub>/Si, glass, and flexible polyimide (PI). For hierarchically structured MAPbI<sub>3</sub> NR arrays with controlled internal nanorod structures, coordination engineering of perovskite precursor solution and toluene drip treatment were utilized to produce nanorods with uniform and compact grains. To test the practical applicability of the fabricated materials, we fabricated high-performance photodetectors based on hierarchical MAPbI<sub>3</sub> NRs, which exhibited broad-range photodetection (from UV to 800 nm) and fast switching behavior (rise and decay times of 27.2 and 26.2 ms, respectively). In addition, MAPbI<sub>3</sub> NR photodetectors exhibited a 18.1–23.7 times higher specific detectivities than those based on MAPbI<sub>3</sub> films due to the fewer charge trap states in NR photodetectors. Furthermore, MAPbI<sub>3</sub> NRs photodetectors on flexible PI substrates show stable light-detection performance under extremely high bending curvature of bending radius ( $r_B$ ) = 3.7 mm. Finally, the ferroelectric properties of MAPbI<sub>3</sub> and the highly anisotropic alignment of MAPbI<sub>3</sub> NR arrays allowed the fabrication of multifunctional photodetectors capable of self-powered and polarization-sensitive light detection. The figure-of-merit characteristics summarized in **Table 3.1** show the high-performance, flexible, and multifunctional light-detection capability of our hierarchical MAPbI<sub>3</sub> NRs in comparison with recently reported MAPbI<sub>3</sub>-based photodetectors.

### 3.2 Experimental Details

**Fabrication of PMMA Nanotemplates:** PMMA nanotemplates were fabricated utilizing nanopatterned PDMS prepared by soft lithographic molding. A mixture of 10:1 weight ratio of PDMS

main base and curing agent (Sylgard 184, Dow Corning) was poured onto a trichloro(1H,1H,2H,2H-perfluorooctyl)silane (FOTS)-treated silicon stamp (LightSmyth) and cured at 70 °C for 4 h on a hot plate. PMMA photoresist (495 PMMA C4,  $M_w = 495$  kDa, MicroChem) was diluted to 0.35%–0.4% with anhydrous chlorobenzene (99.8%, Sigma-Aldrich), and the obtained solution was spin-coated onto the nanopatterned PDMS at 3000 rpm for 40 s without acceleration and dried at 70 °C for 1 h on a hot plate. Transfer of PMMA nanotemplates from the nanopatterned PDMS to the substrate ( $\text{SiO}_2/\text{Si}$ , glass, or PI) was performed by liquid bridge-mediated transfer printing. Typically, ethanol (200  $\mu\text{L}$ ) was dropped onto the PMMA-loaded nanopatterned PDMS, which was then covered by  $\text{O}_2$  plasma-treated substrates without applying external pressure. PMMA nanotemplates were fabricated after detachment of the PDMS stamp and hard-baked at 180 °C for 2 min on a hot plate.

**Fabrication of Hierarchical  $\text{MAPbI}_3$  NR Arrays:** The  $\text{MAPbI}_3$  precursor solution was prepared by dispersing equimolar amounts of  $\text{CH}_3\text{NH}_3\text{I}$  (>99.0%, Dyesol) and  $\text{PbI}_2$  (99.0%, Sigma-Aldrich) in *N,N*-dimethylformamide (>99.5%, Daejung) upon 12 h stirring to a total concentration of 5 wt%, which was adjusted depending on the height of PMMA nanotemplates. A single droplet of the above solution was spin-coated onto PMMA nanotemplates at 3000 rpm for 40 s without acceleration. To promote uniform crystallization of  $\text{MAPbI}_3$  NRs, a single droplet of anhydrous toluene (99.8%, Sigma-Aldrich) was spin coated onto the intermediate  $\text{MAPbI}_3/\text{DMF}$  phase, with subsequent 1-h annealing at 100 °C on a hot plate affording hierarchical  $\text{MAPbI}_3$  NRs. All synthesis, spin-coating, and crystallization steps used to prepare  $\text{MAPbI}_3$  NRs were conducted in a nitrogen-filled glove box. To remove PMMA nanotemplates, the substrate was immersed into toluene for 1 h upon short-time sonication and blown dry with  $\text{N}_2$ .

**Fabrication of  $\text{MAPbI}_3$  NR-Based Photodetector Arrays:** To form a metal electrode, Cr/Au (3 nm/97 nm) were deposited on a 100 nm  $\text{SiO}_2/p^{++}\text{-Si}$  substrate by thermal evaporation followed by photolithography (MA-6, SUSS MicroTec, Germany) with an AZ nLOF 2035 photoresist. PMMA nanotemplates were transferred onto the electrode prepatterned substrate with cross-alignment direction by liquid bridge-mediated transfer printing.  $\text{MAPbI}_3$  NRs were deposited between PMMA nanotemplates following the above-mentioned procedure.

**Characterization:** The morphologies of PMMA nanotemplates,  $\text{MAPbI}_3$  films,  $\text{MAPbI}_3$  NRs/PMMA, and  $\text{MAPbI}_3$  NRs were characterized by field-emission SEM (S-4800, Hitachi, Japan) and AFM (MFP-3D, Asylum Research, USA). The absorption and transmittance of  $\text{MAPbI}_3$  films,  $\text{MAPbI}_3$  NRs/PMMA, and  $\text{MAPbI}_3$  NRs were determined by UV–vis–NIR spectroscopy (Cary 5000, Agilent, USA). The crystal structures of  $\text{MAPbI}_3$  films,  $\text{MAPbI}_3$  NRs/PMMA, and  $\text{MAPbI}_3$  NRs were characterized by XRD (D8 Advance, Bruker, USA). Optical imaging of  $\text{MAPbI}_3$  films,  $\text{MAPbI}_3$  NRs/PMMA,  $\text{MAPbI}_3$  NRs, and  $\text{MAPbI}_3$  photodetector arrays was performed by optical microscopy (BX-53, Olympus, Japan). Point hysteresis loops of  $\text{MAPbI}_3$  films were recorded using PFM with switching spectroscopy PFM mode (MFP-3D, Asylum Research, USA).



**Electrical and Optical Measurements:** The general electrical characteristics of photodetectors were determined using the two probe method at room temperature in vacuum (4200-SCS, Keithley, USA). A monochromator (Cornerstone 130 1/8 m Monochromators, Newport, USA) with a variable slit and a Xe arc lamp (300 W) was used for illumination with light of various wavelengths. To correlate the photocurrent with the optical power of incident light, the latter parameter was varied using a motorized iris diaphragm (62280, Newport, USA). The dependence of the light source optical intensity on wavelength was measured by a calibrated optical power meter (1916-R, Newport, USA) comprising a Si photodetector (818-UV, Newport, USA).

### 3.3 Results and Discussion

**Fabrication of large-area and highly-aligned MAPbI<sub>3</sub> NR arrays:** Figure 3.1a schematically illustrates the fabrication of large-area hierarchical MAPbI<sub>3</sub> NR arrays *via* spin-coating of MAPbI<sub>3</sub> precursor solution on transfer-printed PMMA nanotemplates, which were prepared by soft lithographic molding using nanopatterned PDMS molds (line width: 455 nm, pitch: 833 nm, height: 200 nm). In this process, simple spin-coating of PMMA solution with controlled concentration (0.35%–0.4%) onto the nanopatterned PDMS mold resulted in solution confinement between PDMS line patterns, with the hydrophobic surface of PDMS preventing the coating of PMMA solution onto PDMS ridges. To efficiently transfer the PMMA trapped between PDMS line patterns onto O<sub>2</sub> plasma-treated substrates (SiO<sub>2</sub>/Si, glass, and flexible PI), a liquid bridge-mediated transfer printing technique was adopted.<sup>[33]</sup> In this process, ethanol dropped on the surface was trapped between the PMMA/PDMS pattern and the target substrate, with the liquid bridges formed between PMMA and the substrate by the action of capillary forces dragging down the PMMA nanotemplate to the underlying substrate during ethanol evaporation. Figure 3.2a and 3.2b present photographic and optical microscopy (OM) images, respectively, of the large-area highly aligned PMMA nanotemplate transferred onto the SiO<sub>2</sub>/Si substrate. Atomic force microscopy (AFM) image (Figure 3.2c) indicated that no residual bottom layer was present between the 100 nm thick PMMA nanopatterns, which enabled the formation of alternating hydrophilic and hydrophobic surfaces between O<sub>2</sub> plasma-treated substrates and PMMA nanotemplates. Next, MAPbI<sub>3</sub> NRs were fabricated by spin-coating 5 wt% MAPbI<sub>3</sub> (in *N,N*-dimethylformamide, DMF) precursor solution onto PMMA nanotemplates, subjected to a toluene drip treatment, and crystallized by annealing at 100 °C on a hot plate to obtain uniform and compact grains. It is worth noting that the MAPbI<sub>3</sub> precursor solution was trapped between PMMA nanopatterns without over-coating on top of PMMA ridges due to the hydrophobicity of the PMMA surface. Finally, MAPbI<sub>3</sub> NR arrays on the desired substrates were obtained by removing PMMA nanotemplates by immersion into toluene. The facile solution-phase deposition of the MAPbI<sub>3</sub> precursor onto PMMA nanotemplates enabled the fabrication of large-area (up to 2.5 cm × 2.5 cm) highly aligned MAPbI<sub>3</sub> NR arrays on various substrates including SiO<sub>2</sub>/Si, glass, and flexible PI, as

shown in Figure 3.1b, 3.1c, and **Figure 3.3**. In particular, the solution-processed ultrathin MAPbI<sub>3</sub> NRs (thickness:  $\approx 70$  nm) on flexible PI substrates in Figure 3.1b-(iii) showed skin-conformable property for wearable application.

**Figure 3.4** shows scanning electron microscopy (SEM) and AFM images of PMMA nanotemplates, MAPbI<sub>3</sub> NRs trapped within PMMA nanotemplates, and MAPbI<sub>3</sub> NRs, revealing that the transferred PMMA nanotemplates featured periodic line patterns of 300 nm width and 800 nm pitch without any residual PMMA bottom layer between them (Figure 3.4a and 3.4b). Figure 3.4c and 3.4d indicate that MAPbI<sub>3</sub> NRs with densely packed internal nanorods could be uniformly formed between PMMA nanopatterns by simple spin-coating of MAPbI<sub>3</sub> precursor solution and crystallization. AFM image indicated that the internal nanorods had an average length and thickness of  $\approx 555$  nm (**Figure 3.5a**) and 112 nm (Figure 3.5b), respectively. The formation of internal MAPbI<sub>3</sub> nanorods in hierarchical perovskite NRs is influenced by two factors. First, the coordination engineering of perovskite precursor solution allows one to control the morphologies of perovskite films. Previously, it was reported that the morphology of MAPbI<sub>3</sub> thin films can be controlled by the MAI:PbI<sub>2</sub> ratio of the perovskite precursor solution,<sup>[34]</sup> e.g., rod-like structures and planar films were obtained at 1:1 and 3:1 ratios, respectively. Similarly, we employed a 1:1 MAI:PbI<sub>2</sub> ratio to obtain hierarchically designed perovskite NRs with internal nanorod structures. However, instead of the nanorod morphology, we herein observed aggregated perovskite particles with some voids in the confined space of PMMA nanotemplates due to the occurrence of aggregation during crystallization (**Figure 3.6a**). To prevent aggregation and void formation, a toluene drip treatment was utilized, resulting in the successful fabrication of hierarchical and compact perovskite NRs with nanorod morphology (Figure 3.6b) without damage of PMMA nanotemplates (Figure 3.4c and 3.4d). The above treatment relied on the fact that the introduction of nonpolar solvents such as toluene or chlorobenzene onto the intermediate phase of MAPbI<sub>3</sub>/DMF can induce an abrupt precipitation of perovskite precursors as well as remove residual DMF and excess iodide/methylammonium ions from the surface of MAPbI<sub>3</sub>.<sup>[35–37]</sup> In addition, fast crystallization of MAPbI<sub>3</sub> prevented random aggregation, resulting in the formation of uniform and dense grains. The introduction of nonpolar solvent accompanied by perovskite precursor precipitation and evaporation rate change might affect crystallization kinetics, resulting in the directional growth of internal MAPbI<sub>3</sub> nanorods. Interestingly, the toluene drip treatment did not induce the formation of NR-shaped crystals in the case of MAPbI<sub>3</sub> films (**Figure 3.7**), possibly due to the insufficient extent of solution trapping on a planar substrate without PMMA nanotemplates. Figure 3.4e and 3.4f show images of MAPbI<sub>3</sub> NR arrays (width: 480–540 nm, height: 70 nm) after the removal of PMMA nanotemplates by 1 h dipping in toluene, confirming that PMMA nanotemplates were selectively removed without affecting the morphology of MAPbI<sub>3</sub> NRs.

**Physical properties of MAPbI<sub>3</sub> film and NR arrays:** To investigate the optical properties of MAPbI<sub>3</sub> films, MAPbI<sub>3</sub> NRs/PMMA, and MAPbI<sub>3</sub> NRs, their optical absorption and transmittance

were characterized by UV–vis–NIR spectroscopy (**Figure 3.8a** and **Figure 3.9**), with broad absorption peaks (UV to 800 nm) related to the band gap of MAPbI<sub>3</sub> observed in all cases. In particular, the absorption peak of MAPbI<sub>3</sub> NRs (UV to 650 nm) was more intense than that of MAPbI<sub>3</sub> films, which was attributed to the antireflective properties of the periodic nanogratings of MAPbI<sub>3</sub> NRs.<sup>[29]</sup> Figure 3.8b shows that the band gap of MAPbI<sub>3</sub> NRs could be estimated as 1.556 eV by fitting the Tauc plot based on the transmittance data displayed in Figure 3.9. To investigate the crystal quality of MAPbI<sub>3</sub>, we performed X-ray diffraction (XRD) analysis of MAPbI<sub>3</sub> films, MAPbI<sub>3</sub> NRs/PMMA, and MAPbI<sub>3</sub> NRs (Figure 3.8c), showing that the MAPbI<sub>3</sub> film exhibited three peaks corresponding to the (001) plane of PbI<sub>2</sub> (marked as #) and the (110) and (220) planes of MAPbI<sub>3</sub> at 12.99°, 14.45°, and 28.75°, respectively. For MAPbI<sub>3</sub> NRs/PMMA, only peaks of the (110) and (220) MAPbI<sub>3</sub> planes at 14.57° and 28.91°, respectively, were observed. The intensities of the two MAPbI<sub>3</sub> NR peaks were decreased due to the shielding effect of PMMA nanotemplates and the reduced relative area of MAPbI<sub>3</sub> resulting from the patterned structure. Furthermore, the absence of the PbI<sub>2</sub> peak was indicative of effective MAPbI<sub>3</sub> NR crystallization between PMMA nanotemplates. Notably, the shift to higher scattering angles was attributed to decreased interplanar distances due to the compressive strain resulting from the crystallization of MAPbI<sub>3</sub> NRs in confined PMMA nanotemplates. After the PMMA nanotemplates were removed from MAPbI<sub>3</sub> NR patterns, the PbI<sub>2</sub> peak reappeared, and the (110) and (220) peaks were shifted to lower scattering angles due to the formation of PbI<sub>2</sub> and the release of strain, respectively.

**Optoelectronic characteristics of MAPbI<sub>3</sub> NR-based photodetectors:** **Figure 3.10** shows typical photoconductive behaviors of hierarchical MAPbI<sub>3</sub> NR photodetectors. During photodetector fabrication, we did not remove PMMA nanotemplates to directly evaluate the dependence of photodetector performance on the morphologies of MAPbI<sub>3</sub> excluding the effects of nanograting and the degradation of MAPbI<sub>3</sub> NRs. Figure 3.10a shows an OM image and a schematic representation of photodetector structure, demonstrating that these photodetectors were composed of MAPbI<sub>3</sub> NRs and Cr/Au (3 nm/97 nm) metal electrodes (channel length = 12 μm, channel width = 465 μm) on 100 nm SiO<sub>2</sub>/p<sup>+</sup>-Si substrates. Figure 3.10b shows typical current–voltage (*I–V*) curves of MAPbI<sub>3</sub> NR photodetectors recorded in the dark (black line) and under illumination with light of five representative wavelengths (300 nm: 38.48 μW·cm<sup>-2</sup>, 400 nm: 346.5 μW·cm<sup>-2</sup>, 500 nm: 383.9 μW·cm<sup>-2</sup>, 600 nm: 247.8 μW·cm<sup>-2</sup>, and 700 nm: 107.3 μW·cm<sup>-2</sup>). The photodetectors featured a low dark current of few pA (1.59 pA at an applied voltage of 2 V, inset in Figure 3.10b) due to the polycrystallinity and small thickness of MAPbI<sub>3</sub> NRs (≈70 nm), which is superior to previously reported MAPbI<sub>3</sub>-based photodetectors (dark currents of 6, 16, and 30 pA).<sup>[19, 27, 30]</sup> Illumination resulted in a significant photocurrent increase due to the photogeneration of electron–hole pairs, with the extent of this increase depending on the wavelength and optical power of incident light. Furthermore, the fabricated photodetectors exhibited distinct hysteresis under both dark and

illumination conditions due to the ferroelectric nature of MAPbI<sub>3</sub>,<sup>[38, 39]</sup> which enabled self-powered light detection, as will be discussed later. In view of the fact that stable and fast photoswitching is a critical parameter of high-performance photodetectors, we investigated the photoswitching behavior of MAPbI<sub>3</sub> NR photodetectors under repeated on/off cycling (500 nm, 383.9 μW·cm<sup>-2</sup>), confirming that the observed current changes were regular and stable (**Figure 3.11**). Figure 3.10c presents the photoresponse rise and decay times calculated by analyzing the time intervals of peak current changes from 10% to 90% and from 90% to 10%, respectively, revealing that the investigated photodetectors exhibited fast rise (27.2 ms) and decay (26.2 ms) times at an applied voltage of 2 V.

Figure 3.10d and **Figure 3.12** show the spectral specific detectivities of photodetectors based on MAPbI<sub>3</sub> films and NRs for a wavelength range of 300–800 nm. The specific detectivity ( $D^*$ ) can be defined as  $D^* = R_{ph} \times A^{1/2} \times (2qI_d)^{-1/2}$ , where  $R_{ph}$  is the photoresponsivity,  $A$  is the active area,  $q$  is the elementary charge, and  $I_d$  is the dark current. Specifically, photoresponsivity ( $R_{ph}$ ) can be defined as  $R_{ph} = I_{ph}/PA$ , where  $I_{ph}$  is the photocurrent, and  $P$  is the optical power of incident light. Both photodetectors showed a broad detection range (UV to 800 nm), with their highest specific detectivity and photoresponsivity peaks (**Figure 3.13**) observed at 550 and 500 nm being in agreement with the UV–vis absorption spectra in Figure 3.8a. The maximum specific detectivity of MAPbI<sub>3</sub> NR photodetectors is  $8.21 \times 10^{11}$  Jones under illumination with 300 nm light, which is comparable to the previously reported MAPbI<sub>3</sub> based photodetectors in Table 3.1. In particular, the specific detectivities of MAPbI<sub>3</sub> NR photodetectors were significantly higher than that of photodetectors based on MAPbI<sub>3</sub> films ( $\times 18.1$ – $23.7$  over the entire spectral range). The photoresponsivity of MAPbI<sub>3</sub> NR photodetectors in Figure 3.13 also higher than that of photodetectors based on MAPbI<sub>3</sub> films ( $\times 2.5$ – $3.8$  over the entire spectral range). Even though the fabricated MAPbI<sub>3</sub> films had an island-like morphology (Figure 3.7) similar to that of the recently suggested ultrasensitive photodetectors based on island-structured MAPbI<sub>3</sub> films with large surface-to-volume ratios and enhanced light scattering capability,<sup>[22]</sup> the hierarchical NR structures fabricated herein exhibited better photoresponsive behavior than island-structured MAPbI<sub>3</sub> films. These enhanced specific detectivity and photoresponsivity were attributed to the improved light absorption capability of the hierarchical nanoribbon shape as well as the increased grain size and reduced amount of recombination sites (e.g., defects and voids) of MAPbI<sub>3</sub> NR photodetectors compared to those of MAPbI<sub>3</sub> films (Figure 3.6 and Figure 3.7). **Figure 3.14** shows photoresponsive performances of MAPbI<sub>3</sub> NR photodetectors before and after the toluene drip treatment. The hierarchical MAPbI<sub>3</sub> NR photodetectors after the toluene drip treatment exhibit the highest spectral specific detectivity and photoresponsivity in the visible range (500 to 800 nm) as a result of effective light absorption of hierarchical nanoribbon shape and enhanced crystallinity. To further confirm the enhanced photoresponsivity of hierarchical NR structures, the relationship between the photocurrent and the optical power of incident light was analyzed to estimate the extent of electron–hole generation, recombination behavior, and the amount

of charge trap states in illuminated photodetectors. Figure 3.10e shows that the photocurrent ( $I_{\text{ph}}$ ) of MAPbI<sub>3</sub> film and NR photodetectors illuminated with 500 nm light increased with increasing optical power. Based on power law fitting ( $I_{\text{ph}} \approx P^\theta$ ), the  $\theta$  value of MAPbI<sub>3</sub> NR photodetectors (0.94) was calculated to exceed that of MAPbI<sub>3</sub> film photodetectors (0.69), being closer to the ideal-case value of unity and indicating that the photocurrent of the former photodetectors almost linearly increased with the optical power of incident light. This result implied that MAPbI<sub>3</sub> NRs contained significantly fewer charge trap states than MAPbI<sub>3</sub> films.

The solution-processed fabrication of hierarchical MAPbI<sub>3</sub> NRs has freedom of substrate choice, which facilitate the development of flexible photodetectors on the ultrathin flexible PI substrates as illustrated in **Figure 3.15a** and Figure 3.1b-(iii). To prevent the degradation of MAPbI<sub>3</sub> NRs during flexibility characterization, we deposited PMMA encapsulation layer onto as-fabricated flexible photodetectors. The time-dependent  $I$ - $V$  curves with 0.1 Hz switching of 500 nm light in Figure 3.15b exhibited clear photoswitching behaviors under bent state with extremely high bending curvature of  $r_{\text{B}} = 3.7$  mm. Figure 3.15c showed flexible photodetectors rolled on pen with  $r_{\text{B}} = 3.7$  mm. Figure 3.15d displayed the current variation of MAPbI<sub>3</sub> NRs photodetectors under dark and illumination states according to the bending curvature. Even though we applied bending strain to the flexible photodetectors with vertical direction of NR alignment to diminish the crack generation of metal electrodes, there is no obtrusive degradation of dark and illumination currents below bending curvature of  $r_{\text{B}} = 3.7$  mm due to the innate mechanical flexibility of MAPbI<sub>3</sub>.

**Multifunctional photodetectors based on MAPbI<sub>3</sub> NRs:** The ferroelectric nature of MAPbI<sub>3</sub> NRs allows the fabrication of self-powered photodetectors for wearable and portable electronics lacking external power sources. **Figure 3.16a** and **Figure 3.17** demonstrate the specific detectivity and photoresponsivity of MAPbI<sub>3</sub> NR photodetectors, revealing their zero-bias photodetection capability over a broad spectral range (UV to 800 nm). The MAPbI<sub>3</sub> NRs photodetectors exhibited quite high specific detectivity of  $1.76 \times 10^{11}$  Jones under illumination of 300 nm light even without external bias. Moreover, the photoresponsivity of  $2.2 \text{ mA W}^{-1}$  observed under illumination with 300 nm light (Figure 3.17) was comparable to that of self-powered photodetectors based on the Schottky junction of MAPbBr<sub>3</sub>.<sup>[40]</sup> Moreover, the spontaneous polarization of ferroelectric MAPbI<sub>3</sub> in MAPbI<sub>3</sub> NR photodetectors leads to the generation of built-in electrical potential even in the absence of an external bias, which results in self-powered light detection capability based on the self-separation of photogenerated electron-hole pairs at zero bias.<sup>[41]</sup> To verify the ferroelectric nature of MAPbI<sub>3</sub> films, we investigated their local hysteresis loops using switching spectroscopy piezoresponse force microscopy (SS-PFM). Figure 3.16b clearly shows that the ferroelectric nature of the MAPbI<sub>3</sub> film resulted in phase switching hysteresis and the appearance of amplitude butterfly loops with local coercive voltages of  $\approx +0.5$  and  $+2$  V.

Another advantage of MAPbI<sub>3</sub> NR photodetectors is the unidirectional alignment of patterned NR arrays, which allows polarization-sensitive photodetection. Figure 3.16c shows the variation of photocurrent with the polarization angle relative to the anisotropic alignment of MAPbI<sub>3</sub> NR arrays. In these measurements, the polarization angle of incident light (AM 1.5G filter, 74.79 mW·cm<sup>-2</sup>) was varied by rotating the optical polarizer in intervals of 10°, and maximal photocurrent was observed at a polarization angle of 0° (i.e., when polarization was parallel to the axial direction of MAPbI<sub>3</sub> NR arrays). As shown in Figure 3.16d, the photocurrent gradually decreased as increasing the polarization angle with linear sensitivity of -6.09 pA/°. The measured peak-to-valley ratio of 1.44 was higher than that of single-crystalline MAPbI<sub>3</sub> nanowires (1.3).<sup>[19]</sup> Based on the obtained results, we expect that the polarization sensitivity can be further improved by utilizing light with a specific wavelength below the width of MAPbI<sub>3</sub> NRs instead of white light.

### 3.4 Conclusions

In summary, we successfully fabricated high-performance multifunctional and flexible photodetectors capable of self-powered and polarization-sensitive light detection based on hierarchically structured perovskite NR arrays. The hierarchical MAPbI<sub>3</sub> NR arrays with controlled internal nanorod structures were simply prepared by proper coordination engineering of perovskite precursor solution and toluene drip treatment process. The hierarchical MAPbI<sub>3</sub> NRs arrays exhibited enhanced light absorption and contained fewer charge trap states, thus featuring higher photoresponsivity than MAPbI<sub>3</sub> film. In addition, the hierarchical MAPbI<sub>3</sub> NRs based flexible photodetectors on ultrathin PI showed stable photoresponse under extremely high bending curvature, which are promising for future wearable and skin-attachable optoelectronics. Moreover, the ferroelectricity and highly anisotropic alignment of MAPbI<sub>3</sub> NR arrays are capable of self-powered and polarization-sensitive photodetectors, which can find applications in advanced optoelectronic devices requiring effective photon management and multifunctionalities.

### 3.5 References

- [1] Lopez-Sanchez, O.; Lembke, D.; Kayci, M.; Radenovic, A.; Kis, A. Ultrasensitive Photodetectors Based on Monolayer MoS<sub>2</sub>. *Nat. Nanotechnol.* **2013**, *8*, 497–501.
- [2] Wang, X.; Wang, P.; Wang, J.; Hu, W.; Zhou, X.; Guo, N.; Huang, H.; Sun, S.; Shen, H.; Lin, T.; Tang, M.; Liao, L.; Jiang, A.; Sun, J.; Meng, X.; Chen, X.; Lu, W.; Chu, J. Ultrasensitive and Broadband MoS<sub>2</sub> Photodetector Driven by Ferroelectrics. *Adv. Mater.* **2015**, *27*, 6575–6581.
- [3] Wang, Q.; Li, C. Z.; Ge, S.; Li, J. G.; Lu, W.; Lai, J.; Liu, X.; Ma, J.; Yu, D. P.; Liao, Z. M.; Sun, D. Ultrafast Broadband Photodetectors Based on Three-Dimensional Dirac Semimetal Cd<sub>3</sub>As<sub>2</sub>. *Nano Lett.* **2017**, *17*, 834–841.
- [4] Tian, W.; Wang, Y.; Chen, L.; Li, L. Self-Powered Nanoscale Photodetectors. *Small* **2017**, *13*,

1701848.

- [5] Yuan, H.; Liu, X.; Afshinmanesh, F.; Li, W.; Xu, G.; Sun, J.; Lian, B.; Curto, A. G.; Ye, G.; Hikita, Y.; Shen, Z.; Zhang, S. C.; Chen, X.; Brongersma, M.; Hwang, H. Y.; Cui, Y. Polarization-Sensitive Broadband Photodetector Using a Black Phosphorus Vertical P-N Junction. *Nat. Nanotechnol.* **2015**, *10*, 707–713.
- [6] Cao, L.; White, J. S.; Park, J. S.; Schuller, J. A.; Clemens, B. M.; Brongersma, M. L. Engineering Light Absorption in Semiconductor Nanowire Devices. *Nat. Mater.* **2009**, *8*, 643–647.
- [7] Feng, J.; Yan, X.; Liu, Y.; Gao, H.; Wu, Y.; Su, B.; Jiang, L. Crystallographically Aligned Perovskite Structures for High-Performance Polarization-Sensitive Photodetectors. *Adv. Mater.* **2017**, *29*, 1605993.
- [8] Xie, C.; Yan, F. Flexible Photodetectors Based on Novel Functional Materials. *Small* **2017**, *13*, 1701822.
- [9] Chen, H.; Liu, H.; Zhang, Z.; Hu, K.; Fang, X. Nanostructured Photodetectors: From Ultraviolet to Terahertz. *Adv. Mater.* **2016**, *28*, 403–433.
- [10] Sun, K.; Jing, Y.; Park, N.; Li, C.; Bando, Y.; Wang, D. Solution Synthesis of Large-Scale, High-Sensitivity ZnO/Si Hierarchical Nanoheterostructure Photodetectors. *J. Am. Chem. Soc.* **2010**, *132*, 15465–15467.
- [11] Lim, S.; Um, D.-S.; Ha, M.; Zhang, Q.; Lee, Y.; Lin, Y.; Fan, Z.; Ko, H. Broadband Omnidirectional Light Detection in Flexible and Hierarchical ZnO/Si Heterojunction Photodiodes. *Nano Res.* **2017**, *10*, 22–36.
- [12] Wang, H.-P.; He, J.-H. Toward Highly Efficient Nanostructured Solar Cells Using Concurrent Electrical and Optical Design. *Adv. Energy Mater.* **2017**, *7*, 1602385.
- [13] Gao, P.; Grätzel, M.; Nazeeruddin, M. K. Organohalide Lead Perovskites for Photovoltaic Applications. *Energy Environ. Sci.* **2014**, *7*, 2448–2463.
- [14] Xiao, Z.; Kerner, R. A.; Zhao, L.; Tran, N. L.; Lee, K. M.; Koh, T.-W.; Scholes, G. D.; Rand, B. P. Efficient Perovskite Light-Emitting Diodes Featuring Nanometre-Sized Crystallites. *Nat. Photonics* **2017**, *11*, 108–115.
- [15] Dou, L.; Yang, Y. M.; You, J.; Hong, Z.; Chang, W. H.; Li, G.; Yang, Y. Solution-Processed Hybrid Perovskite Photodetectors with High Detectivity. *Nat. Commun.* **2014**, *5*, 5404.
- [16] Zhao, Y.; Zhu, K. Organic-Inorganic Hybrid Lead Halide Perovskites for Optoelectronic and Electronic Applications. *Chem. Soc. Rev.* **2016**, *45*, 655–689.
- [17] Lyashenko, D.; Perez, A.; Zakhidov, A. High-Resolution Patterning of Organohalide Lead Perovskite Pixels for Photodetectors Using Orthogonal Photolithography. *Phys. Status Solidi A* **2017**, *214*, 1600302.
- [18] Horvath, E.; Spina, M.; Szekrenyes, Z.; Kamaras, K.; Gaal, R.; Gachet, D.; Forro, L. Nanowires of Methylammonium Lead Iodide (CH<sub>3</sub>NH<sub>3</sub>PbI<sub>3</sub>) Prepared by Low Temperature Solution-Mediated

Crystallization. *Nano Lett.* **2014**, *14*, 6761–6766.

- [19] Gao, L.; Zeng, K.; Guo, J.; Ge, C.; Du, J.; Zhao, Y.; Chen, C.; Deng, H.; He, Y.; Song, H.; Niu, G.; Tang, J. Passivated Single-Crystalline  $\text{CH}_3\text{NH}_3\text{PbI}_3$  Nanowire Photodetector with High Detectivity and Polarization Sensitivity. *Nano Lett.* **2016**, *16*, 7446–7454.
- [20] Lee, L.; Baek, J.; Park, K. S.; Lee, Y. E.; Shrestha, N. K.; Sung, M. M. Wafer-Scale Single-Crystal Perovskite Patterned Thin Films Based on Geometrically-Confined Lateral Crystal Growth. *Nat. Commun.* **2017**, *8*, 15882.
- [21] Deng, H.; Yang, X.; Dong, D.; Li, B.; Yang, D.; Yuan, S.; Qiao, K.; Cheng, Y. B.; Tang, J.; Song, H. Flexible and Semitransparent Organolead Triiodide Perovskite Network Photodetector Arrays with High Stability. *Nano Lett.* **2015**, *15*, 7963–7969.
- [22] Zhang, Y.; Du, J.; Wu, X.; Zhang, G.; Chu, Y.; Liu, D.; Zhao, Y.; Liang, Z.; Huang, J. Ultrasensitive Photodetectors Based on Island-Structured  $\text{CH}_3\text{NH}_3\text{PbI}_3$  Thin Films. *ACS Appl. Mater. Interfaces* **2015**, *7*, 21634–21638.
- [23] Gisin, N.; Ribordy, G.; Tittel, W.; Zbinden, H. Quantum Cryptography. *Rev. Mod. Phys.* **2002**, *74*, 145–195.
- [24] Tyo, J. S.; Goldstein, D. L.; Chenault, D. B.; Shaw, J. A. Review of Passive Imaging Polarimetry for Remote Sensing Applications. *Appl. Opt.* **2006**, *45*, 5453–5469.
- [25] Salomatina-Motts, E.; Neel, V. A.; Yaroslavskaya, A. N. Multimodal Polarization System for Imaging Skin Cancer. *Opt. Spectrosc.* **2009**, *107*, 884–890.
- [26] Jacques, S. L.; Ramella-Roman, J. C.; Lee, K. Imaging Skin Pathology with Polarized Light. *J. Biomed. Opt.* **2002**, *7*, 329–340.
- [27] Wang, H.; Haroldson, R.; Balachandran, B.; Zakhidov, A.; Sohal, S.; Chan, J. Y.; Zakhidov, A.; Hu, W. Nanoimprinted Perovskite Nanograting Photodetector with Improved Efficiency. *ACS Nano* **2016**, *10*, 10921–10928.
- [28] Cefarin, N.; Cian, A.; Sonato, A.; Sovernigo, E.; Suran, F.; Teklu, Z.; Zanut, A.; Pozzato, A.; Tormen, M. Nanostructuring Methylammonium Lead Iodide Perovskite by Ultrafast Nano Imprinting Lithography. *Microelectron. Eng.* **2017**, *176*, 106–110.
- [29] Mao, J.; Sha, W. E. I.; Zhang, H.; Ren, X.; Zhuang, J.; Roy, V. A. L.; Wong, K. S.; Choy, W. C. H. Novel Direct Nanopatterning Approach to Fabricate Periodically Nanostructured Perovskite for Optoelectronic Applications. *Adv. Funct. Mater.* **2017**, *27*, 1606525.
- [30] Wang, W.; Ma, Y.; Qi, L. High-Performance Photodetectors Based on Organometal Halide Perovskite Nanonets. *Adv. Funct. Mater.* **2017**, *27*, 1603653.
- [31] Jeong, B.; Hwang, I.; Cho, S. H.; Kim, E. H.; Cha, S.; Lee, J.; Kang, H. S.; Cho, S. M.; Choi, H.; Park, C. Solvent-Assisted Gel Printing for Micropatterning Thin Organic-Inorganic Hybrid Perovskite Films. *ACS Nano* **2016**, *10*, 9026–9035.
- [32] Liu, P.; He, X.; Ren, J.; Liao, Q.; Yao, J.; Fu, H. Organic-Inorganic Hybrid Perovskite Nanowire



Laser Arrays. *ACS Nano* **2017**, *11*, 5766–5773.

[33] Hwang, J. K.; Cho, S.; Dang, J. M.; Kwak, E. B.; Song, K.; Moon, J.; Sung, M. M. Direct Nanoprinting by Liquid-Bridge-Mediated Nanotransfer Moulding. *Nat. Nanotechnol.* **2010**, *5*, 742–748.

[34] Yan, K.; Long, M.; Zhang, T.; Wei, Z.; Chen, H.; Yang, S.; Xu, J. Hybrid Halide Perovskite Solar Cell Precursors: Colloidal Chemistry and Coordination Engineering Behind Device Processing for High Efficiency. *J. Am. Chem. Soc.* **2015**, *137*, 4460–4468.

[35] Jeon, N. J.; Noh, J. H.; Kim, Y. C.; Yang, W. S.; Ryu, S.; Seok, S. I. Solvent Engineering for High-Performance Inorganic-Organic Hybrid Perovskite Solar Cells. *Nat. Mater.* **2014**, *13*, 897–903.

[36] Cohen, B.-E.; Aharon, S.; Dymshits, A.; Etgar, L. Impact of Antisolvent Treatment on Carrier Density in Efficient Hole-Conductor-Free Perovskite-Based Solar Cells. *J. Phys. Chem. C* **2016**, *120*, 142–147.

[37] Kara, K.; Kara, D. A.; Kirbıyık, C.; Ersoz, M.; Usluer, O.; Briseno, A. L.; Kus, M. Solvent Washing with Toluene Enhances Efficiency and Increases Reproducibility in Perovskite Solar Cells. *RSC Adv.* **2016**, *6*, 26606–26611.

[38] Senanayak, S. P.; Yang, B.; Thomas, T. H.; Giesbrecht, N.; Huang, W.; Gann, E.; Nair, B.; Goedel, K.; Guha, S.; Moya, X.; McNeill, C. R.; Docampo, P.; Sadhanala, A.; Friend, R. H.; Siringhaus, H. Understanding Charge Transport in Lead Iodide Perovskite Thin-Film Field-Effect Transistors. *Sci. Adv.* **2017**, *3*, e1601935.

[39] Elumalai, N. K.; Uddin, A. Hysteresis in Organic-Inorganic Hybrid Perovskite Solar Cells. *Sol. Energy Mater. Sol. Cells* **2016**, *157*, 476–509.

[40] Shaikh, P. A.; Shi, D.; Retamal, J. R. D.; Sheikh, A. D.; Haque, M. A.; Kang, C.-F.; He, J.-H.; Bakr, O. M.; Wu, T. Schottky Junctions on Perovskite Single Crystals: Light-Modulated Dielectric Constant and Self-Biased Photodetection. *J. Mater. Chem. C* **2016**, *4*, 8304–8312.

[41] Xiao, Z.; Yuan, Y.; Shao, Y.; Wang, Q.; Dong, Q.; Bi, C.; Sharma, P.; Gruverman, A.; Huang, J. Giant Switchable Photovoltaic Effect in Organometal Trihalide Perovskite Devices. *Nat. Mater.* **2015**, *14*, 193–198.

[42] Liu, Y.; Li, F.; Perumal Veeramalai, C.; Chen, W.; Guo, T.; Wu, C.; Kim, T. W. Inkjet-Printed Photodetector Arrays Based on Hybrid Perovskite  $\text{CH}_3\text{NH}_3\text{PbI}_3$  Microwires. *ACS Appl. Mater. Interfaces* **2017**, *9*, 11662–11668.

[43] Lan, C.; Dong, R.; Zhou, Z.; Shu, L.; Li, D.; Yip, S.; Ho, J. C. Large-Scale Synthesis of Freestanding Layer-Structured  $\text{PbI}_2$  and  $\text{MAPbI}_3$  Nanosheets for High-Performance Photodetection. *Adv. Mater.* **2017**, *29*, 1702759.

[44] Hu, X.; Zhang, X.; Liang, L.; Bao, J.; Li, S.; Yang, W.; Xie, Y. High-Performance Flexible Broadband Photodetector Based on Organolead Halide Perovskite. *Adv. Funct. Mater.* **2014**, *24*, 7373–7380.

[45] Ding, J.; Fang, H.; Lian, Z.; Li, J.; Lv, Q.; Wang, L.; Sun, J.-L.; Yan, Q. A Self-Powered Photodetector Based on a  $\text{CH}_3\text{NH}_3\text{PbI}_3$  Single Crystal with Asymmetric Electrodes. *CrystEngComm* **2016**, *18*, 4405–4411.

[46] Leung, S. F.; Ho, K. T.; Kung, P. K.; Hsiao, V. K. S.; Alshareef, H. N.; Wang, Z. L.; He, J. H. A Self-Powered and Flexible Organometallic Halide Perovskite Photodetector with Very High Detectivity. *Adv. Mater.* **2018**, *30*, 1704611.

\*\*Reprinted in part with permission from S. Lim<sup>†</sup>, M. Ha<sup>†</sup>, and H. Ko<sup>\*</sup> *et al.*, *Adv. Optical Mater.* **2018**, *6*, 1800615. Copyright © 2018, WILEY-VCH Verlag GmbH & Co. KGaA, Weinheim

**Table 3.1** Comparison of results achieved this work and previously reported MAPbI<sub>3</sub> based photodetectors excluding hybrid structures.

Perovskite morphology	Device structure	Responsivity	Detectivity (Jones)	Response time	Detection Range (nm)	Operation voltage	Flexibility	Self-powered detection	Polarization sensitivity
Island-structured thin film <sup>[22]</sup>	Photoconductive	–	–	40 ms	400–800	30 V	–	–	–
Micropatterned thin film <sup>[31]</sup>	Photoconductive	–	–	100 ms	450–800	5 V	–	–	–
Microwires <sup>[42]</sup>	Photoconductive	1.2 A/W at 100 $\mu$ W/cm <sup>2</sup>	$2.39 \times 10^{12}$	10 ms	630	2 V	–	–	–
Thin film with nanograting <sup>[27]</sup>	Photoconductive	3.23 A/W at 1 $\mu$ W/cm <sup>2</sup>	–	–	466, 635	1 V	–	–	–
Nanosheets <sup>[43]</sup>	Photoconductive	410 mA/W at few $\mu$ W/cm <sup>2</sup>	$3.1 \times 10^{11}$	86 ms	405	5 V	–	–	–
Nanonets <sup>[30]</sup>	Photoconductive	10.33 A/W at 28 $\mu$ W/cm <sup>2</sup>	–	20 ms	700	10 V	–	–	–
Networks <sup>[21]</sup>	Photoconductive	0.1 A/W at 100 $\mu$ W/cm <sup>2</sup>	$1.02 \times 10^{11}$	0.3 ms	650	10 V	up to 80°	–	–
Polycrystalline thin film <sup>[44]</sup>	Schottky diode	3.49 A/W (365 nm), 36.7 mA/W (780 nm) at 10 mW/cm <sup>2</sup>	–	0.2 s	300–780	3 V	Flexible	–	–
Bulk single crystal <sup>[45]</sup>	Schottky diode	23.2 mA/W at 38 mW/cm <sup>2</sup>	–	71 ms	375–808	0 V	–	0.24 A/W at 10 nW/cm <sup>2</sup> , 23.2 mA/W at 38 mW/cm <sup>2</sup>	–
Polycrystalline thin film <sup>[46]</sup>	Photoconductive	0.418 A/W at 10 mW/cm <sup>2</sup>	$1.22 \times 10^{13}$	80 ms	White light	1 V	up to 90°	79.4 V/mW·cm <sup>2</sup>	–
Single crystal nanowire <sup>[19]</sup>	Photoconductive	4.95 A/W at hundreds $\mu$ W/cm <sup>2</sup>	$2 \times 10^{13}$	0.1 ms	400–800	1 V	–	–	Peak-to-valley ratio = 1.3
<b>Hierarchical nanoribbon [This work]</b>	Photoconductive	<b>38.9 mA/W at 38.5 <math>\mu</math>W/cm<sup>2</sup></b>	<b><math>8.21 \times 10^{11}</math></b>	<b>27 ms</b>	<b>300–800</b>	<b>2 V, 0 V</b>	<b><math>r_B &lt; 3.7</math> mm</b>	<b>2.2 mA/W, 1.76 <math>\times 10^{11}</math> Jones</b>	<b>Peak-to-valley ratio = 1.44, Sensitivity = -6.08 pA/°</b>

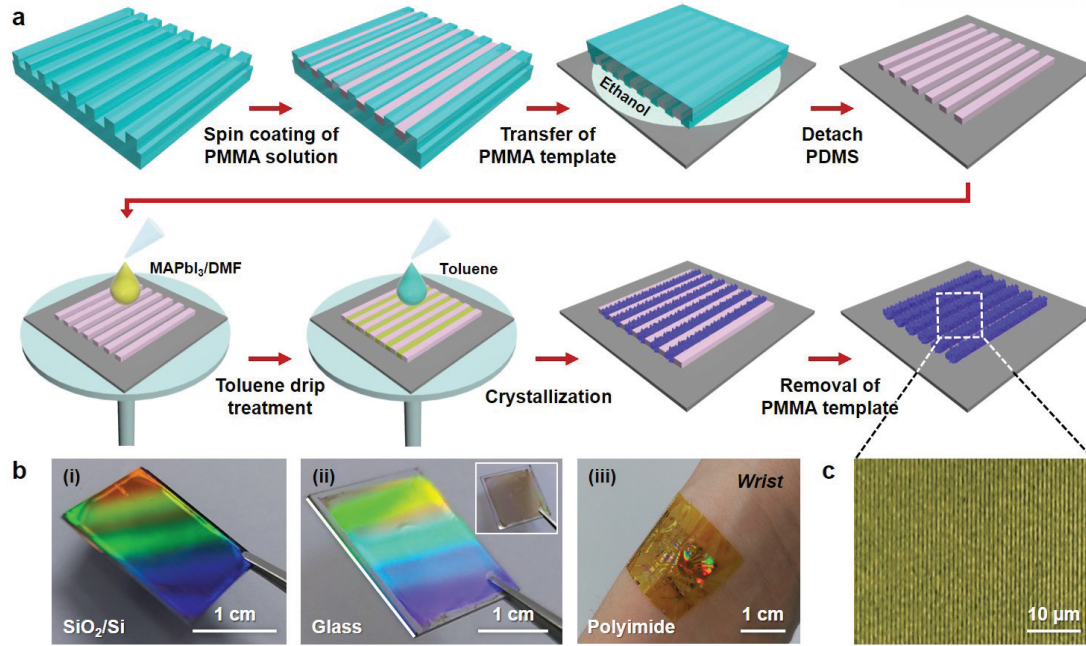


**Figure 3.1** Fabrication of large-area and highly aligned hierarchical MAPbI<sub>3</sub> nanoribbon (NR) arrays. (a) Schematic illustration of the fabrication of MAPbI<sub>3</sub> NR arrays on the arbitrary substrates. (b) Photograph of large-area MAPbI<sub>3</sub> NR arrays on (i) SiO<sub>2</sub>/Si (2 cm × 1.5 cm), (ii) glass (2.5 cm × 2.5 cm, inset image shows nonreflected sample). (iii) MAPbI<sub>3</sub> NRs based flexible photodetectors on polyimide (PI) substrate attached to wrist. (c) Optical microscopy (OM) image of large-area MAPbI<sub>3</sub> NR arrays on SiO<sub>2</sub>/Si substrate.

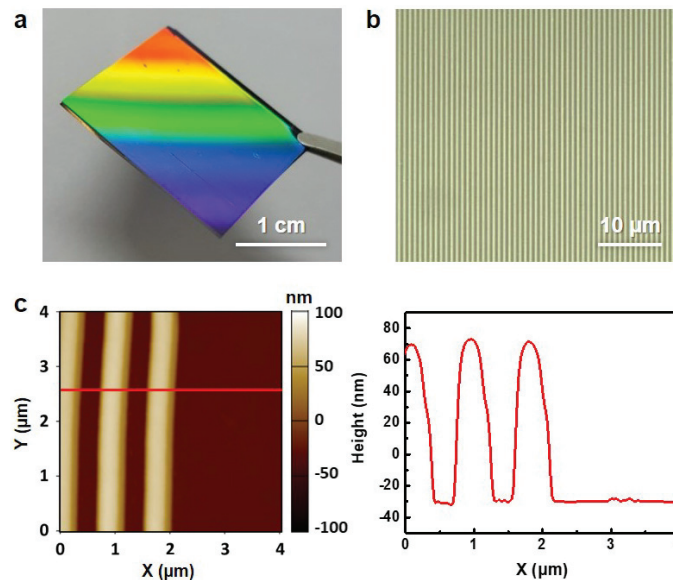


**Figure 3.2** Detailed information about PMMA nanotemplates. (a) Photograph of PMMA nanotemplates on SiO<sub>2</sub>/Si substrate. (b) Optical microscopy (OM) image of PMMA nanotemplates on SiO<sub>2</sub>/Si substrate. (c) Atomic force microscopy (AFM) image of PMMA nanotemplates on SiO<sub>2</sub>/Si substrate. The height of PMMA nanotemplate is 100 nm.

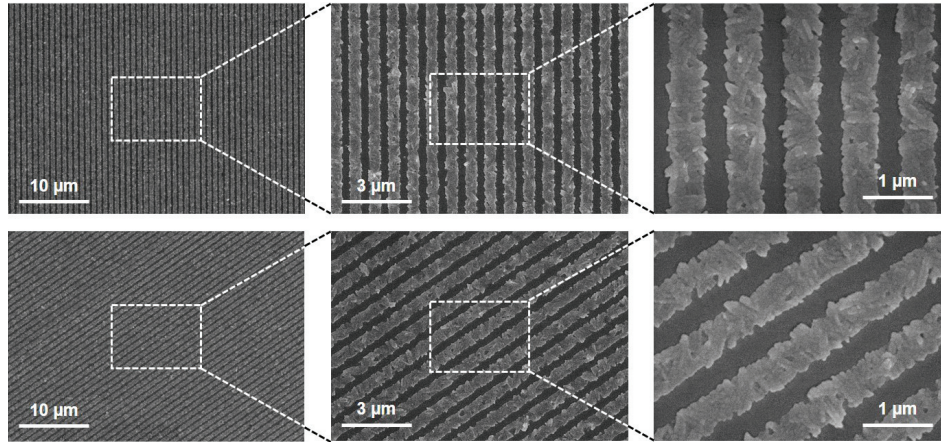


**Figure 3.3** SEM images of large-area and highly aligned MAPbI<sub>3</sub> NR arrays after removal of PMMA nanotemplates.

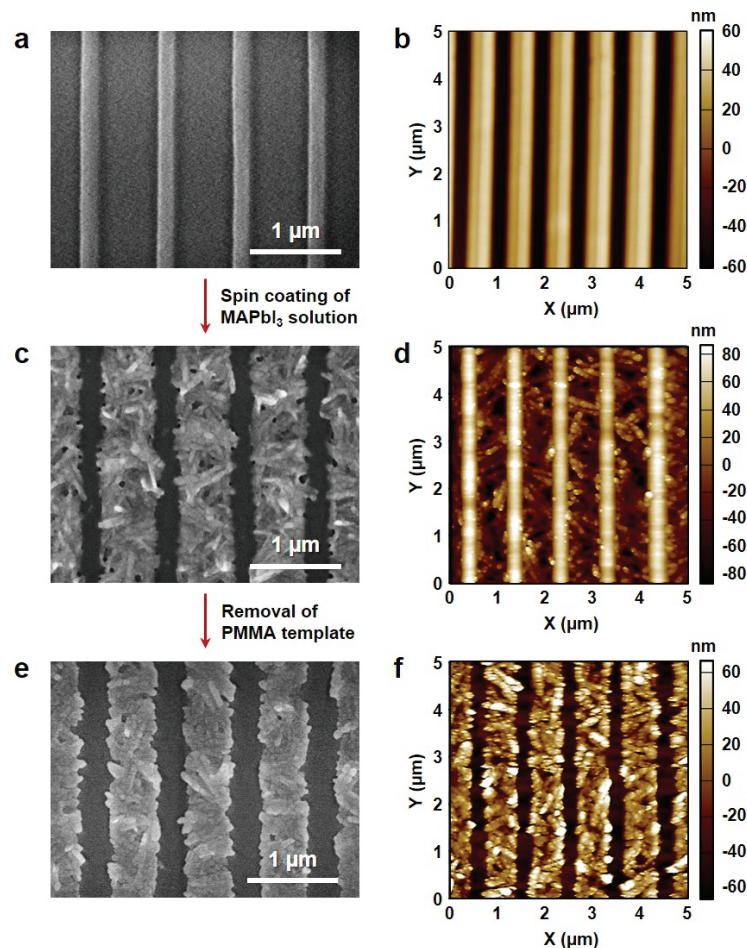


**Figure 3.4** Detailed fabrication process for hierarchical MAPbI<sub>3</sub> NR arrays. (a) Scanning electron microscopy (SEM) image and (b) atomic force microscopy (AFM) image of transferred PMMA nanotemplates on SiO<sub>2</sub>/Si substrate. (c) SEM image and (d) AFM image of MAPbI<sub>3</sub> NRs with PMMA nanotemplates. (e) SEM image and (f) AFM image of MAPbI<sub>3</sub> NRs after removal of PMMA nanotemplates by 1 h dipping in toluene.

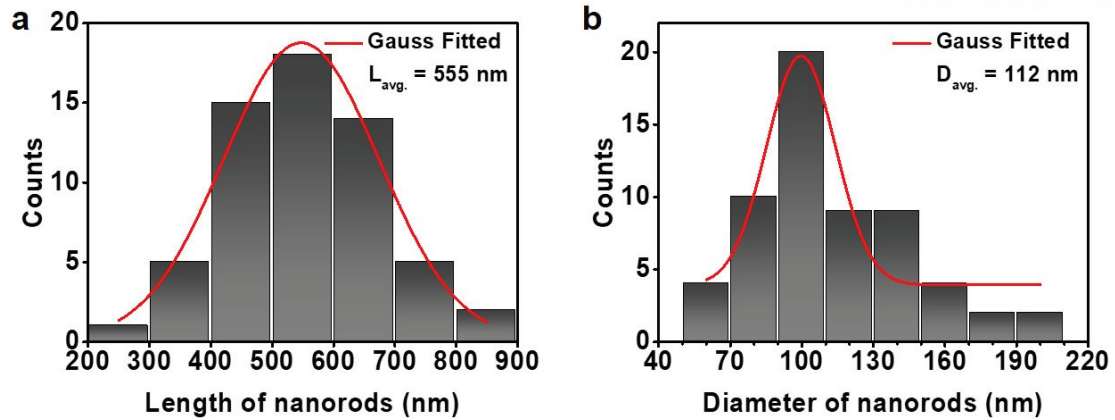


**Figure 3.5** The size of internal nanorods in hierarchical MAPbI<sub>3</sub> NR arrays. Statistics for (a) length and (b) thickness of internal nanorods.

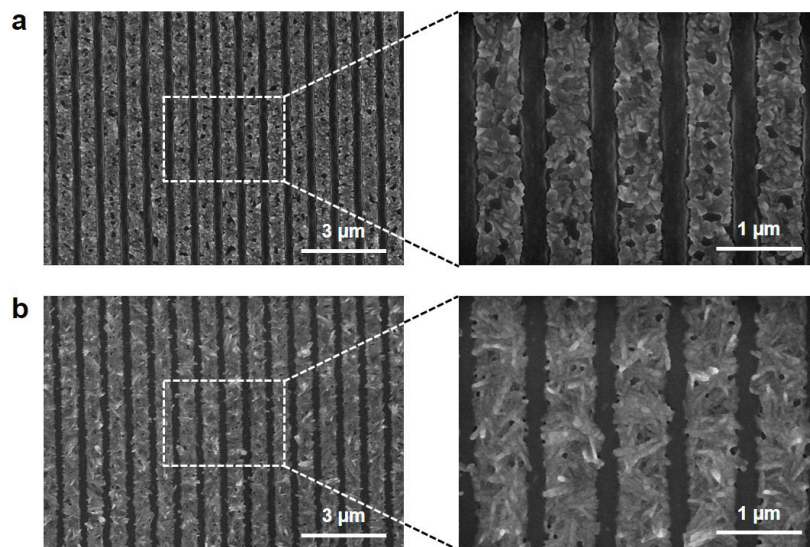


**Figure 3.6** Different morphologies of MAPbI<sub>3</sub> NRs according to the toluene drip treatment. SEM images of (a) MAPbI<sub>3</sub> NRs without toluene drip treatment and (b) MAPbI<sub>3</sub> NRs with toluene drip treatment.

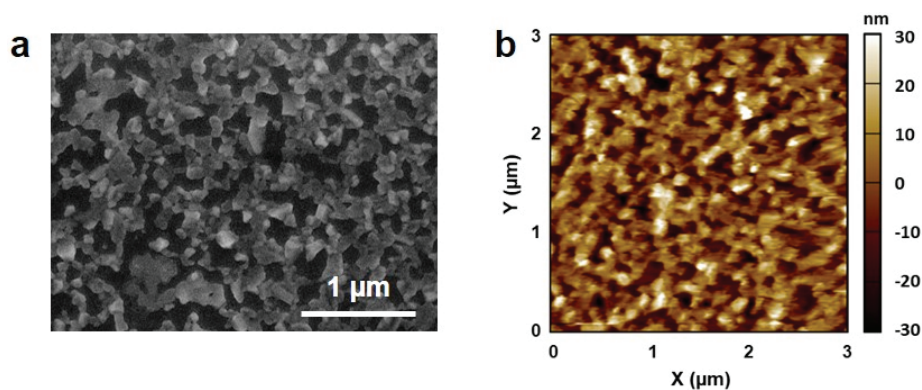


**Figure 3.7** Surface morphology of MAPbI<sub>3</sub> film on a planar substrate. (a) SEM and (b) AFM images of MAPbI<sub>3</sub> film.

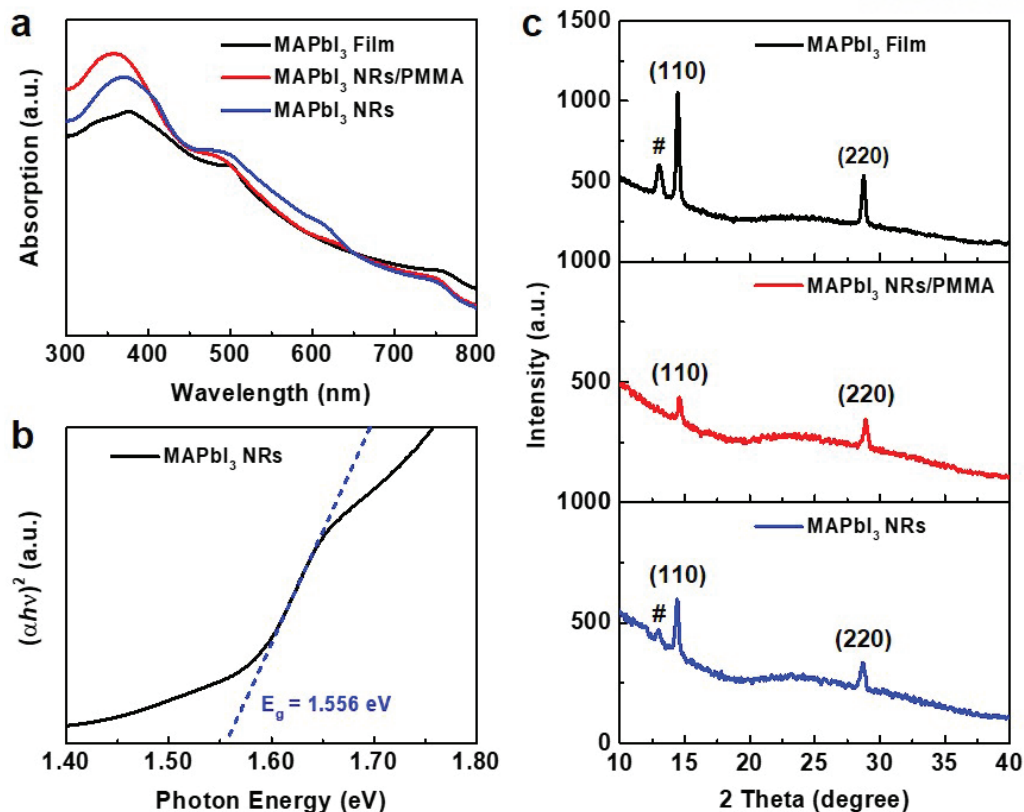


**Figure 3.8** The comparison of MAPbI<sub>3</sub> film and NR arrays in terms of optical property and crystallinity. (a) UV-vis absorption spectra of MAPbI<sub>3</sub> film, MAPbI<sub>3</sub> NRs with PMMA nanotemplates, and MAPbI<sub>3</sub> NRs after removal of PMMA nanotemplates. (b) Tauc plot of MAPbI<sub>3</sub> NRs to calculate optical band gap from the result of transmittance. (c) X-ray diffraction spectra of MAPbI<sub>3</sub> film, MAPbI<sub>3</sub> NRs with PMMA nanotemplates, and MAPbI<sub>3</sub> NRs after removal of PMMA nanotemplates.

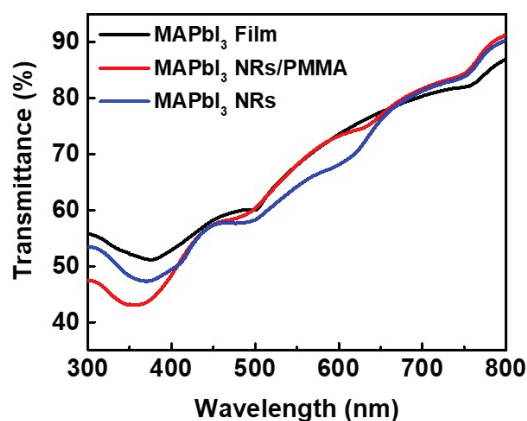


**Figure 3.9** UV-vis transmittance spectra of MAPbI<sub>3</sub> film, MAPbI<sub>3</sub> NRs with PMMA nanotemplates, and MAPbI<sub>3</sub> NRs after removal of PMMA nanotemplates.

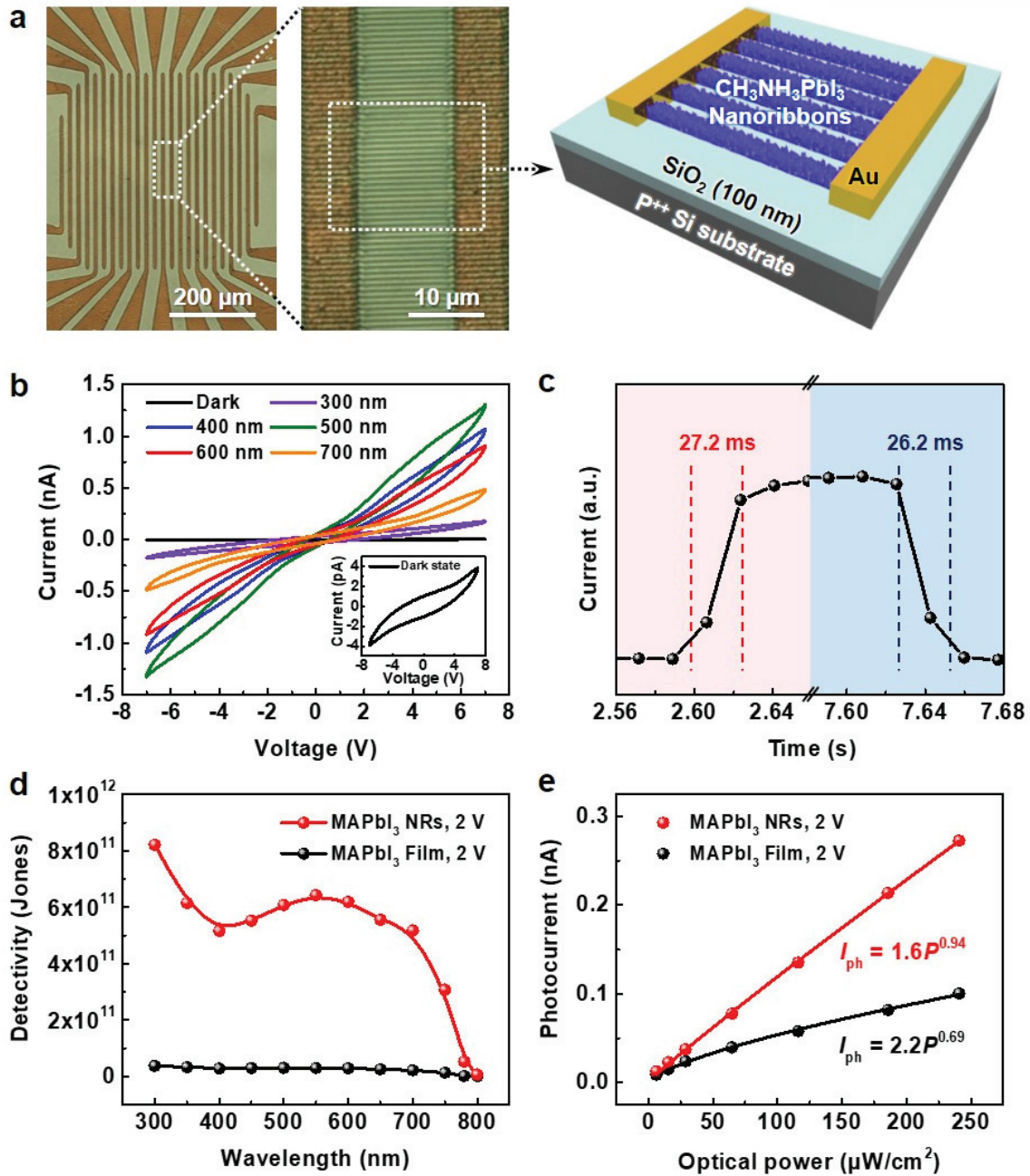


**Figure 3.10** Optoelectronic properties of hierarchical MAPbI<sub>3</sub> NRs based photodetectors. (a) OM images and schematic illustration of hierarchical MAPbI<sub>3</sub> NRs based photodetectors on SiO<sub>2</sub>/Si substrate. (b)  $I$ - $V$  curves of a MAPbI<sub>3</sub> NRs based photodetector in the voltage range from -7 to 7 V under dark condition and with illumination at 5 different wavelengths. (c) Photoresponsive rise and decay times of a MAPbI<sub>3</sub> NRs based photodetector under light illumination ( $\lambda = 500$  nm;  $P = 383.9$   $\mu\text{W}\cdot\text{cm}^{-2}$ ) at an applied voltage of 2 V. (d) Spectral specific detectivity of MAPbI<sub>3</sub> film and NRs based photodetectors from 300 to 800 nm wavelength range at an applied voltage of 2 V. (e) Dependence of photoresponse on different illumination intensities under illumination of 500 nm light at an applied voltage of 2 V.



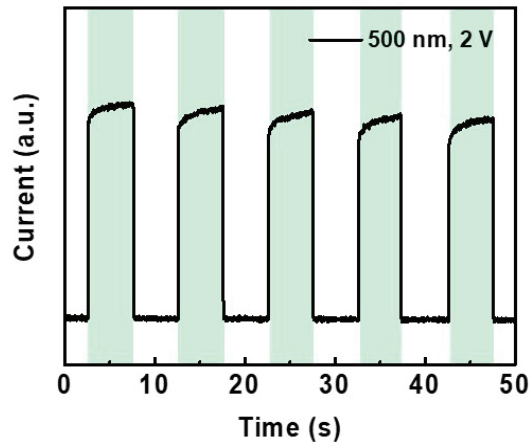


**Figure 3.11** Stable photoswitching behavior of a MAPbI<sub>3</sub> NRs based photodetector under repeated on/off light illumination ( $\lambda = 500$  nm;  $P = 383.9 \mu\text{W}\cdot\text{cm}^{-2}$ ) at an applied voltage of 2 V.

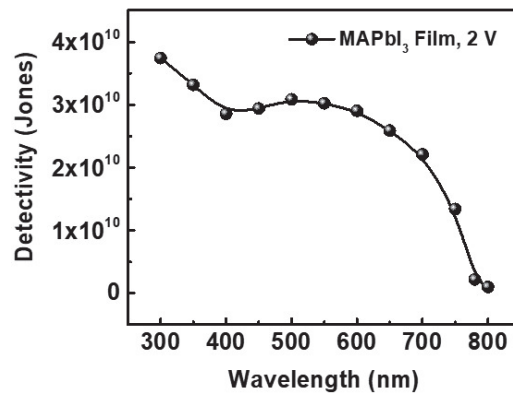


**Figure 3.12** Spectral specific detectivity of MAPbI<sub>3</sub> film based photodetectors at an applied voltage of 2 V.

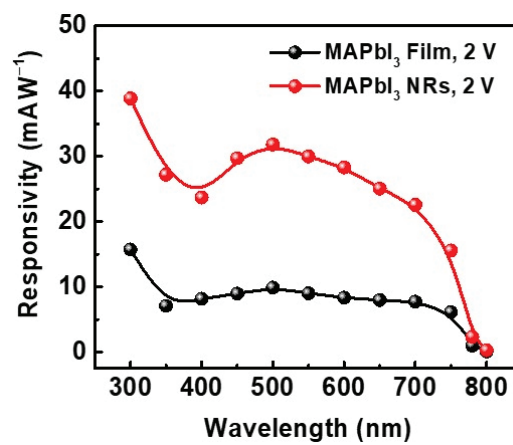


**Figure 3.13** Spectral photoresponsivity of MAPbI<sub>3</sub> film and NRs based photodetectors from 300 to 800 nm wavelength range at an applied voltage of 2 V.

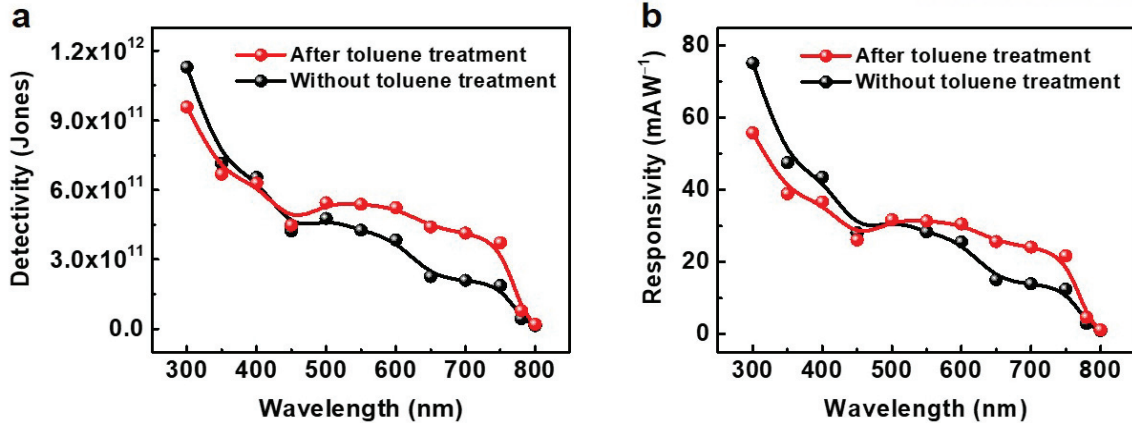


**Figure 3.14** (a) Spectral specific detectivity and (b) photoresponsivity of MAPbI<sub>3</sub> NR photodetectors before and after the toluene drip treatment at an applied voltage of 2 V.

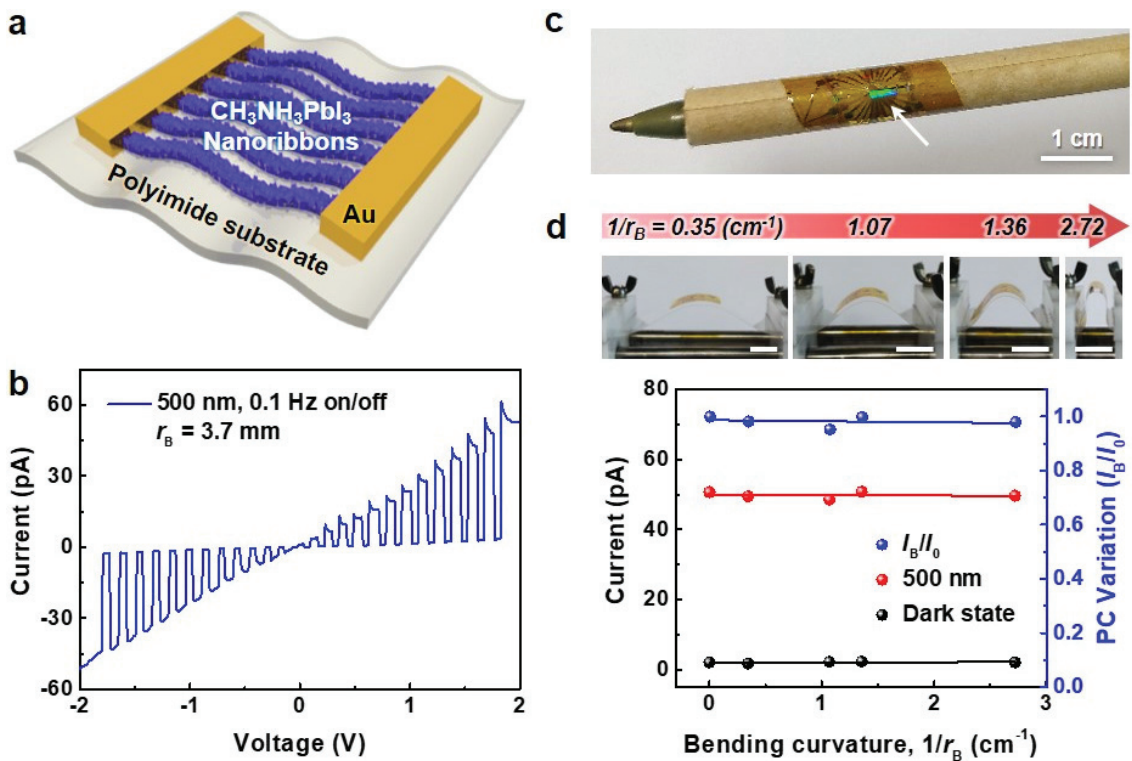


**Figure 3.15** Mechanical flexibility of MAPbI<sub>3</sub> NRs based photodetectors on PI substrate. (a) Schematic illustration of hierarchical MAPbI<sub>3</sub> NRs based flexible photodetectors on PI substrate. (b) Time-dependent  $I$ - $V$  curve of flexible MAPbI<sub>3</sub> NRs based photodetectors with 0.1 Hz switching of 500 nm light in the voltage range from -2 to 2 V. (c) Digital image of rolled flexible MAPbI<sub>3</sub> NRs based photodetectors on pen with  $r_B = 3.7$  mm. (d) Current variation of MAPbI<sub>3</sub> NRs photodetectors under dark and illumination states according to the bending curvature (scale bar: 1 cm).

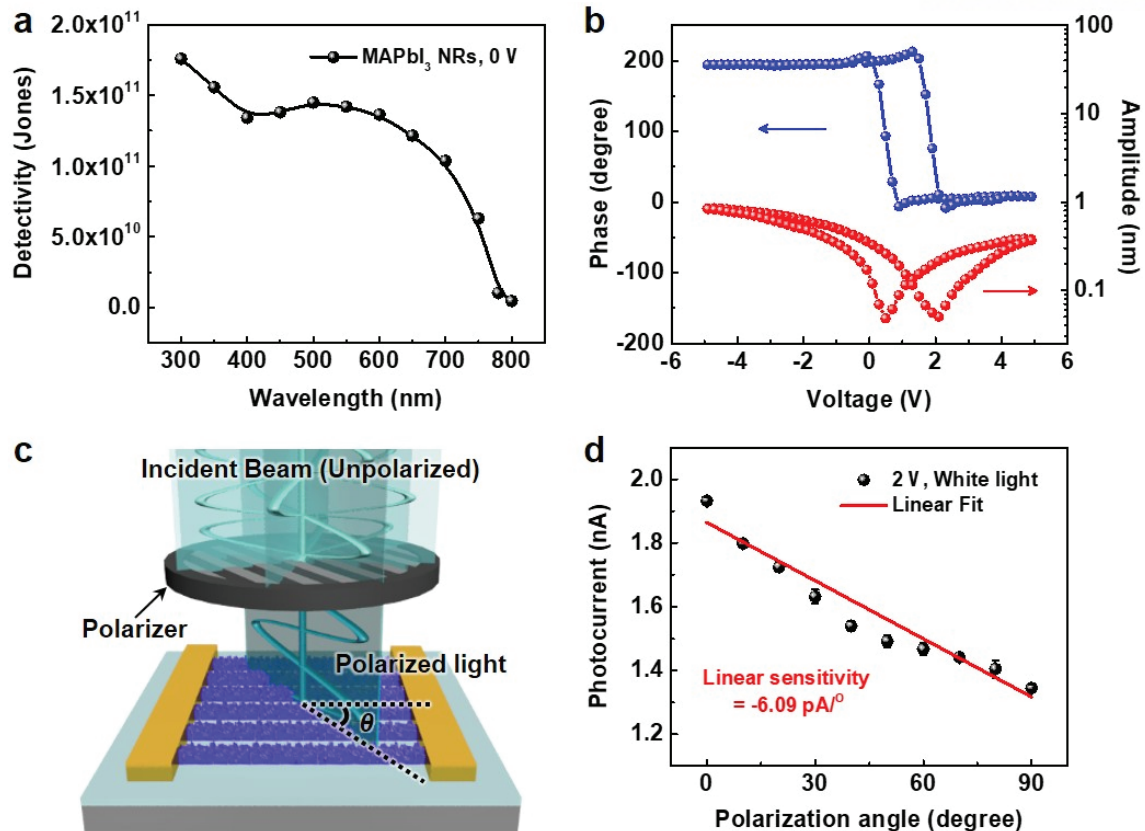


**Figure 3.16** Self-powered and polarization sensitive light-detection capability of MAPbI<sub>3</sub> NRs based photodetectors. (a) Spectral specific detectivity of MAPbI<sub>3</sub> NRs based photodetectors from 300 to 800 nm wavelength range without an applied voltage. (b) Local piezoresponse force microscopy (PFM) hysteresis loops of MAPbI<sub>3</sub> film (blue: phase signal, red: amplitude signal). (c) Schematic illustration of polarization-sensitive photodetectors based on MAPbI<sub>3</sub> NRs. (d) Dependence of photoresponse on different polarization angle (parallel to NRs: 0°, vertical to NRs: 90°) under illumination of white light ( $P = 74.79 \text{ mW} \cdot \text{cm}^{-2}$ ) at an applied voltage of 2 V.

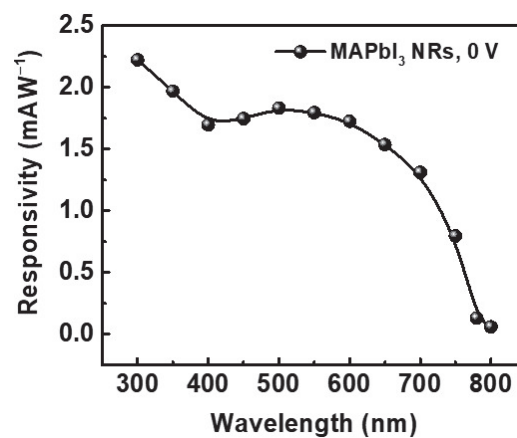


**Figure 3.17** Spectral photoresponsivity of MAPbI<sub>3</sub> NRs based photodetectors from 300 to 800 nm wavelength range without an applied voltage.

## Chapter 4. Skin-Inspired Hierarchical Polymer Architectures with Gradient Stiffness for Space-Free, Ultrathin, and Highly Sensitive Triboelectric Sensors

### 4.1 Introduction

Recently, significant interests in the internet of things (IoT) has boosted the rapid development of flexible, wearable, and skin-attachable electronics, including artificial skins,<sup>[1-3]</sup> human-machine interface systems,<sup>[4, 5]</sup> sustainable power management,<sup>[6-9]</sup> and wireless signal transduction.<sup>[10-12]</sup> For the practical applications of wearable electronics in the fields of IoT, long-term sustainability as well as highly flexible, lightweight, and miniaturized designs are required to provide convenience and comfortable feelings for users as well as to achieve reliable and human friendly electrical devices and sensors. Even though great progress has been made in wearable platforms integrated with flexible, stretchable, and sustainable power systems,<sup>[6, 8, 9]</sup> energy storage systems still remain premature and insufficient for practical use because of the impermanent lifetime, limited capacity, and safety issues for the highly flexible and deformable designs of wearable devices.<sup>[13]</sup> On the other hand, self-powered wearable devices, which can generate power by harvesting ambient energy sources such as kinetic energy from human daily motion and thermal energy from body temperature, show great potential to address power issues in wearable electronics.<sup>[7, 14-18]</sup>

To convert human bodily energy into available electricity, a variety of energy conversion systems have been developed based on piezoelectric,<sup>[15-17]</sup> thermoelectric,<sup>[18]</sup> electromagnetic,<sup>[19]</sup> and triboelectric effects.<sup>[19, 20]</sup> Triboelectricity, a common phenomenon of charge generation occurring on the contact surface of two different materials, can be used to effectively convert frictional contact into electricity.<sup>[20]</sup> The triboelectric devices can provide more diverse choices of flexible materials and higher power generation than other energy harvesting ones. In addition, triboelectric devices can be used as self-powered sensors as well to detect pressure and motion. Previously, Jiang *et al.* demonstrated a self-powered tactile sensor based on microtextured poly(dimethylsiloxane) (PDMS), which showed a pressure sensitivity of 2.28 mV/kPa and a maximum power generation of  $\sim 130$  nW.<sup>[21]</sup> Li *et al.* fabricated a dual-mode triboelectric sensor (TES) that perceived a tactile stimuli with the force sensitivity of 0.028 V/N and a generated output voltage of 10.6 V at 140 N.<sup>[22]</sup>

To achieve both high sensitivity and output power, most of the previous TESs utilized bulk spacers,<sup>[22]</sup> arch shapes,<sup>[23]</sup> and 3D structures<sup>[24]</sup> to provide a large variation of gap distance between opposing surfaces, which is proportional to the triboelectric output voltage.<sup>[14, 25, 26]</sup> Although these designs based on high volumetric structures enhanced the performance of triboelectric devices and sensors, the bulky geometry impeded their applications in flexible and wearable devices.<sup>[27]</sup> Recently, ultrathin and flexible TESs that were based on single-electrode device structures were also reported as

motion tracking sensors.<sup>[28, 29]</sup> Nevertheless, the single-electrode based TESs have limited applications in pressure sensors, because the generation of triboelectric charge is not uniform and can be randomly affected by the contact of different charged materials instead of the applied pressure. In addition, the single-electrode-based TES is not a monolithic design which requires additional connections to induction and reference electrodes to provide the potential differences between them,<sup>[30]</sup> still causing the space constraints for use in wearable devices.

Moreover, the voluminous or nonmonolithic designs of triboelectric devices also make the device packaging a challenge for applications in harsh environments. High air conductivity of humid atmosphere causes discharging of triboelectric charges and thus reduces the triboelectric output performances.<sup>[31-34]</sup> In these applications, fully packaged triboelectric devices are necessary for reliable and sustainable wearable devices. To achieve both fully packaged designs having large flexibility and maximal triboelectric charge generation, morphological and structural control of triboelectric materials and devices is highly required for the body-wearable and high-performance self-powered TESs with ultrathin and flexible form factors.

Here, we propose hierarchical nanoporous and interlocked microridge structured polymer architectures with gradient stiffness for developing spacer-free, ultrathin, highly sensitive, and wearable TESs. Mimicking the gradient stiffness between stiff epidermis and soft dermis layers with interlocked microridge structures in human skin, which can induce stress concentration and efficient transfer to underlying mechanoreceptors, we fabricate interlocked and microridge structured polymer architectures based on stiff poly(vinylidene fluoride-trifluoroethylene) (P(VDF-TrFE)) and soft PDMS layers. Introducing the additional nanoporous structures into the interlocked and microridge structured polymers leads to the effective variation of both volume and gap distance between opposing surfaces without the need of additional bulky spacers. The hierarchically structured polymers in flexible TESs allow the device to maximize the triboelectric charge generation for high-output power density ( $\sim 46.7 \mu\text{W}/\text{cm}^2$ ) and enhanced sensitivity ( $0.55 \text{ V}/\text{kPa}$ ). The ultraflexible TESs can be worn on the human body and thus precisely detect human vital signs of minute arterial pulse waves and bodily motion of finger bending. In addition, the fast triboelectric charging/discharging process enables the perception of high-frequency dynamic stimuli from contact vibrations to acoustic waves, resulting in the recognition of a human voice ( $>6 \text{ kHz}$  of frequency range) for the biometric security system. Finally, for applications in harsh environments, the ultrathin and body-wearable TESs can be fully packaged and worn as a bendable smart glove. The fully packaged and bendable TESs not only detect various sign languages by human hand motions but also endure severe humid environments over 90% RH, which are greatly desirable for applications in next-generation wearable electronics such as prosthetic limbs, wearable fitness trackers, and humanoid robots.

## 4.2 Experimental Details

**Fabrication of Materials:** The hierarchical nanoporous and microridge structured P(VDF-TrFE) and PDMS were fabricated by solvent-assisted micromolding method. First, 10 wt% of P(VDF-TrFE) solution was prepared by dissolving the 70/30 P(VDF-TrFE) copolymer powder (PIEZOTECH, France) in acetone and *N,N*-dimethylformamide mixed solvents (1:1 of volume ratio). Also, PDMS prepolymer (Sylgard 184, Dow Corning) and curing agent (Sylgard 184, Dow Corning) with the ratio of 10:1 were mixed using polar solvents of ethanol and deionized water with different volume ratio (ethanol:deionized water = 3:1), where controlling the solvent evaporation rate and surface tension of mixed polar solvents enables the control of porosity in nanoporous PDMS. While P(VDF-TrFE) was homogeneously dissolved in polar solvents, the mixture of PDMS solution made the phase separation between PDMS and polar solvents, generating many bubbles in the solution. The P(VDF-TrFE) and PDMS-based viscous solution was poured into the inverse microridge-patterned Si molds. The inverse microridge structured Si molds having different width and pitch sizes were fabricated by conventional photolithographic technique with dry etching process. In addition, the inverse microridge-patterned Si molds were coated with self-assembled monolayer (SAM, FOTS (1H,1H,2H,2H-perfluorooctyltrichlorosilane)) (AVC-150M, SORONA, Korea) as an anti-adhesion layer for the easy molding of hierarchical microridge structured polymers. During thermal annealing of P(VDF-TrFE) at 140 °C for 2 h and two steps of curing PDMS at 40 °C for 12 h and 90 °C for 1 h, the residual solvents evaporated, leaving a large number of pores in polymer matrix. After the thermal annealed P(VDF-TrFE) and cured PDMS were detached from the inverse microridge-patterned Si molds, the final thickness of P(VDF-TrFE) and PDMS films was below  $\sim 80 \mu\text{m}$  and  $\sim 300 \mu\text{m}$ , respectively.

**Manufacturing the Devices:** For the fabrication of the ultraflexible TESs, the back sides of the as-prepared P(VDF-TrFE) and PDMS were coated with Ag film ( $\sim 100 \text{ nm}$  thick) by a DC sputtering system (SRN-120M, SORONA, Korea) and Ag NWs (average length of  $\sim 25 \mu\text{m}$  and diameter of  $\sim 32 \text{ nm}$ , Nanopyxis Co., Korea) by spin-coating method. The high electrical conductivity of double-layered Ag film and Ag NWs can minimize the power loss of the self-powered TESs as well as form the electrical pathway by the networking of Ag NWs even in a highly bent state of the TESs. To manufacture the bendable smart glove based on the fully packaged triboelectric sensing arrays, the interlocked and hierarchically structured P(VDF-TrFE) and PDMS were packaged by flexible and transparent laminating tape (3M VHB with 0.5 mm of thickness). Eleven of fully packaged and interlocked films were located on the joints of fingers (sensor size,  $1 \times 1.5 \text{ cm}^2$ ) and wrists (sensor size,  $1.5 \times 1.5 \text{ cm}^2$ ). Each side of electrodes on the interlocked films was connected with wavy shaped Cu wires for the bendable smart glove.

**Characterizations of Materials:** The morphologies of nanoporous and interlocked microridge structured P(VDF-TrFE) and PDMS were characterized by field-emission scanning electron microscopy (FE-SEM) (S-4800, Hitachi, Japan). The surface potential distribution between the

P(VDF-TrFE) and PDMS as well as nanofiber-like surface topology on the P(VDF-TrFE) were characterized using a scanning Kelvin probe microscopy (SKPM) and atomic force microscopy (AFM) (MFP-3D, Asylum Research, Santa Barbara, US), respectively. The mechanical compressive-stress test of PDMS was performed using a precision texture analyzer (TXA, YEONJIN Co., Korea). The structural analysis was performed by the finite element simulations (ABAQUS software), including stress propagation, gap distance, and surface contact area between two polymeric layers under vertical pressure and bending strain. All simulated conditions of the width/pitch sizes and elastic modulus of hierarchical microridge structured polymers were consistent with the experimental conditions. To implement the mechanical contact interaction in response to the applied physical force between two polymeric layers, we executed the general surface-to-surface contact interaction with linear elastic deformation of the interlocked and different surface structured polymers.

**Characterizations of Triboelectric Performance:** The numerically calculated triboelectric potential distribution between interlocked polymers under vertical pressure (98 kPa) and bending strain (115° of bending angle) was solved by Gauss's law for charge conservation through the finite element simulations (COMSOL software). The electrostatic potentials were calculated using dependent variables including theoretical values of relative permittivity ( $\epsilon_r$ ) of P(VDF-TrFE)<sup>[43]</sup> and PDMS<sup>[44]</sup> and gap distance ( $\Delta d$ ) between the interlocked layers. Surface triboelectric charge density ( $\sigma$ ) was experimentally measured. Owing to the contact-electrification effect, the interface of P(VDF-TrFE) and PDMS had spontaneously positive and negative triboelectric charges, respectively. The vertical pressure and bending stress-induced electrical properties were collected by triboelectric voltage, charges, and current signals using oscilloscope (DPO 2022B, Tektronix, US), electrometer (6517B, Keithley, US), and sourcemeter (2450-SCPI, Keithley, US), respectively. The vertical pressure and bending stress were applied by the pushing tester (JIPT, JUNIL TECH, Korea) with a pushing speed of 2 mm/s as the controlled moving displacement and bending tester (JIPT, JUNIL TECH, Korea) with a bending speed from 1 to 21 mm/s depended on the moving distance. To investigate the detection of contact vibration, a small-coin-like vibration motor (DVM1034, Motorbank Co., Korea) was attached to the samples. The vibrational frequency was controlled by reading a vibrometer (ACO 3116, Guangzhou Orimay Electronic Co., Japan). The frequency-dependent triboelectric voltage and current signals were collected by the oscilloscope (DPO 2022B, Tektronix, US) and sourcemeter (2450-SCPI, Keithley, US), respectively. For sensing acoustic waves, we used a commercial speaker (CS-3000plus, VOGUESUN Electronic Co., China), which was dictated *via* a voice enabled software from Google. The sound ( $\sim 92$  dB of sound pressure level, SPL) was then applied to the TESs using the commercial speaker placed at a distance of  $\sim 2$  cm away from the TESs. Both the input of electrical signals to the commercial speaker and corresponding oscillated triboelectric voltage from the output sound of commercial speaker were analyzed by the oscilloscope (DPO 2022B, Tektronix, US). For the discrimination of female and male voice, she or he spoke the words to the TES with  $\sim$

78 dB of SPL at a distance of  $\sim 15$  cm away from the TESs. To evaluate the humid insensitivity, we controlled the humidity by humidifier and measured with humidity sensor (CENTER 310, NEW ENGLAND INSTRUMENT, Australia) in a closed space of pushing tester. For the demonstration of triboelectric performances in a harsh environment, the packaged TESs were soaked into the ultrasonic water bath oscillated with 42 kHz (3510E-DTH, BRANSON ULTRASONICS Co., US) and lighted up a red LED (620 nm of wavelength and DC 2 V of operation voltage) connected to the four bridges rectifier.

### 4.3 Results and Discussion

***Skin-Inspired Polymeric Architectures for Ultrathin and Flexible TESs:*** Figure 4.1a illustrates interlocked microridges having a gradient elastic modulus ( $E$ ) of stiff epidermis and soft dermis layers in human skin, which facilitate effective stress transmission and concentration to microridges and underlying mechanoreceptors. By mimicking this structure and function, we fabricated hierarchical nanoporous and interlocked microridge structured polymers having different elastic modulus using the solvent-assisted micromolding method (Figure 4.1b and **Figure 4.2**). This fabrication process facilitates the control of density and pore size as well as the formation of large-area microtextured polymers (**Figure 4.3** and **Figure 4.4**). In this process, both P(VDF-TrFE) and PDMS were individually dissolved in solvent mixtures of acetone/*N,N*-dimethylformamide and ethanol/deionized water, respectively. Subsequently, the solvents evaporated during thermal annealing, while curing of polymeric mixtures occurred on the inverse microridge-patterned Si template, resulting in hierarchical nanoporous and microridge structures. While the PDMS layer exhibits open porous structures with the pore size distribution from  $\sim 2.2$  to  $5 \mu\text{m}$  (**Figure 4.5**) after solvent evaporation (Figure 4.1c and Figure 4.4), P(VDF-TrFE) results in the formation of inner pores and nanofiber-like surface during thermal annealing due to its high crystallinity (**Figure 4.6** and **Figure 4.7a**). For fabricating TESs, the backside of hierarchical nanoporous and microridge structured P(VDF-TrFE) and PDMS layers were coated with Ag film/Ag nanowires (NWs) electrodes and interlocked with each other (Figure 4.1d), resulting in ultrathin and flexible TESs with total thickness below  $\sim 400 \mu\text{m}$  (Figure 4.1e).

***Triboelectric Output Performances of Self-Powered TESs:*** Being advantageous over previous triboelectric devices, typically utilizing bulk spacers or rigid accessories, the microridge structures between two polymeric layers can act as spacers to provide an effective variation of gap distance between opposing surfaces (Figure 4.1d and **Figure 4.8**). With the sufficient variation of gap distance and contact area, the contact and separation process of the two dielectric layers generates positive and negative triboelectric charges on P(VDF-TrFE) and PDMS layers, respectively. As shown in Figure 4.1f, the interface surface between two dielectric layers was analyzed by scanning Kelvin probe microscopy (SKPM) to verify the surface potential differences between P(VDF-TrFE) and PDMS.



The SKPM image clearly indicates the contrast of surface potential ( $\sim 430$  mV) between the positive P(VDF-TrFE) and negative PDMS surfaces (Figure 4.7b). The surface potential distribution of P(VDF-TrFE) shown in Figure 4.7b exactly matches with the nanofiber-like morphology illustrated in Figure 4.7a, confirming the topological effect on the triboelectric charge generation.

The schematic illustration in **Figure 4.9a** shows the working principle of self-powered TESs during the contact and separation process between the hierarchically structured P(VDF-TrFE) and PDMS layers. Once the two different dielectric polymers come in contact with each other driven by external stress, surface triboelectric charges are generated at the interface of the two dielectric layers, resulting in positive and negative charged surfaces at positive and negative triboelectric materials, respectively, according to the triboelectric series. During the release of the interlocked polymers, compensating charges are built up on each side of the electrodes, generating a current flow through the external circuit. Once the TES system reaches the charge equilibrium state, the two dielectric polymers can be pressed to come closer again, generating a countercurrent flow. Therefore, the regular triboelectric voltage and current signals reversibly appear in response to contact and separation processes as shown in Figure 4.9b and 4.9c.

The self-powered TESs based on hierarchical polymers can generate an output voltage of 64 V and an output current density of  $1.63 \mu\text{A}/\text{cm}^2$  at a vertical pressure of 19.8 kPa and 4 Hz (Figure 4.9b and 4.9c). The maximum power density of self-powered TESs is  $46.7 \mu\text{W}/\text{cm}^2$  at an external load resistance of  $\sim 60 \text{ M}\Omega$  (Figure 4.9d), which is the highest value ever reported for flexible TESs (**Table 4.1**). The self-powered TESs can sufficiently light up a red LED using a rectifying system (see inset of Figure 4.9e). The ultraflexible TES has a potential to further enhance the triboelectric output performance when it is under the high pressure and frequency that make the larger frictional contact and frequent charge generation, which will be discussed later.

**Pressure and Bending Sensitive TESs:** The excellent performance of TESs is attributed to the structural effect of hierarchical nanoporous and interlocked microridge structured polymers having gradient stiffness. We compared the triboelectric output voltage and current density of TESs for different structures with and without nanoporous and microridge structures (**Figure 4.10**). Among different structures, the hierarchical nanoporous and interlocked microridge structures show the highest triboelectric output voltage and current density as well as pressure sensitivity. Nanoporous polymers without microridge structures provide a higher triboelectric output performance than the microridge structured polymers without nanopores, which indicates the greater effect of nanoporous structure on triboelectric performance than the microridge structure. While nanoporous polymers with a low elastic modulus ( $\sim 0.164 \text{ MPa}$ ) could be easily deformed, nonporous polymers having the relatively high elastic modulus ( $\sim 0.267 \text{ MPa}$ ) disturbed the deformation of surface microridge structures, deteriorating triboelectric performance (Figure 4.10 and **Figure 4.11**). The highly

deformable nanoporous polymers give rise to a significantly larger contact area between the interlocked microridge surfaces, which effectively increases the amount of triboelectric charges. In addition to the effects of hierarchical nanoporous and interlocked microridge structures, the gradient stiffness between the upper P(VDF-TrFE) layer with a high elastic modulus and the lower PDMS layer with a low elastic modulus can provide effective stress transmission and concentration to the interlocked microridges,<sup>[35–38]</sup> resulting in the significant deformation of interlocked microridge structures. Such device structure, which possesses the similar gradient elastic modulus in epidermis and dermis layers in human skin, provides  $\sim 1.5$  times higher triboelectric voltage and current density than the device with upper PDMS and lower P(VDF-TrFE) layer (**Figure 4.12a** and 4.12b). The theoretical calculation of stress distribution verifies that the larger stress concentration occurred between the high elastic modulus of P(VDF-TrFE) ( $\sim 1$  GPa)<sup>[39]</sup> and low elastic modulus of PDMS ( $\sim 3$  MPa)<sup>[40]</sup> than that of the interlocked structure between low elastic modulus of PDMS layers (**Figure 4.13a** and 4.13b).

To further understand the structural effect of hierarchical microridge arrays on the performance of TESs, we analyzed the triboelectric charge and potential generation of TESs having different width ( $w$ ) and pitch ( $p$ ) size of microridge arrays ( $w/p = 25/30, 50/60, \text{ and } 100/120 \mu\text{m}$ ) *via* theoretical and experimental methods. As shown in Figure 4.11, hierarchical PDMS microridge arrays with the  $w/p$  size of  $100/120 \mu\text{m}$  exhibit the lowest compressive elastic modulus ( $\sim 0.164$  MPa) due to high porosity ( $\sim 37.3\%$  in **Figure 4.14**), resulting in the largest deformation (**Figure 4.15**) and increase of contact area between the interlocked P(VDF-TrFE) and PDMS microridge structures (Figure 4.15b and 4.15c). Therefore, the microridge arrays with  $w/p$  of  $100/120 \mu\text{m}$  generate a larger amount of surface triboelectric charge density ( $\sigma$ ) than those of planar and smaller sized microridge structures (**Figure 4.16a**). Following the general expressions of the open-circuit voltage ( $V_{OC}$ ) and short-circuit current ( $I_{SC}$ ) (see equations in *Appendix A*),  $V_{OC}$  and  $I_{SC}$  are directly proportional to the amount of surface triboelectric charge density ( $\sigma$ ) which is induced by the intrinsic properties of triboelectric materials and effective surface contact area.<sup>[27]</sup> In addition, the triboelectric output voltage increases as the gap distance ( $\Delta d$ ) increases between triboelectric layers according to the Paschen's law.<sup>[25]</sup> **Figure 4.17a** theoretically verifies that the potential difference from hierarchical microridge arrays increases by increasing width and pitch sizes, which can be attributed to the increase of gap distance (Figure 4.8) and large amount of triboelectric charge density (Figure 4.16a), resulting from the increase of effective surface contact area (Figure 4.15) between triboelectric layers. The experimental results coincide with the theoretical estimation very well. As shown in Figure 4.17b and **Figure 4.18a**, the triboelectric output voltage and current density increase *via* increasing width and pitch sizes. In particular, microridge arrays with  $w/p$  of  $100/120 \mu\text{m}$  show the highest pressure sensitivity ( $\sim 0.55$  V/kPa up to 19.8 kPa), which is higher than the previous TES based on planar P(VDF-TrFE) and

PDMS ( $\sim 0.104$  V/kPa up to 5 kPa).<sup>[41]</sup> The high pressure sensitivity of hierarchical microridge arrays in the low pressure regime is advantageous in monitoring weak pulse pressure of radial artery (Figure 4.17c). Figure 4.17c shows that the triboelectric current signals match with the wrist pulse waves, where A is the systolic peak, B is the point of inflection, C is the diastolic peak, and the corresponding reverse triboelectric current signals are marked by a, b, and c. This result demonstrates that, unlike the previous voluminous or nonmonolithic designs of triboelectric devices, the ultraflexible and monolithic design of a highly sensitive TES in this study enables applications in highly reliable and wearable devices for health monitoring.

Our ultraflexible TESs are also sensitive to the bending strain. The increased bending stress along with the bending angle increases effective frictional contact between interlocked microridge arrays. The triboelectric potential generation induced by bending stress was determined by the effective contact area of interlocked microridges as shown in **Figure 4.19**. While the resulting contact stress between the two layers shows an overall uniform (homogeneous) distribution throughout the microridge arrays under the vertical pressure (Figure 4.15a), a non-uniform (inhomogeneous) stress distribution appears in the case of the bending process (Figure 4.19a and 4.19b). This is because the microridge array of the top layer contracts inward and that of the bottom layer expands outward during bending process. Furthermore, given the same value of the radius of bending curvature, the degree of geometrical mismatch in contact between the two microridge arrays and the concomitant inhomogeneity for the contact stress distribution relatively increases with the larger width/pitch size of the arrays. As a result, the effective contact area becomes smaller for the larger size of interlocked microridge array (Figure 4.19c). With these different aspects between the vertical pressing and bending process, as contrary to the response to vertical pressure, the theoretically calculated electric field of interlocked films from the bending strain exhibits that the electric field of hierarchical microridge arrays increases *via* decreasing width and pitch sizes (Figure 4.17d). Similarly, the triboelectric output voltage and current density increase by reducing the width and pitch sizes of microridge arrays (Figures 4.17e and Figure 4.18b). Consequently, the hierarchical microridge arrays with w/p of 25/30  $\mu\text{m}$  show the highest bending sensitivity ( $\sim 0.1$  V/ $^\circ$  from 16 to 122 $^\circ$  of bending angle), which is the best performance among the previously reported bendable TESs (Table 4.1). When the ultraflexible TESs are attached on the curved joints of fingers (see inset in Figure 4.17f), the highly sensitive TESs can precisely detect the degree of bending angle *via* corresponding triboelectric current signals when the thumb (90 $^\circ$ ), index (110 $^\circ$ ), and middle fingers (100 $^\circ$ ) are bent at a constant velocity (Figure 4.17f).

***Highly Sensitive TESs for Detection from Low to High Frequency of Dynamic Stimuli:*** The highly pressure-sensitive TESs based on the interlocked and hierarchical microridge structured polymers can also detect high-frequency dynamic forces due to the fast adapting triboelectric charging and discharging process. When a vibrating coin on top of the TES generates a contact vibration with a

variable frequency (**Figure 4.20a**), the triboelectric output voltage and current gradually increase by increasing the applied frequency from 73 to 140 Hz (**Figure 4.20b** and **4.20c**). The increase in frequency of the vibrational force can induce a high velocity and acceleration for the high impact force ( $F$ ) based on the impulse-momentum theorem ( $Fdt = mdv$ , where  $t$  is time,  $m$  is mass of material, and  $v$  is velocity), resulting in the increase of contact area and surface triboelectric charge density.<sup>[42]</sup> Both triboelectric output voltage and current are mainly affected by the amount of surface triboelectric charge density ( $\sigma$ ). In particular, the current is directly proportional to the charge flow rate ( $dQ/dt$ ) in equation 7 in *Appendix A*.<sup>[27]</sup> Thus, the output voltage and current as shown in **Figure 4.20b** and **4.20c** linearly increase with the increase of vibrational frequency.

The fast responsive TESs can detect the high-frequency vibration of acoustic waves. To investigate the detection of acoustic vibration, harmonic frequency sound was played using a commercial speaker (**Figure 4.20d**). **Figure 4.20e** shows the input voltage signals to the commercial speaker and the corresponding short-time Fourier transform (STFT) spectrogram for the analysis of oscillated voltage signals. When the sound of “triboelectric sensor” with different speed was played by a commercial speaker (**Figure 4.20e**), the acoustic waveforms could be perceived by our TESs, presenting time-dependent triboelectric output voltage variations (**Figure 4.20f**). The corresponding STFT spectrogram with frequency distribution from 100 Hz to 6.25 kHz matches with the input voltage source (**Figure 4.20e** and **4.20f**). Besides, the sound sensing capabilities of our TESs can not only recognize the low sound pressure level (SPL) of human voice (<78 dB) but also distinguish the different frequency domain of female and male voices as well (**Figure 4.20g**). When female and male voices of the sentences of “I am a girl” and “I am a boy” were tested (**Figure 4.20h**), our TESs can recognize that the frequency domain of female voice covers the entire frequency range from 100 Hz to 6.25 kHz and the male voice results in the spectrogram with higher intensity at a low frequency region (<2 kHz) than the female one (**Figure 4.20h**). In addition, such voice recognizable TESs show high reproducibility and reliability to detect and differentiate the repeated female and male voices of the word “UNIST” (**Figure 4.20i**), which is practically used for the biometric security system.

***Ultrathin and Flexible TESs for a Smart Glove Detecting Sign Language:*** As previously mentioned, our ultrathin and flexible TESs enable the detection of finger bending motion with different bending angle, which facilitates the perception of diverse gestures of human hands. For this purpose, we fabricated a bendable smart glove consisting of 11 TESs laminated with flexible tape and attached on the joints of fingers and wrist, which can detect various hand motions such as bending, spreading, touching, and twisting. The smart glove can recognize the size of objects having different radius (**Figure 4.21**). Holding an object with a small radius induces the large bending angle as well as high bending stress to the bendable TESs (**Figure 4.21a**), resulting in the higher triboelectric current than the object having bigger radius (**Figure 4.21b**). The smart glove can detect and differentiate a variety of hand postures as well for different sign languages of the sentence of “I am”, “happy”, “to

meet”, and “you” (**Figure 4.22** and **Video 4.1**). Except for the index one, other fingers and the wrist are bending, touching, twisting, and spreading motions according to the gesture of sign languages (Figure 4.22a and Video 4.1). For these hand gestures, the smart glove exhibits different contour map patterns for triboelectric output currents (Figure 4.22b). In addition, the smart glove displays blue colors (negative triboelectric currents) for hand holding posture and red colors (positive triboelectric currents) for hand spreading posture, demonstrating the precise differentiation of diverse hand postures. In particular, the sign language of “you” shows the high triboelectric current only on the wrist, because only the joint of wrist moves during the hand gesture change for the sign languages from “to meet” to “you” (Figure 4.22b-(iv)), indicating the detection capability of smart glove for real-time dynamic hand movements. To analyze the detailed signal variations of the bendable TESs attached on different joints of fingers and wrist, we monitored the real-time current variations of TESs for different sign languages. The bone of fingers can be divided into three parts including carpus, metacarpus, and phalange as shown in Figure 4.22c-(i). In comparison with other joints, the joint of wrist at carpus shows notable peaks at the sign language of “happy” because the wrist joint only twists at that hand gesture (Figure 4.22c-(ii)). For the sign language of “to meet”, the joints of thumb 1 (T1) and thumb 2 (T2) show additional up and down current peaks as compared to other joints in Figure 4.22c-(iii) and 4.22c-(iv). Such additional peaks can be attributed to the touch and separation of the thumb joint with the other hand during the sign language gesture of “to meet”, leading to touching and separating current peaks. These results demonstrate that our triboelectric smart glove can perceive the dynamic hand gestures of sign languages, which can find applications in human-machine interfaces, game industry, and communication devices for speech- and hearing-impaired people.

***Flexible and Fully Packaged Design for Humid-Insensitive TESs:*** High repeatability, reliability, and long-term sustainability are critical for the practical use of our high-performance and ultraflexible TESs. The compressive strain–stress curves of the hierarchical nanoporous and microridge structured PDMS do not show the large hysteresis as well as plastic collapse during loading and unloading cycles (Figure 4.11), which verifies the high mechanical stability of the nanoporous and microridge structured PDMS. The hierarchical nanoporous and interlocked microridge structured TESs exhibit an excellent mechanical durability with the repeatable triboelectric output voltage and current generation during 10,000 cycles of pushing with vertical pressure of 98 kPa (**Figure 4.23a** and **4.23b**) and well maintain the nanoporous and microridge structures of each polymer after a cyclic pushing test (Figure 4.23c and 4.23d). However, the triboelectric charging and discharging process is largely affected by the environmental conditions such as atmospheric impurities, ambient temperature, pressure, and humidity.<sup>[33, 34]</sup> Particularly, the high humidity around the triboelectric charged surfaces brings in a thick water layer and high air conductivity, which leads to the discharging of the induced surface triboelectric charges.<sup>[33]</sup> To achieve the long-term sustainability of the triboelectric performance in a harsh environment, the triboelectric devices should be encapsulated or packaged. The spacer-free,

ultrathin, and monolithic design of our TESs enable the full packaging of the device using a simple laminating tape (**Figure 4.24a**), which has been already described in the bendable smart glove (Figure 4.22a). Our fully packaged TESs exhibit the constant triboelectric output voltage and current density even when the relative humidity changes from 20 to 90% RH (Figure 4.24b and 4.24c). Furthermore, our packaged TESs can maintain their triboelectric performance and sensitivity even in the water environment. When the packaged TESs on the smart glove are immersed in an ultrasonic water bath under the high-frequency ultrasonic waves ( $\sim 21$  kHz), the TESs can still generate a power even in the water and instantaneously light up a red LED (Figure 4.24d and **Video 4.2**). In addition to power generation, our packaged TESs can precisely detect the high-frequency ultrasonic waves. The fast Fourier transform (FFT) spectra of triboelectric voltage signals show the distribution of perceived frequency and a high amplitude frequency at 21 kHz (Figure 4.24d). In addition, the STFT spectrogram visually displays the time-dependent frequency distribution and the ultrasonic waveforms (Figure 4.24e). The capabilities of both power generation and sensing in response to ultrasonic waves, even in a harsh environment, can broaden the application fields of our ultraflexible and fully packaged TESs.

#### 4.4 Conclusions

In conclusion, ultrathin, highly sensitive, and wearable TESs were developed by hierarchical polymeric architectures of nanoporous and interlocked microridge structures with gradient stiffness. The hierarchical geometry of nanoporous and interlocked microridge structured polymers could enhance the effective variations of gap distance between interlocked layers without bulk extra spacers and allows for an ultrathin and highly flexible design for wearable TESs. In addition, inspired by gradient stiffness of stiff epidermis and soft dermis layers, which can effectively transfer the external stress, the gradient elastic modulus of interlocked P(VDF-TrFE) and PDMS layers significantly enhanced the triboelectric output performances as well as pressure and bending sensitivities to perceive the minute pulse waves of a radial artery and finger bending motions. Our TESs exhibited the highest power density ( $46.7 \mu\text{W}/\text{cm}^2$ ) and pressure ( $0.55 \text{ V}/\text{kPa}$ ) and bending ( $\sim 0.1 \text{ V}/^\circ$ ) sensitivities ever reported on flexible TESs. Also, the fast responsive TESs could detect the dynamic stimuli from the low frequency of contact vibrations to the high frequency of acoustic waves for recognizing a human voice. The spacer-free and monolithic design of ultraflexible TESs could be not only worn on human hands but also fully packaged for highly reliable and sustainable wearable devices as well. All of these outstanding functionalities of our skin-inspired and ultraflexible TESs are available for both power generation and detection of human vital signs, voice recognition, and real-time monitoring of bodily motion even in a harsh environment, which facilitates broad applications for wearable health monitoring devices, self-diagnostic systems, popular biometric security systems, prosthetic limbs, rehabilitation devices, and humanoid robotics.

#### 4.5 References

- [1] Takei, K.; Takahashi, T.; Ho, J. C.; Ko, H.; Gillies, A. G.; Leu, P. W.; Fearing, R. S.; Javey, A. Nanowire Active-Matrix Circuitry for Low-Voltage Macroscale Artificial Skin. *Nat. Mater.* **2010**, *9*, 821–826.
- [2] Park, S.; Kim, H.; Vosgueritchian, M.; Cheon, S.; Kim, H.; Koo, J. H.; Kim, T. R.; Lee, S.; Schwartz, G.; Chang, H.; Bao, Z. A. Stretchable Energy-Harvesting Tactile Electronic Skin Capable of Differentiating Multiple Mechanical Stimuli Modes. *Adv. Mater.* **2014**, *26*, 7324–7332.
- [3] Shi, M. Y.; Zhang, J. X.; Chen, H. T.; Han, M. D.; Shankaregowda, S. A.; Su, Z. M.; Meng, B.; Cheng, X. L.; Zhang, H. X. Self-Powered Analogue Smart Skin. *ACS Nano* **2016**, *10*, 4083–4091.
- [4] Wang, C.; Hwang, D.; Yu, Z. B.; Takei, K.; Park, J.; Chen, T.; Ma, B. W.; Javey, A. User-Interactive Electronic Skin for Instantaneous Pressure Visualization. *Nat. Mater.* **2013**, *12*, 899–904.
- [5] Jeong, J. W.; Yeo, W. H.; Akhtar, A.; Norton, J. J. S.; Kwack, Y. J.; Li, S.; Jung, S. Y.; Su, Y. W.; Lee, W.; Xia, J.; Cheng, H. Y.; Huang, Y. G.; Choi, W. S.; Bretl, T.; Rogers, J. A. Materials and Optimized Designs for Human-Machine Interfaces via Epidermal Electronics. *Adv. Mater.* **2013**, *25*, 6839–6846.
- [6] Xu, S.; Zhang, Y. H.; Cho, J.; Lee, J.; Huang, X.; Jia, L.; Fan, J. A.; Su, Y. W.; Su, J.; Zhang, H. G.; Cheng, H. Y.; Lu, B. W.; Yu, C. J.; Chuang, C.; Kim, T. I.; Song, T.; Shigeta, K.; Kang, S.; Dagdeviren, C.; Petrov, I.; Braun, P. V.; Huang, Y. G.; Paik, U.; Rogers, J. A. Stretchable Batteries with Self-Similar Serpentine Interconnects and Integrated Wireless Recharging Systems. *Nat. Commun.* **2013**, *4*, 1543.
- [7] Hwang, B. U.; Lee, J. H.; Trung, T. Q.; Roh, E.; Kim, D. I.; Kim, S. W.; Lee, N. E. Transparent Stretchable Self-Powered Patchable Sensor Platform with Ultrasensitive Recognition of Human Activities. *ACS Nano* **2015**, *9*, 8801–8810.
- [8] Lee, Y. H.; Kim, J. S.; Noh, J.; Lee, I.; Kim, H. J.; Choi, S.; Seo, J.; Jeon, S.; Kim, T. S.; Lee, J. Y.; Choi, J. W. Wearable Textile Battery Rechargeable by Solar Energy. *Nano Lett.* **2013**, *13*, 5753–5761.
- [9] Pushparaj, V. L.; Shaijumon, M. M.; Kumar, A.; Murugesan, S.; Ci, L.; Vajtai, R.; Linhardt, R. J.; Nalamasu, O.; Ajayan, P. M. Flexible Energy Storage Devices Based on Nanocomposite Paper. *Proc. Natl. Acad. Sci. U. S. A.* **2007**, *104*, 13574–13577.
- [10] Xu, S.; Zhang, Y. H.; Jia, L.; Mathewson, K. E.; Jang, K. I.; Kim, J.; Fu, H. R.; Huang, X.; Chava, P.; Wang, R. H.; Bhole, S.; Wang, L. Z.; Na, Y. J.; Guan, Y.; Flavin, M.; Han, Z. S.; Huang, Y. G.; Rogers, J. A. Soft Microfluidic Assemblies of Sensors, Circuits, and Radios for the Skin. *Science* **2014**, *344*, 70–74.
- [11] Kim, D. H.; Lu, N. S.; Ma, R.; Kim, Y. S.; Kim, R. H.; Wang, S. D.; Wu, J.; Won, S. M.; Tao, H.; Islam, A.; Yu, K. J.; Kim, T. I.; Chowdhury, R.; Ying, M.; Xu, L. Z.; Li, M.; Chung, H. J.; Keum, H.;

- McCormick, M.; Liu, P.; Zhang, Y. W.; Omenetto, F. G.; Huang, Y. G.; Coleman, T.; Rogers, J. A. Epidermal Electronics. *Science* **2011**, *333*, 838–843.
- [12] Honda, W.; Harada, S.; Arie, T.; Akita, S.; Takei, K. Wearable, Human-Interactive, Health-Monitoring, Wireless Devices Fabricated by Macroscale Printing Techniques. *Adv. Funct. Mater.* **2014**, *24*, 3299–3304.
- [13] Scrosati, B. Nanomaterials: Paper Powers Battery Breakthrough. *Nat. Nanotechnol.* **2007**, *2*, 598–599.
- [14] Wang, Z. L.; Chen, J.; Lin, L. Progress in Triboelectric Nanogenerators as a New Energy Technology and Self-Powered Sensors. *Energy Environ. Sci.* **2015**, *8*, 2250–2282.
- [15] Wang, Z. L. Self-Powered Nanosensors and Nanosystems. *Adv. Mater.* **2012**, *24*, 280–285.
- [16] Hu, Y. F.; Lin, L.; Zhang, Y.; Wang, Z. L. Replacing a Battery by a Nanogenerator with 20 V Output. *Adv. Mater.* **2012**, *24*, 110–114.
- [17] Hansen, B. J.; Liu, Y.; Yang, R. S.; Wang, Z. L. Hybrid Nanogenerator for Concurrently Harvesting Biomechanical and Biochemical Energy. *ACS Nano* **2010**, *4*, 3647–3652.
- [18] Kim, S. J.; We, J. H.; Cho, B. J. A Wearable Thermoelectric Generator Fabricated on a Glass Fabric. *Energy Environ. Sci.* **2014**, *7*, 1959–1965.
- [19] Hu, Y. F.; Yang, J.; Niu, S. M.; Wu, W. Z.; Wang, Z. L. Hybridizing Triboelectrification and Electromagnetic Induction Effects for High-Efficient Mechanical Energy Harvesting. *ACS Nano* **2014**, *8*, 7442–7450.
- [20] Ha, M.; Park, J.; Lee, Y.; Ko, H. Triboelectric Generators and Sensors for Self-Powered Wearable Electronics. *ACS Nano* **2015**, *9*, 3421–3427.
- [21] Jiang, X.-Z.; Sun, Y.-J.; Fan, Z.; Zhang, T.-Y. Integrated Flexible, Waterproof, Transparent, and Self-Powered Tactile Sensing Panel. *ACS Nano* **2016**, *10*, 7696–7704.
- [22] Li, T.; Zou, J. D.; Xing, F.; Zhang, M.; Cao, X.; Wang, N.; Wang, Z. L. From Dual-Mode Triboelectric Nanogenerator to Smart Tactile Sensor: A Multiplexing Design. *ACS Nano* **2017**, *11*, 3950–3956.
- [23] Wang, S. H.; Lin, L.; Wang, Z. L. Nanoscale Triboelectric-Effect-Enabled Energy Conversion for Sustainably Powering Portable Electronics. *Nano Lett.* **2012**, *12*, 6339–6346.
- [24] Guo, H. Y.; Yeh, M. H.; Zi, Y. L.; Wen, Z.; Chen, J.; Liu, G. L.; Hu, C. G.; Wang, Z. L. Ultralight Cut-Paper-Based Self-Charging Power Unit for Self-Powered Portable Electronic and Medical Systems. *ACS Nano* **2017**, *11*, 4475–4482.
- [25] Wang, J.; Wu, C. S.; Dai, Y. J.; Zhao, Z. H.; Wang, A.; Zhang, T. J.; Wang, Z. L. Achieving Ultrahigh Triboelectric Charge Density for Efficient Energy Harvesting. *Nat. Commun.* **2017**, *8*, 88.
- [26] Dharmasena, R.; Jayawardena, K.; Mills, C. A.; Deane, J. H. B.; Anguita, J. V.; Dorey, R. A.;



- Silva, S. R. P. Triboelectric Nanogenerators: Providing a Fundamental Framework. *Energy Environ. Sci.* **2017**, *10*, 1801–1811.
- [27] Niu, S. M.; Wang, S. H.; Lin, L.; Liu, Y.; Zhou, Y. S.; Hu, Y. F.; Wang, Z. L. Theoretical Study of Contact-Mode Triboelectric Nanogenerators as an Effective Power Source. *Energy Environ. Sci.* **2013**, *6*, 3576–3583.
- [28] Yang, J.; Chen, J.; Su, Y. J.; Jing, Q. S.; Li, Z. L.; Yi, F.; Wen, X. N.; Wang, Z. N.; Wang, Z. L. Eardrum-Inspired Active Sensors for Self-Powered Cardiovascular System Characterization and Throat-Attached Anti-Interference Voice Recognition. *Adv. Mater.* **2015**, *27*, 1316–1326.
- [29] Jing, Q. S.; Xie, Y. N.; Zhu, G.; Han, R. P. S.; Wang, Z. L. Self-Powered Thin-Film Motion Vector Sensor. *Nat. Commun.* **2015**, *6*, 8031.
- [30] Niu, S. M.; Wang, Z. L. Theoretical Systems of Triboelectric Nanogenerators. *Nano Energy* **2015**, *14*, 161–192.
- [31] Gu, L.; Cui, N. Y.; Liu, J. M.; Zheng, Y. B.; Bai, S.; Qin, Y. Packaged Triboelectric Nanogenerator with High Endurability for Severe Environments. *Nanoscale* **2015**, *7*, 18049–18053.
- [32] Lee, K. Y.; Yoon, H. J.; Jiang, T.; Wen, X. N.; Seung, W.; Kim, S. W.; Wang, Z. L. Fully Packaged Self-Powered Triboelectric Pressure Sensor Using Hemispheres-Array. *Adv. Energy Mater.* **2016**, *6*, 1502566.
- [33] Nguyen, V.; Yang, R. S. Effect of Humidity and Pressure on the Triboelectric Nanogenerator. *Nano Energy* **2013**, *2*, 604–608.
- [34] Nemeth, E.; Albrecht, V.; Schubert, G.; Simon, F. Polymer Tribo-Electric Charging: Dependence on Thermodynamic Surface Properties and Relative Humidity. *J. Electrostat.* **2003**, *58*, 3–16.
- [35] Shao, F.; Childs, T. H.; Barnes, C. J.; Henson, B. Finite Element Simulations of Static and Sliding Contact between a Human Fingertip and Textured Surfaces. *Tribol. Int.* **2010**, *43*, 2308–2316.
- [36] Gerling, G. J.; Thomas, G. W. The Effect of Fingertip Microstructures on Tactile Edge Perception. Proceedings from the *First Joint Eurohaptics Conference and Symposium on Haptic Interfaces for Virtual Environment and Teleoperator Systems. World Haptics Conference*, March 18–20, 2005, Pisa, Italy; IEEE: New York; pp 63–72.
- [37] Noda, K.; Matsumoto, K.; Shimoyama, I. Tactile Sensor with Standing Piezoresistive Cantilevers, Covered with 2-Layer Skin Type Structures for Texture Detection of Object Surface. Proceedings from the *2008 IEEE/RSJ International Conference on Intelligent Robots and Systems*, September 22–26, 2008, Nice, France; IEEE: New York, 2008; pp 3953–3958.
- [38] Cao, Y.; Feng, Y.; Ryser, M. D.; Zhu, K.; Herschlag, G.; Cao, C.; Marusak, K.; Zauscher, S.; You, L. Programmable Assembly of Pressure Sensors Using Pattern-Forming Bacteria. *Nat. Biotechnol.* **2017**, *35*, 1087–1093.

- [39] Hahm, S. W.; Khang, D. Y. Crystallization and Microstructure-Dependent Elastic Moduli of Ferroelectric P(VDF-TrFE) Thin Films. *Soft Matter* **2010**, *6*, 5802–5806.
- [40] Li, Y. Q.; Samad, Y. A.; Liao, K. From Cotton to Wearable Pressure Sensor. *J. Mater. Chem. A* **2015**, *3*, 2181–2187.
- [41] Parida, K.; Bhavanasi, V.; Kumar, V.; Bendi, R.; Lee, P. S. Self-Powered Pressure Sensor for Ultra-Wide Range Pressure Detection. *Nano Res.* **2017**, *10*, 3557–3570.
- [42] Wu, C.; Liu, R.; Wang, J.; Zi, Y.; Lin, L.; Wang, Z. L. A Spring-Based Resonance Coupling for Hugely Enhancing the Performance of Triboelectric Nanogenerators for Harvesting Low-Frequency Vibration Energy. *Nano Energy* **2017**, *32*, 287–293.
- [43] Bune, A. V.; Fridkin, V. M.; Ducharme, S.; Blinov, L. M.; Palto, S. P.; Sorokin, A. V.; Yudin, S.; Zlatkin, A. Two-Dimensional Ferroelectric Films. *Nature* **1998**, *391*, 874–877.
- [44] Mannsfeld, S. C.; Tee, B. C.; Stoltenberg, R. M.; Chen, C. V. H.; Barman, S.; Muir, B. V.; Sokolov, A. N.; Reese, C.; Bao, Z. Highly Sensitive Flexible Pressure Sensors with Microstructured Rubber Dielectric Layers. *Nat. Mater.* **2010**, *9*, 859–864.
- [45] Wang, X.; Que, M.; Chen, M.; Han, X.; Li, X.; Pan, C.; Wang, Z. L. Full Dynamic-Range Pressure Sensor Matrix Based on Optical and Electrical Dual-Mode Sensing. *Adv. Mater.* **2017**, *29*, 1605817.
- [46] Shi, Q.; Wang, H.; Wang, T.; Lee, C. Self-Powered Liquid Triboelectric Microfluidic Sensor for Pressure Sensing and Finger Motion Monitoring Applications. *Nano Energy* **2016**, *30*, 450–459.
- [47] Fuh, Y.-K.; Chen, P.-C.; Ho, H.-C.; Huang, Z.-M.; Li, S.-C. All-Direction Energy Harvester Based on Nano/Micro Fibers as Flexible and Stretchable Sensors for Human Motion Detection. *RSC Adv.* **2015**, *5*, 67787–67794.
- [48] Pu, X.; Guo, H.; Chen, J.; Wang, X.; Xi, Y.; Hu, C.; Wang, Z. L. Eye Motion Triggered Self-Powered Mechnosensational Communication System Using Triboelectric Nanogenerator. *Sci. Adv.* **2017**, *3*, e1700694.
- [49] Yuan, Z.; Zhou, T.; Yin, Y.; Cao, R.; Li, C.; Wang, Z. L. Transparent and Flexible Triboelectric Sensing Array for Touch Security Applications. *ACS Nano* **2017**, *11*, 8364–8369.
- [50] Fan, Y. J.; Meng, X. S.; Li, H. Y.; Kuang, S. Y.; Zhang, L.; Wu, Y.; Wang, Z. L.; Zhu, G. Stretchable Porous Carbon Nanotube-Elastomer Hybrid Nanocomposite for Harvesting Mechanical Energy. *Adv. Mater.* **2017**, *29*, 1603115.
- [51] Chen, J.; Ding, P.; Pan, R.; Xuan, W.; Guo, D.; Ye, Z.; Yin, W.; Jin, H.; Wang, X.; Dong, S. Self-Powered Transparent Glass-Based Single Electrode Triboelectric Motion Tracking Sensor Array. *Nano Energy* **2017**, *34*, 442–448.
- [52] Yang, J.; Liu, P.; Wei, X.; Luo, W.; Yang, J.; Jiang, H.; Wei, D.; Shi, R.; Shi, H. Surface Engineering of Graphene Composite Transparent Electrodes for High-Performance Flexible

Triboelectric Nanogenerators and Self-Powered Sensors. *ACS Appl. Mater. Interfaces* **2017**, *9*, 36017–36025.

[53] Gong, W.; Hou, C.; Guo, Y.; Zhou, J.; Mu, J.; Li, Y.; Zhang, Q.; Wang, H. A Wearable, Fibroid, Self-Powered Active Kinematic Sensor Based on Stretchable Sheath-Core Structural Triboelectric Fibers. *Nano Energy* **2017**, *39*, 673–683.

[54] Lin, L.; Xie, Y.; Wang, S.; Wu, W.; Niu, S.; Wen, X.; Wang, Z. L. Triboelectric Active Sensor Array for Self-Powered Static and Dynamic Pressure Detection and Tactile Imaging. *ACS Nano* **2013**, *7*, 8266–8274.

\*\*Reprinted in part with permission from M. Ha<sup>†</sup>, S. Lim<sup>†</sup>, S. Cho<sup>†</sup>, C. Baig<sup>\*</sup>, and H. Ko<sup>\*</sup> *et al.*, *ACS Nano* **2018**, *12*, 3964–3974. Copyright © 2018, American Chemical Society

**Table 4.1** Comparison of triboelectric output performances and vertical pressure/bending sensitivity of the results achieved this work with previously reported TESs.

Electrode type	Triboelectric materials	Current density	Voltage	Power density	Pressure sensitivity	Bending sensitivity
Single <sup>[45]</sup>	PDMS	–	5.5 V (> 400 kPa)	–	0.006/kPa (0 – 200 kPa)	0.15 nA/°
Single <sup>[46]</sup>	Liquid/PDMS	2.5 nA (40 N)	3.15 V (16 N)	7.8 nW/cm <sup>2</sup>	0.035 nA/N, 0.0304/N	0.044 nA/°
Single <sup>[47]</sup>	PVDF fiber	6.4 nA/cm <sup>2</sup> (180°)	10 V (180°)	0.064 μW/cm <sup>2</sup>	–	0.044 V/°
Single <sup>[41]</sup>	P(VDF-TrFE) /PDMS	–	30 V (600 kPa, 5 Hz)	–	0.104 V/kPa	–
Single <sup>[48]</sup>	Latex/FEP	–	30 V (20 N)	–	2.5 V/N	–
Single <sup>[49]</sup>	FEP	–	50 V	–	2.79 V/kPa (< 1 kPa)	–
Single <sup>[50]</sup>	Porous CNT/PDMS	56.6 nA/cm <sup>2</sup> (60 N)	55 V (60 N)	3 μW/cm <sup>2</sup>	1 V/N	–
Single <sup>[51]</sup>	PDMS	0.332 μA/cm <sup>2</sup>	318 V	17.08 μW/cm <sup>2</sup>	2.5 V/N, 0.03 μA/N	–
Top-bottom <sup>[52]</sup>	PI, PEDOT:PSS	2.5 μA/cm <sup>2</sup>	52 V	0.12 μW/cm <sup>2</sup>	–	0.0675 V/°, 15.4 /rad
Top-bottom <sup>[53]</sup>	Nylon fiber, bamboo fiber	0.05 μA/cm <sup>2</sup> (44 %strain, 0.5 Hz)	4 V (44 %strain, 0.5 Hz)	0.13 μW/cm <sup>2</sup>	0.016 V/%strain (15 – 100 %)	0.082 V/rad (0.25 – 2.5 rad)
Top-bottom <sup>[21]</sup>	ITO, PDMS	4.73 μA/cm <sup>2</sup>	1.6 V (428.8 kPa)	0.13 μW/cm <sup>2</sup>	2.82 ± 0.187 mV/kPa	–
Top-bottom <sup>[32]</sup>	PTFE, hemispherical Cu/PDMS	1.3 μA	25 V	2.45 μW/cm <sup>2</sup>	0.5 V/N (0 – 40 N) 0.018 μA/N (0 – 40 N)	–
Top-bottom <sup>[54]</sup>	Pyramidal PDMS, Ag NWs	0.3 μA/cm <sup>2</sup>	75 V	22.5 μW/cm <sup>2</sup>	0.31 /kPa	–
Top-bottom <sup>[22]</sup>	PDMS, Cu NWs	1.2 μA (100 Pa)	10.6 V (140 N)	–	0.28 mV/N (40 – 140 N)	–
<b>Top-bottom [This work]</b>	<b>Hierarchical PDMS, P(VDF-TrFE)</b>	<b>1.63 μA/cm<sup>2</sup> (98 kPa, 9.8 N, 4 Hz)</b>	<b>64 V (98 kPa, 9.8 N, 4 Hz)</b>	<b>46.7 μW/cm<sup>2</sup></b>	<b>0.55 V/kPa, 5.34 V/N, 17 nA/kPa, 0.217 μA/N (&lt; 19.8 kPa, 0.4 Hz)</b>	<b>0.1 V/°, 6.1 V/rad, 2.8 nA/°, 0.17 μA/rad (16 – 122°, 0.27 – 2.23 rad)</b>

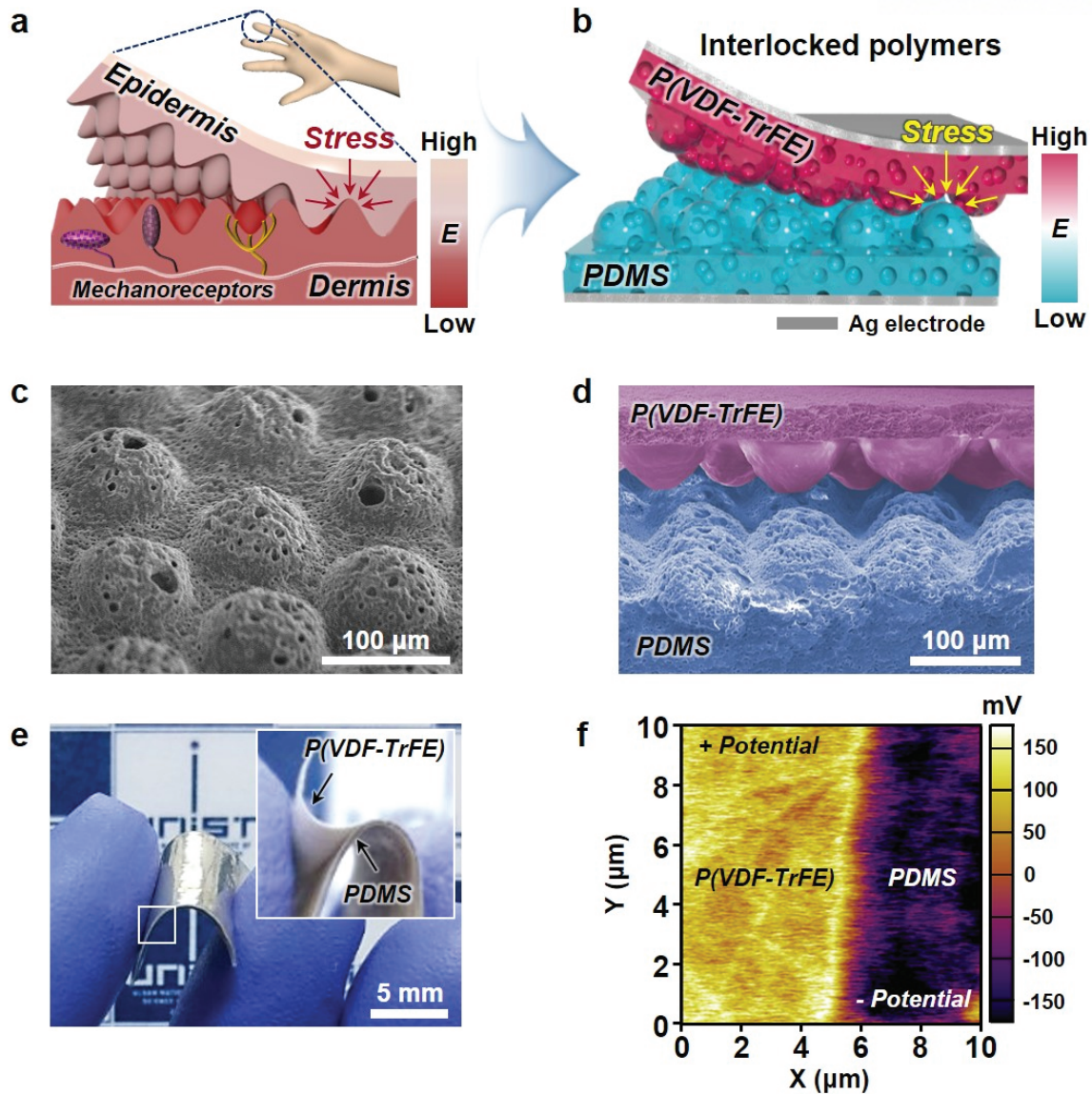


**Figure 4.1** Skin-inspired and hierarchical polymer architectures for spacer-free, ultrathin, and highly sensitive triboelectric sensors (TESs). (a) Structural and functional characteristics of human skin. The different elastic modulus ( $E$ ) of epidermis–dermis layers with interlocked microridges effectively transfer the external stress to underlying mechanoreceptors. (b) Hierarchical and interlocked microridge structured P(VDF-TrFE) and PDMS-based TESs. Scanning electron microscopy (SEM) images of (c) nanoporous and microridge structured PDMS and (d) interlocked with hierarchically structured P(VDF-TrFE). (e) Photograph of ultrathin and flexible TESs. Inset shows the interlocked P(VDF-TrFE) and PDMS layers. (f) Scanning Kelvin probe microscopy (SKPM) image of surface potential distribution between P(VDF-TrFE) and PDMS.

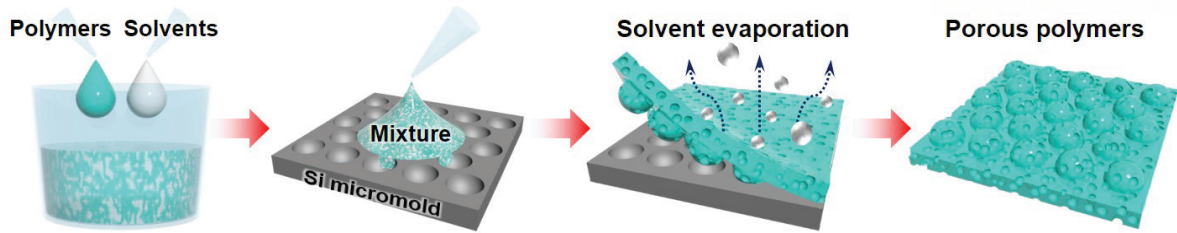


**Figure 4.2** Fabrication of hierarchical polymeric architectures. Schematic illustration of detailed fabrication process for hierarchical nanoporous and microridge-structured polymers by using the solvent-assisted micro-molding technique.

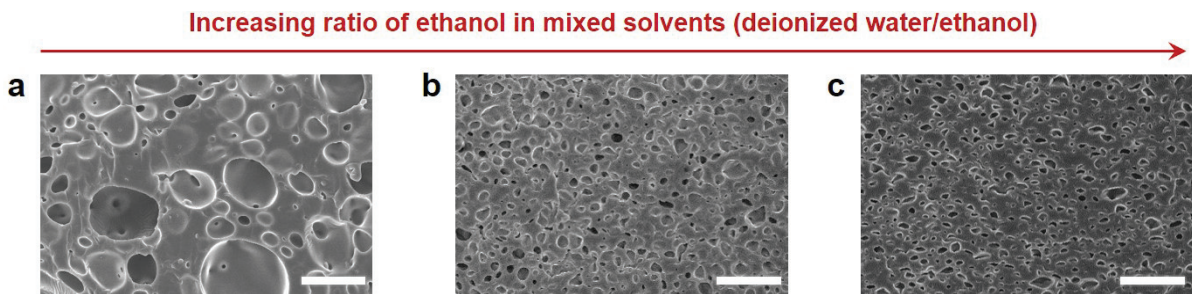


**Figure 4.3** Control the porosity in PDMS depending on the ratio of mixed solvents (deionized water/ethanol). SEM images of porous PDMS based on (a) 40% of deionized water, (b) 20% of deionized water and 20% of ethanol, and (c) 10% of deionized water and 30% of ethanol mixed in PDMS solution (scale bar: 25  $\mu\text{m}$ ).

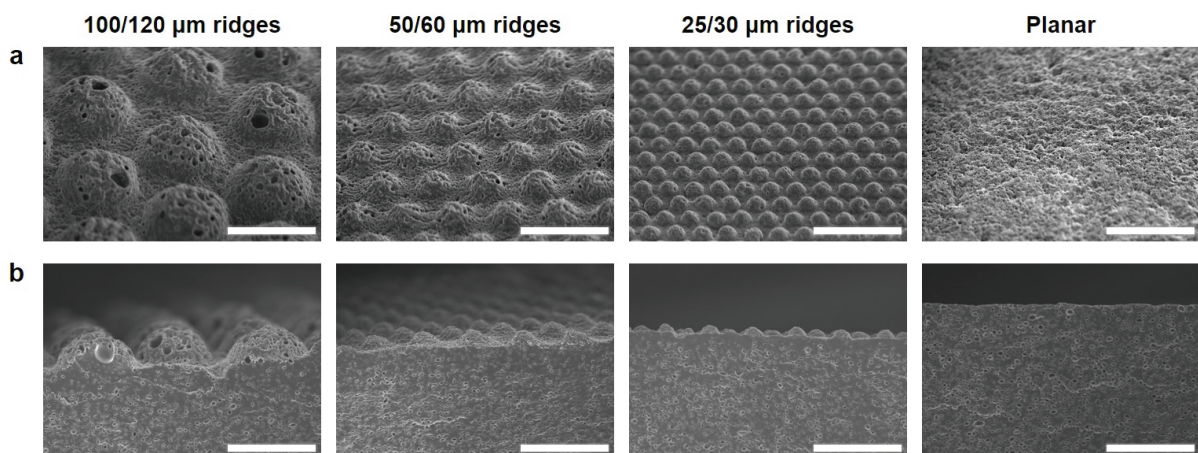


**Figure 4.4** SEM images of (a) tilted and (b) cross-sectional view with different width ( $w$ ) and pitch ( $p$ ) size ( $w/p = 100/120, 50/60, 25/30 \mu\text{m}$ ) of hierarchical microridge-structured and planar PDMS (scale bar: 100  $\mu\text{m}$ ).

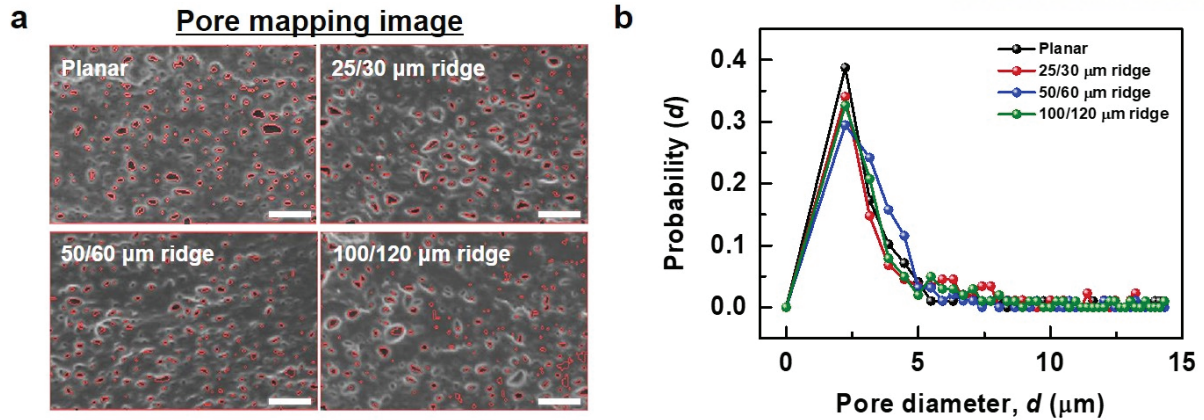


**Figure 4.5** Statistical estimation of pore size distribution in nanoporous PDMS. MATLAB image processing of (a) mapping pores in SEM images (scale bar: 50 μm) and (b) statistically calculated size distribution of pores in nanoporous PDMS with planar and different width/pitch sized microridge structures.

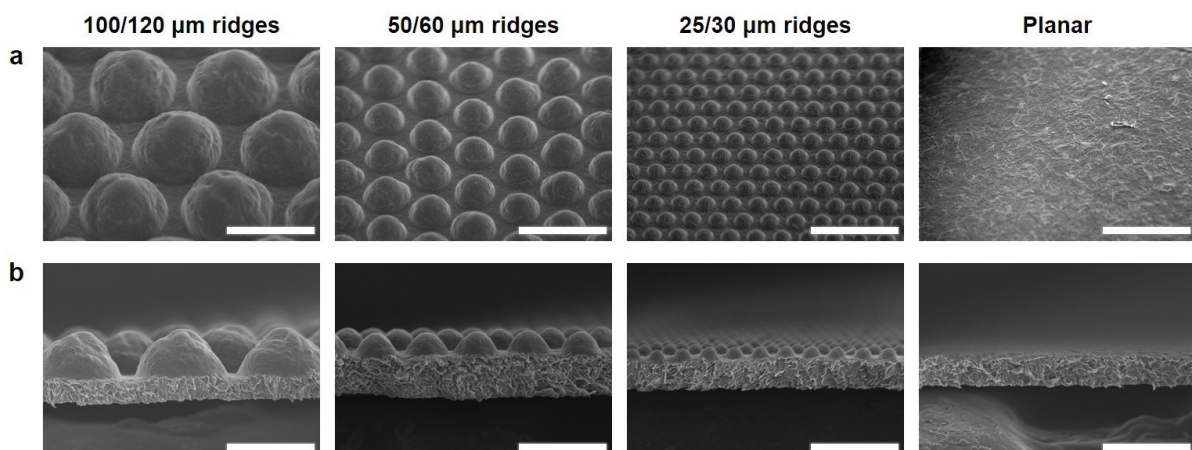


**Figure 4.6** SEM images of (a) tilted and (b) cross-sectional view with different width ( $w$ ) and pitch ( $p$ ) sizes ( $w/p = 100/120, 50/60, 25/30$  μm) of hierarchical microridge-structured and planar P(VDF-TrFE) (scale bar: 100 μm).

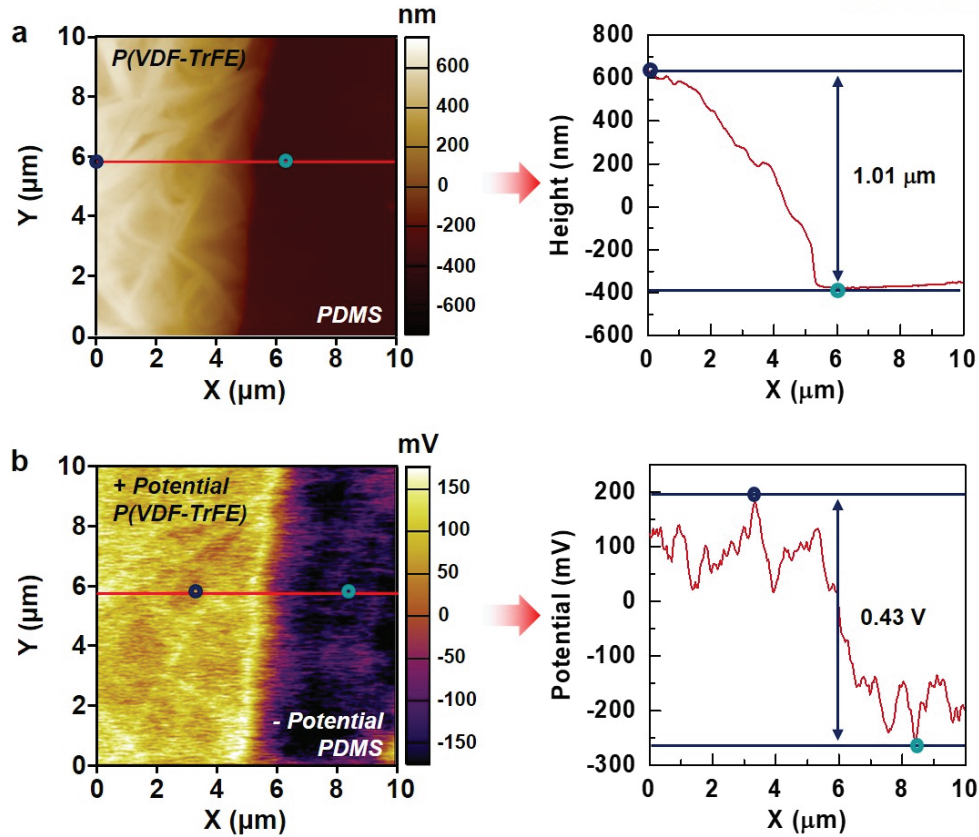


**Figure 4.7** Surface topologies and electrostatic potential distribution between P(VDF-TrFE) and PDMS. (a) AFM image of nanofiber-like morphology of P(VDF-TrFE) with height information ( $\sim 1.01 \mu\text{m}$ ) and (b) SKPM image of surface potential distribution with potential differences ( $\sim 0.43 \text{ V}$ ) between the P(VDF-TrFE) and PDMS.

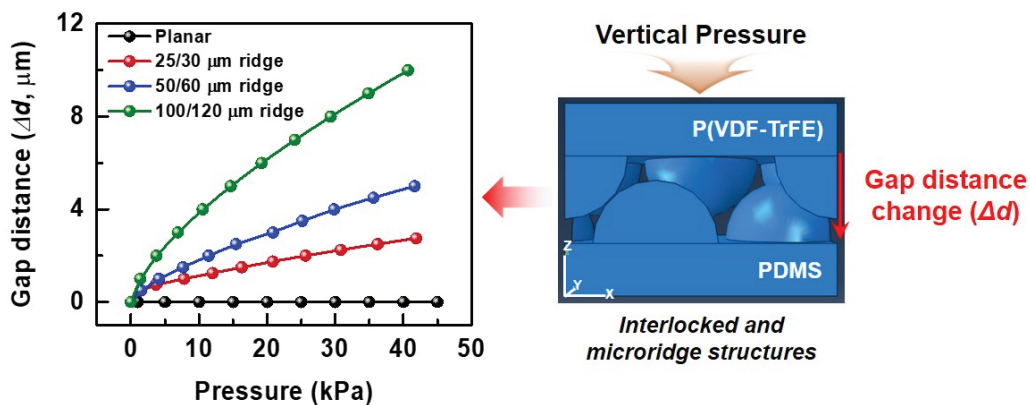


**Figure 4.8** Theoretical analysis of the gap distance change in the interlocked films. The finite element simulations by using ABAQUS software for the gap distance change ( $\Delta d$ ) from the initial gap in the interlocked microridge-structured and planar films with respect to the applied vertical pressure. Note that while the elastic modulus of P(VDF-TrFE) is constant as 1 GPa for all sizes of microridge arrays, that of PDMS decreases with the larger width/pitch size of microridge arrays (see the experimentally measured values of Figure 4.11).



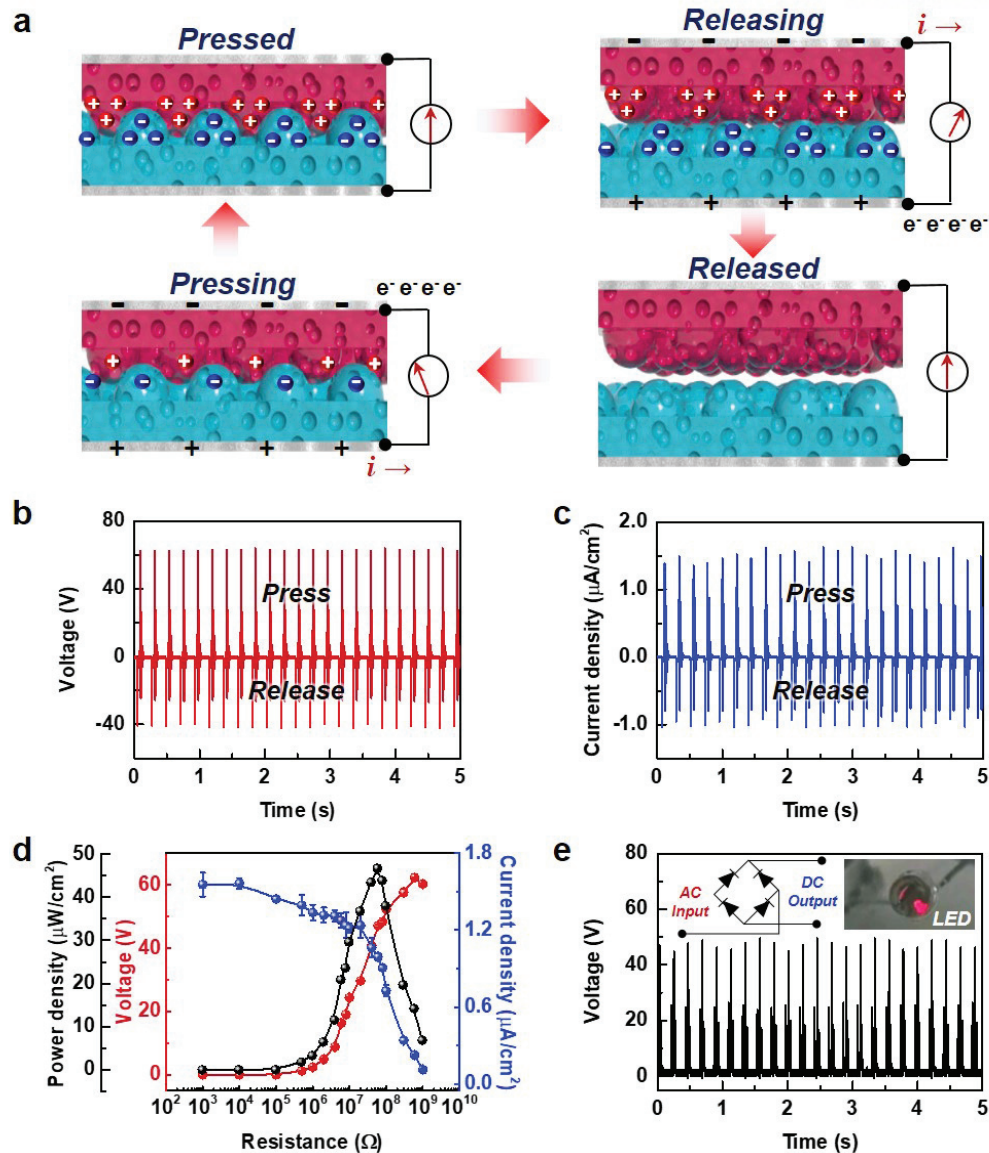


**Figure 4.9** Working principle of self-powered TESs and triboelectric output performances. (a) Schematic illustration of triboelectric charge generation and current flow mechanism between hierarchical and interlocked microridge structured P(VDF-TrFE) and PDMS. Triboelectric output (b) voltage and (c) current density under vertical pressure of 19.6 kPa with 4 Hz. (d) Triboelectric output variations of voltage, current density, and power density with an external load resistance from  $10^3$  to  $10^9$   $\Omega$ . (e) Rectified triboelectric voltage connected with four bridge rectifier and the inset of capability for lighting LED driven by self-powered TES.

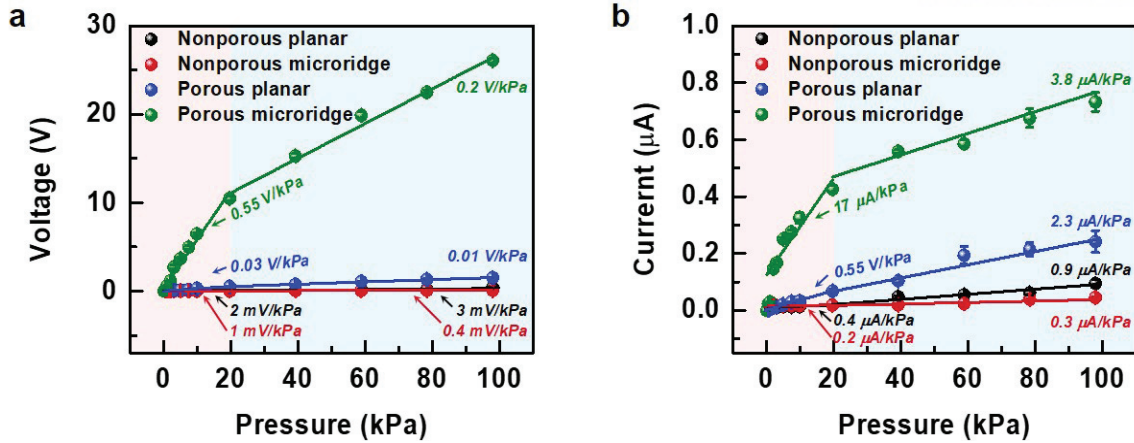


**Figure 4.10** Structural effect for triboelectric output performances and vertical pressure-sensitivity. Triboelectric (a) voltage and (b) current with the different structures including nanoporous, nonporous, and surface microridge-structured interlocked films following the applied vertical pressure.

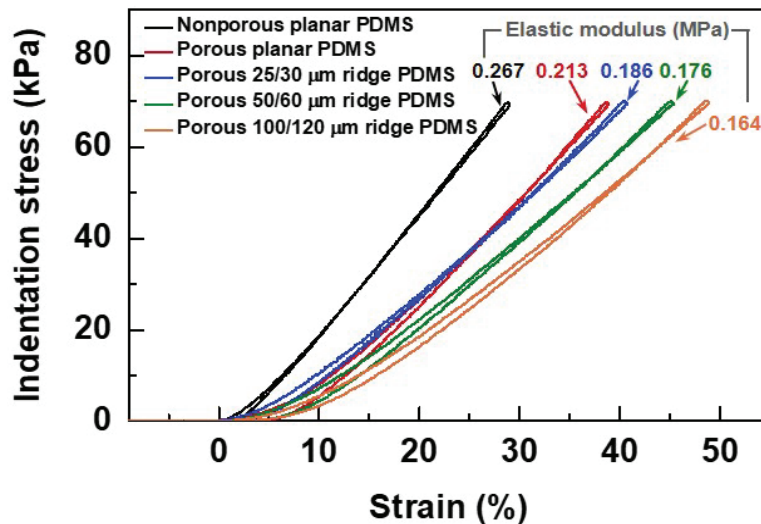


**Figure 4.11** Compressive stress-strain curves with different structured PDMS. The loading and unloading of stress–strain curves and compressive elastic modulus with nonporous, porous and different width/pitch size of microridge-structured and planar PDMS.

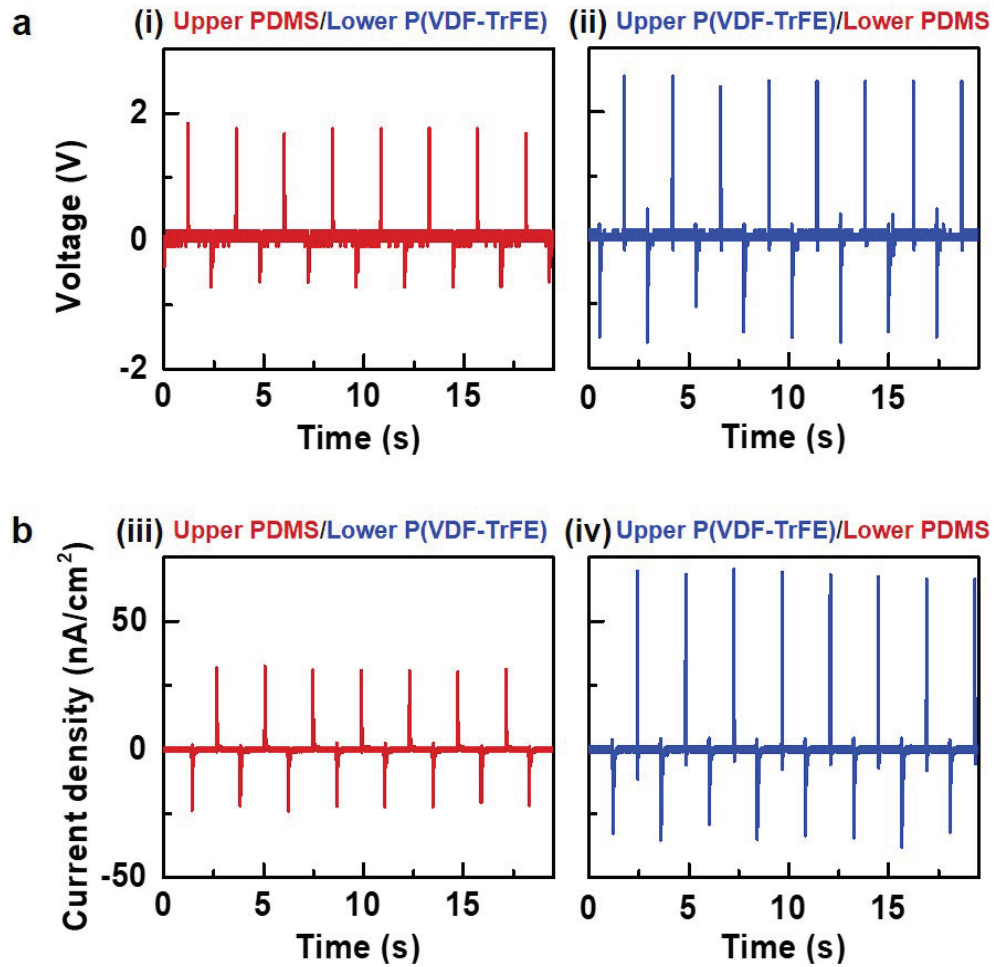


**Figure 4.12** Triboelectric output performances with gradient elastic modulus of interlocked P(VDF-TrFE) and PDMS. Triboelectric output (a) voltage and (b) current density to verify the effect of gradient elastic modulus with (i, iii) upper PDMS/lower P(VDF-TrFE) layers and (ii, iv) upper P(VDF-TrFE)/lower PDMS layers for effective stress transmission as well as increase of triboelectric output performances following the applied vertical pressure.

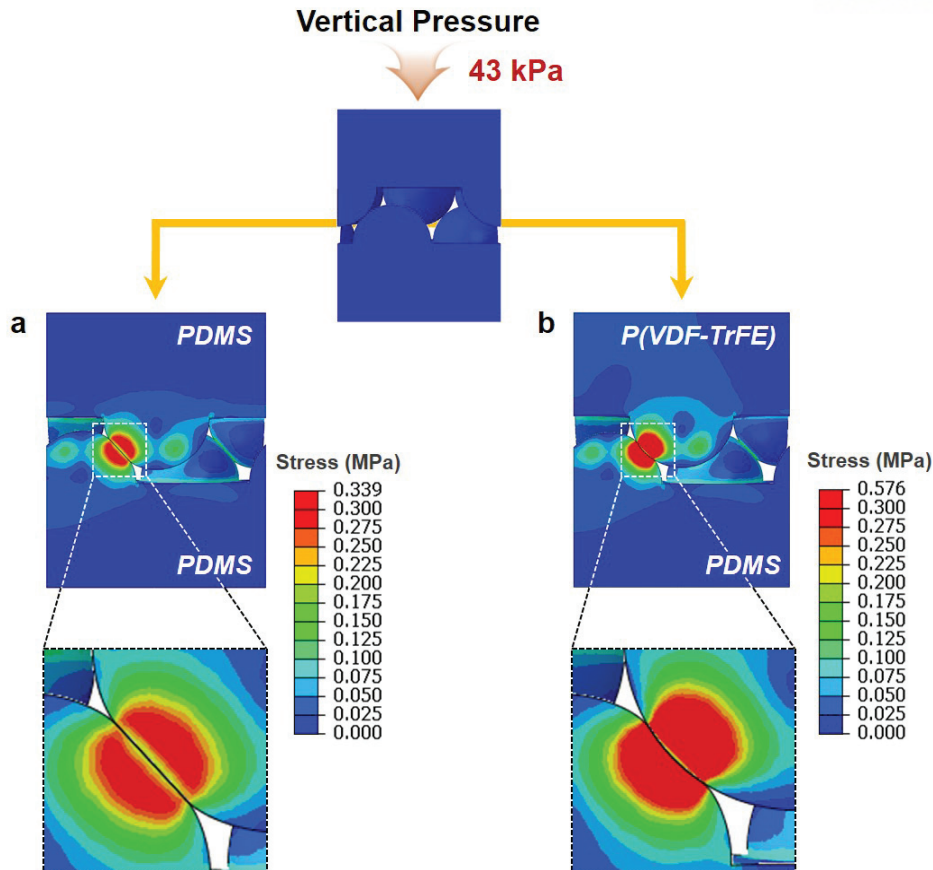


**Figure 4.13** Theoretical analysis of the stress distribution in the interlocked films under the vertical pressure. The finite element simulations of the stress distribution depending on the elastic modulus of interlocked and microridge-structured polymers by using ABAQUS software. The elastic modulus of P(VDF-TrFE) and PDMS is 1 GPa and 3 MPa, respectively. (a) and (b) show the result for the contact interaction for the interlocked PDMS-PDMS and the P(VDF-TrFE)-PDMS layers, respectively.

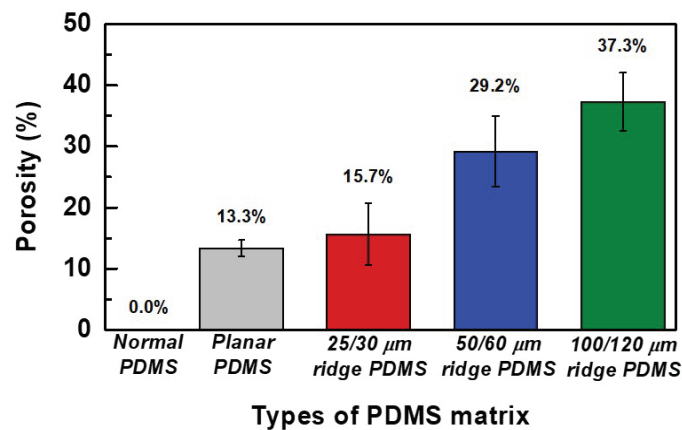


**Figure 4.14** Porosity of nanoporous PDMS. Comparison of porosity in nanoporous PDMS with different width/pitch sized microridge structures.

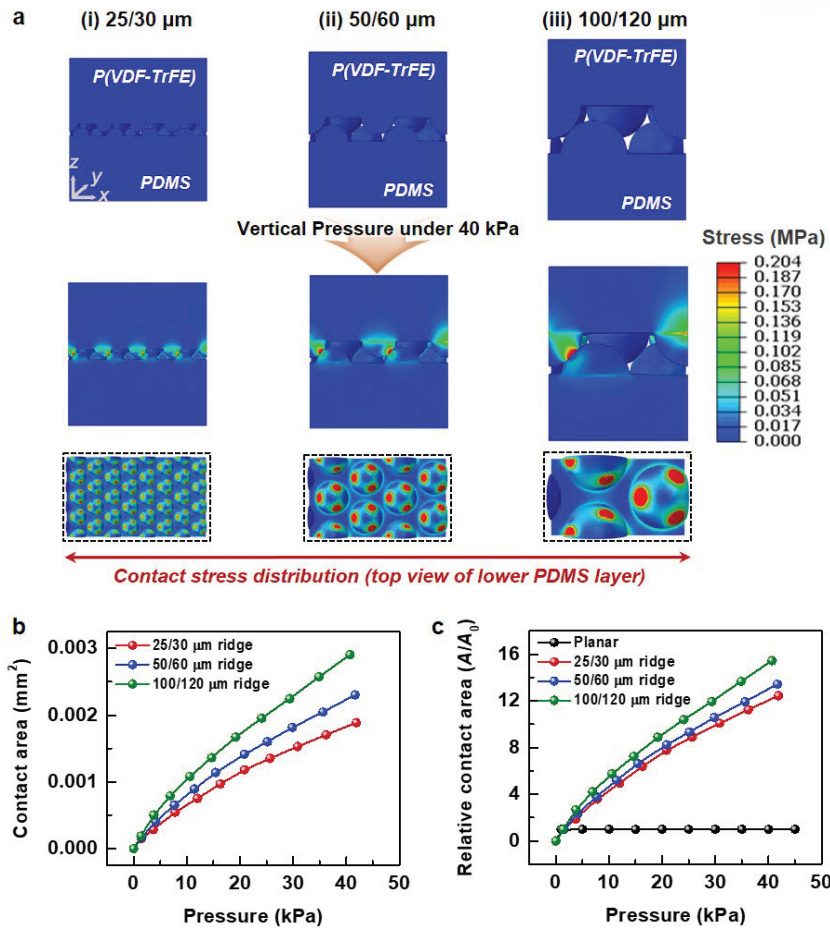


**Figure 4.15** Theoretical analysis of the stress distribution and numerical calculation of the contact area between the interlocked microridges under the vertical pressure. The finite element simulations for the comparison of (a) vertical stress concentration with the different width/pitch size of interlocked and microridge-structured polymers by using ABAQUS software and coincident numerical calculation of (b) contact area and (c) relative contact areal change with respect to the applied vertical pressure. The elastic modulus of P(VDF-TrFE) is 1 GPa, and that of PDMS is varied depending on the width/pitch size of microridge arrays (see the experimental values of Figure 4.11).

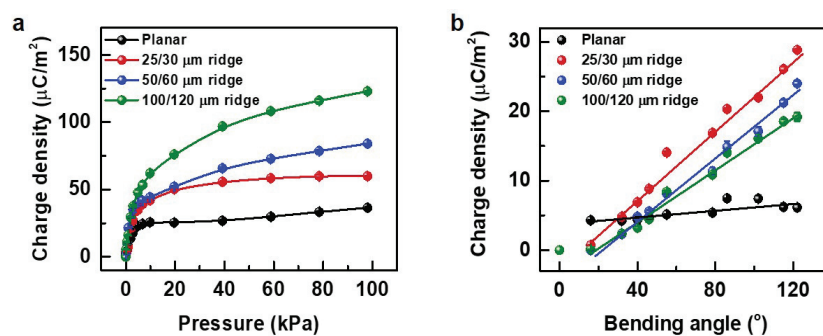


**Figure 4.16** Triboelectric charge density with the different width/pitch size of microridge arrays and planar structure based interlocked films following the amount of applied (a) vertical pressure and (b) bending stress.

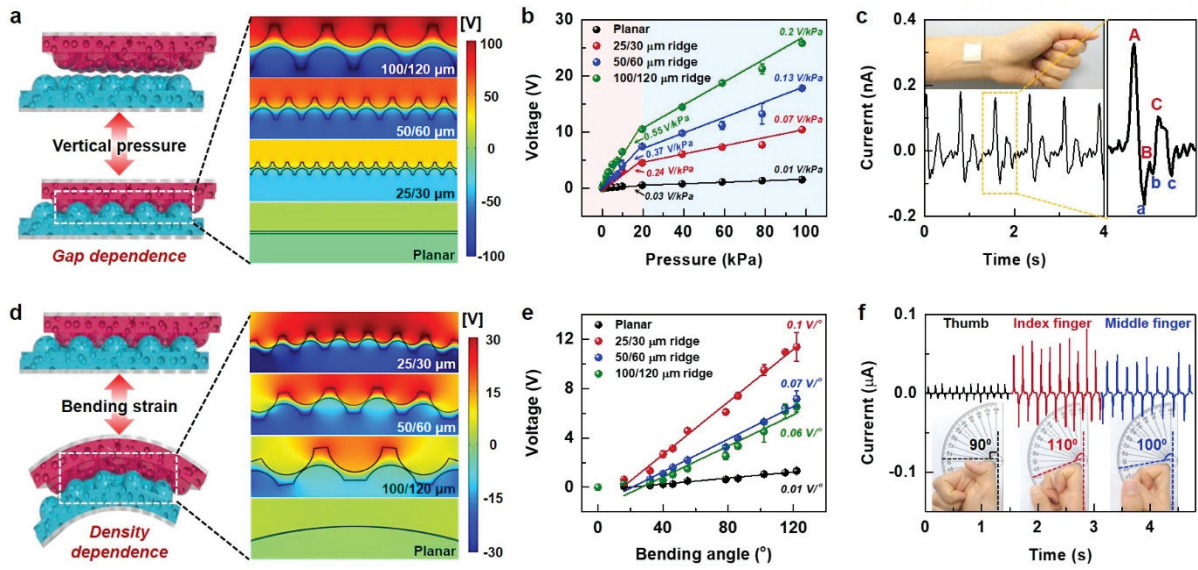


**Figure 4.17** Detection capabilities of vertical pressure and bending strain of ultraflexible TESs. (a) Schematic illustration of gap distance change of TESs under vertical pressure and theoretically calculated electric field distribution by COMSOL simulations depending on the width ( $w$ ) and pitch ( $p$ ) size of interlocked microridge arrays ( $w/p = 25/30, 50/60,$  and  $100/120 \mu\text{m}$ ) and planar structures. (b) Triboelectric voltage variations and pressure sensitivity following the size of interlocked microridge structured and planar films with the applied pressure. (c) Detection capability of radial artery pulse waves by ultraflexible TESs attached on the wrist. (d) Density of point contact between interlocked microridges under bending strain and coincident theoretically calculated electric field distribution by COMSOL simulations. The bending stress-induced (e) triboelectric voltage variations and bending sensitivity following the size of interlocked microridge structured and planar films with different bending angle. (f) Capability to monitor the different angle of finger bending motion by bending sensitive TESs.

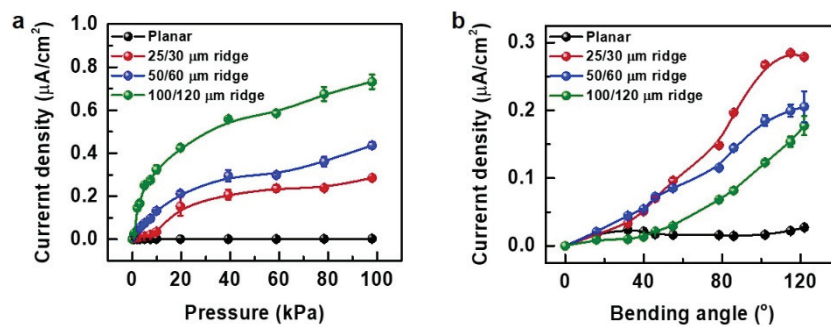


**Figure 4.18** Triboelectric current density with the different width/pitch size of microridge arrays and planar structure based interlocked films following the amount of applied (a) vertical pressure and (b) bending stress.

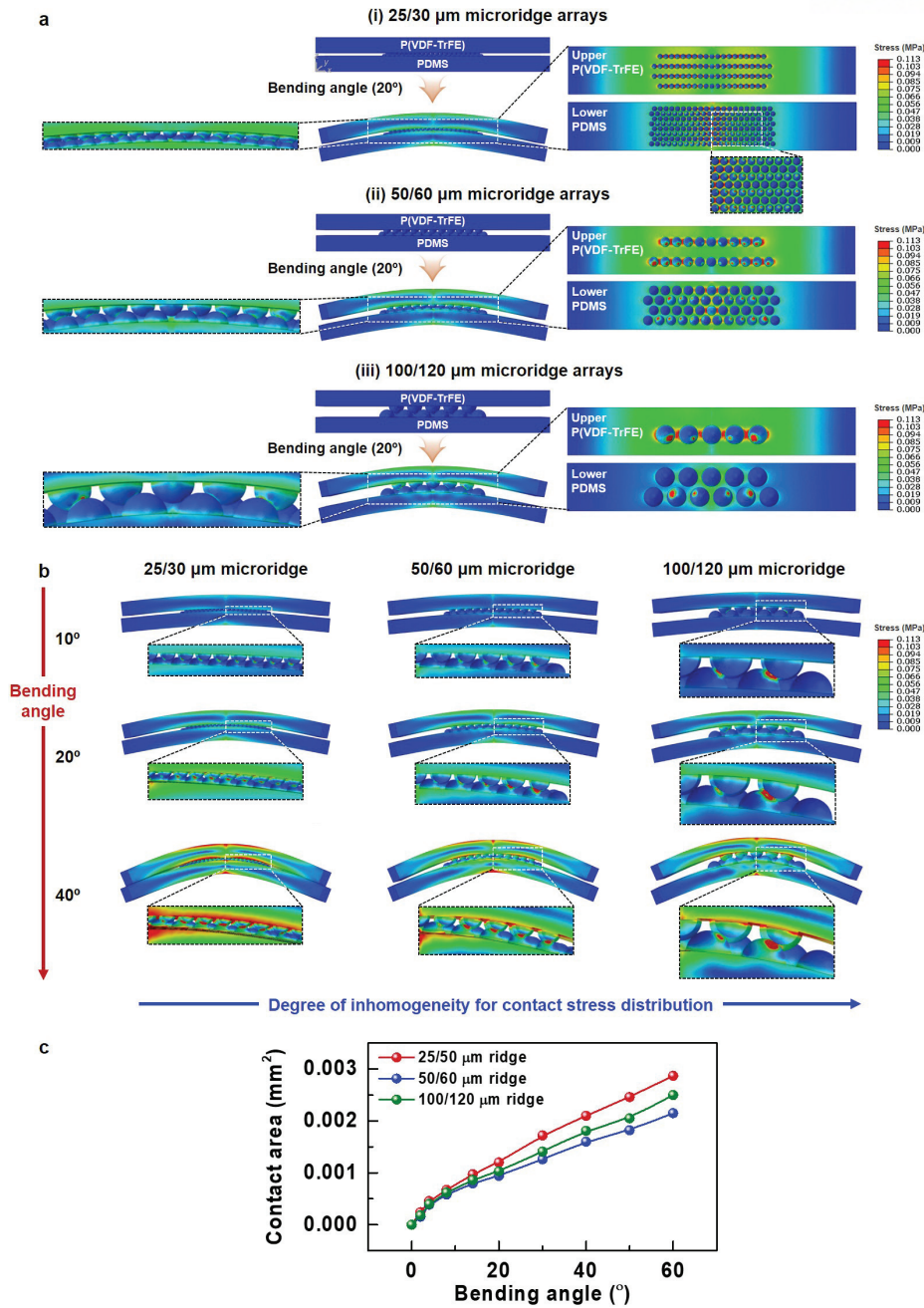


**Figure 4.19** Theoretical analysis of the stress distribution and numerical calculation of the contact area between the interlocked microridges under the bending strain. The finite element simulations for the comparison of (a) bending stress concentration between the different width/pitch ( $w/p = 25/30, 50/60, 100/120 \mu\text{m}$ ) size of interlocked and microridge-structured polymers by using ABAQUS software. (b) Comparison of the degree of inhomogeneity for the contact stress distribution between the different width/pitch size of interlocked microridge arrays. (c) Numerical calculation of contact area change between the interlocked and microridge-structured polymers with different width and pitch sizes as a function of bending strain. The elastic modulus of P(VDF-TrFE) is 1 GPa, and that of PDMS is varied depending on the width/pitch size of microridge arrays (see the experimental values of Figure 4.11).

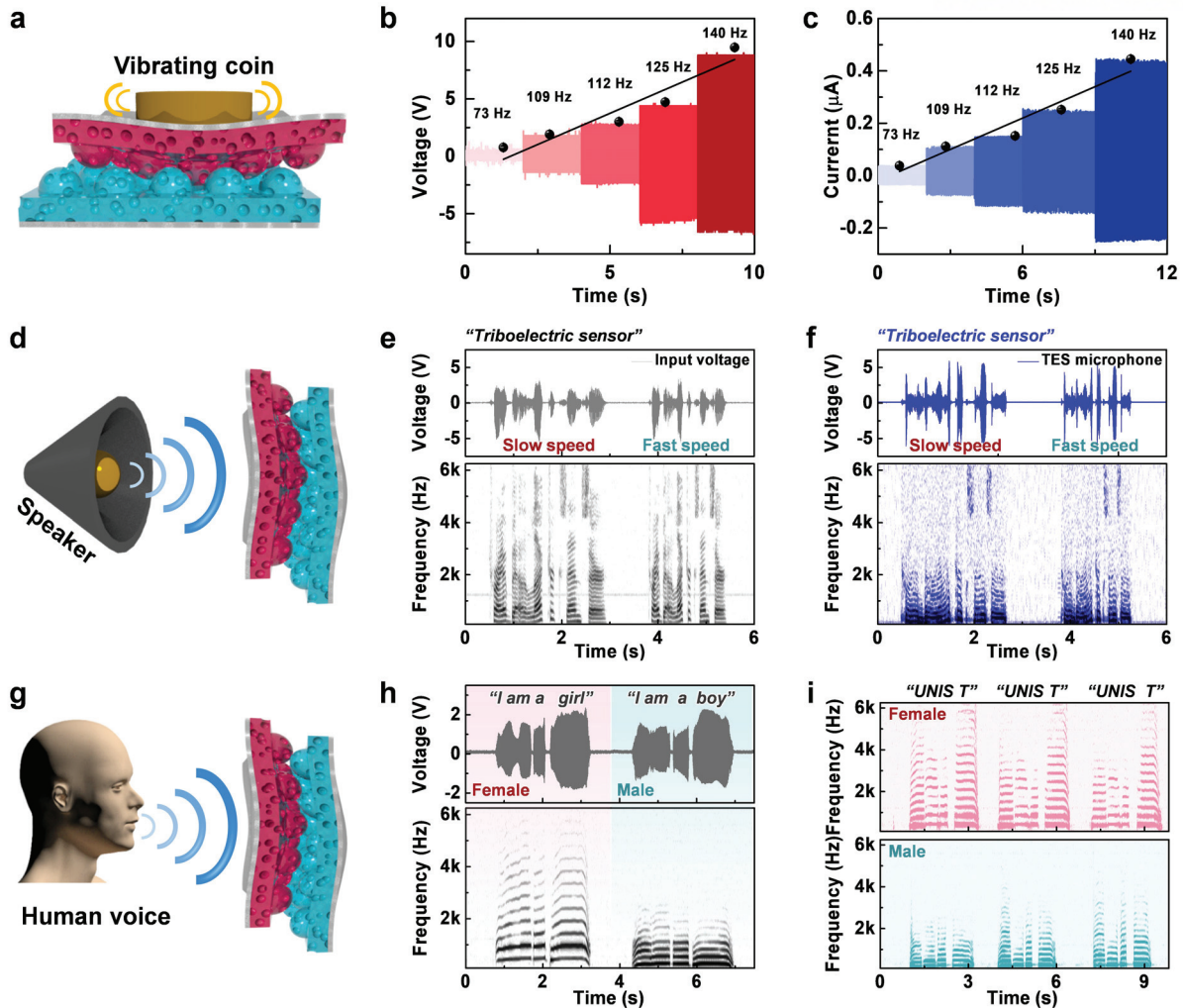


**Figure 4.20** Fast responsive TESs for high-frequency dynamic force sensing and acoustic wave detection. Sensing capabilities of (a) contact vibrations from vibrating coin and frequency-dependent triboelectric (b) voltage and (c) current following the increase of vibrational frequency from 73 to 140 Hz. (d) Sound detection test of TESs at the sound pressure level (SPL) of  $\sim 92$  dB with a fixed distance ( $\sim 2$  cm) from a commercial speaker. The speaker played the sound with the words of “triboelectric sensor” in low and high speed toward the TES. (e) Variations of input voltage signals to the speaker and corresponding short-time Fourier transform (STFT) signals analyzed for the harmonic frequency of acoustic vibrations. (f) The readout triboelectric voltage signals oscillated by the sound of “triboelectric sensor” played by speaker and the STFT spectrogram matched with frequency domain of input source. (g) Capability of human voice recognition of TES with voice of  $\sim 78$  dB and leaving a space of  $\sim 15$  cm between TES and subjects. (h) The oscillated triboelectric voltage signals by talking with the sentences of “I am a girl” and “I am a boy” from the female and male and corresponding STFT spectrogram to distinguish the different frequency domain of female and male voice. (i) Repeatable test to recognize and differentiate the words of “UNIS T” from the female and male voice and coincident STFT spectrogram.



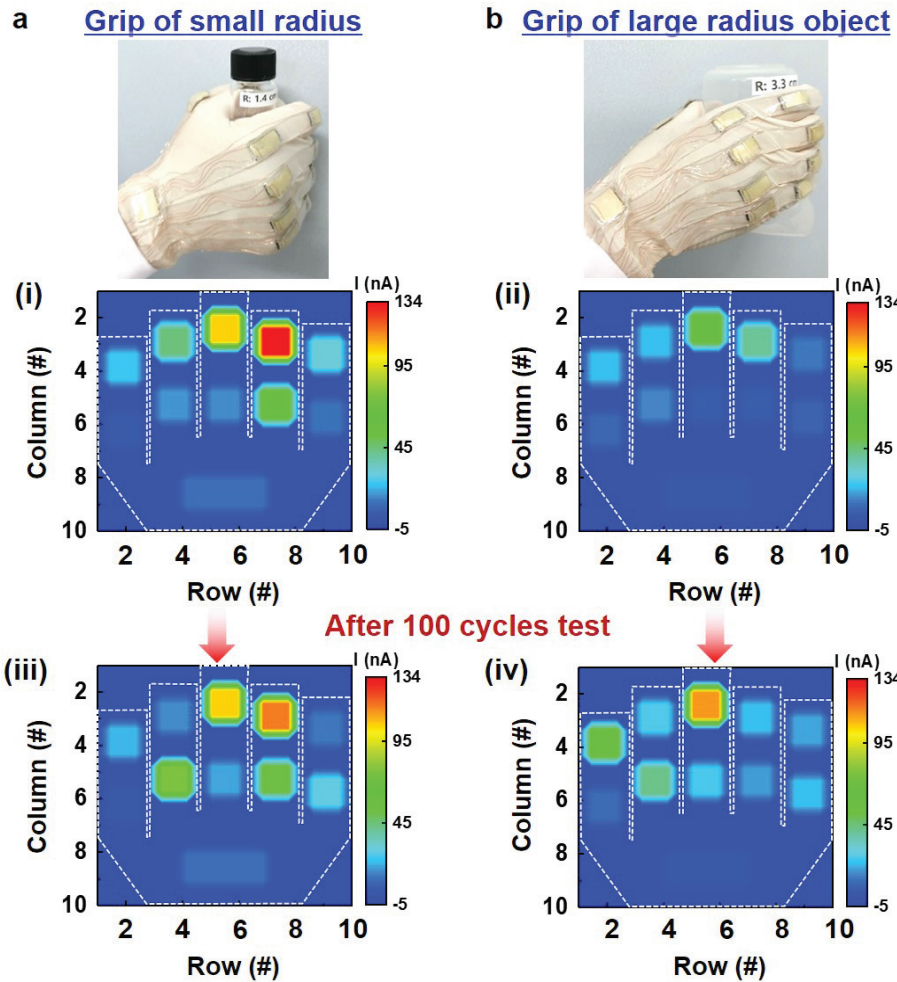


**Figure 4.21** Bendable smart glove for sensing the hand motion of grip of objects. Photographs and contour mapping patterns for grip of (a) small radius ( $\sim 1.4$  cm) of object and (b) large radius ( $\sim 3.3$  cm) of object. The contour mapping arrays of (a)-i, (b)-ii and (a)-iii, (b)-iv demonstrate the responding current signals from the grip of objects in first time and after 100 cyclic folding and unfolding of one's fist, respectively.

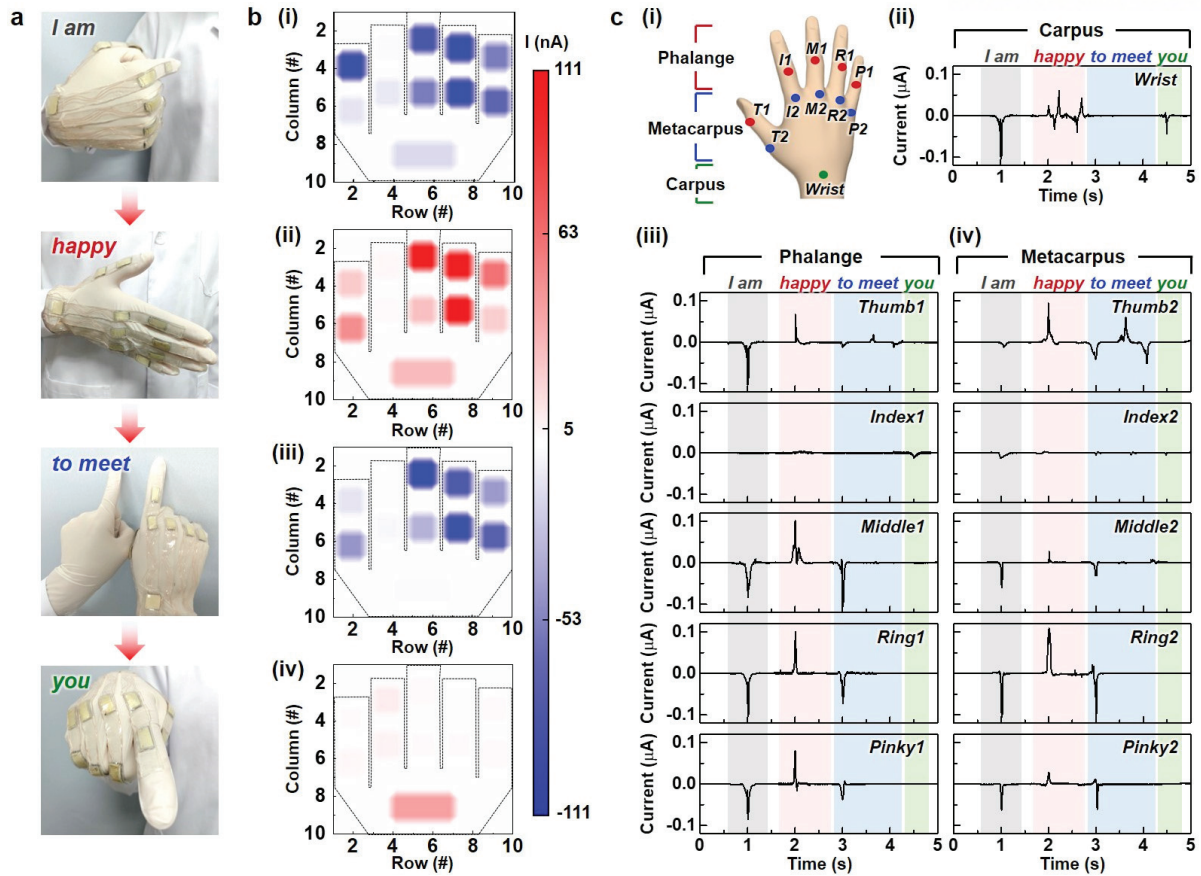


**Figure 4.22** Ultraflexible TESs for bendable smart glove and detection capabilities of sign language. (a) Photographs of bendable smart glove consisting of ultraflexible triboelectric sensing arrays at the joints on the human hand, performing the diverse motion matched with the different sign language of “I am”, “happy”, “to meet”, and “you”. (b) Contour mapping arrays from (i) to (iv) to analyze the triboelectric current signals from each TESs responding to the sign language. (c) Schematic illustration of location at each joints on the hand and corresponding abbreviation of thumb (T), index finger (I), middle finger (M), ring finger (R), and pinky (P) in (i). The hand bones divided with three part of carpus (ii), phalange (iii), and metacarpus (iv) during the real-time monitoring of the triboelectric current signals responding to the sign language.

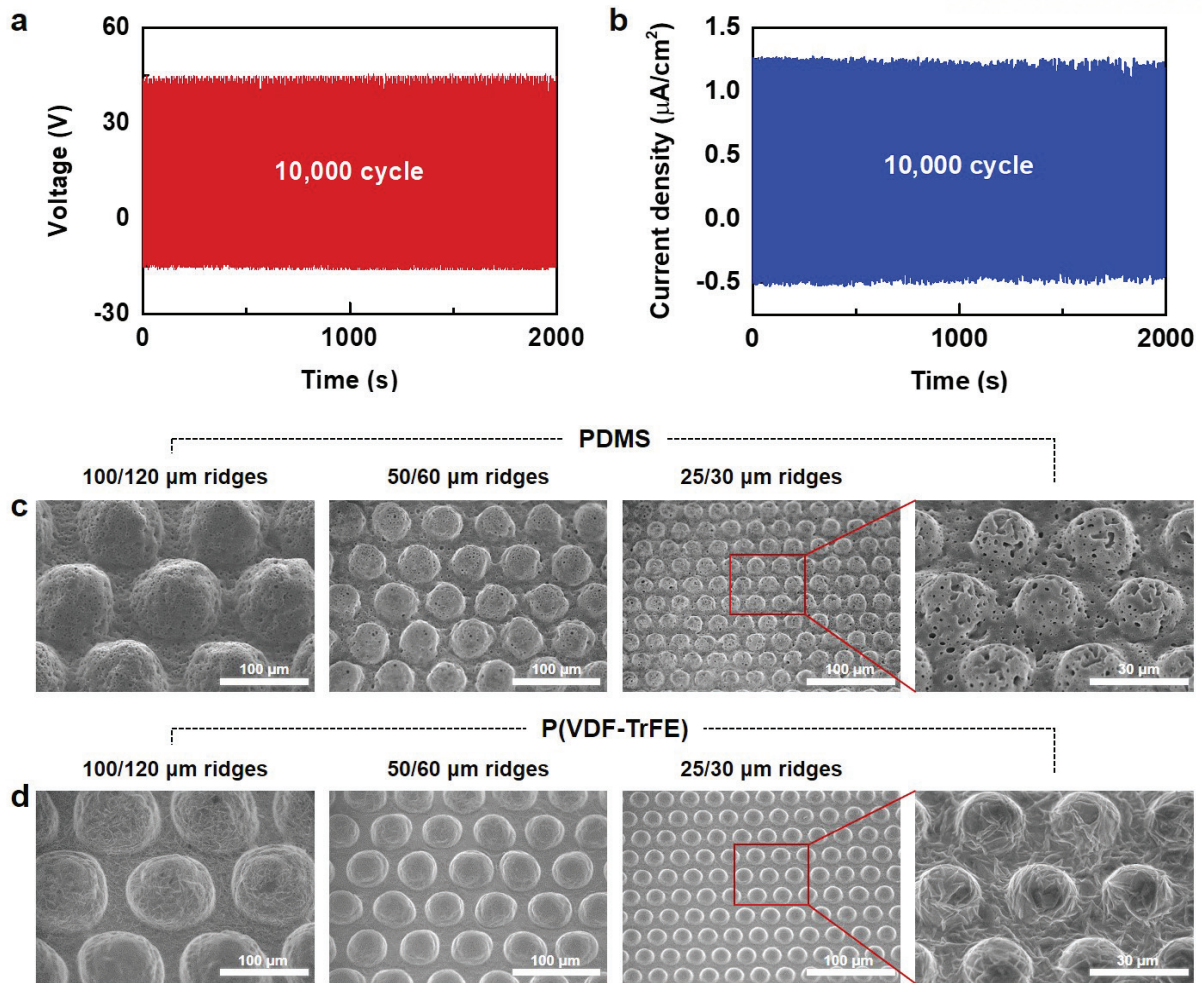


**Figure 4.23** Mechanical durability of TESs. Triboelectric output (a) voltage and (b) current density of interlocked and hierarchical microridge-structured P(VDF-TrFE) and PDMS with repeated loading and unloading ( $\sim 98$  kPa) cycles over 10,000 times. SEM images of nanoporous and microridge-structured (c) PDMS and (d) P(VDF-TrFE) with different width and pitch size after 10,000 cycle of pushing test.

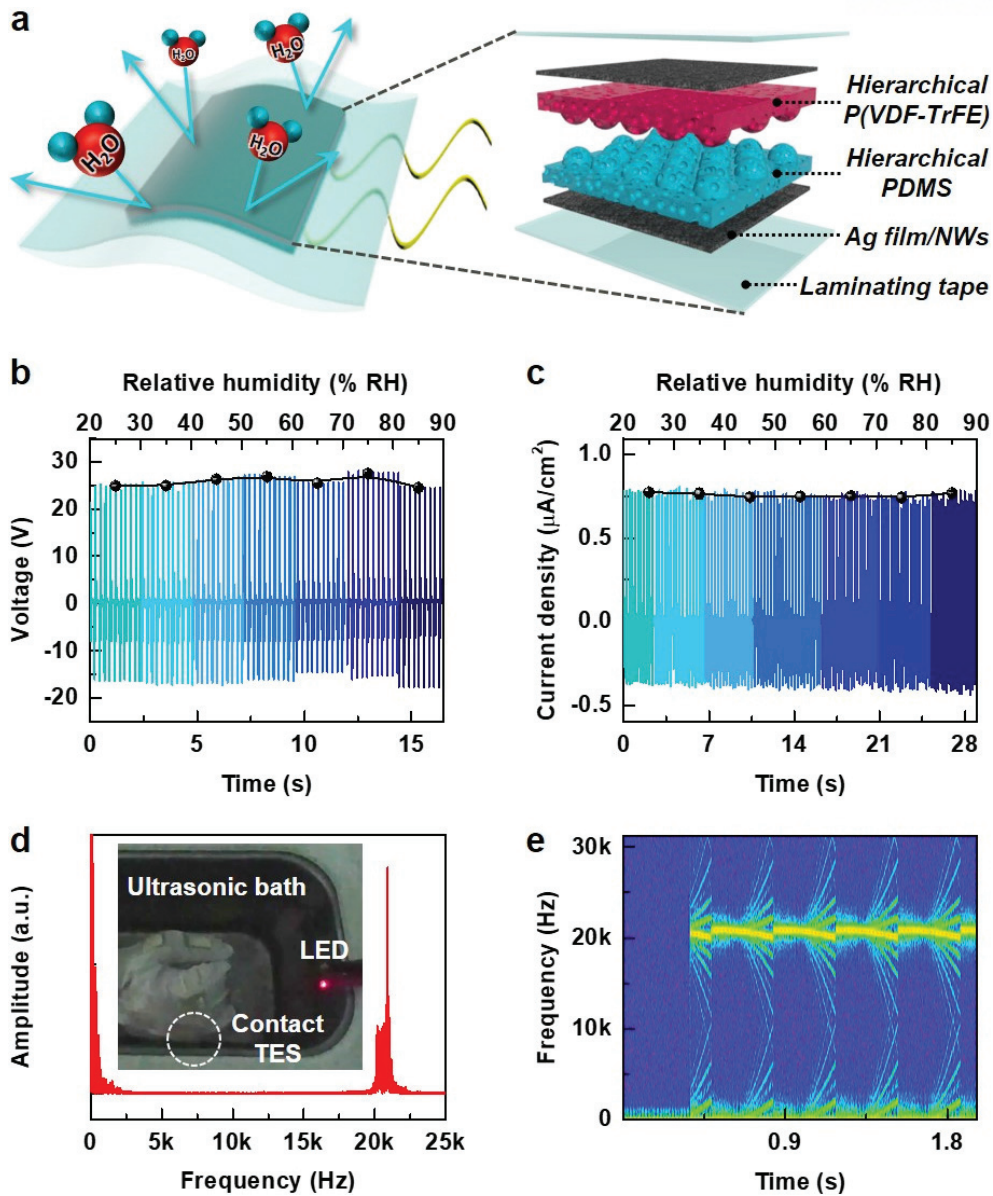


**Figure 4.24** Ultraflexible and fully packaged designs for humid-insensitive TESs. (a) Schematic illustration of humid-insensitive TESs packaged with laminating tape to prevent the permeation of atmospheric moisture. Variations of triboelectric (b) voltage and (c) current signals from the change of ambient relative humidity (20–90% RH). (d) Detection of ultrasonic waves with analysis of the impact frequency level ( $\sim 21$  kHz) from the FFT signals. Inset demonstrates the lighting LED operated by the fully packaged TES in the ultrasonic water bath. (e) Real-time variations of ultrasonic waveforms analyzed by the STFT spectrogram.

## Chapter 5. Summary and Future Perspectives

In this thesis, we have reported studies on the development of highly sensitive and multifunctional flexible sensing devices for future electronics. In particular, we have pursued to assign novel functionalities to flexible photodetectors and mechanosensors for practical applications through unique architectural designs of micro/nanostructured materials. Along with deep understanding on the basic properties of materials, complex fabrication approaches based on the synthesis of nanomaterials and conventional/unconventional lithographic techniques have facilitated the accomplishment of new micro/nanostructured materials based flexible devices.

In Chapter 1, a brief introduction of the flexible photodetectors and mechanosensors was discussed. We explained the sensing mechanisms of photodetectors and mechanosensors with figure-of-merits performances, respectively. Furthermore, existing strategies for improving the performance of devices such as light management techniques for photodetectors and stress transmission approaches for mechanosensors were shortly presented.

In Chapter 2, a hierarchical photodiode design of ZnO nanowires (NWs) on honeycomb-structured Si (H-Si) membranes was demonstrated to exhibit excellent omnidirectional light-absorption ability and thus maintained high photocurrents over broad spectral ranges (365 to 1,100 nm) for wide incident angles ( $0^\circ$  to  $70^\circ$ ), which enabled broadband omnidirectional light detection in flexible photodetectors. Furthermore, the stress-relieving honeycomb pattern within the photodiode micromembranes provided photodetectors with excellent mechanical flexibility (10% decrease in photocurrent at a bending radius of 3 mm) and durability (minimal change in photocurrent over 10,000 bending cycles). When employed in semiconductor thin films, the hierarchical NW/honeycomb heterostructure design acts as an efficient platform for various optoelectronic devices requiring mechanical flexibility and broadband omnidirectional light detection such as flexible image sensors, biomedical imaging, and smart/wearable systems.

In Chapter 3, a hierarchical methylammonium lead iodide (MAPbI<sub>3</sub>) nanoribbon (NR) arrays with controlled internal nanorod structures were fabricated by simple spin-coating with solvent treatment process, and we investigated the suitability of these arrays for high-performance and multifunctional photodetectors. In the UV-to-800-nm range, photodetectors based on the hierarchical MAPbI<sub>3</sub> NR arrays exhibited specific detectivities 18.1–23.7 times higher than those of photodetectors based on MAPbI<sub>3</sub> films due to the effective photon management and reduced charge trap states in the hierarchical MAPbI<sub>3</sub> NR arrays. The solution-processed hierarchical MAPbI<sub>3</sub> NRs can be fabricated on various substrates including ultrathin polyimide, which facilitated the development of flexible photodetectors with highly stable photoresponse under bending strain. Furthermore, the ferroelectricity and the highly anisotropic alignment of MAPbI<sub>3</sub> NR arrays allowed multifunctional photodetectors capable of self-powered and polarization-sensitive light detection, respectively. The

strategy used to fabricate the hierarchical organic–inorganic perovskite NR arrays is believed to be applicable to other types of perovskites and can probably be used to construct various optoelectronic devices based on hierarchical nanostructures.

In Chapter 4, inspired by skin structure and function, we fabricated hierarchical nanoporous and interlocked microridge structured polymers with gradient stiffness for spacer-free, ultrathin, and highly sensitive triboelectric sensors (TESs). The skin-inspired hierarchical polymers with gradient elastic modulus enhanced the compressibility and contact areal differences due to effective transmission of the external stress from stiff to soft layers, resulting in highly sensitive TESs capable of detecting human vital signs and voice. In addition, the microridges in the interlocked polymers provided an effective variation of gap distance between interlocked layers without using the bulk spacer and thus facilitated the ultrathin and flexible design of TESs that could be worn on the body and detect a variety of pressing, bending, and twisting motions even in humid and underwater environments. Our TESs exhibited the highest power density ( $46.7 \mu\text{W}/\text{cm}^2$ ), pressure ( $0.55 \text{ V}/\text{kPa}$ ), and bending ( $\sim 0.1 \text{ V}/^\circ$ ) sensitivities ever reported on flexible TESs. The proposed design of hierarchical polymer architectures for the flexible and wearable TESs can find numerous applications in next-generation wearable electronics.

Overall, this research has demonstrated some flexible electronic devices and sensors with diverse micro/nanofabrication routes. The novel design of micro/nanostructured materials allows to enhance the device performance as well as to accord unique functionalities to both photodetectors and mechanosensors. We expect that the high-performance and multifunctional flexible electronic devices and sensors suggested in this thesis will greatly contribute to improve the technical advancement in wearable electronic sensors as well as future technologies of internet of things, artificial intelligence, and big data for the quality of human life.

## Appendix A: General Expression of the Open-Circuit Voltage ( $V_{OC}$ ) and Short-Circuit Current ( $I_{SC}$ )

Following the Gauss law, the electric fields ( $E$ ) of P(VDF-TrFE), PDMS, and inside air gap are followed by Equations 1–3,<sup>[1]</sup>

$$\text{Electric field of P(VDF-TrFE): } E_1 = -\frac{Q}{A\varepsilon_0\varepsilon_{r1}} \quad (1)$$

$$\text{Electric field of PDMS: } E_2 = -\frac{Q}{A\varepsilon_0\varepsilon_{r2}} \quad (2)$$

$$\text{Electric field of inside air gap: } E_{air} = -\frac{(Q-A\sigma(t))}{A\varepsilon_0} \quad (3)$$

where  $\varepsilon_0$ ,  $\varepsilon_{r1}$ , and  $\varepsilon_{r2}$  are individual permittivity of air, P(VDF-TrFE), and PDMS, and  $Q$  is the amount of charges on both electrodes induced by potential,  $A$  is the area of electrodes,  $\sigma$  is the triboelectric charge density. Therefore, the triboelectric voltage in the contact-separation mode of triboelectric devices can be derived as follows (Equation 4)

$$V = E_1T_1 + E_2T_2 + E_{air}d = -\frac{Q}{A\varepsilon_0}\left(\frac{T_1}{\varepsilon_{r1}} + \frac{T_2}{\varepsilon_{r2}} + d(t)\right) + \frac{\sigma d(t)}{\varepsilon_0} = -\frac{Q}{A\varepsilon_0}(B + d(t)) + \frac{\sigma d(t)}{\varepsilon_0} \quad (4)$$

Where  $T_1$ ,  $T_2$ , and  $d$  are the thickness of P(VDF-TrFE) and PDMS and air gap distance, respectively. Because TESs are in the open-circuit (OC) condition without charge transfer ( $Q = 0$ ) and in the short-circuit (SC) condition for zero total voltage ( $V = 0$ ), the open-circuit voltage ( $V_{OC}$ ) and short-circuit current ( $I_{SC}$ ) are shown in Equations 5–7

$$V_{OC} = \frac{\sigma d(t)}{\varepsilon_0} \quad (5)$$

$$Q_{SC} = \frac{A\sigma d(t)}{(B+d(t))} \quad (6)$$

$$I_{SC} = \frac{dQ_{SC}}{dt} = \frac{AB\sigma v(t)}{(B+d(t))^2} \quad (7)$$

where  $v(t)$  is the velocity of contact-separation motion.

### Reference

[1] Niu, S. M.; Wang, S. H.; Lin, L.; Liu, Y.; Zhou, Y. S.; Hu, Y. F.; Wang, Z. L. Theoretical Study of Contact-Mode Triboelectric Nanogenerators as an Effective Power Source. *Energy Environ. Sci.* **2013**, *6*, 3576–3583.

## Appendix B: List of Achievements

### Peer Reviewed Research Publications [†: Equal contribution]

1. Saewon Kang, Jaeki Jeong, Seungse Cho, Yung Jin Yoon, Seungyoung Park, **Seongdong Lim**, Jin Young Kim and Hyunhyub Ko\*, “Ultrathin, Lightweight and Flexible Perovskite Solar Cells with an Excellent Power-Per-Weight Performance”, *J. Mater. Chem. A* **2019**, *7*, 1107.
2. **Seongdong Lim**, Minjeong Ha, Youngsu Lee, and Hyunhyub Ko\* “Large-Area, Solution-Processed, Hierarchical MAPbI<sub>3</sub> Nanoribbon Arrays for Self-Powered Flexible Photodetectors”, *Adv. Optical Mater.* **2018**, *6*, 1800615.
3. Minjeong Ha†, **Seongdong Lim**†, and Hyunhyub Ko\*, “Wearable and Flexible Sensors for User-Interactive Health-Monitoring Devices”, *J. Mater. Chem. B* **2018**, *6*, 4043. (Featured as Top 5% most-read articles published in *J. Mater. Chem. B* during Q2 2018)
4. Minjeong Ha†, **Seongdong Lim**†, Soowon Cho†, Youngoh Lee, Sangyun Na, Chunggi Baig\*, and Hyunhyub Ko\*, “Skin-Inspired Hierarchical Polymer Architectures with Gradient Stiffness for Space-Free, Ultrathin, and Highly Sensitive Triboelectric Sensors”, *ACS Nano* **2018**, *12*, 3964. (24th Humantech paper award)
5. Ziyauddin Khan\*, Baskar Senthilkumar, **Seongdong Lim**, Ravi Shanker, Youngsik Kim, and Hyunhyub Ko\*, “Redox-Additive-Enhanced High Capacitance Supercapacitors Based on Co<sub>2</sub>P<sub>2</sub>O<sub>7</sub> Nanosheets”, *Adv. Mater. Interfaces* **2017**, *4*, 1700059.
6. **Seongdong Lim**, Doo-Seung Um, Minjeong Ha, Qianpeng Zhang, Youngsu Lee, Yuanjing Lin, Zhiyong Fan, and Hyunhyub Ko\*, “Broadband Omnidirectional Light Detection in Flexible and Hierarchical ZnO/Si Heterojunction Photodiodes”, *Nano Res.* **2017**, *10*, 22. (22nd Humantech paper award)
7. Doo-Seung Um, Youngsu Lee, **Seongdong Lim**, Seungyoung Park, Hochan Lee, and Hyunhyub Ko\*, “High-Performance MoS<sub>2</sub>/CuO Nanosheet-on-One-Dimensional Heterojunction Photodetectors”, *ACS Appl. Mater. Interfaces* **2016**, *8*, 33955.
8. Doo-Seung Um, Youngsu Lee, **Seongdong Lim**, Jonghwa Park, Wen-Chun Yen, Yu-Lun Chueh, Hyung-jun Kim, and Hyunhyub Ko\*, “InGaAs Nanomembrane/Si van der Waals Heterojunction Photodiodes with Broadband and High Photoresponsivity”, *ACS Appl. Mater. Interfaces* **2016**, *8*, 26105.
9. Hochan Lee, Doo-Seung Um, Youngsu Lee, **Seongdong Lim**, Hyung-jun Kim and Hyunhyub Ko\*, “Octopus-Inspired Smart Adhesive Pads for Transfer Printing of Semiconducting Nanomembranes”, *Adv. Mater.* **2016**, *28*, 7457.
10. Minjeong Ha, **Seongdong Lim**, Jonghwa Park, Doo-Seung Um, Youngoh Lee, and Hyunhyub



- Ko\*, “Bioinspired Interlocked and Hierarchical Design of ZnO Nanowire Arrays for Static and Dynamic Pressure-Sensitive Electronic Skins”, *Adv. Funct. Mater.* **2015**, *25*, 2841. (Frontispiece)  
(21st Humantech paper award)
11. Jonghwa Park, Youngoh Lee, **Seongdong Lim**, Youngsu Lee, Youngdo Jung, Hyuneui Lim, Hyunhyub Ko\*, “Ultrasensitive Piezoresistive Pressure Sensors Based on Interlocked Micropillar Arrays”, *BioNanoScience* **2014**, *4*, 349.
  12. Doo-Seung Um, **Seongdong Lim**, Youngsu Lee, Hochan Lee, Hyung-jun Kim, Wen-Chun Yen, Yu-Lun Chueh, and Hyunhyub Ko\*, “Vacuum-Induced Wrinkle Arrays of InGaAs Semiconductor Nanomembranes on Polydimethylsiloxane Microwell Arrays”, *ACS Nano* **2014**, *8*, 3080.
  13. Kyung-Ho Kim, Doo-Seung Um, Hochan Lee, **Seongdong Lim**, Joonyeon Chang, Hyun Cheol Koo, Min-Wook Oh, Hyunhyub Ko\*, and Hyung-jun Kim\*, “Gate-Controlled Spin-Orbit Interaction in InAs High-Electron Mobility Transistor Layers Epitaxially Transferred onto Si Substrates”, *ACS Nano* **2013**, *7*, 9106.
  14. Hyojin Moon, Woo Gyum Kim, **Seongdong Lim**, Young Ji Kang, Hyun-Hee Shin, Hyunhyub Ko, Sung You Hong, and Sebyung Kang, “Fabrication of Uniform Layer-by-Layer Assemblies with Complementary Protein Cage Nanobuilding Blocks *via* Simple His-tag/Metal Recognition”, *J. Mater. Chem. B* **2013**, *1*, 4504.

## Book Chapters

---

1. Minjeong Ha, **Seongdong Lim**, and Hyunhyub Ko\*, “Flexible and Stretchable Medical Devices [Chapter 12. Flexible Health-Monitoring Devices/Sensors]”, *John Wiley & Sons* (2018).

## Academic Activity

---

### International conference and presentation

1. **[Oral]** *Invited by Prof. Xavier Crispin* “Hierarchical Micro/Nanostructured Hybrid Materials for Multifunctional and Flexible Photodetectors” Linköpings universitet, Norrköping, Sweden (2018.06.28)
2. **[Oral]** *2018 E-MRS Spring Meeting and Exhibit*, European Materials Research Society, “Hierarchical Micro/Nanostructured Hybrid Materials for High-Performance and Multifunctional Photodetectors” Strasbourg, France (2018.06.18-22)
3. **[Oral]** *The 4th International Conference on Advanced Electromaterials (ICAE 2017)*, The Korean Institute of Electrical and Electronic Material Engineers (KIEEME), “Omnidirectional

Photodetectors Based on Hierarchical ZnO Nanowires on Flexible Honeycomb-Structured Si Membranes” Jeju, Korea (2017.11.21-24)

4. **[Participant]** *2016 Inter-Academy-Seoul Science Forum (IASSF)*, The Korean Academy of Science and Technology, “Invited as a promising young scientist of Korea” Seoul, Korea (2016.11.02-03)
5. **[Oral]** *The 16th International Meeting on Information Display (IMID)*, The Korean Information Display Society, “Hierarchically Designed ZnO Nanowire Arrays on Honeycomb-Structured Si Membranes for Omnidirectional and Flexible Photodetectors” Jeju, Korea (2016.08.23-26)
6. **[Poster]** *2015 MRS Fall Meeting*, Materials Research Society, “Hierarchically Designed ZnO Nanowire Arrays on Si Honeycomb Structures for Highly Efficient Omnidirectional and Flexible Photodetectors” Boston, Massachusetts, USA (2015.11.29-12.04)
7. **[Poster]** *The 15th International Meeting on Information Display (IMID)*, The Korean Information Display Society, “Hierarchical ZnO Nanowire Arrays on Si Honeycomb Structures for Flexible and Omnidirectional Photodetectors” Daegu, Korea (2015.08.18-21)
8. **[Participant]** *2014 MRS Spring Meeting*, Materials Research Society, “Epitaxial Transfer Printing of High-Performance III-V/Si Hetero-Junction Photodiodes” San Francisco, California, USA (2014.04.21-25)

### **Domestic conference**

1. **[Poster]** *2018 Annual Fall Meeting of The Polymer Society of Korea*, The Polymer Society of Korea, “Multifunctional and Flexible Photodetectors Based on Hierarchical Micro/Nanostructured Hybrid Materials” Gyeongju, Korea (2018.10.10-12)
2. **[Poster]** *KIEEME Annual Summer Conference 2016*, The Korean Institute of Electrical and Electronic Material Engineers (KIEEME), “Hierarchical ZnO Nanowires on Honeycomb-Shaped Si Membranes for Highly Efficient Omnidirectional and Flexible Photodetectors” Gyeongju, Korea (2016.06.22-24)
3. **[Oral]** *2016 MRS-K Spring Meeting*, Materials Research Society of Korea, “Omnidirectional and Flexible Photodetector Based on Hierarchical ZnO Nanowires on Honeycomb-Structured Si Membranes” Yeosu, Korea (2016.05.18-20)
4. **[Poster]** *2015 Annual Spring Meeting of The Polymer Society of Korea*, The Polymer Society of Korea, “Fabrication of Hierarchical Nanowire on Honeycomb Structures for Flexible and Omnidirectional n-ZnO NWs/p-Si Heterostructure Photodetectors” Daejeon, Korea (2015.04.08-10)

5. **[Poster]** *2014 Annual Fall Meeting of The Polymer Society of Korea*, The Polymer Society of Korea, “Omnidirectional and Flexible n-ZnO/p-Si Heterojunction Photodetectors” Jeju, Korea (2014.10.06-08)
6. **[Participant]** *2013 Annual Fall Meeting of The Polymer Society of Korea*, The Polymer Society of Korea, “Wrinkling behavior of III-V semiconductor nanomembranes on micropatterned soft substrates” Changwon, Korea (2013.10.10-11)

### **Honors and Awards**

---

- Outstanding Graduate Student Award, Department of Energy Engineering, UNIST (2018)
- Young scientist award in 2018 E-MRS spring meeting, Symposium W - Hybrid materials: state of the art and new frontiers, European Materials Research Society (2018)
- 24th Humantech paper award, Bronze award in Material Science & process, Samsung Electronics (2018)
- Selected as a promising young scientist of Korea, The Korean Academy of Science and Technology (2016)
- 22nd Humantech paper award, Bronze award in Physical Devices, Samsung Electronics (2016)
- 21st Humantech paper award, Gold award in Material Science & Process, Samsung Electronics (2015)

## Acknowledgements

It is a great honor to successfully finish my 7 years Ph.D. course. This work would not have been possible without the help and support of a lot of people, and I would like to express my sincere appreciation in this page.

First of all, I hope to give great thanks and deep respect to my advisor, Prof. Hyunhyub Ko. I was able to arrive at this point in safety thanks to his continuous encouragement and guidance as well as strong patience for watching me grow as an independent researcher for 8 years from the undergraduate. I will treasure all the things I learned from him and continue to strive to be a better researcher. Furthermore, I really thank my thesis committee members, Prof. Sang Kyu Kwak, Prof. Chang Young Lee, Prof. Sang Il Seok, and Prof. Myoung Hoon Song for their willingness and advice on my work.

I would like to express my gratitude to current and old Functional Nanomaterials and Devices Laboratory (FNL) members whose assistance has been a great help to my work. I will never forget all the memories that I have had with FNL members during the past 8 years. Especially, I would like to thank Dr. Jiwon Lee, Sehee Ahn, and Young-Eun Shin who helped me adapt to the laboratory and gave me the example of a good life in laboratory. Furthermore, I am grateful to Dr. Doo-Seung Um who devoted considerable effort and time on advice and counsel for me as a senior in life and a team member. Additionally, I would like to thank Youngsu Lee for his dedicated help and support.

I wish to extend special acknowledgement to Dr. Minjeong Ha. I have no doubt that I have enjoyed my Ph.D. course and overcame many difficulties with your sincere support and encouragement. It is the greatest luck of my life to meet you, and I'll always remember our time together.

Finally, none of this would have been possible without the incredible trust and support given to me by my family. I am deeply indebted to my parents, Gyeonguk Lim and Okin Kim. I was able to concentrate on my research without any concern thanks to their endless love and support. Also, I really appreciate my younger brother, Seongbeom Lim, for being a strong buttress at home on my behalf. The time we spent together on the weekend was a lot of helps to me.

I would like to attribute this glory to all those who have given me generous support, love, and believe. I promise to be a nice man and good son as well as an excellent researcher to repay your support and kindness.

## 감사의 글

지난 10년간 UNIST에서의 긴 시간을 잘 마무리하고 박사학위를 받아 감사의 글을 쓰게 되는 이 시점에서 감회가 새롭습니다. 많은 분의 도움이 없었다면 지금의 이 시간은 오지 않았을 것이기에 이 글로써 짧게나마 감사를 표하고자 합니다.

먼저 2011년 학부 인턴부터 지금까지 8년이 넘는 시간 동안 저를 독립적인 연구자가 될 수 있도록 지도해주신 고현협 교수님께 진심으로 감사드립니다. 더 좋은 연구를 위해 아낌없는 지원을 해주시고, 항상 부족하지만 홀로 생각할 시간을 주시고, 느리지만 인내심을 가지고 지도해주신 덕분에 성공적으로 박사학위를 취득할 수 있었습니다. 교수님께서 지도해주신 모든 것들을 잊지 않고 정진하여 자랑스러운 제자가 될 수 있도록 노력하겠습니다. 또한, 바쁘신 와중에도 저의 박사학위 심사위원을 맡아 주시고 많은 조언과 격려를 해주신 광상규 교수님, 이창영 교수님, 석상일 교수님, 송명훈 교수님께도 감사의 말씀을 드립니다. 좋은 말씀도 많이 해주시고, 찾아볼 때마다 연구에 매진하고 계시는 모습을 보면서 다시 한번 초심을 되새길 수 있었습니다.

편한 마음으로 연구할 수 있도록 도와준 기능성 나노 소자 연구실 (FNL)의 구성원 모두에게도 감사를 전하고 싶습니다. 먼저, 저를 연구실에 잘 적응할 수 있도록 도와주신 지원 누나와 제가 마지막까지 성실하게 연구실 생활을 할 수 있도록 초기에 연구실 생활의 모범을 보여주신 세희 누나와 영은 누나에게 감사합니다. 또한, 연구실 선배이자 인생 선배로서 지금까지도 저에게 조언과 관심을 아끼지 않으시는 두승이 형에게 항상 감사하고, 화목한 분위기의 연구실을 잘 조성해 주신 세원이 형과 종화 형에게도 감사합니다. 같은 반도체 팀 후배로서 연구실의 굿은일을 도맡아 하는 영수도 졸업까지 많은 도움을 주시고 고맙고, 호찬이, 승영이, 영오, 아영이, 승세, 정희, 두 진영이, 영렬이 형, 상윤이, 동희, 유정이에게 연구실 동기와 후배로서 좋은 추억을 함께해줘서 고맙다는 말 전합니다. 우리 연구실이 더욱더 번창하길 기원해봅니다.

연구를 진행하는 동안 연구실 외에 나노소자공정실의 김형일 선생님, 김민재 선생님, 박동규 선생님, 이루다 선생님, 강해라 선생님에게도 많은 도움을 받았습니다. 매번 귀찮으셨을 텐데 항상 본인 일처럼 잘 도와주셔서 감사드립니다.

UNIST에 입학해 첫 룸메이트로 만나서 지금까지 인연을 계속하고 있는 201호 친구들, 승욱이 형, 민이 형, 태영이, 예녹이, 근욱이, 원경이, 신명이도 박사과정의 힘든 기간에 큰 힘이 돼 주어 고맙고, 앞으로도 자주는 못 보겠지만 각자의 위치에서 더욱 성공하길 바랍니다. 또한, 명절마다 만나서 재미없는 박사과정 얘기 들어주고 매번 먼저 안부 물어주는 친구 근오와 성렬이에게 고맙다는 말 전합니다.

연구실 동기이자 연인인 민정이에게 특별한 감사를 전하고 싶습니다. 그녀와 함께했기에 힘든 시간을 잘 극복하고 즐겁게 박사과정을 수행할 수 있었다고 믿어 의심치 않습니다. 모든 일에 열정적으로 참여하는 그녀의 모습은 연구자로서 저에게 큰 자극제였으며, 그녀가 보내준 전폭적인 지지와 응원 덕분에 포기하지 않고 앞으로 나아갈 수 있었습니다. 언제나 저의 활력소가 되어주고 함께 해주어서 감사합니다. 사랑합니다.

마지막으로 세상에서 가장 소중한 우리 가족에게 감사함을 전합니다. 10년이라는 긴 시간 동안 타지에서 공부하는 아들을 변함없는 믿음으로 지지해주시고 응원해주신 아버지와 어머니께 감사드립니다. 그 사랑에 보답할 수 있도록 노력할 테니 항상 건강 잘 챙기셨으면 좋겠습니다. 그리고 집에 갈 때마다 함께 시간 보내주고 응원해 준 동생 성범이도 고맙고, 자신의 안전도 잘 챙기는 경찰이 되길 바랍니다.

이 시간이 올 때까지 저를 위해 많은 도움과 사랑과 믿음을 주었던 모든 이에게 이 영광을 돌리며, 이에 보답할 수 있도록 훌륭한 연구원이자 좋은 사람이 될 것이라 약속하며 이 글을 마칩니다.

2019년 5월 20일

임 성 동

